REVIEW ARTICLE

Check for updates

[FeFe]-Hydrogenases: maturation and reactivity of enzymatic systems and overview of biomimetic models

Julian T. Kleinhaus,[†a] Florian Wittkamp,[†a] Shanika Yadav,[†a] Daniel Siegmund [b] and Ulf-Peter Apfel [*ab]

While hydrogen plays an ever-increasing role in modern society, nature has utilized hydrogen since a very long time as an energy carrier and storage molecule. Among the enzymatic systems that metabolise hydrogen, [FeFe]-hydrogenases are one of the most powerful systems to perform this conversion. In this light, we will herein present an overview on developments in [FeFe]-hydrogenase research with a strong focus on synthetic mimics and their application within the native enzymatic environment. This review spans from the biological assembly of the natural enzyme and the highly controversial discussed mechanism for the hydrogen generation to the synthesis of multiple mimic platforms as well as their electrochemical behaviour.

a Inorganic Chemistry I, Ruhr University Bochum, Universitätsstraße 150, 44801 Bochum, Germany. E-mail: ulf.apfel@rub.de

b Department of Electrosynthesis, Fraunhofer UMSICHT, Osterfelder Str. 3, 46047 Oberhausen, Germany. E-mail: ulf.apfel@umsicht.fraunhofer.de

† These authors contributed equally.

I Introduction

Hydrogen plays an ever-increasing role in our modern society and is anticipated to serve as a green and sustainable energy carrier as well as storage in future. While already produced on a large scale, current production of hydrogen is industrially realized by reforming of fossil fuels. Notably, only a small fraction is currently generated by water splitting.

Contrary to the industrial generation of hydrogen and the political as well as societal demands to use more hydrogen, nature has almost perfected the handling of this small molecule. In a small number of eukaryotes (green algae) but more importantly in specialised anaerobe microorganisms (bacteria as well as archaea) hydrogen can act as the primary energy carrier. Among the enzymes that allow for hydrogen transformation, [FeFe]-hydrogenases are the most competent. The active site of these enzymes commonly comprises a hexanuclear Fe-cofactor, consisting of a [4Fe–4S]- and a [2Fe–2S]-cluster. The most commonly investigated [FeFe]-hydrogenases are from *Clostridium pasteurianum* (*Cp*), *Desulfovibrio desulfuricans* (*Dd*) and *Chlamydomonas reinhardtii* (*Cr*).[1,2] Notably, these enzymes can be regarded as "fuel and electrolysis cells" and allow for the reversible interchange of protons to hydrogen with a turnover

Julian T. Kleinhaus received his MSc in Chemistry in 2019 from the Ruhr-University Bochum. Under the supervision of Prof. Dr U.-P. Apfel, he focused on establishing synthesis routes for new [FeFe]-hydrogenase mimics. During his PhD studies in the Apfel group, he investigates novel electrocatalytic applications for biomimetic and bio-inspired catalysts.

Julian T. Kleinhaus

Florian Wittkamp joined the group of Ulf-Peter Apfel in 2014 for his undergraduate studies and changed to the field of [FeFe]-hydrogenases in 2015. He got his PhD from the Ruhr-University Bochum in 2020. In his thesis he discussed the chemistry of the [FeFe]-hydrogenases' active site und is currently still interested in designing new biomimetic models as possible replacement for the native H-cluster.

Florian Wittkamp

1668 | *Chem. Soc. Rev.*, 2021, **50**, 1668–1784

This journal is © The Royal Society of Chemistry 2021

frequency of up to over 10 000 μmol (H$_2$) min mg^{-1} (enzyme) under mild conditions (−0.413 V *vs.* standard hydrogen electrode, pH 7).[3] It is thus very plausible that this enzyme system received increased attention and scientists all over the world have taken the active centres of hydrogenases as a template to design mimetics which display a comparable activity for the hydrogen evolution reaction. We will herein attempt to provide a complete picture on developments in this field in the last two decades since the structure of the active site of [FeFe]-hydrogenases was revealed. Starting out from recent advances in artificial maturation of fully functional enzymes, we will continue in describing the reactivity of the natural H-cluster. Going further, we will present synthetic pathways towards [FeFe]-hydrogenase mimics, show the plentiful chemical alterations and their impact on the structure as well as their electrochemical properties. As a subject of growing interest, our discussion will furthermore shed light on the possibility of photocatalytic hydrogen evolution using hydrogenase mimics.

Part A: the chemistry of [FeFe]-hydrogenases

II Maturation of natural and semi-artificial [FeFe]-hydrogenases

2.1 Native *in vivo* maturation

The biosynthesis and assembly of the complete active site of [FeFe]-hydrogenases, called H-cluster, requires the interaction of several maturase proteins HydG, HydE and HydF (see Fig. 1 for an overview). Its whole structure is rather uncommon in biology and consist of two individual iron–sulphur clusters, which are linked by a cysteine sidechain. The first is a [4Fe–4S]-cluster, herein abbreviated with [4Fe]$_H$, which is responsible for electron delivery and serves as electron reservoir by switching between an oxidized and reduced state during the catalytic cycle. The second iron-sulphur cluster is a [2Fe–2S]-cluster. This subsite will be abbreviated [2Fe]$_H$ and represents the actual active centre, being the site of catalytic turnover. Depending on the position relative to [4Fe]$_H$, the single iron atoms are termed proximal iron (Fe$_p$) and distal iron (Fe$_d$), respectively. Fe$_p$ is octahedrally coordinated by the cysteine's thiolate, a terminal CO and CN$^-$ ligand each, two bridging sulphides that form the [2Fe–2S]-cluster and an additional μ-CO ligand, which is in a bridging binding mode between both iron atoms. Fe$_d$ shows identical ligands but lacks the thiolate of the cysteine therefore showing a square-pyramidal coordination sphere. At the open binding site substrates, *e.g.* H$^+$ in the H$_{hyd}$ state and H$_2$ in the H$_{ox}$–H$_2$ state, as well as inhibiting diatomic gases like CO (**H$_{ox}$-CO**) and O$_2$ (**H$_{ox}$–O$_2$**) may bind. [2Fe]$_H$ is further coordinated by a secondary amine *via* the bridging sulphides, why this ligand is mostly called adt (azadithiolate, precisely: bis(sulfido-methyl)amine). The whole [2Fe]$_H$ cluster, bearing the adt ligand, is therefore casually called ADT. For a complete graphical representation of the H-cluster see Fig. 1, red box.

Shanika Yadav

Shanika Yadav received her BSc (2015) and MSc (2017) degree in Chemistry from University of Pune, India. In 2019, she received the "DAAD-Graduate School Scholarship" and joined the group of Prof. Ulf-Peter Apfel as a PhD student. Her current research focuses on synthesis of active site mimics of [FeFe]-hydrogenases and investigation of oxygen sensitivity of the enzyme.

Daniel Siegmund

Daniel Siegmund obtained his PhD at the University of Bochum for his work on the development of novel organometallic anti-biotics with Prof. N. Metzler-Nolte. In 2018 he joined the Fraunhofer Institute for Environmental, Safety and Energy Technology (UMSICHT) in Oberhausen where he is currently a group leader for electrocatalysis in the department of energy. His research interests focus on the development of precious metal-free electrocatalysts for hydrogen evolution and CO$_2$-reduction as well as the establishment of sustainable electrocatalytic synthesis processes for organic commodity and fine-chemicals.

Ulf-Peter Apfel

Ulf received his PhD from the Friedrich-Schiller University Jena. After a postdoctoral stay at MIT (2011/2012), he started his independent career at the Ruhr University Bochum funded by the "Fonds der Chemischen Industrie" and the DFG as an Emmy Noether group leader. He holds a professorship at the Ruhr University Bochum since 2019 and is leading the department Electrosynthesis at Fraunhofer UMSICHT. His research interests are in the field of technical electrochemistry with a special emphasis on the electrochemical reduction of CO$_2$ and protons and catalyst design.

This journal is © The Royal Society of Chemistry 2021

Chem. Soc. Rev., 2021, **50**, 1668–1784 | **1669**

Fig. 1 Overview of biological maturase machinery of [FeFe]-hydrogenases. White: N-terminal radical SAM functionality in HydG to initiate the degradation of tyrosine. Grey: reactions performed by HydG yielding a $Fe_2S_2(CO)_4(CN)_2$ core or a $FeS(CO)_2CN$ synthon. Yellow: putative PLP dependent conversion of serine by serine dehydratase and serine hydroxymethyltransferase to ammonia and 5,10-methylene tetrahydrofolate. Blue: putative reactivity of HydE. Green: possible substrates of HydF and assembled $[2Fe]_H$-precursor on HydF. Red: completely matured HydA. PDB entries: HydA: 4XDC, apo-HydF: 3QQ5.2.

In 2010, Mulder and coworkers showed that without HydG, HydE and HydF, the H-cluster contains only the $[4Fe]_H$-cluster (apo-HydA) leading to a change of the quaternary structure of the enzyme. This change results in a positively charged channel leading directly to the active centre, which is used to incorporate $[2Fe]_H$ and is closed in the presence of the complete H-cluster.[4] HydG is part of the radical *S*-adenosyl-L-methionine (SAM) enzyme superfamily and accordingly has the usual reactivity:[5] SAM chelates an iron atom of a $[4Fe–4S]^+$-cluster *via* the carboxy and amine function of methionine. The remaining iron atoms are bound to the protein environment by cysteine residues. The Fe–S cluster induces a reductive cleavage of the bound SAM by an inner-sphere electron transfer, resulting in a highly reactive 5′-deoxyadenosyl radical (5′-DA•) and methionine remains on the now oxidised $[4Fe–4S]^{2+}$-cluster. 5′-DA• abstracts a hydrogen radical of an enzyme specific substrate, forming 5′-DAH and enabling various downstream reactions. In the case of HydG, 5′-DA• abstracts one of the hydrogens of a tyrosine amine group.[6] The resulting tyrosine radical (Tyr•) undergoes a homolytic bond cleavage between

C_α and C_β and decomposes into a 4-hydroxybenzyl radical (4-HOB•) and dehydroglycine (DHG). DHG can subsequently undergo a base-assisted decomposition to form CO as well as CN^- and thus serves as a potential source of the biologically unusual ligands for $[2Fe]_H$.[7–9]

Besides the N-terminal radical SAM functionality, HydG has another Fe–S cluster in C-terminal position: An auxiliary [5Fe–5S]-cluster, which was investigated by EPR spectroscopy and X-ray crystallography.[10] The *g*-values of 9.5, 4.7, 4.1, and 3.7, which are unusual for biological Fe–S clusters, represent an $S = 5/2$ spin. This unusual observation is caused by a ferromagnetic coupling between a $[4Fe–4S]^+$-cluster ($S = 1/2$) and an additional high-spin Fe^{2+} ($S = 2$). Both are connected by a bridging sulphide of a nonproteinic cysteine (Cys). The additional iron is further coordinated by a histidine (His) residue and two water molecules.[11]

The CO and CN^- ligands obtained by the radical SAM functionality first substitute the aqua ligands of the additional iron resulting in a $[4Fe–4S][(Cys)Fe(CO)(CN)(His)]^-$ complex. Subsequently, histidine can also be exchanged by a further CO
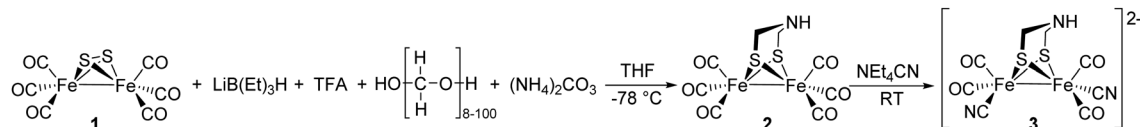
Fig. 2 Synthesis of $Fe_2(adt)(CO)_6$ (**2**) and $Fe_2(adt)(CO)_4(CN)_2$ (**3**) presented by Li and Rauchfuss in 2002.

with the remaining second cyanide binding to the $[4Fe–4S]^+$-cluster and liberating the $[(Cys)Fe(CO)_2(CN)]^-$ complex which serves as a synthon for $[2Fe]_H$. This cyanide-induced release mechanism explains the 4:2 CO:CN ratio of the putative $[2Fe]_H$-precursor. Four tyrosine molecules are required to assemble the putative $[2Fe]_H$-precursor and converted into four CO and four CN^-, two of which are cyanides responsible for the release of the synthon $[(Cys)Fe(CO)_2(CN)]^-$.[6,11]

The role of the synthon has recently been further investigated by Britt and Rauchfuss.[12] Therein, a biomimetic synthon $[FeI_2(CO)_3CN]^-$ together with cysteine was added to a HydA maturation solution consisting of apo-HydA, HydE and HydF only. In the absence of HydG, this mixture was able to completely activate HydA. Furthermore, with ^{13}C and ^{15}N labels and by using selenocysteine, cysteine was unequivocally shown to be the source of the bridging sulphides within the $[2Fe–2S]$-cluster but does not provide the $NH(CH_2)_2$ bridge.[12]

Like HydG, HydE is an enzyme of the radical SAM family with two $[4Fe–4S]$-clusters, as demonstrated by EPR spectroscopy,[13] or one $[4Fe–4S]$- and one $[2Fe–2S]$-cluster, according to X-ray studies.[14] Notably, due to the one-week duration of crystal growth in the X-ray study conducted by Fontecilla-Camps, a degradation of the C-terminal $[4Fe–4S]$-cluster may have occurred and potentially results in the observed $[2Fe–2S]$-cluster. However, the $[4Fe–4S]$-cluster can be removed by mutation without loss of maturase-specific activity and is therefore considered functionally irrelevant for *in vivo* maturation.[14]

Notably, the role of HydE in the HydA maturase machinery has not yet been finally clarified.[7] However, due to its C–S bond formation activity[15] it is assumed that the enzyme is involved in the biosynthesis of the adt ligand.[13] Serine has recently been identified as the source of the $NH(CH_2)_2$ moiety. More specifically, ^{13}C and ^{15}N labels in combination with EPR, HYSCORE- and ENDOR spectroscopy showed that the NH_2 and β-CH_2 groups are incorporated into the adt bridge.[16] It could, however, not be clarified if a further substrate is involved, since possibly only one of the CH_2 groups is derived from serine, or whether two serine molecules are needed for the complete construction of the bridge. HydE might therefore use serine to assemble the adt bridge. Here, the serine dehydratase and serine hydroxymethyltransferase were also considered as potentially involved enzymes that convert serine to pyruvate and NH_4^+ and subsequently with tetrahydrofolate (H_4folate) to glycine and 5,10-methylene-H_4folate, respectively. Glycine and pyruvate were excluded as possible building blocks of the H-cluster.[12,16] However, NH_4^+ and 5,10-methylene-H_4folate, a biological methyl group donor, came into consideration as potential intermediates. With NH_4^+ and 5,10-methylene-H_4folate as reagents, the adt moiety could potentially be introduced into the

precursor, $[Fe_2S_2(CO)_4(CN)_2]^{2-}$, comparable to the artificial establishment of the $[2Fe]_H$-cluster by Li and Rauchfuss in 2002 (Fig. 2).[17]

Furthermore, apo-HydA is activated by HydF, if the latter was expressed together with HydE and HydG.[18,19] As EPR and IR spectroscopy as well as XRD and XAS studies have shown, HydF already contains a $[2Fe–2S]$-cluster alike $[2Fe]_H$. Thus, this maturase enzyme is at the end of the activation chain and passes along the almost completed cluster to HydA.[20] HydF serves as a scaffold for the iron–sulphur synthon, which was inferred from co-purification of HydE and HydG with HydF and confirmed *in vitro* through a combination of surface plasmon resonance and co-purification experiments using recombinant proteins of *C. acetobutylicum*.[18,21–25]

2.2 *In vitro* maturation with artificial H-clusters

In 2013, the groups of Happe, Lubitz and Fontecave showed that chemically synthesised $[2Fe–2S]$-models with modified bridging dithiols can replace the native $[2Fe]_H$ and were successfully incorporated into the apo-enzyme (Fig. 3).[26,27] In contrast to the biological process (see above), maturation was achieved utilising a mixture of apo-*Cr*HydA1 and HydF from *T. maritima*, which was first incubated with the synthetic cluster $[Fe_2(SCH_2XCH_2S)(CO)_4(CN)_2]^{2-}$ (X = NH (adt), CH_2 (pdt), O (odt)). The successful incorporation into HydA1 of *Chlamydomonas reinhardtii* was demonstrated by the specific CO and CN^- bands in the enzyme's IR spectrum. Notably, only the variant with X = NH revealed enzyme-specific hydrogen evolution in the presence of methyl viologen and sodium dithionite at 37 °C.[27] With this study, two major uncertainties in [FeFe]-hydrogenases were finally resolved. First, X equals NH in the native [FeFe]-hydrogenase. Previous XRD studies were only capable to narrow down the options to adt, pdt and odt due to the identical electron count.[3,28] Thus, early suggestions by Fontecilla and coworkers from 2001 and results obtained from ^{14}N-HYSCORE measurements by the group of Lubitz in 2009 were once and for all proven right.[29,30] Second, it was shown that although the [FeFe]-hydrogenases were obtained from different organisms, *T. maritima* and *C. reinhardtii*, the maturase enzymes are identical in function.

Even more remarkable – the very same groups showed that *Cr*HydA1 can be activated without the use of the maturase HydF and is spectroscopically indistinguishable from naturally produced enzymes.[26] Herein, the apo-hydrogenase itself is incubated with the synthetic $[2Fe]_H$-precursor (Fig. 4).

This completely artificial process further simplifies the complicated biological maturation process and enables the production and isolation of significantly larger amounts of mature enzymes.[9,26] Especially for spectroscopic applications,

Fig. 3 Overview of HydF depended semi-artificial maturation of HydA. PDB entries: Apo-HydA: 4XDD, HydA: 4XDC, apo-HydF: 3QQ5.
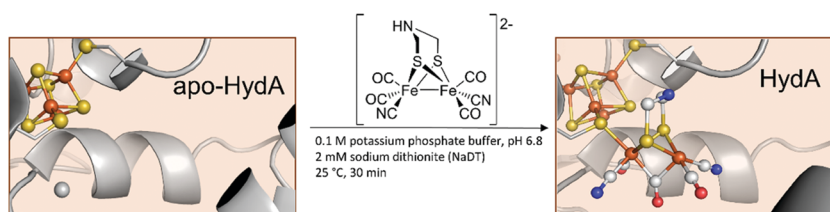

Fig. 4 Schematic representation of the artificial maturation of HydA. PDB entries: Apo-HydA: 4XDD, HydA: 4XDC.

large quantities of high-purity and fully matured enzymes are required. The development of semi-artificial hydrogenases therefore enabled the deciphering of the catalytic mechanism and mode of action of [FeFe]-hydrogenases and thus the possibility to gain information for a new generation of bio-mimetic [FeFe]-hydrogenase catalysts.

Using this artificial approach, however, only 14 different non-native diiron sites were tested so far for their ability to mature apo-HydA1 from *C. reinhardtii*.[31] Although mimics of the binuclear subcluster with an altered bridging dithiolate ligand (propanedithiolate, oxadithiolate, thiadithiolate, *N*-methyl-azadithiolate (adt^{Me}), dimethyl-azadithiolate) and three variants containing only one CN^- ligand were successfully inserted into the apo-enzyme, the activity of those semi-artificial enzymes was below 1% of the native enzyme. In all cases, the insertion process was followed by IR-spectroscopy and the incorporation of the $[2Fe]_H$-mimics is visible by significant line narrowing of the CO/CN^- bands compared to measurements of the sole cluster-mimics in solution. This narrowing indicates a loss of vibrational freedom of the ligands and also implies interaction with the protein backbone. This effect was likewise observed for apo-HydA1 matured with adt-loaded HydF or solely adt.[26,27] Upon isolation of the corresponding adt matured enzyme, multiple signals in the CO region are present indicating a mix of H_{ox}, $H_{red'}$, H_{red}, H_{sred} and minor amounts of H_{hyd}. Contrary, enzymes matured with odt, adt^{Me} and sdt show only H_{ox} and odt is present in H_{hyd} directly indicating varied H-cluster reactivities of the respective semi-artificial enzymes.

Using the same approach, artificial active sites that were modified at the metal or chalcogenide positions were introduced to apo-*Cr*HydA1 and apo-*Cp*1.[32,33] In 2017, Kertess *et al.* presented the semi-artificial enzymes *Cr*HydA1 and *Cp*I that were matured with the selenium derivative of the native cluster, ADSe (**4**). Remarkably, these enzymes showed up to native-like activity regarding proton reduction, but less stability against O_2-degradation and cannibalisation. Thus, significant amounts of H_{ox}-CO were found directly after maturation, which influenced the activity in F-cluster bearing *Cp*I (see Section 3.9) more than in HydA1.[32]

Later in 2018, Sommer *et al.* presented a hybrid-enzyme with a [RuRu]-analogue of ADT, which was investigated due to the interesting reactivity of the noble metal towards hydrogen. Both versions, $[Ru_2(adt)(CO)_4(CN)_2]^{2-}$ (**5**) and the protonated species bearing a bridging hydride (**5-μH**) were found to be in the same state, namely H_{hyd}, after incorporation into the protein environment.[33] Especially the isomerization of the hydride shows the remarkable influence of the protein backbone on the structure of the diiron subsite, stabilizing the thermodynamically less stable terminal hydride (Fig. 5).

2.3 *In vivo* maturation with artificial H-clusters

A more recent approach regarding [FeFe]-hydrogenase maturation and, especially, its modification and *in vivo* investigation was presented by Berggren and coworkers in 2017.[34] The researches transferred the results of the *in vitro* maturation experiments (Section 2.2) to an *in vivo* system consisting of apo-*Cr*HydA1 that was heterologously overexpressed in *E. coli* (Fig. 6). In opposition to former experiments, the hydrogenase was not extracted from its host but left inside the living cells. Since *E. coli* lacks the maturation machinery HydEFG, the hydrogenases inside the cells remain inactive. However, in analogy to the *in vitro* experiments, addition of 1 mg **3** to the cell cultures (O.D. = 0.2 ± 0.02) resulted in a 35- to 40-fold increase over the background H_2 evolution activity, indicating successful activation of the apo-enzymes.[34] The described results represent the first intracellular activation of an apo-enzyme not including improved cellular import functions and opens up the field for *in vivo* spectroscopic investigation of [FeFe]-hydrogenases by *e.g.* EPR and FTIR.[35,36] Even more remarkable is the follow-up study as a joint research of the

1672 | *Chem. Soc. Rev.*, 2021, **50**, 1668–1784

This journal is © The Royal Society of Chemistry 2021

Fig. 5 Synthetic subsite models with chalcogen or metal exchange that has been implemented into apo-enzymes.

Fig. 6 Graphical representation of the artificial *in vivo* maturation of bacteria *e.g. E. coli*.

groups of Berggren and Lindblad, who targeted the modification of the photoautotrophic cyanobacterium *Synechocystis* PCC 6803. This bacterium harbours a bidirectional [NiFe]-hydrogenase for energy household. However, for biotechnological energy applications, high rates of hydrogen evolution are wanted. Here, the [NiFe]-hydrogenase is by far surpassed by [FeFe]-hydrogenases. Therefore, the hydrogenase *Cr*HydA1 was expressed in a hydrogenase deficient mutant of *Synechocystis* PCC 6803 (*Δhox*) as well as in the wild type (WT) organism, containing the native [NiFe]- and the additional [FeFe]-hydrogenase. Upon addition of compound **3**, *Synechocystis* *Δhox* *Cr*HydA1 and WT-*Cr*HydA1 showed a hydrogen evolution activity of approx. 62 and 48 (nmol O.D.$^{-1}$ mL^{-1}), respectively, whereas the organisms without **3** showed almost zero activity (*Synechocystis* *Δhox* *Cr*HydA1) and 17 (nmol O.D.$^{-1}$ mL^{-1}) for WT-*Cr*HydA1. This nice work of bio-engineering underlines that the hydrogen production rates of *Synechocystis* can be increased by enzyme optimization and opens a new field of artificially improved enzymes for biotechnological hydrogen production.[37]

III Reactivity of the H-cluster within the enzyme

The hydrogenase activity of green algae was investigated already 80 years ago by Gaffron and coworkers, who found *S. obliquus* to metabolize H$_2$ upon reduction of CO$_2$ in photosynthesis.[38,39] Among all algae, *C. reinhardtii* with an *in vitro* activity of 200 nmol H$_2$ (µg *Cr a* h)$^{-1}$ bears by far the most investigated [FeFe]-hydrogenase HydA1.[40–42] This hydrogenase contains solely one Fe–S cluster assembly, called H-cluster, and no additional accessory Fe–S cluster for *e.g.* electron transport as in hydrogenases from *D. desulfuricans* and *C. pasteurianum*.[43–47] Its simplicity thus makes HydA1 most convenient for researching the molecular proceedings of H$_2$ turnover during catalysis.

The H-cluster consists of a [4Fe–4S]- and a [2Fe–2S]-cluster, which are linked and electronically coupled *via* a cysteinyl

thiolate.[1,3,28,48,49] The cubic iron cluster, embedded into the protein by three additional cysteine residues, is part of the electron chain and, more importantly, is the midpoint of a proton coupled electron transfer (PCET) at the beginning of the catalytic cycle.[50–52] The diiron subsite conducts the catalytic proton reduction and is the focal point on mimics of the [FeFe]-hydrogenases as we will discuss in Section IV. The diiron site consists of a proximal iron that has an octahedral ligand environment and a distal iron in a square pyramidal coordination with an open binding site for substrates (H$^+$/H$_2$) and exogenous ligands such as CO and O$_2$ (Fig. 8). This geometry of the H-cluster in its **H$_{ox}$** state is called "rotated state", which refers to the rotation of the distal iron relative to the C_{2v} symmetric Fe$_2$S$_2$(CO)$_6$ core. This special geometry opens a vacant binding site for catalytic turnover and is a unique feature of this active site and was a dominant motif for the design of H-cluster mimics for hydrogen evolution (Fig. 8, Section 5.1).[53]

We now want to review the reactivity of the H-cluster within the native protein environment. This will include the natural [FeFe]-hydrogenase HydA1 from *C. reinhardtii*, but also hydrogenases from other organisms like *C. pasteurianum*, *D. desulfuricans*, the sensory hydrogenase HydS from *T. maritima* as well as the half-synthetically obtained hydrogenases. Besides different organisms, we will especially highlight the man-made alterations within the [FeFe]-hydrogenases, ranging from different [2Fe–2S]-cluster to mutants, for spectroscopic or stability reasons.

3.1 ADT-bridged [FeFe]-hydrogenase from *C. reinhardtii*

*Cr*HydA1(ADT) is the active enzyme version of the [FeFe]-hydrogenase from *C. reinhardtii* (therefore denoted *Cr*), in which all intermediates of the catalytic cycle are generally available. Note that more than ten different redox states of the enzyme are nowadays accessible, in which protonation and reduction may occur at different moieties of the H-cluster
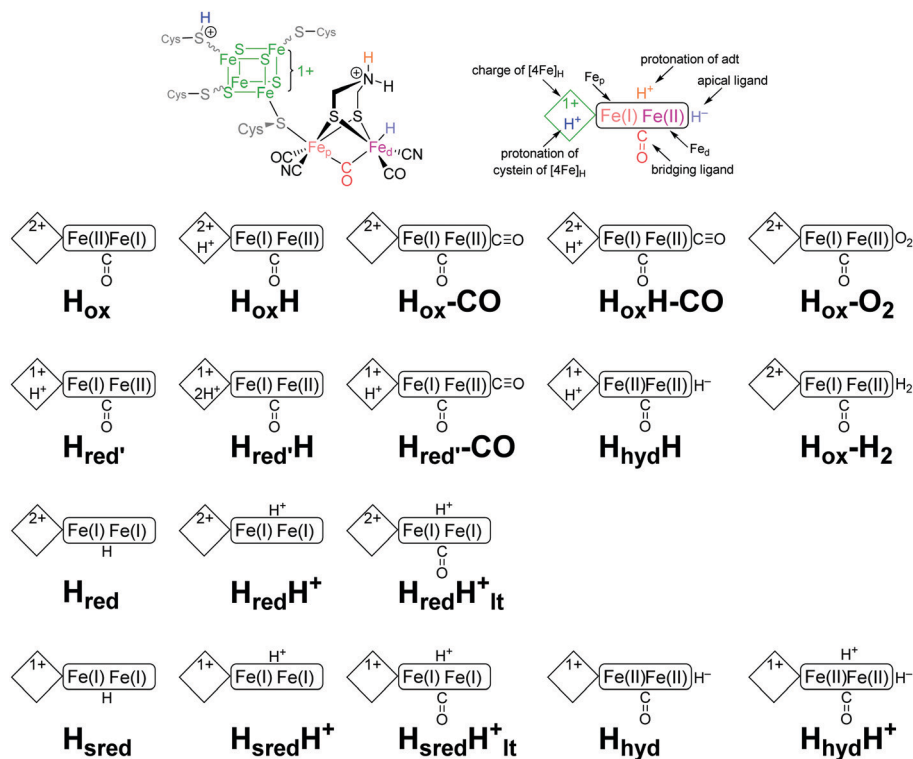
Fig. 7 Overview of all considered H-cluster states within this review.

Fig. 8 H-cluster of [FeFe]-hydrogenases with indicated rotated motif of the distal iron atom (green) vs. the $Fe_2S_2(CO)_6$ core in C_{2v} symmetry (red).

during catalysis (Fig. 7). As shown in the experiments on *Cr*HydA1(ADT) with NaDT (sodium dithionite) or H_2, selective enrichment of the intermediate states is challenging, often resulting in blurred spectroscopic results, which impede the exact determination of the nature of each redox state. Using difference spectra is one potential option to handle this problem in IR-spectroscopy. However, for this approach specific equipment is required, which is not accessible in all laboratories.

Therefore, hybrid enzymes, having a bridgehead moiety that differs from adt, as well as mutants providing selectively exchanged amino acids within the peptide backbone are promising options to influence the activity of the enzyme and therefore the accessibility of the H-clusters' redox states. In the next section, we therefore discuss those modifications and

highlight the differences towards *Cr*HydA1(ADT) and their opportunities for spectroscopic applications.

3.2 Reactivity of *Cr*HydA1(ADT) towards oxidising conditions

H_{ox} is the oxidised resting state of the H-cluster and therefore starting point of most conducted experiments. This state can be enriched by treating the enzyme with mildly oxidising reagents such as thionine buffered at pH 8 (E^0 = 60 mV vs. SHE at pH 7). However, due to cannibalisation under these conditions, a mixture of H_{ox} and H_{ox}-CO (Section 3.3) is achieved.[54,55] The cannibalisation process is based on the degradation of a fraction of the enzyme sample under influence of e.g. light or oxygen.[54,56,57] Thereby, the released CO binds to the intact H-cluster from a non-degraded enzyme and blocks the active site while forming H_{ox}-CO.[58] Therefore, H_{ox} can be better enriched by auto-oxidation under inert conditions (e.g. N_2), which results in a near quantitative enrichment of this state.[55,59]

The electronic structure of the enzymes resting state H_{ox} from *Cr*HydA1 was investigated by different techniques. EPR spectroscopy (Table 1) on native *Cr*HydA1 which was not treated with any oxidant or reductant (termed "as-isolated") shows a rhombic 2.1 signal (g = 2.100, 2.037, 1.996) and an axial 2.05 signal (g = 2.052, 2.007).[55,57,60] The former signal resembles the EPR signal of H_{ox} that is known from measurements on hydrogenases from *D. desulfuricans* (*Dd*H).[49,54] The axial signal accounts for the presence of H_{ox}-CO in the as-isolated samples, likewise known from *Dd*H,[56,62,63] and is absent in auto-oxidised samples.[55] ENDOR-spectroscopy (ENDOR = electron nuclear double resonance) on native *Dd*H in combination with

1674 | *Chem. Soc. Rev.*, 2021, **50**, 1668–1784

This journal is © The Royal Society of Chemistry 2021

Table 1 EPR values of known H-cluster states in different organisms

state	*Cr*HydA1			*Dd*H			*Cp*I			*Cp*II			*Tm*HydS	
	g-Value		Ref.	g-Value		Ref.	g-Value		Ref.	g-Value		Ref.	g-Value		Ref.
H_{ox}	2.10, 2.037, 1.996		60	2.100, 2.040, 1,999		49	2.10, 2.04, 2.00		49	2.078, 2.027, 1.999		49	2.113, 2.045, 2.001		61
H_{ox}-CO	2.052, 2.007		60	2.065, 2.007, 2.001		49	2.07, 2.01, 2.01		49	2.032, 2.017, 1.997		49	2.045, 2.918, 2.007		61
H_{red}	Silent			Silent			Silent			Silent			Silent		
H_{sred}	2.076, 1.943, 1.868		60	^{a}			^{a}			^{a}			^{a}		
$H_{red'}$	Silent			Silent			Silent			Silent			Silent		
H_{hyd}	Broad signal centred between 2.3 and 2.07		55	^{a}			^{a}			^{a}			^{a}		

^{a} Not reported.

Mössbauer spectroscopy on hydrogenase II from *C. pasteurianum* (*Cp*II)[48] concluded that H_{ox} is best described as a mixed-valent paramagnetic $[4Fe–4S]^{2+}$–$[Fe_p^{1+}Fe_d^{2+}]$ complex with the net spin density on the proximal iron atom.[29,49] Due to close similarity of EPR signals from *Dd*H and *Cr*HydA1, H_{ox} was assigned to a $[4Fe–4S]^{2+}$–$[Fe_p^{1+}Fe_d^{2+}]$ state.[55,60] The development of artificial H-cluster maturation (Section 2.2) enabled access to higher amounts of pure *Cr*HydA1, which is especially advantageous for spectroscopic applications and crystallisation experiments. Likewise, the site-selective labelling with ^{57}Fe, *i.e.* labelling either $[4Fe]_H$ or $[2Fe]_H$, became possible with the *in vitro* approach for the first time. Based on this artificially matured *Cr*HydA1, recent studies using site-selective X-ray absorption and emission spectroscopy (XAE-spectroscopy) came to opposing results as compared to ENDOR spectroscopy and suggested a $[4Fe–4S]^{2+}$–$[Fe_p^{2+}Fe_d^{1+}]$ cluster with the net spin density at the distal instead of the proximal iron.[64] As a result, XAE- and EPR spectroscopy remain inconclusive regarding the oxidation states of iron within the diiron site. However, it cannot be concluded, if this discrepancy is a result of technical insufficiencies or is even related to the different enzymes used (*Dd*H and *Cp*I/II exhibit additional Fe-clusters besides the H-cluster that might account for the inconclusive results).

Since the ligand environment of H_{ox} is build up from three CO and two CN^- ligands,[3,28] IR spectroscopy is yet another strong method for its characterisation and the exact position of ligand vibrations is very sensitive to the electron density and cluster geometry.[26,27,65] Typically, vibrations of terminally bound carbonyl ligands are found between 2020 cm^{-1} and 1940 cm^{-1}, whereas their bridging relatives show less intense signals between 1850 cm^{-1} and 1750 cm^{-1}. In addition, terminally bound cyanide ligands characteristically reveal bands between 2120 cm^{-1} and 2020 cm^{-1}.

For example, H_{ox} has a very characteristic IR-spectrum revealing two cyanide bands at 2088 cm^{-1} and 2072 cm^{-1}, two terminal CO bands at 1964 cm^{-1} and 1940 cm^{-1} and the bridging carbonyl at 1800 cm^{-1}.[55,56,60,64,66] In 2016, Stripp and coworkers presented a method to selectively label the H-cluster with ^{13}CO by controlling the hydration of a protein film and exposing it to ^{13}CO gas under light irradiation.[56,59] This enabled the CO band assignment to the specific ligands. Furthermore, DFT calculations on all isotope labelled H-cluster variants further suggested largely uncoupled CO vibrations of the Fe–Fe bridging carbonyl (μ-CO, band α, 1800 cm^{-1}) as well as the terminal ligands
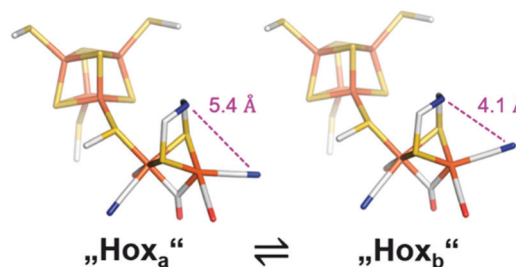

Fig. 9 Conceivable isomers of H_{ox}. Out of two structural isomers of the active-ready oxidised state, "$H_{ox}a$" represents the crystallized geometry while "$H_{ox}b$" is characterized by a partly rotated, distal CN^- ligand. Reprinted from ref. 67 with permission from the American Chemical Society, Copyright 2019.

at the distal ($_dCO$, band β, 1940 cm^{-1}) and proximal ($_pCO$, band γ, 1964 cm^{-1}) iron atoms.[59]

While the experimentally supported DFT-model and the observed structure from protein crystallography are well in line,[3,28] a second structure with an apical CN^- was likewise found to be a suitable state (Fig. 9, $H_{ox}b$).[59,67] However, while $H_{ox}a$ was obtained based on XRD measurements at low temperature (approx. 80 K),[3,28] the structure $H_{ox}b$ stems from a DFT calculation/IR spectra analysis conducted at room temperature. Thus, $H_{ox}b$ might be a higher energy state of H_{ox}. While the reason for this discrepancy is not known, H-cluster flexibility might be an important feature in order to stabilise redox states with additional ligands at the distal iron (*i.e.* H_{ox}-CO and H_{hyd}, Section 3.5).[67,68] The exact assignment of the spectroscopic bands furthermore enabled insight into the electronic structure as well and allowed to resolve the discrepancy from EPR and XAE-spectroscopy, which remained inconclusive regarding the oxidation states of the diiron site. According to IR-spectroscopy, the $[Fe_p^{2+}Fe_d^{1+}]$ configuration should be favoured, since the CO band of the proximal ligand is shifted to higher wavenumbers compared to the signal of $_dCO$ thus supporting the EPR analysis and hints towards a decreased electron density at the proximal iron centre.

3.3 Reactivity of *Cr*HydA1(ADT) towards CO

As mentioned in the previous section, cannibalisation by treatment with thionine leads to H_{ox}-CO besides H_{ox}. Intentionally, this state can be enriched by treatment of H_{ox} with exogenous CO gas.[62,66] Hammerström, Lubitz and coworkers reported that

This journal is © The Royal Society of Chemistry 2021

Chem. Soc. Rev., 2021, **50**, 1668–1784 | **1675**

the additional carbonyl within H_{ox}-CO can be released by a laser pulse with an energy of 355 nm. Using time-resolved FTIR spectroscopy, a half-life of $t_{1/2} = 13 \pm 5$ ms of the dissociated CO could be determined, before rebinding occurs.[69] The molecular structure of the H-cluster in its H_{ox}-CO state was likewise investigated by X-ray crystallography of the CO inhibited hydrogenase I from *C. pasteurianum* (*Cp*I). As expected, electron density that arises from a diatomic ligand was found in apical position of the distal iron, which is accompanied by an elongation of the Fe–Fe distance from 2.56 Å in H_{ox} to 2.71 Å in H_{ox}-CO.[49,62] The IR spectrum of H_{ox}-CO likewise accounts for the extra CO by an additional band in the region of terminal carbonyl ligands (Table 2, $_{d2}$CO, band δ, 2012 cm^{-1}), while bands β and γ shift to 1962 cm^{-1} and 1968 cm^{-1}, respectively.[56,58–60,64,70] These band positions reveal a vibrational coupling of the carbonyl ligands, as already reported by Albracht and coworkers.[66] A pronounced vibrational coupling between all terminal CO ligands was later uncovered by DFT calculations.[59] The nature of the diatomic apical ligand, however, cannot be determined by XRD analyses due to the close geometric and electronic resemblance of CO and CN$^-$. While an apical CO is favoured by most research groups, IR spectroscopy accompanied by DFT analysis suggested a rotation of the distal iron, enabled by the cluster flexibility (see above) and resulting in an apical CN$^-$ instead of an apical CO.[59,64] The electronic structure of H_{ox}-CO is thus still under rigorous debate. The [4Fe–4S]-cluster, consisting of two antiferromagnetically coupled hs-Fe^{II}Fe^{III} ($S = 9/2$) subclusters, is overall in a +2 ($S = 0$) state, similar to H_{ox}. Interestingly, although for singlet spin states such as observed for [4Fe]$_H$ no hyperfine coupling (hfc) should be observed, a pronounced spin exchange between [4Fe]$_H$ and [2Fe]$_H$ results in a strong hfc that differentiates H_{ox}-CO from H_{ox}, where no hfc is observed. Mössbauer,[48,71,72] EPR,[49,71] and X-ray spectroscopy[64,73] as well as computational studies,[64,73] agree well with this finding and suggest a $S \neq 0$ state for [2Fe]$_H$. However, the electronic structure has to be different than in H_{ox} due to the observed hfc of [4Fe]$_H$. Here, early Mössbauer studies by Popescu and Münck favoured a paramagnetic Fe^{II}Fe^{III} state, whereas a Fe^{I}Fe^{II} could not be excluded.[48] The latter description was, however, favoured by Lubitz and coworkers performing ENDOR measurements on ^{57}Fe enriched *Dd*H and suggesting an electronic configuration with a paramagnetic Fe^I in proximal position.[49] Although most of the spin density is at Fe$_d$, a substantial spin delocalisation over the whole cluster was reported as well, which is induced by the binding of the additional CO.[63] Due to the spin coupling between [4Fe]$_H$ and [2Fe]$_H$ and the resulting spin distribution, the EPR spectrum of H_{ox}-CO differs from H_{ox} although the redox state seems to be the same. This coupling results in an axial 2.07 signal ($g = 2.065, 2.007, 2.001$).[49,54,63] The strong spin distribution was also detected by XAE spectroscopy on HydA1 from *C. reinhardtii* that assigned H_{ox}-CO as [4Fe–4S]$^{2+}$–[Fe$^{1.5+}$Fe$^{1.5+}$]$^{3-}$, corroborated by DFT calculations.[64]

3.4 Reactivity of *Cr*HydA1(ADT) towards reducing reagents – A: sodium dithionite (NaDT)

Relative to H_{ox}, multiple single and double reduced H-cluster redox states are known. These can be accessed by treatment of the as isolated or H_{ox} enriched species with chemical reducing agents. At first, we want to consider treatment of H_{ox} with sodium dithionite (NaDT), which has a potential of -660 mV *vs.* SHE at pH 7 and is one of the most frequently used reducing agents in the hydrogenase community. In these assays, NaDT compensates the lack of a physiological electron donor and enables the formation of hydrogen.

Treatment of as-isolated *Cr*HydA1 with a 17-fold concentration of NaDT at pH 8, followed by direct freeze quenching of the samples in liquid N$_2$ results in the loss of H_{ox} specific IR bands in favour of multiple signals (Fig. 10, entry A).[60] Those signals were originally attributed to the single reduced [4Fe–4S]$^{2+}$–[Fe^{I}Fe^I] complex and a double reduced species that is called H_{sred} (= "super reduced"). However, due to the presence of a second bridging CO signal, the existence of H_{ox} in this assembly cannot be excluded. Especially the corresponding EPR spectrum (Q-band, FID detected) points to the presence of unreacted H_{ox}, showing the characteristic rhombic 2.1 signal. In addition, a broad signal with lower g values ($g = 2.076, 1.943, 1.868$) is present in the resulting spectrum. This signal resembles a reduced [4Fe–4S]-cluster, which has to stem from a double reduced H-cluster, since [4Fe–4S]$^{2+}$–[Fe^{I}Fe^I] (H_{red}) and [4Fe–4S]$^+$–[Fe^{II}Fe^I] ($H_{red'}$) are EPR silent.[74] Therefore, the double reduced H_{sred} has to be denoted as [4Fe–4S]$^+$–[Fe^{I}Fe^I] rather than a [4Fe–4S]$^{2+}$–[Fe^{I}Fe^0].[60]

Contrary, King and coworkers observed different results in their IR and EPR spectroscopic investigation under reducing conditions. While a 2-fold NaDT concentration and incubation at 4 °C overnight led to the same states as observed by Lubitz and coworkers (Fig. 10, entry B), a 10- to 20-fold NaDT concentration and incubation at room temperature for one minute led to decreasing bands at 1933 cm^{-1}, 1883 cm^{-1} and emerging bands at 1979 cm^{-1}, 1803 cm^{-1} as well as 1861 cm^{-1} (Fig. 10, entry C), which were not observed in the spectra of Lubitz and coworkers.[55]

Subsequently, EPR spectroscopy was used to disentangle the mixture of states found by IR spectroscopy. Samples reduced with 2 equiv. NaDT at 4 °C afford the H_{red}, $H_{red'}$ and H_{sred} states according to IR spectroscopy. The corresponding EPR spectrum shows a broad signal between $g = 2.3$ and 2.07. Since H_{sred}

Table 2 IR band frequencies of CO and CN$^-$ ligands in *Cr*HydA1

State	ν(CN$^-$)/cm^{-1}	ν(CO)/cm^{-1}	Ref.
H_{ox}	2088, 2070	1964, 1940, 1802	75
$H_{ox}H$	2092, 2074	1970, 1946, 1812	75
H_{ox}-CO	2091, 2081	2012, 1968, 1962, 1808	51
$H_{ox}H$-CO	2094, 2086	2006, 1972, 1966, 1816	51
$H_{red'}$	2084, 2066	1962, 1933, 1792	51
$H_{red'}H$	2086, 2068	1966, 1938, 1800	51
$H_{red'}$-CO	2086, 2076	2002, 1967, 1951, 1793	70
H_{red}	2070, 2033	1961, 1915, 1891	75
$H_{red}H^+$	2071, 2032	1968, 1917, 1891	76
$H_{red}H^+$lt	2079, 2041	1916, 1894, 1810	77
H_{sred}	2068, 2026	1953, 1918, 1882	75
$H_{sred}H^+$	2067, 2027	1953, 1917, 1881	76
$H_{sred}H^+$lt	2070, 2026	1919, 1882, 1803	77
H_{hyd}	2082, 2068	1978, 1960, 1860	75

1676 | *Chem. Soc. Rev.*, 2021, **50**, 1668–1784

This journal is © The Royal Society of Chemistry 2021

Fig. 10 Schematic representation of IR band positions of NaDT reduced *Cr*HydA1 (colored background) in comparison with currently known states (grey background). The concentration factor (*x*) of NaDT is related to the protein concentration. IR signatures of known states are taken from Table 3. References for entries A–G: A,[60] B and C,[55] D,[51] E,[78] F and G.[77]

should be the only EPR active state, this broad signal must occur from this double reduced species. In addition, the temperature and power properties of the broad EPR signal was found to fit best to a reduced [4Fe–4S]-cluster consistent with the findings of Lubitz and coworkers for H_{sred}. Contrary, utilizing 10- to 20-fold concentrated NaDT reduced samples (Fig. 10, entry C), signals of a hitherto unknown state were observed. The EPR spectrum shows a 90% contribution of a broad rhombic signal of *g* = 2.077, 1.935, 1.880 and minor contributions from rhombic 2.1 signal (H_{ox}). Again, a reduced [4Fe–4S]-cluster was suggested to be the origin of this signal. Notably, according to a *post hoc* IR analysis, the dominant species in this sample is H_{hyd}, which was postulated as an intermediate species within the native reaction cycle, *e.g.* a $[4Fe–4S]^+–[Fe^IFe^I]–H^+$ or a $[4Fe–4S]^+–[Fe^{II}Fe^{II}]–H^-$.[55] Therefore, H_{hyd} seems to accumulate under strongly reducing conditions, whereas $H_{red'}$ cannot be found. Both possible H_{hyd} species are uncharacterized intermediates at the beginning of the H_2 splitting cycle or at the very end of the H^+ reduction cycle, respectively.

The experiments described so far were all performed at pH 8. However, the interconversion of protons and molecular hydrogen is according to the law of mass action always dependent on the pH. Therefore, accumulation of intermediate states was thought to be easier when increasing or decreasing the

proton concentration and thus, shifting the equilibrium to a specific H-cluster state. Following this approach, treatment of *Cr*HydA1 in its H_{ox} state with a 4-fold concentration of NaDT at pH 4 resulted in an unknown species with upshifted CO/CN$^-$ frequencies by 4 to 6 cm^{-1} *vs.* H_{ox} instead of accumulation of a reduced species that would have been accompanied with downshifted CO and CN$^-$ frequencies (Fig. 10, entry D). The formation of this species was shown to be reversible when switching back to pH 8.[51] This new species was denoted as $H_{ox}H$, indicating a tentative protonation event at the H-cluster but an overall similar redox state as H_{ox}. Interestingly, no change in the IR pattern could be observed in the absence of NaDT, which points to the necessity of reducing ("turn-over") conditions. Although the transition from H_{ox} to $H_{ox}H$ is not a PCET, since both, $[4Fe]_H$ and $[2Fe]_H$ remain in the same oxidation state according to IR-supported DFT calculations, the pH and NaDT dependent formation of $H_{ox}H$ suggests involvement of a PCET in its formation. Potentially, $H_{ox}H$ is the endpoint of the catalytic cycle, which is PCET based.[51] Deprotonation of $H_{ox}H$ is thus the last step of the H_2 formation cycle and results in the regain of H_{ox}. DFT calculations along with IR spectroscopy were performed to investigate the presence of an additional proton within $H_{ox}H$. The band correlation agreed best with a protonation at the cysteine S9 at $[4Fe]_H$, whereas protonation at one of the four bridging sulphides of the [4Fe–4S]-cluster led to strong cluster distortions and protonation at the first ligand sphere or at $[2Fe]_H$ led to substantial stronger shifts of the CO and CN$^-$ frequencies.[51] Experiments at pH 8 show that H_{hyd} can be found alongside with H_{ox}, H_{red} and H_{sred} under strongly reducing conditions.[55] Drastically increasing the concentration of NaDT (20- to 30-fold) while simultaneously increasing the proton concentration to pH 6 yields almost pure H_{hyd} with minor amounts of H_{red} and H_{ox} (Fig. 10, entry E).[78] This sample was further analysed by NRVS (nuclear resonance vibrational spectroscopy), providing vibrational information only for Mössbauer active elements, *e.g.* iron. The resulting spectrum shows two high energy bands at 675 cm^{-1} and 744 cm^{-1}, characteristic for a terminal bound hydride. Upon changing the medium from H_2O to D_2O both signals are replaced by a new signal at lower energy (629 cm^{-1}), in line with H/D exchange of this terminal hydride.[78] The NRVS spectra were taken as basis for sophisticated DFT calculations to determine a possible structure for H_{hyd}. The best overall agreement between calculated and measured spectra was obtained for a $[4Fe–4S]^+–[Fe^{II}Fe^{II}]–H^-$ species, in which the amine is neutral and with the amine proton pointing towards the hydride forming an internal hydrogen bond.[78] Another hydrogen bond is formed between the lone pair of the amine and the adjacent thiol group of Cys169, which is believed to be the last amino acid in a proton channel towards the H-cluster.[79] Besides the proposed H_{hyd} structure, arrangements with a protonated bridge structure ($R_2NH_2^+$) were tested as well with very low agreement between the calculated and observed spectra. However, such a state was not completely ruled out but considered as potential intermediate species between H_{hyd} and the H_2 releasing/uptaking state.[78]

Besides the influence of the pH value, the relevance of the temperature at which the experiments are performed was highlighted as well. Incubation with an approx. 10- to 20-fold concentration of NaDT (a 20 mM solution NaDT was used for reduction of CrHydA1; however the concentration of the enzyme is not stated) gave a mixture of H_{hyd}, H_{sred}, H_{red} and in minor amounts $H_{red'}$ and H_{ox} both, at 280 K and 40 K.[77] However, at 40 K the intensity of the signal at 1803 cm^{-1} increases strongly. This signal was assigned to a double reduced H-cluster state, which bears a bridging CO that is not detected in H_{sred}[60,80] (bridging hydride) or $H_{sred}H^+$[76] (semi-bridging CO and adt-H$^+$). This assignment is based on the concomitant increase of H_{sred} signals at 40 K. We therefore denote this species as $H_{sred}H^+$-lt that is claimed as [4Fe–4S]$^+$–[Fe^{I}Fe^I] with protonation at the amine, to distinguish between low- and high-temperature states. The low-temperature IR measurements were further strengthened by NRVS measurements and DFT calculations in which both a μ-CO and a μ-H were considered. Models including μ-H produced a high-energy signal around 740 cm^{-1} which was observed in synthetic μ-H models and experiments of [NiFe]-hydrogenases as well,[81] but not found in experiments on [FeFe]-hydrogenases.[77] A μ-H ligand under these conditions was therefore rendered unlikely, while in conclusion a μ-CO ligand was favoured. However, the unchanged frequency of μ-CO compared to H_{ox} is not explained and remains inconclusive from our point of view. The reduction of [4Fe]$_H$ within the $H_{ox} \leftrightarrow H_{red'}$ transition results in a downshift of the μ-CO frequency of 8 cm^{-1}.[51,74,76,82] The same IR band in $H_{sred}H^+$-lt does not shift compared to H_{ox}, although it should result in a larger shift of the μ-CO frequency $vs.$ H_{ox} due to the reduction of [2Fe]$_H$. However, it must be considered that the measurements at 40 K are under non-physiological conditions, which shows that the temperature at which [FeFe]-hydrogenases are investigated, indeed can influence the outcome of the experiment by means of trapping the H-cluster in different states compared to measurements at room temperature.

3.5 Reactivity of CrHydA1(ADT) towards reducing reagents – B: hydrogen (H₂)

Notably, comparable reactivity alterations were observed upon exchange of the reducing agent – $e.g.$ substituting NaDT as reductant with H₂. Under physiological conditions, the former results in formation of H₂ and oxidation of an external electron donor, while the latter variant results in the final reduction of an electron acceptor and formation of protons. This interplay is of utmost importance for balancing energy levels of hydrogenases in living organisms. As an additional benefit from changing to H₂ as reducing agent is the determination of the reversibility of catalytic states. If the respective states are accessible from both approaches, H₂ formation and oxidation, theses states are most likely part of a catalytic cycle, while states that are accessible only by one method might lead to biologically less-relevant resting states or artificial, naturally non-appearing states.

According to IR spectroscopy, flushing of CrHydA1 with 100% H₂ for 15 minutes at 4–24 °C and pH 8 yields H_{sred} with

Fig. 11 Schematic representation of IR band positions of H₂ reduced CrHydA1 (coloured background) in comparison with currently known states (grey background). IR signatures of known states are taken from Table 2. References for entries: A,[55] B,[60] C and D,[82] E and F,[51] G to I,[75] J and K,[67] L.[72]

minor amounts of H_{red}, $H_{red'}$ and eventually very small amounts of H_{ox} (Fig. 11, entries A, B).[55,60] All reduced states can also be accessed by reduction with NaDT, rendering these three states potential intermediate candidates for a H₂ formation cycle. It seems that, depending on the applied temperature, either H_{sred} (higher temperatures, entry B) or H_{red} (lower temperatures, entry A) are favoured. However, due to the opposed measurement temperatures, $i.e.$ 100 K for samples flushed with H₂ at 24 °C and 294 K for samples prepared at 4 °C, a qualitative analysis of this trend cannot be deduced.

It is worth mentioning that under 100% H₂, all single and double reduced species are observed. Here, lower amounts of reducing agents, $i.e.$ 10% H₂ in N₂, result in formation of the single reduced species H_{red} and $H_{red'}$ at the expanse of H_{ox}, while H_{sred} seems to be absent in those samples according to IR spectroscopy (Fig. 11, entries E, F).[51]

The absence of H_{sred} in 10% H₂ treated samples is an advantage compared to all NaDT reduced species. Herein, persistent contributions from H_{sred} crowding the IR spectrum were reported, impeding an evaluation of the resulting spectra. Moving from alkaline pH 8 to more acidic pH 6 (Fig. 11, entries E, F)[51] at constant H₂ concentrations (10%) favoured the formation of H_{red}, H_{ox} and minor amounts of H_{hyd} over $H_{red'}$ and H_{sred} and $vice versa$.[51,72] This behaviour was also observed in a redox titration experiment of CrHydA1(ADT) at different

1678 | $Chem. Soc. Rev.$, 2021, **50**, 1668–1784

This journal is © The Royal Society of Chemistry 2021

pH values (Section 3.6) and was accounted to a "non-classical" intra H-cluster PCET, *i.e.* as transition from a $[4Fe–4S]^+–[Fe^I Fe^{II}]$ ($H_{red'}$) to a $[4Fe–4S]^{2+}–[Fe^I Fe^I]$ (H_{red}) cluster.[76] Simultaneously to the decrease of the $H_{red'}$ marker band at 1933 cm^{-1}, switching from alkaline to acidic pH decreases the signal of the bridging carbonyl at 1972 cm^{-1} with the same rate and indicates that $H_{red'}$ most likely bears a μ-CO, ligand as opposed to H_{red}.[51,76] Therefore, the PCET from $H_{red'}$ to H_{red} was suggested to be coupled to a ligand rearrangement, which has been considered challenging to merge with the large hydrogen turn-over rates of [FeFe]-hydrogenases.[51,68,83]

The previously described conditions used by Stripp and coworkers gave small amounts of H_{hyd} upon increasing the proton concentration to pH 6. This work was later revisited by Winkler and coworkers: upon changing the pH from 8 to 4 while purging a sample of HydA1 with 100% H_2 led to IR bands at 1978 cm^{-1}, 1960 cm^{-1}, 1891 cm^{-1} and 1860 cm^{-1}.[75] While the signal at 1891 cm^{-1} stems most likely from H_{red}, the remaining bands were assigned to H_{hyd} (Fig. 11, entries G, H). This example shows, how Le Chatelier's principle can be applied to enrich specific catalytic states of [FeFe]-hydro-genases within the complex biological environment.[67,75] The simultaneous increase of starting material (H_2) and proton concentration (*i.e.* pH < 6) prevents deprotonation of the H-cluster and traps H_{hyd}. The deprotonation step is therefore presumably involved in the $H_{hyd} \rightarrow H_{red'}$ or $H_{hyd} \rightarrow H_{sred}H^+$ conversion.

However, there is an ongoing discussion about the importance and the assignment of specific states leading to sometimes severe alterations of suggested mechanistic schemes. Nevertheless, and independent of the preferred reaction scheme, H_{hyd} was unequivocally suggested to be a key intermediate in the hydrogen cycle.

Identical results were observed using a dry H_2 stream (Fig. 11, entry I) explained by the loss of proton acceptors, *i.e.* the aqueous medium, and therefore accumulation of H^+ within the enzyme. It was suggested that the lost proton acceptors are equivalent to an increase of the proton concentration by lowering the pH, which yields H_{hyd} as well.[75] A similar effect was observed upon impairing the proton transfer path by *e.g.* disrupting it *via* mutagenesis or exchanging the bridgehead of $[2Fe]_H$ (Sections 3.7 and 3.8).[64,75,78,84,85]

3.6 FTIR spectroelectrochemistry of *Cr*HydA1(ADT)

As shown in the previous section, treatment of *Cr*HydA1(ADT) with reducing agents generally results in a mix of various redox states depending on the redox potential of the used reductants (Fig. 10 and 11). Importantly, preparing specific desired redox states can be controlled by using electrochemical approaches. In addition, since the redox potentials can be selectively adjusted, each redox state of the H-cluster can be enriched to almost complete purity. Especially in combination with IR or EPR spectroscopy (spectroelectrochemistry, SEC), electro-chemical measurements become a powerful tool to investigate *e.g.* proton coupled electron transfers or the redox states in general.[52,58,70,74,76,80,86]

At −300 mV *vs.* NHE or more anodic potentials and broadly independent of pH, H_{ox} is populated according to SEC-IR experiments (Fig. 12, entries A, E, L).[74,76,80] First experiments on *Cr*HydA1 at open circuit potential (OCP) and pH 8 (Fig. 12, entry J) afforded H_{ox}-CO from the cannibalisation process besides H_{ox}. The amount of H_{ox}-CO increased upon switching to −260 mV indicating additional enzyme damage, while the concentration of H_{ox} decreases. Interestingly, going to even more cathodic potentials (−430 mV) led to a complete loss of H_{ox}-CO, while $H_{red'}$ was enriched to almost purity with only minor impurities (Fig. 12, entry N).[58] This behaviour shows that inactive H_{ox}-CO can be reactivated by applying a sufficient reducing potential as long as no exogenous CO is added to the sample. Applying a potential of −300 mV at pH 8 in the presence of exogenous CO yields H_{ox}-CO instead of H_{ox} (Fig. 12, entries Q, T) as well as $H_{red'}$-CO if more reducing conditions are applied (Fig. 12, entries R, S, U).[70,74] Nevertheless, H_{ox}-CO can be found at potentials as low as −600 mV (Fig. 12, entry U). The midpoint potential of the H_{ox}-CO $\rightarrow$ $H_{red'}$-CO conversion was determined to be −360 ± 10 mV at pH 5 (Fig. 12, entries V, W) and −530 ± 30 mV at pH 8 (Fig. 12, entries T, U),[70] which is in line with earlier experiments determining a midpoint potential.[74] A similar pH dependent behaviour was likewise found for the $H_{ox} \rightarrow H_{red'}$ couple in *Cr*HydA1(PDT) (Section 3.7). A shift of 60 mV per pH unit indicates a proton dependent formation of $H_{red'}$-CO according to the Nernst equation (PCET).[70] This protonation event was also assigned to the $H_{ox} \rightarrow H_{ox}H$ transition. It was claimed that the proton herein is located at the $[4Fe]_H$ stabilizing cysteine S9.[51] This protonation decreases the electron density of $[4Fe]_H$ and facilitates the reduction of the [4Fe–4S]-cluster, which is in line with the more anodic midpoint potential at pH 5 (protonated Cys S9) *vs.* pH 8 (unprotonated Cys S9). Supposedly, the electronic structure of $H_{red'}$-CO is therefore best described as $[4Fe–4S]^+–[Fe^I Fe^{II}]$ comparable to the electronic state of $H_{red'}$.[70] The molecular structure of $H_{red'}$-CO is comparable to H_{ox}-CO with an apical vacancy, blocked by CO.[70] According to a DFT-FTIR correlation, rotational freedom of the diiron site can lead to an apical CN$^-$ ligand stabilised by the adjacent NH bridgehead. Notably, no CO-inhibited form of a reduced $[2Fe]_H$ state (H_{red} or H_{sred}) was found under the tested conditions, *i.e.* 100% CO, pH 5 or 8 and −100 to −800 mV *vs.* NHE, which was attributed to a saturated coordination sphere of Fe_d.[70] Therefore, the coordination sphere of the double reduced diiron sites has to be saturated by another ligand, such as a hydride.[80]

Another transition of interest is $H_{red'} \rightarrow H_{red}$, which was addressed *via* H_2 reduction experiments at different pH values by Stripp[51] as well as Lubitz and coworkers.[76] In these experiments, protein films of *Cr*HydA1(ADT) were investigated for their IR band signatures at different pH values upon scanning the potential from −200 mV to −600 mV (Fig. 12, entries E to I). The IR signals at 1933 cm^{-1} and 1891 cm^{-1} were both found to have a maximum at −380 mV at pH 7, while being absent at −210 mV and −540 mV, respectively (Fig. 12, entries E, G, I). Originally, both IR bands were assigned to the same intermediate.[58,60,74] However, at pH 10 the band at
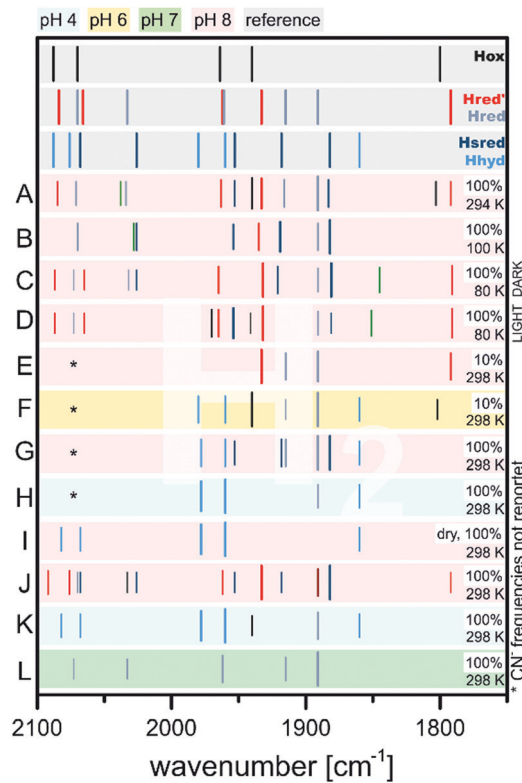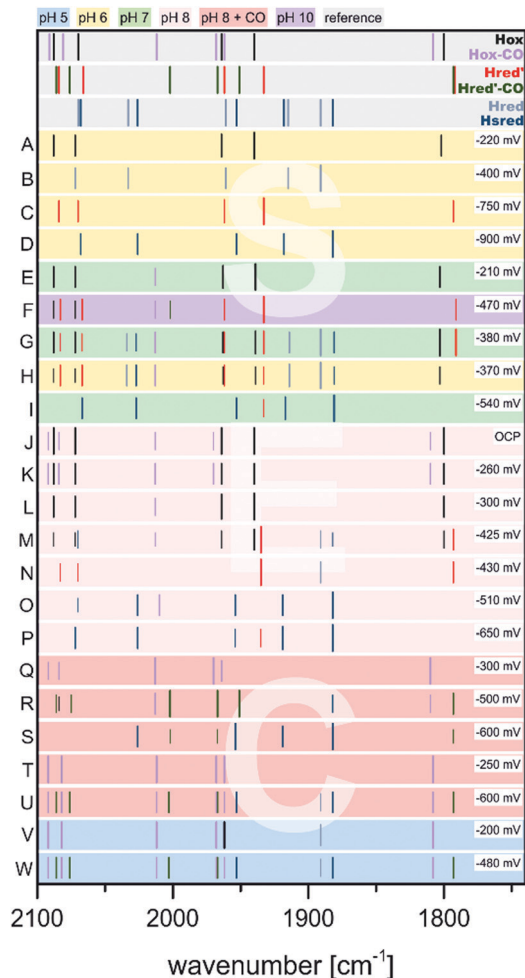
Fig. 12 Schematic representation of IR band positions of electrochemically reduced *Cr*HydA1 (coloured background) in comparison with currently known states (grey background). IR signatures of known states are taken from Table 2. References to entries: (A to D),[80] (E to I),[76] (J, K, N, O),[58] (L, M, P to S),[74] (T to W).[70]

1891 cm^{-1} cannot be found in the IR spectra during the potential scan, while the band at 1933 cm^{-1} occurs upon shifting to more reducing potentials (Fig. 12, entry F) and indicates a pH dependency of these IR bands. On the other hand, acidic conditions were shown to favour the species responsible for the band at 1891 cm^{-1} (Fig. 12, entry H). Due to the acidic conditions at which the latter species was observed, it was subsequently attributed to a reduced protonated form $\mathbf{H_{red}H^+}$. (Note: $\mathbf{H_{red}H^+}$ and $\mathbf{H_{red}}$ show the same IR band signature. We herein use both abbreviations to account for their different protonation state, which is not finally clarified and under severe debate within the community; for additional discussion see Section 3.10 'The catalytic cycle' at the end of this section). Consequently, the band at 1933 cm^{-1} was assigned to an unprotonated reduced form, $\mathbf{H_{red'}}$ (called $\mathbf{H_{red}}$ in the original literature). As a result of this study, the IR signatures of the single reduced H-cluster states $\mathbf{H_{red'}}$ and $\mathbf{H_{red}/H_{red}H^+}$ were assigned as $2084, 2066, 1962, 1933$ and 1792 cm^{-1} for $\mathbf{H_{red'}}$ and $2070, 2033, 1961, 1915$ and 1891 cm^{-1} for $\mathbf{H_{red}}$, respectively.[76] $\mathbf{H_{red'}}$, the

species assembling at alkaline pH, exhibits very small downshifts within the IR spectrum (3 to 7 cm^{-1}) of the CO and CN$^-$ vibrations compared to $\mathbf{H_{ox}}$. A reduction of $[4Fe]_H$ in $\mathbf{H_{red'}}$ is therefore more feasible than a reduced diiron site and is associated with higher shifts of the CO/CN$^-$ frequencies compared to $\mathbf{H_{ox}}$ and $\mathbf{H_{red}}$. Thus, transition from $\mathbf{H_{red'}}$ to $\mathbf{H_{red}}$ is seemingly coupled to an electron transfer from $[4Fe]_H$ to $[2Fe]_H$, which is orchestrated by the pH. If the proton pressure is sufficiently high to protonate the diiron site of $\mathbf{H_{red'}}$ ($[4Fe-4S]^+-[Fe^IFe^{II}]$), the electron migrates from $[4Fe]_H$ to $[2Fe]_H$, resulting in $[4Fe-4S]^{2+}-[Fe^IFe^I]$. According to Sommer *et al.*, this value is pH 6, whereas $\mathbf{H_{red'}}$ dominates already at pH 8 and both are equally present at pH 7.[76] This delicate behaviour might be suitable for pH sensing, inducing subtle changes within the protein backbone upon going from $\mathbf{H_{red'}}$ (alkaline) to $\mathbf{H_{red}}$ (acidic).[72,76] The midpoint potential of the $\mathbf{H_{ox}} \rightarrow \mathbf{H_{red'}}$ transition was found to be -375 ± 10 mV *vs.* SHE with a strong pH-dependency determined by the protonation event at $[2Fe]_H$. The latter event results in a plateau of the midpoint potential for high or low pH. For lower pH, the midpoint potential shifts by -50 mV from pH 7 to 6. This observation is also in line with the $\mathbf{H_{ox}\text{-}CO} \rightarrow \mathbf{H_{red'}\text{-}CO}$ transition, which shows a linear behaviour with a potential shift of 55 mV pH^{-1} between pH 5 and 8. Both processes are consistent with a PCET from $\mathbf{H_{ox}}$ to $\mathbf{H_{red'}}$. While the molecular structure of $\mathbf{H_{red}}$ is thoroughly discussed in literature, up to now its structure was not finally confirmed.[52,61,76,77,80,87,88]

If the potential is swept to more reducing conditions as required for the $\mathbf{H_{red'}} \rightarrow \mathbf{H_{red}}$ transition, a set of IR bands at $2068, 2026, 1953, 1918$ and 1882 cm^{-1} that is similar to the pattern of $\mathbf{H_{red}}$ is observed. However, this set is slightly downshifted and better resembles the $\mathbf{H_{sred}}$ state that is known from NaDT and H_2 reduction experiments.[55,60] The small average downshift of about 5 cm^{-1} of the CO/CN$^-$ frequencies is in line with a reduction of $[4Fe]_H$, as was observed for the $\mathbf{H_{ox}} \rightarrow \mathbf{H_{red'}}$ transition. The electronic structure of $\mathbf{H_{sred}}$ is therefore most likely a $[4Fe-4S]^+-[Fe^IFe^I]$ state, which was already found by EPR spectroscopy as well (Section 3.4).[55,60] The potential needed to accumulate $\mathbf{H_{sred}}$ is likewise pH dependent. At pH 7 and 8, $\mathbf{H_{sred}}$ is obtained as the major species at potentials < -510 mV *vs.* NHE (Fig. 12, entries O, P). Notably, at less cathodic potentials minor $\mathbf{H_{sred}}$ amounts are still present next to $\mathbf{H_{ox}}$ and the single reduced species $\mathbf{H_{red'}}$ and $\mathbf{H_{red}}$ (Fig. 12, entries G, I, M). If the proton concentration is increased to pH 5, *i.e.* conditions that favour the formation of $\mathbf{H_{red}}$, $\mathbf{H_{sred}}$ is accessed more easily and found already at potentials of -480 mV. However, at pH 10, *i.e.* conditions that favour $\mathbf{H_{red'}}$ over $\mathbf{H_{red}}$, $\mathbf{H_{sred}}$ cannot be found.[76] This behaviour of $\mathbf{H_{sred}}$ indicates that it is potentially formed from $\mathbf{H_{red}}$ in the reaction cycle, whereas it cannot be accessed from $\mathbf{H_{red'}}$.

3.7 Influence of alternative dithiolate bridges on the reactivity of the H-cluster

One of the most striking advantages of the (semi-)artificial maturation process (Section 2.2) is the possibility to implement H-cluster mimics that are different from native *Cr*HydA1(ADT) enabling altered reactivity patterns of the hybrid-enzymes.[31]

1680 | *Chem. Soc. Rev.*, 2021, **50**, 1668–1784

This journal is © The Royal Society of Chemistry 2021

These differences in reactivity can then be utilised to target specific H-cluster states and transitions that are otherwise not observable within the native enzymes due to rival reaction pathways, *e.g.* $H_{red'} \rightarrow H_{red}$ *vs.* $H_{red'} \rightarrow H_{hyd}$ or the simultaneous enrichment of multiple states. Such an enrichment of multiple states severely hampers a precise analysis and leads to discrepancies when putting together all the mechanistic puzzle pieces. However, only in case of a similar electronic structures of both, native ADT and the semiartificial enzymes, respectively, proper statements on the various pathways and intermediates are valid. Otherwise the spectroscopically obtained results cannot be transferred from the semiartificial enzyme to the native ADT containing enzyme. For example, a comparable electronic structure of *Cr*HydA1(PDT) compared to the native enzyme can be anticipated due to the similar IR band positions of their CO stretching frequencies, *e.g.* in the H_{ox} resting state.[74] Likewise, the molecular structures of the semiartificial enzyme variants PDT, EDT, ODT and SDT with a propanedithiolate, ethanedithiolate, oxadithiolate and a thiadithiolate bridge are presented in Fig. 13. In all cases, the artificial H-clusters closely resemble the native [FeFe]-hydrogenase with a bridging carbonyl and an open binding site at the distal iron atom under cryogenic conditions of the XRD experiments.[89] The principle of CO-ligand rearrangement that occurs upon artificial maturation, *i.e.* loss of one carbonyl and adopting the rotated structure, is therefore independent of the bridging moiety and seems to be a general feature of $[2Fe]_H$ mimics – at least as long as the steric bulk within the mimic does not prevent accessing the maturation channel.[31]

One of the most frequent alteration of [FeFe]-hydrogenases in literature concerning bridgehead variations in the enzyme and likewise in biomimetic catalysts (see Section 4) is the utilization of the PDT variant (Fig. 13A). Depending on the maturation conditions, it exclusively adopts either H_{ox} or $H_{red'}$ upon maturation. Notably, the PDT variants lack the possibility to enter the H_{red}, H_{sred} as well as H_{hyd} states due to the missing amine functionality and therefore the possibility to undergo an

Fig. 13 Molecular structures of the H-cluster from *C. pasteurianum* artificially matured with (A) propanedithiolate (PDT), (B) ethanedithiolate (EDT), (C) thiadithiolate (SDT) and (D) oxadithiolate (ODT) containing $[2Fe]_H$ clusters. PDB entries 5BYR (PDT), 6H63 (EDT), 5BYQ (ODT), 5BYS (SDT).

intramolecular PCET from $H_{red'}$ to H_{red} or a classical PCET to H_{hyd}.[31,51,76,90]

The H_{ox} state of PDT shows an IR spectrum that is equal to that of H_{ox}^{ADT} showing overall similar electronic situations as well as symmetry and thus support the identical structural features found by XRD experiments in their solid state.[51,52,74,90] Likewise, the EPR spectrum of H_{ox}^{PDT} resembles that of H_{ox}^{ADT}, showing a rhombic signal centred at 2.1 ($g = 2.094$, 2.039, 1.998) further supporting the anticipated $[4Fe–4S]^{2+}$–$[Fe^{II}Fe^{I}]$ state already deduced from FTIR/DFT studies.[74] Under 100% H_2 at pH 8, H_{ox}^{PDT} undergoes a one-electron reduction and fully converts a single product, namely $H_{red'}^{PDT}$. This observation is in stark contrast to the ADT samples, in which H_{red} and H_{sred} are found as well.[55,59,60,67] Furthermore, the IR spectrum of $H_{red'}^{PDT}$ shows CN^- vibrations at 2084 cm^{-1} and 2065 cm^{-1} as well as vibrations of the CO ligands at 1962, 1934 cm^{-1} and 1798 cm^{-1} which are comparable to those of the $H_{red'}^{ADT}$ spectrum.[51] Increasing the proton concentration from pH 8 to 4 while keeping H_2 reducing conditions led in case of ADT to the formation of H_{hyd}.[75] However, since the PDT analogue is not capable to adopt the H_{hyd} state, another state accumulates under these conditions that shows minor upshifted IR frequencies of all CN^-/CO vibrations as compared to $H_{red'}$, *i.e.* 2084, 2068, 1966, 1938 and 1802 cm^{-1}. A similar shift was observed for ADT upon reducing HydA1 at pH 4 with 2 equiv. NaDT and was denoted to a protonation of cysteine S9 at the $[4Fe]_H$. This state was called $H_{ox}H$ accounting for the additional protonation (Fig. 7). According to DFT calculations, the same protonation was suggested for $H_{red'}$. The new upshifted band pattern found in PDT is therefore best explained by a second protonation at one of the $[4Fe]_H$ binding cysteines. According to DFT studies, cysteine S9 is highly favoured as potential protonation site.[51] Due to the additional proton, the new double protonated state is called $H_{red'}H$. Notably, this state cannot be found in ADT, since then only H_{hyd} is found under otherwise identical conditions as reported for $H_{red'}H$.[75]

Furthermore, H_2 reduction experiments on *Cr*HydA1(PDT) show that the H_{ox} and $H_{red'}$ analogues can be very easily enriched to purity. While high purity H_{ox} samples can also be obtained in case of HydA1(ADT), $H_{red'}$ commonly comes along with H_{red} and H_{sred}, especially at pH $\leq$ 7. Nevertheless, Lubitz and coworkers were capable to determine the potential of the $H_{ox} \rightarrow H_{red'}$ transition of HydA1(ADT) to be -375 ± 10 mV *vs.* SHE.[76] A linear correlation between H_{ox} and $H_{red'}$ was found for the CO inhibited species, which are not able to form a reduced $[2Fe]_H$-cluster species.[70] Contrary, utilising PDT enzyme derivatives enables a direct investigation of the $H_{ox} \rightarrow H_{red'}$ transition *e.g.* by SEC-IR techniques without the need of CO inhibition and without side reactions.

Fig. 14 presents the Pourbaix diagram of the transition potentials for $H_{ox} \rightarrow H_{red'}$ (black) and $H_{ox}H \rightarrow H_{red'}H$ (blue) as function of pH value following the peak intensity of the respective marker bands at 1941 cm^{-1} (H_{ox}), 1934 cm^{-1} ($H_{red'}$), 1945 cm^{-1} ($H_{ox}H$) and 1938 cm^{-1} ($H_{red'}H$) as well as subsequent lowering the applied potential from -100 mV to -800 mV *vs.* NHE.[52] The E/pH-slopes of 55 $\pm$ 5 mV pH^{-1}

This journal is © The Royal Society of Chemistry 2021

Chem. Soc. Rev., 2021, **50**, 1668–1784 | **1681**

Fig. 14 Pourbaix diagram showing the transition potentials for $H_{ox} \rightarrow H_{red'}$ (black) and $H_{ox}H \rightarrow H_{red'}H$ (blue) as function of pH value. The slopes are 55 ± 5 mV pH^{-1} (black) and 50 ± 3 mV pH^{-1} (blue) with an approximate off-set of 50 mV that elevates the $H_{ox}H \rightarrow H_{red'}H$ potential above the H/H$_2$ reference (red traces, 59 mV pH^{-1}). Error bars illustrate the quality of the Nernstian fit. Figure and caption are adopted with permission from reference. Reprinted from ref. 52 with permission from John Wiley and Sons, Copyright 2017.

($H_{ox} \rightarrow H_{red'}$, black) and 50 ± 3 mV pH^{-1} ($H_{ox}H \rightarrow H_{red'}H$, blue) indicate a proton coupled reduction of the H-cluster (PCET). Furthermore, the 50 mV lowered reduction potential required for the $H_{ox}H \rightarrow H_{red'}H$ transition suggests a protonation of $[4Fe]_H$ directly affecting the transition potential. This pH dependent transition from $H_{ox}H$ to $H_{red'}H$ is clearly located above the H/H$_2$ reference line (red), which also explains the spontaneous reduction of $H_{ox}H$ in the presence of H$_2$.[52] These results are in contrast to the earlier results on the $H_{ox} \rightarrow H_{red'}$ transition in CrHydA1(PDT) revealing a midpoint potential of -345 mV at pH 8.[74] The respective transition potentials deviate by approximately 130 mV. This discrepancy was, however, hitherto not addressed in the literature afterwards and remains undissolved so far.

The results of these spectroelectrochemical experiments on CrHydA1(PDT) support the assumption of a proton dependent

reduction of the [4Fe–4S]-cluster in $H_{red'}$.[51] Whereas the formation of H_{red} requires the protonation of the native adt bridge, the very same protonation is inhibited due to the absence of the amine in PDT samples.[76] In both cases, a PCET step directs the additional charge either to the $[4Fe]_H$ or $[2Fe]_H$. The results on CrHydA1(PDT) are in line with the findings for a CO inhibited species of CrHydA1(ADT), which shows a 60 mV pH^{-1} linear correlation between the H_{ox}-CO $\rightarrow$ $H_{red'}$-CO midpoint potential and pH. However, the transition to $H_{red'}$, in case of the CO inhibited species, is overall 70 mV more cathodic, showing the influence of the additional CO ligand substitution and leads to an increased electron density at $[4Fe]_H$ and therefore an inhibited reducibility.[64,91] The $H_{ox} \rightarrow H_{red'}$ transition in non-inhibited CrHydA1(ADT) was determined to be -353 ± 10 mV vs. SHE at pH 7. Compared to the results of CrHydA1(PDT), the midpoint potential of the native enzyme is approx. 50 mV more anodic.[76] The selective conversion from H_{ox} to $H_{red'}$ was further utilized to address the concentration dependency of the formation rate of $H_{red'}$. Diluting the enzyme within bovine serum albumin (BSA) results in a severe drop of the $H_{ox} \rightarrow H_{red'}$ conversion rate.[51] This behaviour was explained by an intermolecular electron transfer (disproportionation) between different [FeFe]-hydrogenase enzymes via two-electron reduced species formed upon treatment with H$_2$. Likewise, a comparable behaviour was found in whole cell experiments utilising CrHydA1 expressed in E. coli. Monitoring the IR signatures of the H-cluster while purging E. coli cells with 1% H$_2$ (99% N$_2$), did neither reveal the specific marker band of $H_{red'}$ (1933 cm^{-1}) nor H_{sred} (1882 cm^{-1}). Both states possess a reduced [4Fe–4S]-cluster, which obviously is hardly trappable in living cells.[35]

Contrary to such reduced states, CrHydA1(PDT) and other hybrids (e.g. CrHydA1(SDT), CrHydA1(EDT) and CrHydA1(ODT)) enabled the selective formation of H_{ox} upon prolonged exposure to N$_2$ at pH $\geq$ 8 (auto-oxidation). The CN$^-$ and CO frequencies (Table 3) of EDT and SDT resemble those of the ADT and PDT variants, indicating an equal electron density at the Fe-centres. According to quantum chemical calculations at QM/MM and

Table 3 IR band frequencies of CO and CN$^-$ ligands in hybrid-CrHydA1

State	ν(CN$^-$)/cm^{-1}	ν(CO)/cm^{-1}	Ref.	State	ν(CN$^-$)/cm^{-1}	ν(CO)/cm^{-1}	Ref.
	PDT				**EDT**		
H_{ox}	2090, 2073	1965, 1941, 1810	52	H_{ox}	2090, 2074	1965, 1941, 1809	67
H_{ox}-CO	2094, 2083	2014, 1972, 1965, 1812		H_{ox}-CO	2094, 2081	2019, 1975, 1967, 1812	67
$H_{ox}H$	2090, 2075	1969, 1945, 1814	52	$H_{ox}H$	2094, 2076	1969, 1945, 1814	67
$H_{ox}H$-CO	2095, 2086	2013, 1974, 1968, 1816		$H_{ox}H$-CO	2098, 2087	2071, 1974, 1968, 1819	67
$H_{red'}$	2084, 2066	1963, 1934, 1798	52	$H_{red'}$	2085, 2067	1961, 1933, 1798	67
$H_{red'}$-CO	Not observed			$H_{red'}$-CO	2091, 2080	2015, 1971, 1956, 1807	67
$H_{red'}H$	2084, 2068	1966, 1938, 1802	52				
	ODT				**SDT**		
H_{ox}	2086, 2070	1972, 1948, 1812	75	H_{ox}	2088, 2070	1969, 1942, 1810	67
H_{ox}-CO	2096, 2085	2038, 1979, 1967, 1811	67	H_{ox}-CO	2094, 2081	2019, 1975, 1967, 1812	67
$H_{ox}H$	2093, 2078	1974, 1950, 1813	67	$H_{ox}H$	2091, 2076	1974, 1950, 1814	67
$H_{ox}H$-CO	2096, 2087	2032, 1980, 1971, 1815	67	$H_{ox}H$-CO	2096, 2085	2020, 1978, 1971, 1816	67
$H_{red'}$	2083, 2070	1964, 1943, 1804	67	$H_{red'}$	Not observed		67
$H_{red'}$-CO	2095, 2081	2011, 1978, 1930, 1806	67	$H_{red'}$-CO	Not attempted		67
H_{hyd}	2081, 2076	1978, 1962, 1862	75				

1682 | Chem. Soc. Rev., 2021, **50**, 1668–1784

This journal is © The Royal Society of Chemistry 2021

DFT levels of theory, the overall electronic configuration of all hybrid-enzymes was likewise suggested to be equal to ADT.[67]

Under an atmosphere of 1% CO, all hybrid-enzymes in their oxidised forms adopt the H_{ox}-CO state with the known IR band signature. However, while ADT, ODT and EDT immediately form H_{ox}-CO with near quantitative yields, SDT and PDT revealed slower kinetics and adopt the H_{ox}-CO state only in 65% and 20% yield, respectively. Even in an atmosphere of 100% CO, those two hybrids do not fully convert to the CO inhibited form. In line with those CO inhibition experiments, the decay of H_{ox}-CO to H_{ox} is very fast for SDT and PDT, while it is slow for EDT and very slow and incomplete for ODT and the native ADT forms. In Section 3.3, we already discussed the CO inhibition of CrHydA1 and mentioned the possibility of an apical CN$^-$ ligand in H_{ox}-CO based on a partial rotation of $_dCN^-$ in H_{ox}.[59] The rotation of Fe_d to an apical cyanide ligand in its CO inhibited form might explain the different reactivity of the hybrid enzymes towards CO: While ADT stabilises negatively charged ligands in apical position such as CN$^-$ or H$^-$[78] and thus explains the fast CO inhibition and slow decay of H_{ox}-CO^{ADT}, the other hybrids lack the possibility to form this hydrogen bond. Instead, destabilisation of an apical cyanide leading to an altered kinetic was suggested. Further influences of the non-ADT bridgeheads are the steric repulsion in case of SDT and PDT or electrostatic attractions for ODT and likewise SDT. EDT seems to be unbiased due to the missing bridgehead. Therefore, no stabilising or destabilising effects occur resulting in fast CO inhibition and decelerated H_{ox}-CO decay.[67] Although obvious differences regarding the distal cyanide ligand between native ADT and the hybrid enzymes are present, the CN$^-$ frequencies within their IR spectra do not change. This observation cannot be explained from inner sphere ligand coordination and supports the necessity to also discuss outer sphere coordination, i.e. towards the protein environment. This potential influence will be discussed in a separate section concerning the proton transfer pathway (Section 3.8).

Like for CrHydA1(PDT), hybrid enzymes containing ODT, EDT and SDT bridgeheads were tested for their ability to oxidise H$_2$, thereby adopting the reduced H-cluster states. We already discussed, that PDT does not adopt a diiron-site-reduced form (H_{red}, H_{red}, H_{hyd}) but is trapped in $H_{red'}$ upon reduction with H$_2$.[31,51,52,67] Whereas SDT stays in the H_{ox} state, indicating no reaction with H$_2$, EDT accumulates the H_{hyd} state after initial formation of $H_{red'}$ but returns to H_{ox} very fast in case of dwindling H$_2$. Contrary, the ODT version accumulates H_{hyd} under H$_2$ at a very low reaction rate, which was explained by the diminished ability of the ether headgroup to heterolytically support cleavage of H$_2$, while for ADT H_{hyd} was accumulated at low pH and simultaneous H$_2$ or NaDT reduction.[75,78] Likewise, the regain of H_{ox} from ODT upon switching from H$_2$ to N$_2$, is slower compared to ADT, but faster compared to EDT. In retrospect, it was shown that the amine base of the native H-cluster is of substantial importance, not only for the H$_2$ development, but also for H$_2$ oxidation, by stabilising the apical hydride via a hydrogen bond between NH and H$^-$.[75,78] As in H_{ox}-CO, with a proposed apical CN$^-$ ligand, this stabilisation is

the reason for the different formation and decay rates of ADT vs. hybrid-enzymes, in which an outer-sphere coordination was suggested to stabilise H_{hyd} and H_{ox}-CO.

The IR spectrum of H_{hyd}^{ODT} (2081, 2068, 1978, 1962 and 1868 cm^{-1}) shows blue shifted CO bands compared to H_{ox}^{ODT}, which indicates a decreased electron density within the [2Fe]$_H$-cluster. A $Fe^{II}Fe^{II}$ configuration and a reduced [4Fe–4S]$^+$-cluster most accurately explains this finding and is further supported by the characteristic EPR signal of reduced [4Fe–4S]-clusters adopting the same redox state as found in H_{hyd}^{ADT}.[84] The H_{hyd} state is best described with a terminal H$^-$ at the apical position of Fe_d and was indirectly observed by the different kinetics of hybrid-enzymes and further exploited from H/D exchange experiments revealing the bridging CO in trans position to the apical ligand of Fe_d. Due to the trans effect, an H/D exchange trans to μ-CO, results in a downshifted frequency of the bridging CO and indeed this shift is observed in FTIR experiments performed on CrHydA1(ODT). The bands of the terminal CO and CN$^-$ did not shift upon the H/D exchange.[75,84] Likewise, NRVS measurements on CrHydA1(ODT) displayed high energy bands at 670 cm^{-1} and 727 cm^{-1} for the bending of a terminally bound hydride (Fe_d–H), which shifts towards lower energy (564 cm^{-1} and 625 cm^{-1}) in case of a D$_2$O/D$_2$ environment.[84] Notably, the results from nuclear resonance vibrational spectroscopy (NRVS) experiments on CrHydA1(ODT) differ from those on ADT, which gave significantly different bands for Fe_d–H at 675 cm^{-1} and 744 cm^{-1}, respectively.[78] The DFT based model of H_{hyd} from the NRVS measurements on CrHydA1(ADT) suggests a hydrogen bond between the terminal hydride and the amine headgroup, which cannot be formed in case of the ether moiety of ODT. Although serving as good model for the terminal hydride due to the accumulation of H_{hyd}, the ODT variant of the H-cluster is not able to correctly mimic the hydrogen bonding network between Cys169, NH and Fe_d–H, which is of eminent importance for the reactivity of [FeFe]-hydrogenases.[78] A further possibility to enrich pure H_{hyd} is to impair the proton transfer activity within the enzyme. This can be performed by site directed mutagenesis (SDM) of amino acids within the proton transfer pathway (PTP).[64,75,84–86,92]

3.8 Influence of the proton transfer pathway and mutations thereof on the reactivity of the H-cluster

The main trajectory for protons between bulk water and the H-cluster is formed by an H-bond network between the side chains of the five amino acids R286, E282, S319, E279 and C299 (from the surface to the H-cluster, numbering corresponds to CpI), two water molecules Wat826 and Wat1120 (cumulated as W1 in Fig. 15, PDB-ID 4XDC, chain B) and the secondary amine of [2Fe]$_H$.[79,93,94] In order to address all amino acids to an individually adequate extend, we will start discussing the most inner located amino acid C299 (C169 in CrHydA1) and its mutants and continue going outwards residue by residue. The first amino acid that undergoes a weak hydrogen bond to the NH moiety of the H-cluster is cysteine C299/C169 (CpI/CrHydA1). This side chain is 3.5 Å away from the amine based on the crystal structure 4XDC of CpI. A second hydrogen

This journal is © The Royal Society of Chemistry 2021

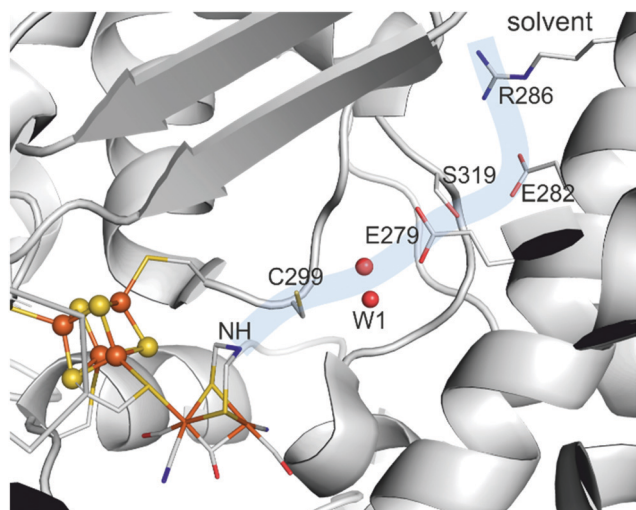Chem. Soc. Rev., 2021, **50**, 1668–1784 | **1683**

Fig. 15 Proton Transfer Pathway (PTP) of [FeFe]-hydrogenase I from *Clostridium pasteurianum* between bulk water and the H-cluster *via* R286(R148), E282(E144), S319(S189), E279(E141), water complex W1 and C299(C169). Amino acid codes in parentheses are the respective residues in *Cr*HydA1. Protein structure from PDB entry 4XDC.

bond (3.2 Å) is formed between the thiol moiety of C299/C169 and W1.[79] This inner core of the H-bond network stays rigid during proton uptake and release independent of the H-cluster redox state as shown by IR spectrocopy.[95]

Due to the direct interaction of C299/C169 and the amine of [2Fe]$_H$, this amino acid was the target of numerous mutagenesis studies.[64,67,79,85,86,92,96] All performed modifications result in a diminished hydrogenase specific activity, which reflects the importance of the interplay between the cysteine's thiol group, the adjacent water complex and the amine bridge. Most modifications at this position were performed to enrich the H-cluster redox state H$_{hyd}$. Since it was found that a lack of the proton shuttling ability of the [FeFe]-hydrogenases, *e.g.* by changing ADT to ODT[75,84] or blocking the proton transfer pathway H$_{hyd}$ can be enriched, C299A/C169A[64,85] and C299S/C169S[86,92,96] mutants of *Cp*I or *Cr*HydA1 were used to trap the enzyme in H$_{hyd}$ for further spectroscopic investigations of this state. Remarkably, the crystal structure of the C299A$_{CpI}$ mutant (Fig. 16A, green) shows an additional water molecule W$_{C299A}$ occupying the vacant space of the cysteine's thiol. However, this water molecule is not capable to restore the complete

enzymatic activity of the mutant but accepts a proton from the H-cluster upon H$_2$ oxidation also leading to an enrichment of the H$_{hyd}$ state.[79] In contrast to alanine and serine mutants, which show less than 0.2% of the hydrogenase specific activity, the C299D/C169D mutants show 25% and 65% remaining activity, respectively (Table 4). The pH-dependent activity optimum of C299D$_{CpI}$, however, is shifted from pH 8 (native) to pH 6.5 and shows an altered but intact protonation equilibrium within the PTP.[79]

The next amino acid of the proton transfer path is glutamic acid E279/E141, which strongly interacts with W1 (2.5 Å) *via* a stable *trans* complex.[97,98] Furthermore, it only weakly interacts with S319/S189 (3.6 Å), indicating a discontinued proton transfer in the H$_{ox}$ state. Stripp and coworkers determined E279/E141 as the key residue upon switching from proton release to its uptake.[95] Adjusting the *Cr*HydA1 to H$_{red}$ requires a proton from the PTP to enter the H-cluster, *i.e.* proton uptake reactivity.[51,76] According to IR spectroscopy, E141 of *Cr*HydA1 thereby forms an H-bond to S189 closing the gap between the inner and outer core of the PTP and enables a more continuous proton transport. In line with these results, E141D$_{CrHydA1}$ loses 90% of its activity due to the longer distances between D141 and W1 and S189, respectively (Table 4).[79] The remaining activity of glutamine and alanine mutants at this position is below 1%, indicating the complete loss of the proton transfer ability. In contrast to C299A, the crystal structure of E279A does not show an additional water molecule rescuing the proton transport (Fig. 16B), which explains the low residual remaining activity. In line, the mutant E279A adopts the H$_{hyd}$ state under H$_2$ oxidising conditions, since the proton transport pathway is interrupted at this position.[79]

S319/S189 is the first residue of the outer PTP and its side chain is 3.6 Å apart from E279/E141 and serves as H-bond acceptor during proton uptake. It further tightly interacts with E282/E144, which is only 2.8 Å apart, as H-bond acceptor and donor during proton release and uptake, respectively.[95] Both mutants, S319A of *Cp*I and S189A of *Cr*HydA1 show approx. 5% activity regarding H$_2$ evolution at pH 6.8 relative to the respective native enzymes (Table 4). The crystal structure of S319A from *Cp*I (Fig. 17A) shows an additional water molecule W$_{S319A}$,

Fig. 16 Native *Cp*I(ADT) in comparison with its mutants *Cp*I-C299A (A, green) and *Cp*I-E279A (B, magenta). In case of the C299A mutant, water W* adopts the position of the absent thiol. Protein structures from PDB entries 4XDC (native), 6GLY (C299A) and 51A3 (E279A).

Table 4 H$_2$ production activity of SDM variants targeting the putative PT pathway in *Cp*I and HydA1. H$_2$ production activities of PT pathway variants determined at pH 6.8 are presented in % relative to the respective wild-type activity[79]

*Cp*I mutant	H$_2$-Production activity/%	*Cr*HydA1 mutant	H$_2$-Production activity/%
C299A	0	C169A	0
C299D	30	C169D	65
C299S	0.05	C169S	0.1
E279Q	0.65	E279Q	0.2
E279A	0.06	E279A	0.1
E279D	30	E279D	5
S319A	5	S189A	10
E282Q	5	E144Q	0.45
E282A	60	E144A	45
E282D	80	E144D	50
R286A	90	R148A	55
R286L	300		

1684 | *Chem. Soc. Rev.*, 2021, **50**, 1668–1784

This journal is © The Royal Society of Chemistry 2021

Fig. 17 Native *Cp*I(ADT) in comparison with its mutants *Cp*I-S319A (A, yellow) and *Cp*I-E282A (B, grey). In case of the S319A mutant, water W$_{S319A}$ adopts a position near the serine vacancy, closing the PTP. The crystal structure of E282A shows to invaded water molecules W$_{E282A}$1 and W$_{E282A}$2, one at the vacancy of the carboxylic acid and one more outwards, forming a makeshift proton pathway between bulk solvent and S319. Protein structures from PDB entries 4XDC (native), 6GM4 (S319A) and 6GM1 (E282A).

which does not exactly occupy the vacant –OH site of serine but is in proximity to E279 and E282 and closes the proton transfer path. As seen before in C299A, the makeshift water molecule changes the pH-dependent activity of the mutant to the highest activity between pH 6.5 and 7. However, in contrast to the C299A mutant, this modification does not lead to the accumulation of H$_{hyd}$ under H$_2$ oxidizing conditions but shows the reduced species H$_{red}$, H$_{sred}$ and H$_{red'}$ besides H$_{ox}$.

Due to the missing possibility of S319A to form H-bonds to its neighbours, the next amino acid residue in the PTP, glutamic acid E282, points more towards the arginine residue R286 at the edge between enzyme and solvent. In native [FeFe]-hydrogenases, E282/E144 and S319/S189 interact *via* a hydrogen bond of 2.8 Å length. The deprotonated side chain might further form a salt bridge to the guanidine moiety of arginine R286.[99] Mutants of E282/E144 show overall diminished activity regarding H$_2$ evolution, which is, however, less pronounced as observed for *e.g.* E279/E141. Like for the more inwards positioned glutamic acid, E282Q/E144Q show only 5% and 0.5% remaining H$_2$ release activity and a pH-dependent activity maximum between pH 6 and 6.5 according to the altered pK_a value of the glutamine residue (Table 4). Remarkably, the aspartic acid mutants E282D/E144D show 80% and 50% remaining activity, respectively (Table 4). This contrasts the respective E279D/E141D mutants, which show significantly less activity. This discrepancy demonstrates the significance of the distinct amino acid residues for the catalytic PTP. However, the importance of proper amino acids within PTP appears to decrease from the H-cluster to the enzyme's surface. Interestingly, the E282A/E144A mutants show 60% and 50% residual activity, which again drastically differentiates E282/E144 from the inner laying E279/E144 (Table 4). The remarkable activity of these mutants most likely stems from two water molecules invading from the bulk solvent into the PTP (Fig. 17B). One is located directly at the vacancy of native E282, 2.5 Å away from the hydroxyl moiety of S319, and another one is placed more outwards in proximity to the bulk solvent, as revealed by XRD studies of E282A from *Cp*I. Therefore, those water molecules build up an H-bond network from the solvent to S319, taking care of proton transfer in the outer core of the PTP. However, as

previously described for other mutants, this is well in line with a slight shift of the maximal activity from pH 8 to pH 7.[79] Besides its H-bond towards S319/S189, the side chain of the glutamic acid residue E282/E144 interacts with R286/R148, which is positively charged/protonated under physiological conditions and therefore forms a salt bridge with negatively charged/deprotonated E282/E144 of 2.8–3.1 Å.[79,95] IR spectroscopic investigations on the R148 from *Cr*HydA1 propose a neutral side chain during proton uptake (formation of H$_{red}$), which renders the arginine residue the first proton donor.[95] A permanently neutral charge at the position of R286/R148 was achieved by the R286L mutant.[93] Surprisingly, under conditions of non-rate limiting electron transport, *i.e.* using methyl viologen as mediator, the R286L mutant from *Cp*I surpasses its native counterpart by the factor of three and is therefore the only mutant with increased activity in comparison to the native enzyme. This interesting finding was explained by the absence of the salt bridge between R286 and E282 that neutralises the negative charge of the carboxylic acid. In R286L, this charge is still present increasing the driving force for protons to enter the PTP.[93,99] Furthermore, E282 is more exposed to the bulk solvent in R286L, as seen from Zn^{2+}-inhibition experiments.

3.9 Influence of an additional F-domain on the reactivity of the H-cluster

The reactivity discussed so far is based on results from [FeFe]-hydrogenases HydA1 from *C. reinhardtii*. Especially due to the possibility to artificially mature this enzyme, most research concentrates on this "blueprint" for H-cluster reactivity. The main difference between HydA1 and other [FeFe]-hydrogenases is the electron supporting chain of two [4Fe–4S]-clusters, so called F-clusters, which are absent in eukaryotic *Cr*HydA1 but present in prokaryotic hydrogenases, *e.g.* *Dd*H and *Cp*I. The F-clusters will be denoted as $_d$[4Fe]$_F$ (distal F-cluster, relative from the H-cluster) and $_p$[4Fe]$_F$ (proximal F-cluster). We will stress the resulting differences in reactivity after describing the similarities between HydA1 and prokaryotic hydrogenases. The H$_{ox}$ state of *Cr*HydA1, *i.e.* the smallest possible [FeFe]-hydrogenase, exhibits only the H-domain and is characterized by a rhombic EPR signal (g = 2.10, 2.037, 1.996), an IR signature with uncoupled vibrations for each CO/CN$^-$ ligand (2088, 2070, 1964, 1940, 1802 cm^{-1}) and an electronic structure with an oxidised [4Fe–4S]$^{2+}$ cluster and a bi-valent diiron site (Fe^{II}Fe^{I}). Upon CO binding, the IR pattern changes to 2091, 2081, 2012, 1968, 1962 and 1808 cm^{-1}, respectively, accounting for the additional CO ligand and the EPR spectrum changes from a rhombic to an axial signal (g = 2.052, 2.007). The IR spectra of H$_{ox}$ and H$_{ox}$-CO from *Dd*H (hydrogenase from *D. desulfuricans*) show characteristic signatures similar to H$_{ox}$ and H$_{ox}$-CO from *Cr*HydA1 (see Tables 2 and 3).[56] Likewise, the EPR spectrum of *Dd*H in the oxidised state agrees with the observed spectrum of HydA1 (see Table 1) but shows additional signals for the F-cluster.[54,91] In case of H$_{ox}$, a broad rhombic signal (g = 2.059, 1.935, 1.877) is present in the spectrum as well. This was assigned to $_d$[4Fe]$_F$ since a spin coupling between the H-cluster and $_p$[4Fe]$_F$ is expected and would result in an overall EPR silent state if the

distal H-cluster is reduced.[91] The overall electronic and molecular structure of the H-cluster in H_{ox} and H_{ox}-CO from CrHydA1 and DdH can therefore considered as identical, which is also in line with matching ^{57}Fe hyperfine values, examined by HYSCORE spectroscopy, from both enzymes.[49,71] However, differences occur for reduced enzymes.[91] Under slightly reducing conditions, i.e. 50 µM NaDT, the IR spectrum of DdH(PDT) shows a mixture of H_{ox}^{PDT} and $H_{red'}^{PDT}$. However, the typical rhombic signal of H_{ox} in the EPR disappears, whereas the broader rhombic signal ($g = 2.059, 1.935, 1.877$) remains in the spectrum and another broad signal around $g = 2.01$ appears. This result was explained by an equilibrium between a state, in which both F-clusters are reduced and the H-cluster is oxidised ($F_{red}/F_{red}/H_{ox}$), and a state in which the H-cluster and $_d[4Fe]_F$ are reduced while $_p[4Fe]_F$ is oxidised ($F_{red}/F_{ox}/H_{red}$). In the former state, $_p[4Fe]_F$ and the H-cluster combine to an electronically coupled cluster pair, resulting in an altered EPR spectrum compared H_{ox} (broad $g = 2.01$), while in the latter state both, the H-cluster and the proximal F-cluster are EPR silent.[91] To account for this equilibrium, the respective states are called F_{red}/H_{ox} and $F_{ox}/H_{red'}$ with both states bearing an EPR active reduced distal F-cluster. Notably, the IR maxima of e.g. F_{red}/H_{ox} shift by approx. 1 cm^{-1} compared to F_{ox}/H_{ox}, which was observed in high-res SEC-IR experiments.[91] Based on these EPR results, an effect of the cluster pairing regarding the transition potentials of the H-cluster is likely. The apparent midpoint potential of the $H_{ox} \rightarrow H_{red'}$ transition in DdH(PDT) is -500 mV vs. SHE at pH 8, which is certainly more negative than that observed for CrHydA1(PDT) (depending on the reference: 25 mV[52] or 155 mV[74] more negative). Furthermore, the two-state population, followed by IR spectroscopy, does not show a Nernstian behaviour. This is a result of redox anti-cooperativity, which was rationalised by simulating the resulting population curves. Therein, the extra electron upon reduction of F_{ox}/H_{ox} was allowed to equilibrate between $_p[4Fe]_F$ (F_{red}/H_{ox}) and $[4Fe]_H$ ($F_{ox}/H_{red'}$), where the ratio was determined by the respective cluster potential. Taking the small IR band deviation of 1 cm^{-1} for reduced $_p[4Fe]_F$ into account, the new four-state population curves became strictly Nernstian. The new model includes a reduction potential of $[4Fe]_H$, which depends on the redox state of $_p[4Fe]_F$. If $_p[4Fe]_F$ is already reduced, a more negative potential for $[4Fe]_H$ was observed and vice versa, i.e. redox anti-cooperative behaviour.[91]

In CrHydA1, CO inhibition leads to increased electron density at $[4Fe]_H$ and results in a more negative reduction potential compared to non-inhibited species (Section 3.3). The same observation was found for DdH(ADT) as well. The potential shift of $[4Fe]_H$ is strong enough to prevent an equilibrium between F_{red}/H_{ox}-CO and $F_{ox}/H_{red'}$-CO due to the much more positive reduction potential of $_p[4Fe]_F$. Therefore, F_{red}/H_{ox}-CO is exclusively present. To achieve $H_{red'}$-CO, a second electron is needed to enter the $F_{red}/H_{red'}$-CO state, which is again, as observed for DdH(PDT), formed at much more negative potential due to anti-cooperativity (Fig. 18).
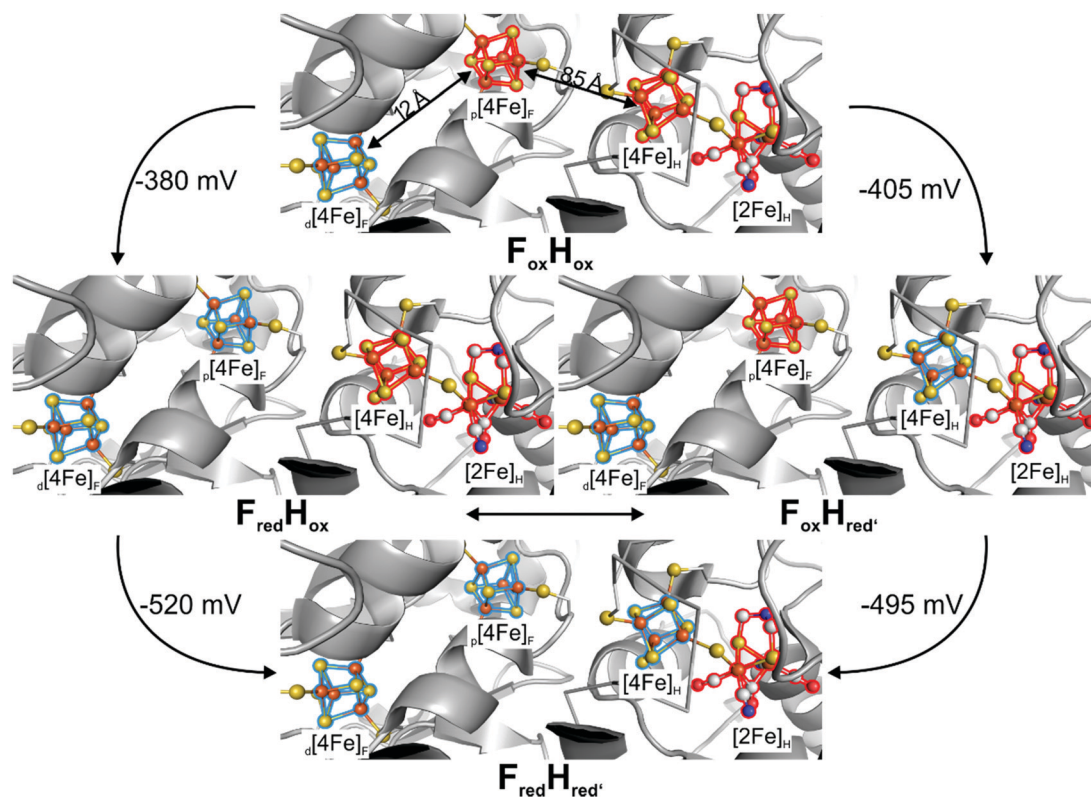

Fig. 18 Four-state model of the redox-anticooperative effect, which results from the additional F-clusters in [FeFe]-hydrogenases (except HydA1). Clusters coloured in red are oxidized, clusters coloured in blue are reduced. Model depicted from ref. 91.

1686 | Chem. Soc. Rev., 2021, **50**, 1668–1784

This journal is © The Royal Society of Chemistry 2021

These findings explain why $\mathbf{H_{red'}}$-CO in DdH cannot be observed under the conditions of CrHydA1.[91]

Even more interesting is the comparison of CrHydA1(ADT) and DdH(ADT) since former shows a fascinating pH-dependent behaviour regarding single-electron reduced species: at alkaline pH (*i.e.* pH ≥ 8) $\mathbf{H_{red'}}$ is favoured, while at acidic pH $\mathbf{H_{red}}$ is preferred (see Section 3.6).[76] Due to the amine bridge, such a behaviour can be expected for DdH as well but is observed to another extent. At pH 6, $\mathbf{H_{red}}$ dominates upon reducing the potential, while $\mathbf{H_{red'}}$ is not observed. This is in line with the findings from HydA1. Interestingly, $\mathbf{H_{sred}}$, which replaces $\mathbf{H_{red}}$ at even more negative potentials in CrHydA1 cannot be found in DdH under the same conditions. The hypothesis explaining the absence of $\mathbf{H_{sred}}$ in DdH is that the second electron, required to form $\mathbf{H_{sred}}$ and finally liberate H_2 can be stored in the F-clusters instead of the H-cluster. Due to the anti-cooperative effect of the additional [4Fe–4S]-cluster, the H-cluster's pK_a shifts towards a value close to that of $\mathbf{H_{sred}}$ in HydA1. Therefore, bacterial hydrogenases may be able to skip $\mathbf{H_{sred}}$ (the participation of $\mathbf{H_{sred}}$ in the catalytic cycle is, however, anyway under debate) and directly form $\mathbf{H_{hyd}}$. $\mathbf{H_{hyd}}$ was found in DdH under the same conditions as in CrHydA1, being low pH and constant H_2 supply, showing the importance of this state in both organisms.[80] Decreasing the proton concentration to pH 8 results in $\mathbf{H_{red'}}$ being formed in HydA1. However, in DdH $\mathbf{H_{red}}$ is still the dominant species. Although the amount of both species in DdH increases simultaneously at potentials between −200 and −400 mV, $\mathbf{H_{red'}}$ vanishes beyond this potential. According to simulations, the proximal F-cluster is reduced at approximately −400 mV, which results in an anti-cooperative effect and renders the reduction of [4Fe]$_\text{H}$ less likely to occur. Apparently, the pK_a of the amine bridgehead shifts from ≈7.7 for HydA1 to ≈9.3 in DdH due to the redox anti-cooperativity.[91] However, the influence of a protonation at the stabilising cysteine residue S9 of the [4Fe]$_\text{H}$, which might be influenced by the reduction of the proximal F-cluster, was considered as possible explanation. This should be addressed in an additional study since the formation of $\mathbf{H_{ox}H}$ under similar conditions as in CrHydA1 was reported for DdH as well. $\mathbf{H_{ox}H}$ is associated with the H-cluster in oxidised form with an additional proton at cysteine S9, which causes minor (4 to 6 cm^{-1}) IR band shifts.[51] The complex situation of two different protonation events (cysteine S9 and adt) besides the three different reducible clusters ($_\text{p}$[4Fe]$_\text{F}$, [4Fe]$_\text{H}$ and [2Fe]$_\text{H}$) makes the interplay of protons and electrons in DdH a very interesting topic to study albeit a challenging one.

Like DdH, hydrogenase I from *C. acetobutylicum* (CaI) bears two additional F-clusters next to the H-cluster within the protein frame. Compared to CrHydA1 and DdH, the IR spectrum from auto-oxidised CaI in the $\mathbf{H_{ox}}$ state shows slightly down-shifted CN$^-$ (2082 cm^{-1} and 2070 cm^{-1}) and upshifted CO stretching frequencies (1969, 1646 and 1800 cm^{-1}). The EPR spectrum, however, closely resembles that of DdH and CrHydA1 showing a rhombic 2.1 signal (g = 2.009, 2.039, 1.999).[100] At acidic pH, the IR bands slightly shift towards higher wavenumbers, as was observed for CrHydA1 and DdH in the $\mathbf{H_{ox}} \rightarrow \mathbf{H_{ox}H}$

conversion as well, which indicates a similar reactivity at this point.[51,101] Due to the accessory F-clusters, the reactivity of CaI seems to be very close to that of DdH.[91] At pH 8, upon reducing the enzyme by NaDT or by photocatalytic electron supply, $\mathbf{H_{red}}$ is formed indicated by the marker band at 1899 cm^{-1} within the IR spectrum, whereas $\mathbf{H_{red'}}$ is dominant under these conditions in HydA1. The reduction is likewise accompanied with a seemingly broad rhombic signals within the EPR spectrum that can be assigned to the reduced F-clusters (g = 2.043, 1.941, 1.911 and g = 2.073, 1.930, 1.868), which was also observed in DdH.[91,100]

At 13 K, the IR spectrum of NaDT reduced CaI shows bands at 2055, 2040, 1921, 1899 and 1801 cm^{-1}. More interestingly, a μ-CO band is observed under these conditions. As previously described for CrHydA1, this may arise from the cryogenic conditions at which the spectrum was recorded.[77,102] Changing conditions to D_2O did not yield any observable shifts, which renders a terminal bound hydride at Fe$_\text{d}$ unlikely. Unfortunately, no room temperature data are available to discuss the existence of a bridging CO *vs.* a bridging H$^-$, which is proposed as one possible structure of a single-reduced H-cluster inter-mediate as well.[80]

Experiments on CrHydA1, in which specific amino acids were exchanged by site directed mutagenesis showed that *e.g.* $\mathbf{H_{hyd}}$ is enriched without the need of increasing both, proton concentration and H_2 pressure.[75] This is also true for CaI, whose IR spectrum shows the presence of two formerly unobserved species at room temperature upon changing C298 to Serine. Decreasing the temperature to 10 K results in the vanishing of bands at 2042 cm^{-1}, 2022 cm^{-1}, 1892 cm^{-1}, 1978 cm^{-1} and 1781 cm^{-1}, which were assigned to $\mathbf{H_{sred}}$. The remaining bands at 2083 cm^{-1}, 2067 cm^{-1}, 1977 cm^{-1}, 1964 cm^{-1} and 1851 cm^{-1} were assigned to $\mathbf{H_{hyd}}$. The fact that both states, $\mathbf{H_{hyd}}$ and $\mathbf{H_{sred}}$, are only observed if the proton path is blocked, renders them possible tautomers and endpoints of the catalytic H_2 oxidation. As discussed above for DdH, the existence of reduced F-clusters can compensate the second reduction step from a single reduced to a double reduced H-cluster species before $\mathbf{H_{hyd}}$ is formed. There, $\mathbf{H_{sred}}$ is not observed and a proposed transient state in the $\mathbf{H_{red}H^+} \rightarrow \mathbf{H_{hyd}}$ transition. Most likely, this is also the case for CaI since the F-clusters should show the same effect here. Additionally, H/D exchange experiments showed that the $\mathbf{H_{red}H^+} \rightarrow \mathbf{H_{hyd}}$ transition is slower in case of D_2O, resulting in accumulation of $\mathbf{H_{red}H^+}$. The slowed kinetics implicate an intramolecular proton transfer for the transition from $\mathbf{H_{red}H^+}$ to $\mathbf{H_{hyd}}$. Both enzymes, DdH and CaI, exhibit additional F-clusters for electron relay and most likely changing the H-cluster's electronics. To determine the general function of these additional clusters, all enzymes excluding CrHydA1 should be investigated regarding their redox anti-cooperativity as performed on DdH. This includes enzymes from *Clostridiae* (CaI and CpI) and eventually HydS from *T. maritima*, which exhibits F-clusters as well and is known as sensory [FeFe]-hydrogenase.[61] Sensory-type hydrogenases exhibit a third accessory [4Fe-4S]-cluster at the C-terminus, which is ligated by a $Cx_2Cx_4Cx_{16}C$ motif. Although the H-cluster of TmHydS is structurally the same as in CrHydA1, CaI and DdH, the reactivity

This journal is © The Royal Society of Chemistry 2021

Chem. Soc. Rev., 2021, **50**, 1668–1784 | **1687**

of the sensory-type hydrogenase is dramatically different from the prototypical-type hydrogenases, which were described above. First indication of the altered reactivity is the 100-fold and 5-fold lower activity in H_2 production and oxidation, respectively, of *Tm*HydS compared to *Cr*HydA1.[61] This can be explained by the altered amino acid ligation of the H-cluster compared to *e.g. Cp*I. While Cysteine (C299) is the endpoint of the PTP in prototypical *Cp*I, an alanine (A131) occupies this position in *Tm*HydS. Likewise, methionine residues M353 and M497, which are part of the H-cluster's coordination sphere in *Cp*I, are replaced by G177 and S267 in *Tm*HydS, respectively.[103] Mutagenesis experiments of *Cp*I showed that variants of respective amino acids, *i.e.* C299S, 353L and M497L, led to diminished activity as well.[104] In addition, upon maturation of apo-HydS with an artificially synthesised H-cluster (under 2% H_2), an IR spectrum with CN^- bands at 2055 and 2022 cm^{-1} and CO bands at 1894, 1871 and 1763 cm^{-1} is observed (Table 5). While this pattern is not changed under reductive conditions (H_2 or NaDT), oxidation with thionine led to an altered spectrum of 2088, 2079, 1971, 1947 and 1806 cm^{-1} that resembles H_{ox} spectra of *e.g. Dd*H and *Ca*I. In conclusion, HydS exclusively adopts a reduced state under already minor amounts of reducing agents, which is not observed for other [FeFe]-hydrogenases. The latter shows major amounts of H_{ox} upon maturation under the same conditions. The 30 to 80 cm^{-1} downshift *vs.* H_{ox} of IR bands in the reduced state implies a reduction of $[2Fe]_H$ as in H_{red} of *Cr*HydA1. However, the observed CO/CN^- frequencies do not match those from H_{red} in HydA1, especially the observed μCO band in *Tm*HydS cannot be associated to an H_{red}-like state (compare Tables 2 and 5). Therefore, the reduced state in *Tm*HydS is called H_{red*}.

3.10 The catalytic cycle(s) of [FeFe]-hydrogenases

Despite the intensive investigation on the catalytic cycle of [FeFe]-hydrogenases in the last decades, up to today, not "one and only" working mechanism of this enzyme family is known. However, based on the reactivity described in this section, some cycles were suggested, which will be briefly described in this section. Especially, we aim at identifying similarities and major discrepancies of those cycles, which are mainly based on inconsistent findings on the reduced H-cluster states H_{red} and H_{sred}. It is evident from the results presented in this

section that the exact nature of the states involved in the catalytic cycles is an ongoing matter of a lively debate in the community and hence we will leave the final judgement to the reader as we do believe that all of those currently reported mechanisms have strengths and weaknesses. We anticipate that future theoretical and experimental insights will lead to continuous reassessments and changes in the catalytic cycles.

In Fig. 19–21, three proposed catalytic cycles are presented, which are adapted from a recent joint publication of the groups of Lubitz, Birrell and Dyer.[105] From sub-turnover time-resolved IR spectroscopy, the authors derived cycle C, since all contained states were identified in their experiments. However, mechanisms A and B are very similar to C, considering the main H-cluster states H_{ox}, H_{red} and H_{hyd}. All cycles start with H_{ox}, which is the overall accepted entry point of the catalytic cycle. H_{ox} is characterised by many different techniques (see above) as a $[4Fe–4S]^{2+}$–$[Fe_p^{2+}Fe_d^{1+}]$-cluster with a bridging μ-CO ligand and an apical vacancy at the distal iron, with an eventually slightly apical rotated CN^- ligand.[29,49,64,67] From here, the first reduction event occurs at the [4Fe–4S]-cluster, which is especially plausible in hydrogenases with additional F-clusters as electron delivery chain but also true for HydA1, which lacks this chain of [4Fe–4S]-clusters.[41,51,57,82] However, the exact mechanisms of the electron transfer are different in cycles A *versus* B and C. While in cycle B and C a simple electron transfer forms H_{red}, a PCET is responsible for $H_{red'}$ formation in cycle A. $H_{red'}$ is described similar to H_{red}, as a $[4Fe–4S]^{1+}$–$[Fe_p^{2+}Fe_d^{1+}]$-complex with an H_{ox} like molecular structure, but with an additional proton at one of the [4Fe–4S]-cluster stabilising cysteines (in blue colour in Fig. 20).[51,52,88]

PCETs are common in nature and advantageous for a multi-electron process due to the balanced charge of the reduced moiety.[106] In all cycles the next state, which could be trapped and thoroughly investigated by numerous different techniques is H_{hyd}. However, the mechanism to get there differentiates the cycles. While in cycle A a second PCET from $H_{red'}$ directly results in H_{hyd}, cycles B and C follow a successive mechanism of separate proton- and electron-transfer steps. A proton transfer to H_{red} results in the formation of $H_{red}H^+$, which electronic structure was characterized by Lubitz and coworkers as $[4Fe–4S]^{2+}$–$[Fe_p^{1+}Fe_d^{1+}]$ with a protonated amine bridgehead,

Table 5 IR frequencies of known H-cluster states from hydrogenases with an additional F-domain

State	$\nu(CN^-)/cm^{-1}$	$\nu(CO)/cm^{-1}$	Ref.	State	$\nu(CN^-)/cm^{-1}$	$\nu(CO)/cm^{-1}$	Ref.
		DdH				***Tm*HydS**	
H_{ox}	2093, 2079	1965, 1940, 1802	75	H_{ox}	2087, 2079	1971, 1947, 1806	61
$H_{ox}H$	2097, 2082	1965, 1940, 1802	75	H_{ox}-CO	2090	2016, 1973, 1964, 1805	61
H_{ox}-CO	2096, 2089	2017, 1972, 1963, 1812	91	H_{red*}	2055, 2022	1894, 1971, 1763	61
H_{red}	2079, 2040	1915, 1892, 1962	75	H_{sred*}	2047, 2013	1900, 1861, 1751	61
H_{hyd}	2089, 2079	1980, 1963, 1860	75				
		***Ca*I**				***Cp*I**	
H_{ox}	2082, 2070	1969, 1646, 1800	101	H_{ox}	2082, 2071	1970, 1947, 1800	75
H_{red}	2052, 2035	1914, 1894	101	$H_{ox}H$	2084, 2073	1975, 1953, 1809	75
$H_{red}H^+$	2055, 2040	1921, 1899, 1801	101	H_{red}	2071, 2053	1915, 1899, 1962	75
H_{hyd}	2080, 2063	1975, 1960, 1849	101	H_{sred}	2065, 2039	1922, 1894, 1958	75
				H_{hyd}	2082, 2068	1984, 1968, 1856	75

1688 | *Chem. Soc. Rev.*, 2021, **50**, 1668–1784

This journal is © The Royal Society of Chemistry 2021

Fig. 19 Main proposed catalytic cycles A–C adapted from ref. 87 and 105.

Fig. 20 Shortened catalytic cycle A from Fig. 3.11 and secondary cycle, which is based on bridging hydrides. Red protons: catalytic PTP, blue proton: accessory PTP. *$H_{ox}H$ might be involved in this conversion.

Fig. 21 Schematic representation of the catalytic cycle of [FeFe]-hydrogenase, based on the states observed under whole-cell conditions including the protonated hydride species ($H_{hyd}H^+$). Figure and caption from ref. 35.

which is why the additional electron from the four-iron cluster has to migrate to the diiron site.[76] In cycle C, the following electron transfer forms $H_{sred}H^+$, that isomerises to H_{hyd}. In cycle B, the latter state is directly formed upon electron transfer. Considering the functionality of the amine bridge within the PTP, an intermediate with a protonated bridgehead

is feasible – at least as very short-lived transient state – even in cycle A. This shows the hen-and-egg problem of a PCET, which may be facilitated *via* an electron–proton-transfer or an proton–electron-transfer.[107]

Starting from H_{hyd}, the second protonation of the H-cluster *via* the catalytic PTP results in the formation of H_2 and the regain of H_{ox}. In cycle A, the H-cluster passes through $H_{ox}H$, an H_{ox}-like state that still holds the non-catalytic proton near the [4Fe–4S]-cluster. Cycles B and C further contain the intermediate species H_{ox}-H_2 and/or $H_{hyd}H^+$, which is feasible considering the role of the amine bridge. The $H_{hyd}H^+$ state was recently observed in *in vivo* studies on HydA1 containing *E. coli* cells and is a plausible intermediate in the $H_{hyd} \rightarrow H_{ox}$ conversion.[35]

Blanking out the non-catalytic proton in cycle A, cycles B and C can be considered as more detailed mechanisms of cycle A. All used H-cluster states share the H_{ox}-like geometry with a bridging CO, which was supposed to be a prerequisite for fast turn over. However, in recent literature, structures containing a bridging hydride instead of a bridging CO were discussed as well.[80,88] Those structures are thermodynamically more stable and therefore might not justify fast turn-over rates as observed for [FeFe]-hydrogenases, hence they were placed in a secondary cycle (Fig. 20) with exclusively bridging hydrides, which was formerly denoted as "slow cycle".[87] We already discussed that both single-electron-reduced states $H_{red'}$ and H_{red} can be formed upon reducing H_{ox} and that pH dictates whether the electron resides at the [4Fe–4S]-cluster, stabilising the H_{ox}-like structure at more alkaline pH, or migrates to the diiron subsite forming H_{red} ($H_{red}H^+$) at pH $\leq$ 6. At this point, a problem regarding the nomenclature of the specific states arises. The state which is entered as first species in all cycles, *i.e.* [4Fe–4S]$^{1+}$-[Fe$_p^{2+}$Fe$_d^{1+}$], is called H_{red}[76,77,105] or $H_{red'}$,[51,72,87,88] depending on the additional proton near the [4Fe–4S]-cluster. The single-electron-reduced [4Fe–4S]$^{2+}$-[Fe$_p^{1+}$Fe$_d^{1+}$] state is called H_{red}[80,87,88] or $H_{red}H^+$,[76,77,102,105] depending on the described intermediate and considered mechanism. The same is true for the double reduced state $H_{sred}/H_{sred}H^+$.

Unfortunately, no XRD studies that would give hints towards the spatial structure of those single reduced states are present. Therefore, EPR and vibrational spectroscopy in combination with computational techniques are the methods of choice to characterise the molecular structure of each Hcluster state. While EPR spectroscopy can electronically distinguish between [4Fe–4S]$^{1+}$-[Fe$_p^{2+}$Fe$_d^{1+}$] and [4Fe–4S]$^{2+}$-[Fe$_p^{1+}$Fe$_d^{1+}$], the determination of the actual structure requires better suited techniques. Along this line, Lubitz and coworkers proposed the structure of $H_{red}H^+$ in 2017 based on the pH dependency of this state (Section 3.6).[76] Since the secondary amine is the most basic site within the H-cluster and simultaneously the endpoint of the catalytic PTP, a structure with a protonated bridge (NH$_2^+$) and a (semi-)bridging CO was justified. Later, this structure was further strengthened by IR und NRVS measurements. There, a bridging CO signal at 1810 and 1803 cm^{-1} was found within the IR spectrum of $H_{red}H^+$ and $H_{sred}H^+$, respectively. The absence of a high energy μ-H$^-$ band in the respective NRVS supported the assumption of a protonated amine bridge for these structures.[77] As mentioned in Section 3.4, these measurements were, however, conducted at 40–70 K, rendering a direct comparison with spectroscopic results obtained at room temperature cumbersome. IR spectroscopy at room temperature did not

show a bridging or semi-bridging CO ligand.[51,72] However, in models without μ-CO ligands, the clear pH-dependent formation of H_{red} was addressed *via* a bridging hydride for H_{red} and H_{sred} incoming from the catalytic PTP (Fig. 20 left cycle).

Computational simulations on those structures were in overall good agreement with observed spectra.[80] H_{ox} − H_{red} NRVS difference spectra revealed major differences at the [2Fe–2S]-subsite for H_{red}, whereas the [4Fe–4S]-cluster in H_{red} and H_{ox} is identical. Again, simulations were carried out for a structure with a μ-H$^-$ ligand, which agreed well with the found spectra.[80] Interestingly, a high energy band at approx. 750 cm^{-1} for a bridging hydride was absent in these simulation and present in simulation of Birrell and coworkers.[77]

The current data situation does not allow to favour one of the proposed structures for $H_{red}/H_{red}H^+$ and $H_{sred}/H_{sred}H^+$ in an unbiased fashion. However, the discussion on these H-cluster states indeed improved the knowledge on the working mechanism of [FeFe]-hydrogenases – at least, if *in vitro* measurements of isolated enzymes are considered. Recently, *in vivo* measurements on living *E. coli* cells that were genetically modified to express the hydrogenase HydA1 and artificially matured with a synthetic precursor of the diiron site, were performed.[35] Here, no [4Fe–4S]$^{1+}$-[Fe$_p^{2+}$Fe$_d^{1+}$]-like state was found, instead H_{red} was enriched under 1% H_2 (99% N$_2$). Addition of 2 mM NaDT and acidification of the cells led to formation of $H_{ox}H$. Additional treatment with H_2 afforded H_{hyd}. Increasing the NaDT concentration to 100 mM enabled the detection of H_{hyd} even at pH 8. When the pH was lowered at these conditions, a new species with approx. 15 cm^{-1} upshifted CO bands compared to previously reported CO signals of H_{hyd} occurred. These signals were attributed to the $H_{hyd}H^+$ species, comprising a protonated amine bridge, which was hard to enrich in isolated HydA1 and was therefore not characterised – although postulated (Fig. 20). This state is the missing link between H_{hyd} and H_{ox} (Fig. 21) and provides insight into the H_2 formation and cleavage.[35]

Part B: structural and functional models of [FeFe]-hydrogenases

IV Synthesis of H-cluster models – bridge alterations, metal exchange and ligand substitution

4.1 From enzymes to biomimetic H-cluster models

The pioneering progress in the analysis of natural systems led to the identification of the crucial framework and functional properties of the active site of [FeFe]-hydrogenases. Since the detailed structural characterisation of the natural system at the end of the last century,[28,108] synthetic chemists have constantly devoted efforts towards mimicking the enzyme subsite. These mimics range from small transition metal dinuclear carbonyl clusters to elaborate artificial protein replications.[31–33]

1690 | *Chem. Soc. Rev.*, 2021, **50**, 1668–1784

This journal is © The Royal Society of Chemistry 2021

However, it should herein be mentioned that [2Fe–2S]-mimics were already described in the early 20th century without the knowledge of the hydrogenases' active site but paved the way towards the fundamental synthetic strategies to assemble these cluster mimics. It is furthermore noteworthy that with the exceptional work of Rauchfuss, Darensbourg and Pickett after the elucidation of the enzyme structure, the iron sulphur chemistry underwent a renaissance and became a significant part of bioorganometallic chemistry. The tremendous modification efforts to the catalytic subsite are mainly driven to either achieve ideal catalytic efficiency approaching that of the natural enzyme or to understand the underlaying catalytic mechanism which results in a hitherto unmatched proton reduction activity of the natural system. The diiron subsite can be modified in multiple ways, including e.g. the modification of the bridging S–S linker length, exchanging the bridging sulphur-atoms with other chalcogens or pnictogens, substitution of carbonyl ligands or even the incorporation of other metals. We herein attempt to provide a comprehensive overview on the plentiful modification options.

4.2 H-cluster models with altered dithiolate bridges

4.2.1 Methanedithiolate models.
The first synthesis of a diiron methanedithiolate complex was described by Seyferth et al. already in 1981 from in situ generated $Li_2Fe_2S_2(CO)_6$ (6) and CH_2I_2. This synthesis afforded the desired compound $Fe_2(\mu\text{-}SCH_2S)(CO)_6$ ((7), Fig. 22) in a yield of 25%. Notably, the reaction of CH_2I_2 with $Fe_2(SH)_2(CO)_6$ (8) resulted in significantly improved yields of 84%.[109] In 2012, Liu et al.[110] described a facile novel synthetic route towards a $-S_2C\text{=}CR_2$ linker. Following this route, $Fe_2(\mu\text{-}S_2C\text{=}CHPh)(CO)_6$ (9) was obtained by the reaction of $Fe_3(CO)_{12}$ (10) and 2-phenyl-ethenethione as well as its tautomer (2-phenylethyne-1-thiol). The low yield (4%) of the model yet remains unexplained due

to the extensive and complicated chemistry of thiols with $Fe_3(CO)_{12}$.

In that direction, $Fe_2(C_8H_{12}S_3)(CO)_6$ (11, $C_8H_{12}S_3$ = 3,3-dimethyl-4-(propan-2-ylidene)-thietane-2,2-bis(thiolate)) was obtained via the reaction of tetramethyl-1,3-cyclobutane-dithione with $Fe_3(CO)_{12}$. A plausible synthetic mechanism for the formation of 11 involves the rearrangement of the dithione to a beta-thiolactone followed by sulphur insertion to yield the respective thiolene, which upon reacting with $Fe_3(CO)_{12}$ yields 11.

Furthermore, $Fe_2(\mu\text{-}S_2C\text{=}CHC(O)C_6H_4R)(CO)_6$ (12R, R = F, OMe) with unsaturated functionalities at the thiolate linker were described by Zamora and coworkers.[111,112] While the reaction of $Fe_2(CO)_9$ (13) and $(HS)_2C\text{=}CHC(O)C_6H_4R$ in diethyl ether gave the respective saturated products (14R), a 1 : 1 molar ratio of $Fe_3(CO)_{12}$ and corresponding ligand in THF yielded the unsaturated product (12R) (Fig. 23). Upon further increasing the ligand amount, a mixture of both products was obtained. Although these models show structural similarities with the active site of the enzyme, they generally lack further investigations on their catalytic activity.

4.2.2 Ethanedithiolate (EDT) models.
In the early 1960s, King et al. described the first synthesis of $Fe_2(edt)(CO)_6$ (15, Fig. 24) obtained via the reaction of $Fe(CO)_5$ and 1,2-ethanedithiol.[113] In a later attempt, the complex was also obtained by reacting $Fe_2(CO)_9$ with ethanedithiol/dithiocarbonates ($C_2H_4S_2CO$).[114,115] Subsequently, Huttner et al. reported that complexes of the type $Fe_2(S_2(CH_2)_n)(CO)_6$ (n = 2, 3) can be generally synthesised by the reaction of $Fe_3(CO)_{12}$ with the respective thiols under reflux conditions. These modified synthetic pathways significantly improved the yields of the respective [2Fe–2S]-complexes from 0.3% to 65% and can thus be regarded as key achievements towards a modern hydrogenase research.[116]

With these synthetic possibilities at hand, various modifications have been carried out. Donovan et al. reported the modified analogues $Fe_2((SCHR)_2)(CO)_6$ (16R, R = CH_3, CH_2OH) wherein methyl and hydroxymethyl groups were introduced to the ethanedithiolate linker.[117] In the absence of any acid, the complexes displayed cathodic shifts in their reduction potential increasing with the number of methyl groups incorporated within the thiolate linker. When studied in the presence of e.g. 4-tert-butylphenol as a proton source, a catalytic peak was observed at approximately -2.2 V vs. Fc/Fc$^+$ for all complexes. Along this line, $Fe_2(SCH_2CH(CH_2OH)S)(CO)_6$ (17) providing an
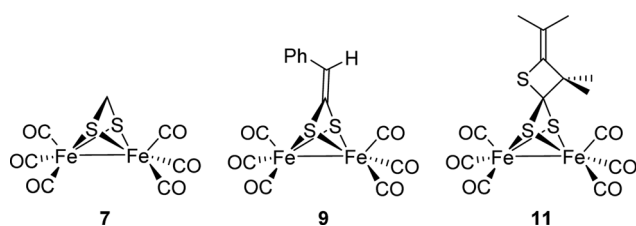

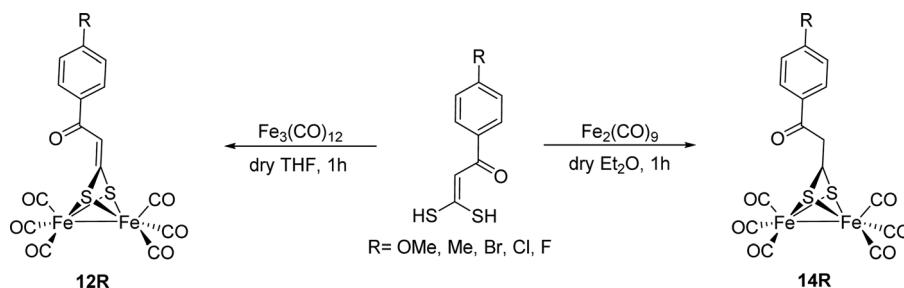Fig. 22 Structure of exemplary methanedithiolate complexes.

Fig. 23 Influence of the reaction conditions on the product obtained as described by Toledano et al.[111,112]
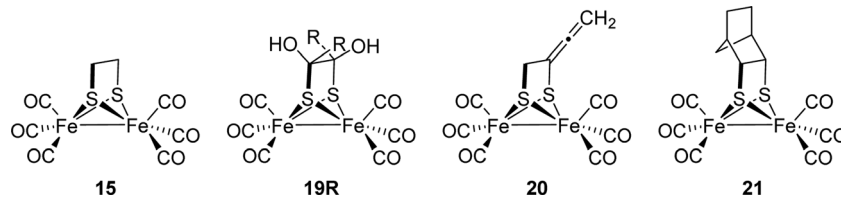
Fig. 24 Exemplary EDT models.

additional hydroxyl group at the ethane bridge was synthesised to study the influence of hydrogen bonding within the protonation experiments. It was expected that the hydroxyl group can act as a proton shuttle. While Pickett and coworkers revealed a high degree of hydrogen bonding, which results in self-polymerised cyclic hexamers,[118] the model was, however, catalytically inactive.[117] In addition, the edt complex was modified with a sulfonate moiety to enable catalysis in water. Using ascorbic acid as a proton donor and $[Ru(bpy)_3]^{2+}$ as photosensitizer, the modified edt-complex was reported to generate 88 equivalents of H_2 per catalyst equivalent.[119]

Edt-complexes can likewise be obtained by reaction of $Fe_2(SH)_2(CO)_6$ and diketones – here, reactions e.g. with glyoxal or benzil resulted in the formation of $Fe_2((SC(OH)R)_2)(CO)_6$ (**18R**, R = H or Ph, Fig. 24). The rigid unsaturated dithiolate linkers have been broadly known to assist in the facile reduction of the [2Fe–2S]-models via delocalisation of the charge density from the iron centres through p–π interaction.[120]

Likewise, the edt-model $Fe_2(SCH_2C(S)=C=CH_2)(CO)_6$ (**19**, Fig. 24) was synthesised by the reaction of $Li_2Fe_2S_2(CO)_6$ with excess 1,4-dichloro-2-butyne. Herein, the electron withdrawing nature of the substituent, reduces the electron density at the iron centre thereby resulting in slightly milder potentials for electrochemical reduction (−1.60 V vs. −1.66 V of $Fe_2(pdt)(CO)_6$ (**20**)). The unsubstituted diiron buta-2,3-diene-1,2-dithiolato model was found to be capable of proton reduction of CH_3COOH with a low overpotential of −0.65 V in MeCN.[121]

Since the rotated structure of the complexes bearing a bridging carbonyl group is a catalytically relevant key intermediate, studies were also conducted to estimate the influence of steric bulk at the dithiolate linker on stability of the rotated state. Here, model **21** with a rigid norbornane structure was synthesised from norbornyltrithiolane (exo-3,4,5-trithiatricyclo[5.2.1.0]decane) and $Fe_2(CO)_9$ and was subsequently studied using photoelectron spectroscopy in comparison to $Fe_2(pdt)(CO)_6$, $Fe_2(bdt)(CO)_6$ and 2,3-pyridinedithiolato analogues.[122] While the reorganization energies of the 1,2-benzenedithiolate, 2,3-pyridinedithiolate, and 1,3-propanedithiolate complexes are comparable, the norbornane model revealed the largest overall reorganization energy. However, the reorganization energies of all models are small compared to the enzymatic active site and further corroborates the importance of the secondary coordination sphere on the proton reduction at unmatched biological rates.[122]

4.2.3 Propanedithiolate (PDT) models. The historical unambiguity in the exact nature of the bridgehead atoms led to great efforts in developing models of the active sites.

One example for such a model system that was thought to possess biological relevance is $Fe_2(pdt)(CO)_6$ (**20**) and numerous complexes were reported with modifications on the bridgehead carbon (Fig. 30). In this section, $Fe_2(pdt)(CO)_6$ models are described with focus on modified dithiolate linkers.

The PDT model was originally prepared from $Fe(CO)_5$ by a reaction with tetrathiacyclophane in 30% yield.[123] Later, this method was modified, and 1,3-dithianes were employed leading to an increased yield of 42%.[124] Nowadays, the synthetic methodology of employing $Fe_3(CO)_{12}$ as the starting material along with propanedithiol enables excellent yields of up to 92% (Fig. 25).[116]

In general, $Fe_2(pdt)(CO)_6$ based analogues can be synthesised from the oxidative addition of cyclic disulphides to $Fe_2(CO)_9$ or by the reaction of the respective dithiols with $Fe_3(CO)_{12}$ (Fig. 25). These facile pathways usually lead to the desired complexes in high yields. Alternatively, reaction of $Fe_2S_2(CO)_6$ with $LiEt_3BH$, CF_3COOH along with a suitable dihalide compound $(R_1R_2C(CH_2X)_2$ where X = Cl, Br) can be carried out as shown in Fig. 25. However, usually this method gives lower yields as compared to the first two pathways.

Examples of early modified $Fe_2(pdt)(CO)_6$ complexes date back to 1982, when Seyferth et al. investigated the reaction of $Fe_2(SH)_2(CO)_6$ with mesityl oxide and α,β-unsaturated ketones in the presence of amines (e.g. triethylamine or piperidine) to afford complex **22**.[125] Another early report of this class of complexes described the synthesis of a model bearing valeric acid and its C_1-functionalized derivatives. Comparably, complexes **23** to **25** were obtained upon treating $Fe_2(CO)_9$ with α-lipoic acid or its ester/amide derivatives in THF.[126] Also, the unsymmetrical complex **26** bearing a cyclohepta-4,6-diene unit in the bridge has been reported and was obtained upon treating $Fe_2(CO)_9$ with the respective trithiolane compound (i.e. 2,3,4-trithiabicyclo[4,3,1]deca-6.8-diene) in THF.[127]

Likewise, as the nature of the bridging ligands exerts significant influence on the electrochemical properties of the models, their systematic study was thought to be essential. Hereby, models with longer $(–S(CH_2)_nS–)$ (n = 4–8) dithiolate linkers were reported. Prior to reaction, however, disulphide formation was performed to suppress the formation of polymeric complexes and to favour the formation of the [2Fe–2S]-mimics. The required cyclic disulphides were obtained upon reacting the respective dithiols $(HS(CH_2)_nSH)$ (n = 4 to 8) and iodine in a Et_3N solution. Upon refluxing the disulphides with $Fe_3(CO)_{12}$, the respective sub-site mimics **27** to **31** were obtained. It was shown that oligomerization can hardly be suppressed leading to di-, tetra- as well as hexametallic

1692 | Chem. Soc. Rev., 2021, **50**, 1668–1784

This journal is © The Royal Society of Chemistry 2021

Fig. 25 Synthetic pathways to PDT and derivatives.

complexes. Likewise, the increased length of the dithiolate linker had negligible influence on the electrochemical properties of the corresponding complexes.[128]

4.2.3.1 PDT models with C_2-modifications at the dithiolate linker. Most alkyl chain C_2-modifications of the dithiolate linker were – and still are – performed at the C_2 position of the pdt-ligand. Although the general catalytic properties of the resulting model compounds cannot be altered to a significant extent, modified bridges do enable the alteration of physical properties, *e.g.* solubility, size and adhesive capabilities as well as the introduction of additional functional groups for the linking to surfaces or macromolecules.

Solubility is a key issue in HER-catalyst research and especially in larger scale, solvation in aqueous media is preferred for environmental reasons along with the parallel use of water as solvent and substrate. However, $Fe_2(pdt)(CO)_6$-like compounds comprise a bad solubility in water due to their non-polar character. Addressing this issue, the solubility of models is usually increased through CO-ligand substitution in favour of phosphines[129,130] or by encapsulating the models in a water-soluble framework (*e.g.* dextrins[131] or micelles[132]). The introduction of polar headgroups at the C_2 position of the dithiolate linker is a further possibility to improve the solubility of the $[2Fe]_H$-subsite models.

Weigand and coworkers showed that upon introducing sugar residues to the C_2 position of **20** (Fig. 26) and $Fe_2(pd-Se)(CO)_6$ (**32**) the biomimetic catalysts became water soluble.[133] The synthesis of those compounds (**33** and **34**) followed the well-established route *via* reacting $Fe_3(CO)_{12}$ with the respective protected dithiol or diselenolane in tetrahydrofuran under reflux and a follow up deprotection of the sugar moiety with sodium methoxide. Interestingly, the selenium version shows an improved stability as well as activity regarding HER in aqueous media, which was explained by the increased electron-donating properties of selenium and therefore stronger

Fig. 26 Structure of PDT with modifications at the C_2 position of the dithiolate linker.

π-backdonation to the CO ligand from the iron centres, resulting in a stronger Fe–C bond. Both models provided good solubility in $H_2O:MeCN$ (5:1) and acted as proton reducing catalysts using acetic acid or water as substrate.[133]

Besides sugar residues at the pdt-bridge, more simple models comprising a hydroxy group at the bridge exist as well. This model (**35**) was synthesised to gain information on the influence of the hydrogen bonding network between the single complexes in solution and to mimic the natural environment of the H-cluster.[134] Using 1,3-disulfanylpropan-2-ol, a binuclear $Fe_2(pdt)(CO)_6$-like structure (**35**) was obtained, which is arranged in a helical structure in solid state forming H-bonds between the single hydroxy groups. For the longer butane linker 1,4-dithiothreitol, however, a cyclic tetranuclear complex (**36**) was formed, in which two dithiolate bridges coordinate two different $Fe_2(CO)_6$ moieties. In a follow up study, the hydroxy group in **35** was modified *via* two ways: (a) masked by a methyl group to investigate the influence of the oxygen atom without the hydrogen bonding network to neighbouring complexes (**37**) or (b) by adding an additional alkyl group to the C_2 position of the pdt-bridge (**38**).[135]

Notably, such modifications do not alter the catalytic properties of the resulting cluster compared to the hydroxy derivative **35**. These results once again show that derivatisation of the pdt-linker does not necessarily influence the catalytic mechanism of [FeFe]-hydrogenase models, unless pK_a and electron density are dramatically changed. A change in reactivity, however, can

be achieved by elongation of the C_2–OH distance *e.g.* by implementing an additional methylene group in the bis-(hydroxymethyl)-functionalised $Fe_2((ECH_2)_2C(CH_2OH)_2)(CO)_6$ (E = S (**39**), Se (**40**)) complexes.[136] The solid state structure of those complexes also revealed a significant intermolecular H-bonding network, forming a rod-shaped cluster with tetra-hedrally arranged OH groups. Notably, the reduction potential determined as E_{44} = −1.53 V and E_{45} = −1.49 V *vs.* $Fc^{+/0}$, respectively, which is significantly anodically shifted due to facilitated structural changes upon reduction compared to PDT that exhibits its averaged first reduction at −1.66 V *vs.* $Fc^{+/0}$ (see Section VI). Furthermore, as the resulting anionic species in solution is potentially stabilised *via* intermolecular hydrogen bonding from the hydroxymethyl moiety to either the Fe or the chalcogen atom, respectively. The anion was found to be capable of H_2 production from CH_3COOH *via* a proposed ECEC mechanism.[136]

Another way to modify OH-functionalized complexes is the subsequent derivatisation with a carboxylic chloride in presence of Et_3N and offers a wide range of possible alterations. Song *et al.* described an alternative synthesis of **35** from $Li_2Fe_2S_2(CO)_6$ and 1,3-dibromo-2-propanol and further derivatised the OH-modified bridge (**41** to **43R**) as described in Fig. 27 to explore their influence on the catalytic properties.[137] Herein, model **42** is of special interest, as the pendant phosphine coordinates to one of the iron centres, thereby resembling a closer [2Fe–3S] H-cluster model.[138,139] However, electrocatalytic activity regarding proton reduction was yet solely reported for model **41** bearing the ketone group.[137]

The structural features of a headgroup-bound ligand, which can coordinate to the iron centres as shown in complex **42**, was also addressed by Pickett and coworkers.[140] A series of models of the type $Fe_2((SCH_2)_2C(CH_3)(CH_2S-p-C_6H_4X)(CO)_5)$ (X = CN (**44**), NO_2 (**45**), NH_2 (**46**)) and $Fe_2((SCH_2)_2C(CH_3)(Y))(CO)_5)$ (Y = 2-pyridine (**47**), CH_2OH (**48**), CH_2NH_2 (**49**), CH_2SMe (**50**)) was

subsequently synthesised.[138–140] It is worth mentioning that models **47** to **50** display a pH dependent CO-binding ("on" or "off"). The labile bridgehead substituent acts either as a chelating ligand or as a base. Upon protonation under CO-atmosphere the hexacarbonyl compound is generated, which can be reversed with addition of bases wherein ligand to CO displacement occurs. The influence of the coordination of the pendant thioether on the reactivity of **50** is discussed in Section 5.2.

Following organometallic advances, the interest to develop $[2Fe]_H$ analogues displaying better catalytic behaviour or which could be strategically integrated into electrocatalytic systems gained tremendous popularity.[141–143] Thus, models with easily transformable functionalities such as carboxylic acid groups (**51**) were introduced to $Fe_2(pdt)(CO)_6$-like models by reacting $Fe_3(CO)_{12}$ with *e.g.* 1,2-dithiolane-4-carboxylic acid. The carboxyl group enables the functional binding of suitable amines *via* amide bond formation *e.g.* with aniline, and therefore allows the covalent attachment to amino-functionalized pyrolytic graphite electrode surfaces – interesting candidates for the design of heterogeneous electrocatalysts.[141,144] The catalytic mechanisms and potentials after attachment of the $Fe_2(pdt)(CO)_6$-like model to the surface, seem to be unchanged compared to a "free" complex.

4.2.3.2 Chalcogenide and pnictogenide substituted PDT models. As mentioned in the previous section, the selenium version of a sugar-substituted $Fe_2(pdt)(CO)_6$-like complex shows a higher proton reduction activity and improved stability in aqueous media. To this end, various Se-substituted models (**32**, **52** to **55**) were reported, which can be obtained by refluxing $Fe_3(CO)_{12}$ with either 1,3-diselenocyanatopropane, a modified diselenolane or 1,3,5-triselanacyclohexane (Fig. 28).[145]

In the same manner, models **56** to **58** bearing an oxetane ring were synthesized.[146] The subsequent investigation of these

Fig. 27 Representative modifications of OH-derivatized complexes.[137]

1694 | *Chem. Soc. Rev.*, 2021, **50**, 1668–1784

This journal is © The Royal Society of Chemistry 2021

Fig. 28 Synthesis of selenium modified H-cluster models.

chalcogenide substituted models regarding their proton reduction capabilities revealed a decreasing activity on moving from S- to Te-analogues owing to an increased Fe–Fe distance and hence disfavouring a bridging ligand, e.g. a hydride from direct protonation or a CO ligand from the so called "rotated state".[145,146] A further trend that can be observed upon changing sulphur to selenium or even tellurium is a decreasing reorganization energy for the reduction from a Fe^IFe^I to a Fe^IFe^0 cluster, which balances the increasing electron density at the iron centres due to the sulphur exchange with stronger electron donors.

Along this line, models with additional methylene groups inside the linker were synthesised via reaction of $Fe_3(CO)_{12}$ and the respective 1,2-thiaselenane or 1,2-thiatellurane (59 and 60).[147] Using these models, likewise the change of the reorganization energy upon exchange of sulphur by its heavier homologues was studied and lowered energies were observed.[148]

Additionally, to study the influence of the steric bulk on the reduction properties, methyl substituents (61 and 62) were introduced on the bridgehead carbon of the diselenide linker.[148] The altered reduction behaviour along with catalytic abilities of these complexes will be discussed in Section 6.3.

In addition to the above presented synthesis pathways, the reaction of dihalides and $Fe_2E_2(CO)_6$ (E = S, Se, Te) is a further valuable approach (compare with Fig. 25). Following this synthetic scheme, $Fe_2((TeCH_2)_2CH_2)(CO)_6$ (63) was obtained from the reaction of $Fe_2Te_2(CO)_6$ and $Br(CH_2)_3Br$.[149]

Motivated by a lower acidity of phosphines (R_2PH) as compared to the corresponding thiols, it was likewise postulated that diiron diphosphido models display an enhanced basicity of the iron centres resulting in stable terminal hydrides upon protonation.[141,150–154] To achieve diiron diphosphido analogues, the diphosphines $(CH_2)_n(PPhH)_2$ (n = 2, 3) were refluxed in the presence of $Fe_3(CO)_{12}$ affording complexes 64 and 65. Furthermore, these models were transformed to the diphosphine substituted analogues $Fe_2\{(CH_2)_3(PPh)_2\}(CO)_4(\kappa^2$-dppv) (66a) and $Fe_2\{(CH_2)_3(PPh)_2\}(CO)_4(\kappa^2$-dppbz) (66b). Due to the increased metal basicity they were predicted to undergo

protonation at the metal centre. However, slow protonation at the metal centre resulting in a bridging hydride state was observed in low temperature experiments (−90 °C).[155] For a detailed discussion of the protonation behaviour of H-cluster mimics see Section 5.3.

4.2.3.3 H-cluster models with other group 14 elements in the bridgehead position. The exchange of the C_2 carbon for its heavier homologues (Fig. 29) strongly influences the properties of the resulting complexes. A report by Glass et al., for example, described the synthesis of a tin substituted hydrogenase analogue – $Fe_2((SCH_2)_2SnMe_2)(CO)_6$ (67).[156] The complex was obtained from $Fe_2(SH)_2(CO)_6$, $Me_2Sn(CH_2I)_2$ and Et_3N. Later on, studies on a series of silicon modified dithiolato diiron models were described by Apfel et al.[157] The $Fe_2((SCH_2)_2SiR_1R_2)(CO)_6$ (68 to 70, $R_1 = R_2 = Me$, $(CH_2)_n$ n = 4, 5) complexes were obtained by reacting $Fe_3(CO)_{12}$ and the corresponding bis(mercapto-methyl)silanes. Moreover, the Si-bridged tetranuclear model $(CO)_6Fe_2(SCH_2)_2Si(CH_2S)_2Fe_2(CO)_6$ (71) was synthesised from $Si(CH_2SH)_4$ and $Fe_3(CO)_{12}$. Due to C/Si exchange, the basicity of the sulphur centres increased resulting in a higher probability of S protonation. The group of Weigand and coworkers continued the study on such Si-substituted models and further reported a series of $Fe_2((SCH_2)_2SiR)(CO)_6$ models with bulky Si-bridgehead substituents (R = Si-substituted fluorene (72), xanthene (73) and thioxanthene (74)).[158,159] Furthermore, to investigate the role of bulky dithiolato linkers and their influence on redox properties, models with Ge- and Sn-containing linkers were reported. Adapting the synthetic approach, reaction of $R_2Sn(CH_2I)_2$ (R = Me, Ph) as well as $Me_2Ge(CH_2Cl)_2$ and $Fe_2(SLi)_2(CO)_6$ resulted in the corresponding complexes $Fe_2((SCH_2)_2ER_2)(CO)_6$ (E = Sn (67, 75), R = Me, Ph; Ge (76), R = Me). In case of Sn, the cyclic tetrairon models 77 and 78 were also obtained alongside in low yields (<9%). Notably, while for $E(CH_2S^-)_2$, (E = S, O, NR', CR_2, Si) the bridge adopts a chair/boat geometry, in case of Ge- and Sn-substituted models, the FeSCECS ring preferentially adopts an almost planar geometry indicating the deformability of these rings due to less

This journal is © The Royal Society of Chemistry 2021

Chem. Soc. Rev., 2021, 50, 1668–1784 | 1695
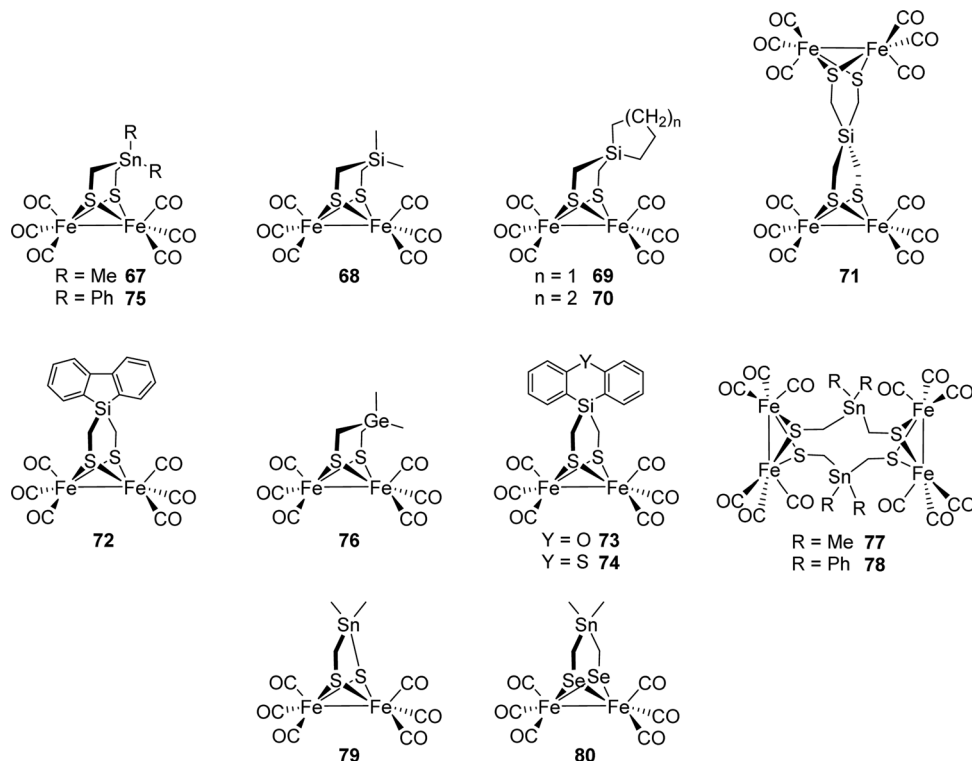
Fig. 29 Literature-known exchanges of the bridgehead carbon atom by heavier analogues.

torsional strain.[160] These studies were further extended and models with selenium substituted Sn-bridges were reported.[161] $Fe_2((Se_2(CH_2)_nSnMe_2)(CO)_6$ (n = 1 (**79**), 2 (**80**)) were obtained from $Me_2Sn(CH_2Se)_2$ or $Me_2Sn(CH_2Se)Se$ and $Fe_3(CO)_{12}$ and the desired complexes were obtained in moderate yields (20 to 30%). Herein, also the chalcogenide substitution along with C/Sn exchange causes an increased basicity of the metal core thereby facilitating its protonation.

Notably, the silicon bearing aromatic system possesses light harvesting properties.[162,163] The [FeFe]-hydrogenase model **72** with the covalently attached photosensitizer 1-silafluorene was synthesised *via* the reaction of 1,1′-bis(chloromethyl)-1-sila-fluorene and $Fe_2S_2(CO)_6$. Photochemical H_2 evolution experiments were then performed in acetonitrile using trifluoroacetic acid as proton donor and triethylamine as electron donor revealing a turnover number (TON) of 29 and a turnover frequency (TOF) of 2.2 h^{-1}.[164]

4.2.3.4 PDT models with secondary sphere modifications. In Section 4.2.3.1, we already presented mimics that were easily modified by amide bond formation between a carboxylic acid at the C_2 position of the dithiolate bridge and a modified amine. Along this line, [2Fe–2S]-clusters were also incorporated into larger matrices such as *e.g.* (bio-)polymers. Incorporating the previously highlighted mimics into a larger matrix was shown to enable its protection from undesired influences of foreign substrates and higher complex stability was anticipated. $Fe_2(pdt)(CO)_6$ models were immobilized on various polymers (*e.g.* polyacrylic acid[132,165] and polystyrene–polyethylene glycol[166])

through an amide bond between **81** and amines of the proteins or a redox active group enabling a study of electron transfer processes in such systems. Contrary to those expectations, the PEG environment facilitated degradation of the iron cluster by CO loss and subsequent binding of the ether-oxygen. Likewise, a more unstable behaviour against acidic media was found caused by the surrounding ether moieties in the polymer.[166]

4.2.4 Azadithiolate (ADT) models. Even before the final structural elucidation, it was suggested that a secondary amine in the enzymatic cofactor, in close vicinity to the diiron site, would facilitate a low energetic pathway for proton hydride combination due to its protonation accounting for the unsurpassed catalytic efficiency.[2,29] The importance of an amine-bridge was further supported by DFT calculations.[167]

The synthesis of $Fe_2(adt)(CO)_6$-like models was first reported in 2001. Here, the dilithium salt of $Fe_2S_2(CO)_6$ was obtained *via* reaction of $Fe_2S_2(CO)_6$ with $Li[BEt_3H]$ and afforded the N-functionalized models $Fe_2(adt^R)(CO)_6$ (R = Me (**82**), allyl (**83**), $(CH_2)_2SMe$ (**84**)) upon reaction with the respective bis-(chloromethyl)amine precursor bridges.[168,169] It was further reported that the bridges can be generated *via* chloromethylation of various primary amines by a successive reaction with para-formaldehyde in CH_2Cl_2 and the following addition of $SOCl_2$.[169] This method opened up the field for easily accessible N-func-tionalized models of the [2Fe–2S]-subsite hydrogenases mimics.

Subsequently, Li and Rauchfuss synthesized the cofactor mimic **2** bearing a secondary amine.[17] Here, condensation of $Fe_2(SH)_2(CO)_6$, which was obtained *via* protonation of $Li_2Fe_2-S_2(CO)_6$, and urotropine $((CH_2)_6N_4)$ gave the desired complex in

1696 | *Chem. Soc. Rev.*, 2021, **50**, 1668–1784

This journal is © The Royal Society of Chemistry 2021
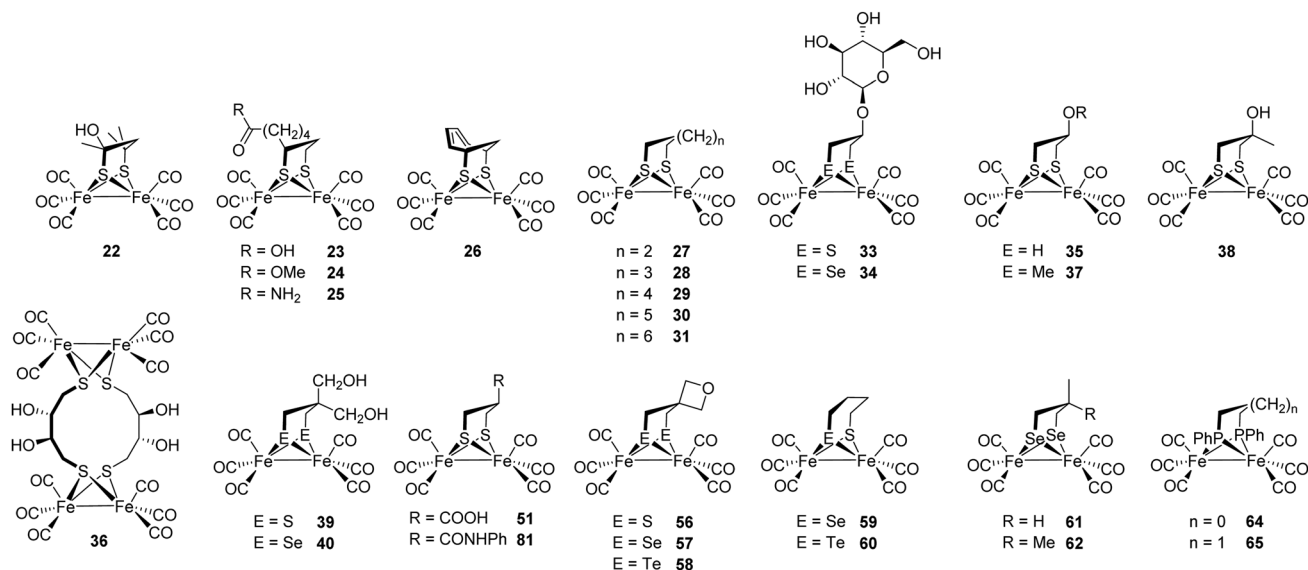
Fig. 30 Representative PDT models presented in this section.
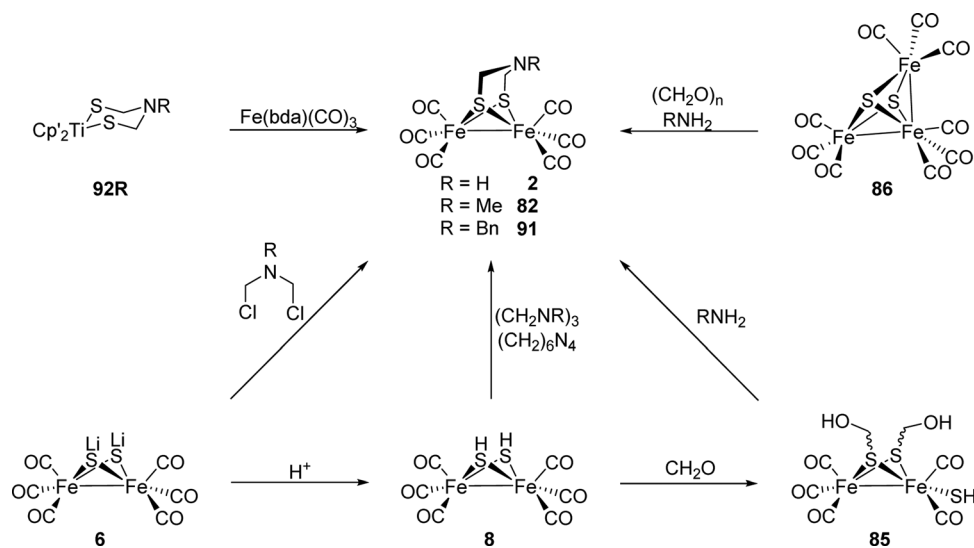
Fig. 31 Synthetic pathways towards $Fe_2(adt^R)(CO)_6$ mimics. (Cp' = MeC_5H_4).

moderate yields of 24%. The yield could be improved to *ca.* 40% when using a premixed solution of $(NH_4)_2CO_3$ and paraformaldehyde instead of urotropine.[17] As shown in Fig. 31, the reaction might proceed *via* the formation of intermediate $Fe_2(SCH_2OH)_2(CO)_6$ (**85**), which feasibility and reactivity was later studied by Stanley *et al.*[120] Another route to obtain **2** in 28% yield was the reaction of $Fe_3S_2(CO)_9$ (**86**) with ammonium carbonate $((NH_4)_2CO_3)$ and paraformaldehyde.[17]

A further method to prepare $Fe_2(adt)(CO)_6$ was presented by Wang *et al.* who reported on the synthesis of this complex using organosilicon protecting groups (Fig. 32). The group employed alkylsilylchlorides ($^iPr_3SiCl$ (**87**), Et_3SiCl (**88**), $^tBuMe_2SiCl$ (**89**)) along with ammonia and paraformaldehyde, which was reacted with $Fe_2(SH)_2(CO)_6$ resulting in the highest yield of 36% after deprotection with TFA in case of **87**.[170]

In 2010, Rauchfuss *et al.* investigated a rather unusual pathway to obtain $Fe_2(adt^R)(CO)_6$ (R = Me (**82**), Ph (**90**), Bn (**91**)). Herein, the organotitanium complex $(MeC_5H_4)_2Ti(adt^R)$ (**92R**) was used as an azadithiolate transfer agent to [Fe(bda)-$(CO)_3$] (bda = benzylideneacetone) giving $Fe_2(adt^{Ph})(CO)_6$ in 42% yield.[171]

In 2015, a synthesis for isotope-labelled $^{57}Fe_2(adt)(CO)_6$ starting from $^{57}FeBr_2$ was reported (Fig. 33).[71] Analogous to the synthesis of **1** reported by Hieber,[172] ^{57}**1** is formed from the reaction of $[H^{57}Fe(CO)_4]^-$ (^{57}**93**) and elemental sulphur. Since the established routes towards the native cofactor are based on iron carbonyl chemistry, and labelling of $Fe(CO)_5$ with ^{57}Fe is challenging on laboratory scale, this new route was developed to avoid $Fe(CO)_5$ (or derivatives thereof) as starting material. This allowed for explicit spectroscopic investigations by NRVS

This journal is © The Royal Society of Chemistry 2021

Chem. Soc. Rev., 2021, **50**, 1668–1784 | **1697**

Fig. 32 Alternative synthesis of complex **2**.
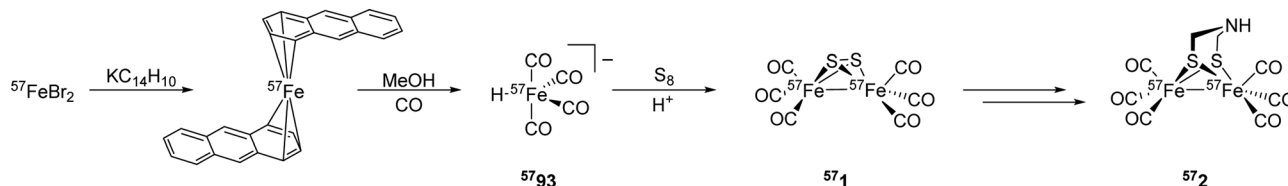
Fig. 33 Synthetic pathway to $^{57}Fe_2(adt)(CO)_6$.

and Mössbauer of $[2^{57}Fe]_H$ first in its $\mathbf{H_{ox}}$-**CO** state and later in $\mathbf{H_{ox}}$, $\mathbf{H_{hyd}}$ and $\mathbf{H_{ox}}$-$\mathbf{O_2}$ as well (see Section III).[64,71]

Extending the chalcogenide exchange to the adt models as well, the enzyme cofactor was synthesised with selenium. The straightforward synthetic route comprises of coupling of carbamate protected amine with $Li_2Fe_2Se_2(CO)_6$ (**94**) followed by deprotection with BF_3 and Me_2S (Fig. 34).[32,173] Deprotection of **95** afforded the target product **96** in 20% yield, which was further subjected to ligand exchange resulting in $[Fe_2(adSe)\text{-}(CO)_4(CN)_2]^{2-}$ (**4**). This complex could also be embedded into apo-*Cr*HydA1 and apo-*Cp*I (see Section 2.2).[32]

4.2.4.1 N-Alkyl modified ADT models. The conceptually most obvious modification of the amine-linker is a simple alkyl chain, which is, however, not much reported in literature.[17,168,174–176] The shortest version, model **82** bearing a methyl moiety, can be synthesized according Fig. 31 or by salt-elimination using $Li_2Fe_2S_2(CO)_6$ and methylbis(chloromethyl)-amine.[17,168] The methyl group resides either in axial or equatorial position, which is dependent on a balance between the anomeric effect (favours an axial position) and steric repulsions between the methyl group and the carbonyl ligands (favours an equatorial positions).[168] Compared to $Fe_2(adt)(CO)_6$, the methyl substitution changes the catalytic properties in two ways: (1) the inductive effect of the methyl group increases the electron density and therefore the basicity of the amine bridge and (2) the electron density of the iron

centres is increased *via* hyperconjugation of the N_{1p} and C–S σ^* orbitals. This changed electron density is, however, not visible by a shift of the CO-frequencies within the IR spectra, but results in a shift of the first reduction potential from -1.58 V for NH (**2**) to -1.72 V for the NMe derivative (**82**) (*vs.* Fc/Fc^+). As a result, the methyl substitution allows for the use of less acidic proton sources during the proton reduction while the potential that has to be applied to reduce the system is more negative.[17,168,170,176]

Along this line, $Fe_2(adt^R)(CO)_6$ (**97**, R = $(CH_2)_2NHTs$) was synthesised but amine deprotection was unsuccessful, thereby restricting its further application. In addition, the tetranuclear model **98** was reported containing two linked adt-units.[177]

Lengthening the alkyl chain substituents increases the steric bulk around the metal centres and is advantageous in terms of mimicking specific H-cluster redox states. Modifications with longer alkyl chains range from simple ethyl groups to more complex cyclic alkyls.[17,120,174,176,178–185] The synthetic protocols are similar to those for $Fe_2(adt^R)(CO)_6$ (R = H, Me). Both strategies, condensation of the respective amine with (*para*)-formaldehyde and the following reaction with $Fe_2(SH)_2(CO)_6$ or the salt-elimination method can be regularly found in literature. The electron donor abilities of the alkyl-moieties increase from ethyl to isopropyl/*sec*-butyl to *tert*-butyl, which is reflected by a more cathodic potential, decreasing average CO-frequencies, as well as an increasing Fe–Fe bond distance.[176,182] However, the differences in electronic parameters between
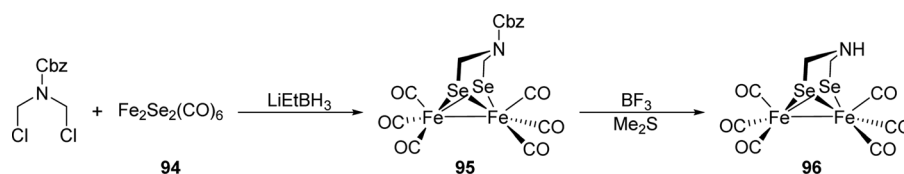
Fig. 34 Synthetic pathway to $Fe_2(adSe)(CO)_6$ (**96**).
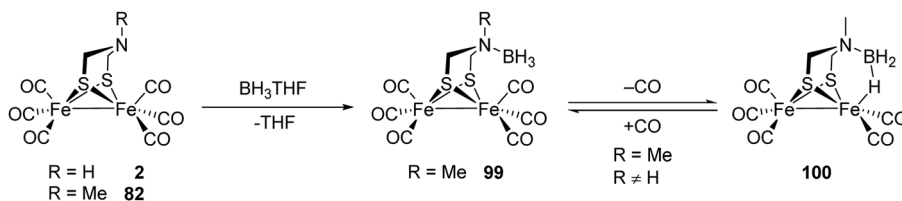
Fig. 35 Binding of BH_3 to the Fe centre.

the respective alkyl chain modifications are almost non-significant.[179–183,186]

To shed light into the protonation behaviour of the active site, the acid base chemistry between the adt moiety and BH_3 was investigated with model system **2** and **82**.[175] Treating $Fe_2(adt^{Me})(CO)_6$ with one equivalent of $BH_3 \cdot THF$, wherein the N-coordinating BH_3 group of model **99** binds to the Fe upon decarbonylation afforded complex **100** (Fig. 35). This study served as an illustration for the analogous binding of H_2 to the iron centre in the enzyme.[175]

4.2.4.2 N-Modification of ADT models by esters and amides. In Section 4.2.3, we reported on modifications of $Fe_2(pdt)(CO)_6$-like complexes with hydroxy- or carboxylic acid-functional groups *via* esterification reactions or formation of amides.

The same methodology can be applied to $Fe_2(adt)(CO)_6$-like structures as well. These functional and structural models have been extensively studied to reveal the mechanism of the enzyme.[187–189]

Song *et al.* as well as Sun and coworkers reported on the functionalization of hydroxy-modified $Fe_2(adt^R)(CO)_6$ (**101**, R = CH_2CH_2OH) to various N-modified complexes (Fig. 36).[186,190] As observed for hydroxy-modified pdt-models,[134] the hydroxy group of **101** forms an intermolecular H-bond network.[186] *Via* addition of derivatised carboxylic chlorides, aromatic groups (**102** to **105**) can be added to the bridge. In addition, a terephthalic acid bridged dimer (**106**) and a thioacetate derivate (**107**) have been reported.[186,190] However, as also observed for pdt-models, the catalytic properties of these models cannot be altered by changing the substituents at the nitrogen atom.[190]
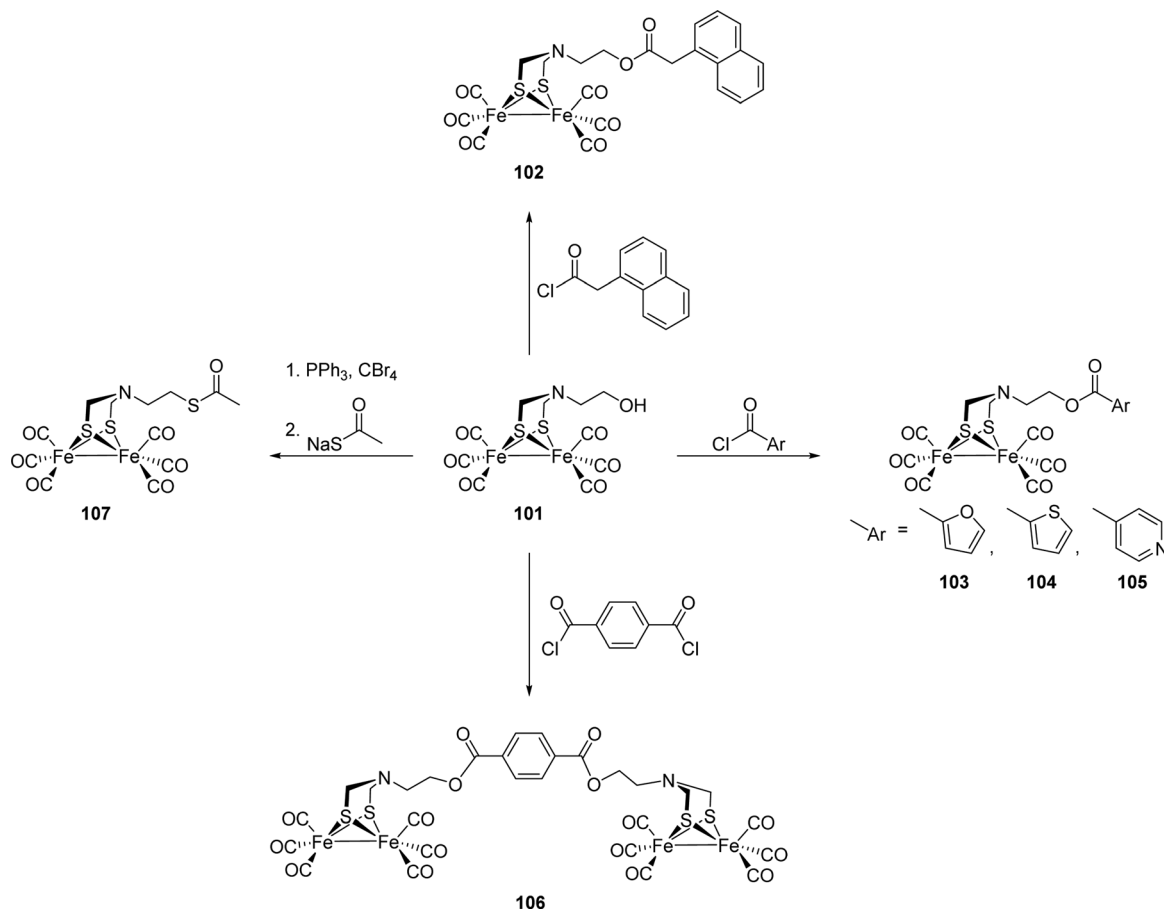
Fig. 36 Towards the syntheses of *N*-alkanol modified models.

This journal is © The Royal Society of Chemistry 2021

Chem. Soc. Rev., 2021, **50**, 1668–1784 | **1699**

Extending this concept to adSe derivatives, Gao *et al.* reported a series of double as well as triple cluster cores by linking multiple molecules of $Fe_2(SeCH_2)_2NR(CO)_6$ (R = $(CH_2)_2OH$) (**108**).[173]

Instead of hydroxy alkyl-modified amines, the introduction of carboxylic acids was performed with the same overall aim. $Fe_2((SCH_2OH)_2(CO)_6$ was reacted with the corresponding amino acids ((2-aminomethyl)benzoic acid, 2- or 4-aminobutyric acid) and afforded the desired hexacarbonyl products **109** to **111**.[191]

The group of Song reported an additional modification scheme with diverse models bearing *N*-acyl functionalities (**112** to **116**) (Fig. 37).[192] For example, model **116** was obtained upon reaction of **2** with 2-chloroacetic acid or chloroacetyl chloride and subsequent treatment with potassium thioacetate. Due the electron withdrawing substituents, these complexes display first reduction potentials in the range of −1.49 V to −1.54 V *vs.* $Fc^{+/0}$, which is milder than for unmodified complex **2** (−1.58 V).[170] Likewise, these models serve as a template for designing systems suitable for photocatalytic studies by modifying the acyl group.[192]

4.2.4.3 N-Aryl modified ADT models. Subsequently, an ADT model series of substituted *N*-phenyl complexes (**117** to **121**) was established.[193] Crystal structures of the *ortho*-substituted models show sp³-hybridisation of the bridgehead nitrogen, while the *para*-substituted models **119** and **120** display a rather sp²-behavior at the nitrogen. Due to the steric influence of the substituents, the lone pair of the nitrogen is unable to delocalise into the aromatic ring and hence these substituted models are capable of conducting proton reduction at near neutral pH 5.5 with low overpotentials in aerobic conditions. On the other hand, *ortho* unsubstituted models with electron withdrawing substituents (Br and NO_2) at the *para* position, required harsher acidic conditions for proton reduction due to the diminished basic nature of the nitrogen.[193]

In view of developing the ADT models, the nitro functionalized model **120** model was established by treating $Fe_2S_2(CO)_6$ with *N,N*-bis(chloromethyl)-4-nitroaniline followed by reduction with Pd/H_2. This procedure yields the corresponding amine derivative $Fe_2((adt^R)(CO)_6$ (**122**, R = *p*-$C_6H_4NH_2$).[194] Additionally, condensation of *N,N*-bis(chloromethyl)-*p*-methoxyaniline with $Li_2Fe_2S_2(CO)_6$ afforded $Fe_2((adt^R)(CO)_6$ (**123**, R = *p*-C_6H_4OMe).[195] The different electronic effects of the ring substituents are evident in the reductive behaviour of these models. Due to the electron withdrawing nature, the nitro-substituted model **120** is reduced at more positive potential as compared to the amino **122** and the methoxy derivative **123** (E_{120} = −1.42 V *vs.* E_{122} = −1.56 V and E_{123} = −1.61 V).[194,195] As these previous studies on aromatic substituents suggested a decreased reduction potential, Jiang *et al.* introduced furan, thiophene and pyridine substituents on the $Fe_2(adt^R)(CO)_6$ models (**124** to **126**).[196,197] Herein, the electronic interactions between the heterocycles and the metal centre *via* linking C, N, S atoms, influences the redox behaviour.

Fig. 37 Syntheses of *N*-acyl modified models.

1700 | *Chem. Soc. Rev.,* 2021, **50**, 1668–1784

This journal is © The Royal Society of Chemistry 2021

Additionally, bromine was introduced at the thiophene ring in **127** to facilitate functionalization. This bromothiophene model is catalytically active with $HClO_4$ at a potential of -1.09 V *vs.* Fc/Fc^+, which is significantly lower as reported for other ADT models.[196]

Extending the study to ADSe mimics, complexes with *N*-aryl diselenide bridges were synthesised (**128** to **130**).[198] Introduction of different substituents (CH_3, NO_2, H) at the *para* positions of the aryl ring aimed at studying the inductive effects. Electrochemical results were in accordance with the trends observed for sulphur bearing models, *i.e.* the nitro substituted complex was more easily reduced than the alkyl substituted complex. Also, crystallographic studies show that sulphur to selenium replacement is responsible for slight elongation of the Fe–Fe bond.[198]

In a more recent approach, the [2Fe–2S]-cluster was attached to a variety of molecules such as nucleosides, redox active fragments (ferrocene and ruthenocene), and luminescent markers (boron-dipyrromethenes–BODIPYs) by introducing an azide functionality (**131**) and subsequent Cu-catalysed Huisgen cycloaddition (Click-reaction) between terminal alkynes and azides. Advantages of this strategy are high tolerance towards sensitive substrates and a broad range of various functional groups. It was further shown that the resulting triazole rings from the click-reaction can be protonated by strong acids such as H_2SO_4 and therefore serve as model for the native adt bridge.[199]

4.2.4.4 N/P exchange in ADT models. Even though phosphorus is the heavier analogue of nitrogen, little effort has been conducted to establish active site mimics of [FeFe]-hydrogenases bearing phosphorus in the linker (Fig. 38). A preceding attempt to introduce a tertiary phosphine bridge resulted in ligand substitution in complex **132R** (R = Ph, CH_2Fc) due to the high nucleophilicity of the phosphine.[200] Therefore, models **133R** wherein phosphorus is incorporated into the bridging position were synthesized from $Li_2Fe_2S_2(CO)_6$ and phosphine oxides $O{=}P(R)(CH_2Cl)_2$ (R = Ph, OEt) to avoid interaction of the lone pair phosphorus with the iron centre.[201,202] Furthermore, this $O{=}P$ functionality was identified as the protonation site in this model system. Recently, a new strategy to synthesize complexes wherein the phosphorus occupies the bridgehead position

was reported. There, $Fe_3(CO)_{12}$ and the respective dithiols $O{=}PR(CH_2SH)_2$ (R = OEt, OMe, OPh, OH, Me) were reacted in THF at room temperature to obtain the desired compounds **133R** in moderate yields of approx. 40%.[202]

Another aza-diphosphido model **134** was synthesized *via* deprotonation of a $Fe_2(PPhH)_2(CO)_6$ precursor with MeLi and further incorporation of a $(Cl(CH_2)_2)NR$ (R = CH_2CH_2OMe) linker (Fig. 39). Notably, protonation of these aza-diphosphido analogues occurs exclusively at the amine bridgehead.[203]

4.2.5 Oxadithiolate (ODT) models. Based on the first crystal structures of [FeFe]-hydrogenases, $[Fe_2(odt)(CO)_4(CN)_2]^{2-}$ (**135**) was one of the mimics considered to be the putative active site, since the central oxygen atom has the same number of electrons as the actual active sites head group NH.[3,14] Its precursor $Fe_2(odt)(CO)_6$ (**136**) was originally prepared *via* acidification of $Fe_2(SCH_2OH)_2(CO)_6$, and later from $Li_2Fe_2S_2(CO)_6$ and $(ClCH_2)_2O$ *via* salt-elimination (Fig. 40).[17,204] Compared to $Fe_2(adt)(CO)_6$, the average CO frequency of the oxadithiolate derivate is slightly upshifted from 2018 to 2024 cm^{-1} in hexane indicating the influence of the electron withdrawing oxygen group on the overall electronic structure of the diiron cluster.[17] However, this electron withdrawing behaviour is not reflected in the respective first reduction potential, which is identical for both complexes at -1.58 V *vs.* Fc/Fc^+.

For the oxadithiolate models, sulphur to heavier homologue exchange was carried out and $Fe_2(odSe)(CO)_6$ (**137**) and $Fe_2(odTe)(CO)_6$ (**138**) complexes were reported. While **137** was obtained in 45% yield from addition of $(HSeCH_2)_2O$ to $Fe_3(CO)_{12}$,[205] **138** was synthesised in 21% yield from $Fe_2Te_2(CO)_6$ and $(ClCH_2)_2O$.[206]

As already reported for the model counterparts **2** and **20**, substitution of CO with more electron donating ligands such as CN^-, PR_3, NHCs and $Cp(CO)_2FeSPh$ was carried out to further influence the electron density at the iron centres.[181,185,207–210] Additionally, tetranuclear models wherein the modified ligand system (dppf, $(Ph_2PCH_2)_2NCH_2)_2$, $(Ph_2PCH_2CH_2OCH_2)_2$ and $1,4{-}(CN)_2C_6H_4$) connect two [2Fe–2S]-cores have been synthesised and crystallographically elucidated.[204]

4.2.5.1 O/S exchange in ODT models. In contrast to the little explored N–P exchange in adt, incorporation of the heavier
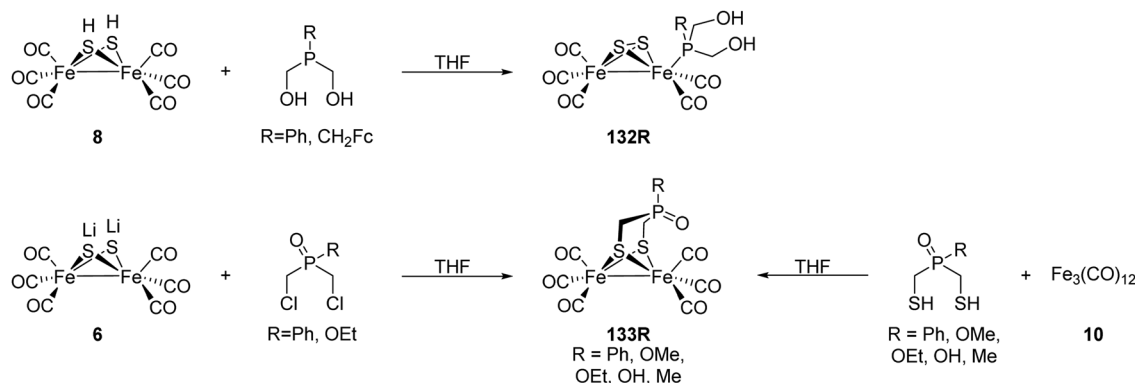
Fig. 38 Synthetic pathways to phosphorus substituted subsite models.

This journal is © The Royal Society of Chemistry 2021

Chem. Soc. Rev., 2021, **50**, 1668–1784 | **1701**

Fig. 39 ADT derived complexes.

Fig. 40 Synthesis routes towards $Fe_2(odt)(CO)_6$.

homologue sulphur is much more common in odt complexes. According to IR spectroscopy, both models do not show significant electronic differences although sulphur is less electron withdrawing than oxygen.[204,211] The first reduction potential of $Fe_2(sdt)(CO)_6$ (**139**), however, is shifted from $E_{146} = -1.58$ V to $E_{150} = -1.51$ V *vs.* Fc/Fc$^+$, showing a more severe change in the electron density at the iron centre.[204,211]

The synthesis of **139** was reported initially by Song *et al.* in 2007, using 1,2,4-trithiolane as starting material, which was reacted with $Fe_3(CO)_{12}$ in refluxing THF to yield the desired complex in 42% yield.[211] In parallel, Windhager *et al.* reported various model complexes (**140** to **142**) containing S-substituted bridge structures obtained by reacting $Fe_2(CO)_9$ with different sulphur substituted heterocycles. It was observed that larger

1702 | *Chem. Soc. Rev.*, 2021, **50**, 1668–1784

This journal is © The Royal Society of Chemistry 2021
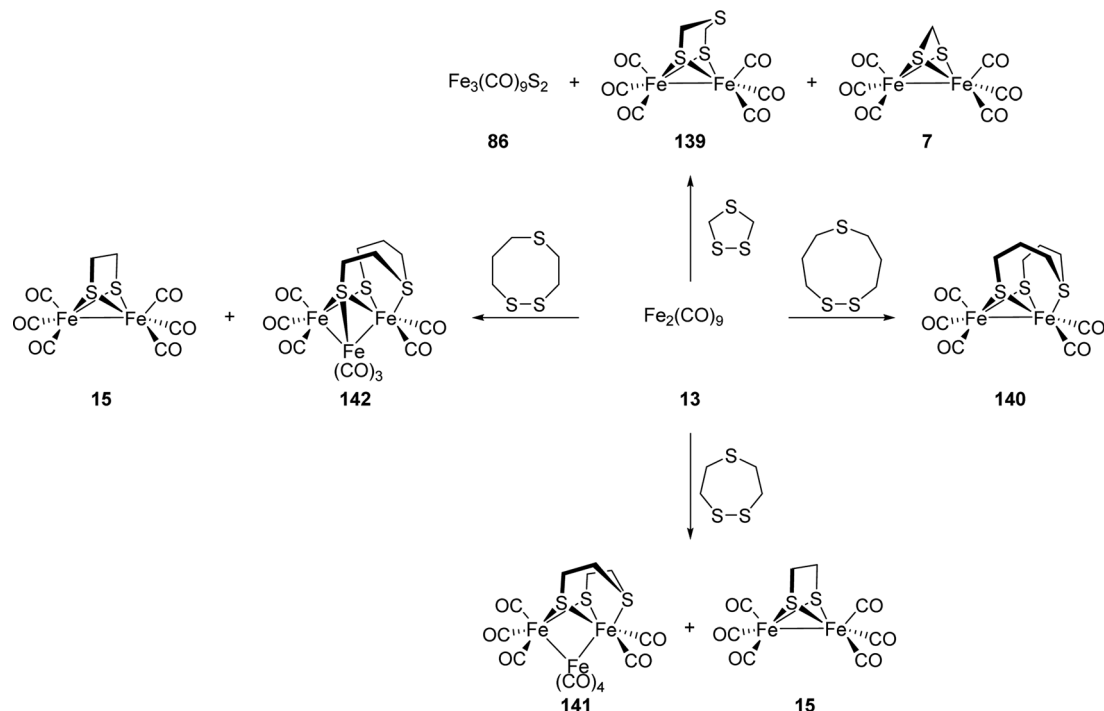
Fig. 41 Syntheses of multi-metallic complexes from sulphur heterocycles.
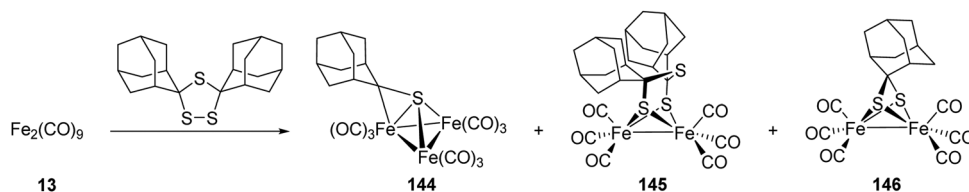
Fig. 42 Synthetic pathways to novel sdt complexes from Fe$_2$(CO)$_9$.

heterocycles yield trinuclear clusters (**141** and **142**). The flexibility of the linker strongly affects the structure of the resulting models, *e.g.* the 7- and 8-membered heterocycles yield triiron clusters wherein the thioether moieties coordinate to one of the Fe centres each. Applying the 9-membered thio compounds affords the diiron complex **140** (Fig. 41).[212]

The treatment of diiron thiadithiolate with Cp(CO)$_2$Fe(BF$_4$), prepared *in situ* from Cp(CO)$_2$FeI and AgBF$_4$, led to cationic model **143a** (Fig. 43). This model corroborates the ability of

Fig. 43 Trimetallic subsite models with coordination of the bridgehead sulphur to metal centres.

the bridgehead sulphur atom to likewise coordinate to metal centres.[211] Taking advantage of this coordinating capability, the parent Fe$_2$(sdt)(CO)$_6$ model was reacted with M(CO)$_5$(THF) (M = Cr, W) (prepared *in situ* by photolysis of M(CO)$_6$ in THF) and afforded the multi-metallic complexes **143b** and **143c**.[213] These complexes were designed to profit from combined redox properties of the different metals involved; however, they were unstable under electrochemical conditions and hence could not be studied for their catalytic properties.[213]

Additionally, the introduction of substituted 1,2,4-trithiolanes leads to various di-, tri- and tetranuclear models and is exemplarily shown for the diadamantyl-substituted trithiolane in Fig. 42. The synthesis proceeds through an oxidative addition of the disulphide bond to Fe$_2$(CO)$_9$ yielding models **144** to **146**.[214]

4.2.5.2 Oxidation of SDT-like models. The Fe$_2$(sdt)(CO)$_6$ models were likewise studied for their chemical oxidation response, as it was reasoned that the activity of [FeFe]-hydrogenases is hampered under aerobic conditions due to oxidation of the cofactor.[215] Sulphur-oxidation was achieved through reaction of varying equivalents of dimethyldioxirane (DMD)

This journal is © The Royal Society of Chemistry 2021

Chem. Soc. Rev., 2021, **50**, 1668–1784 | **1703**
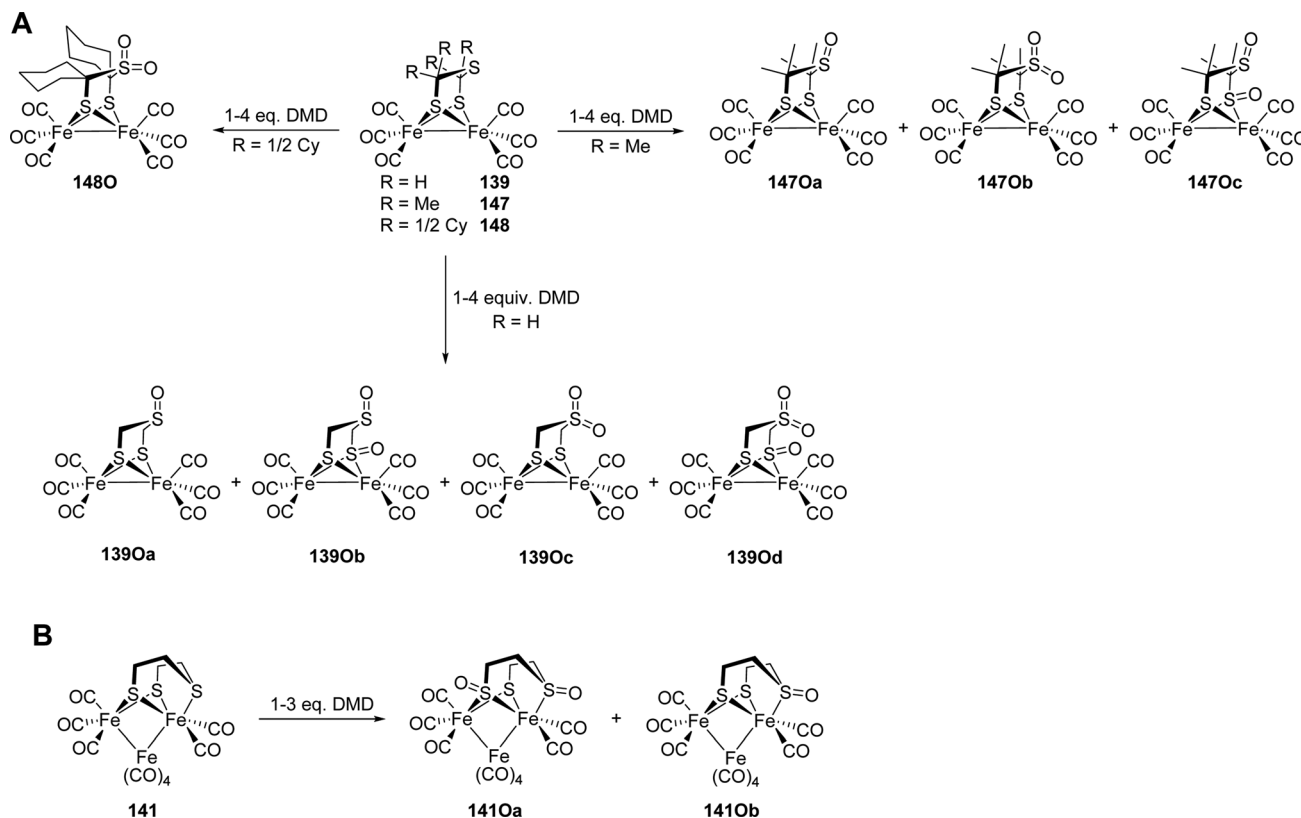
Fig. 44 Chemical oxidation of thiadithiolate models-resulting various oxidised complexes.

with SDT and derived precursors, yielding S-oxidised models (Fig. 44A).[216] These oxidation investigations were carried out on models **139**, **147** and **148** with different substituents on the methylene carbons (R = H, Me, 1/2Cy). An increasing susceptibility for oxidation products with decreasing steric bulk of the substituents was observed. Also, the triiron model **141** was subjected to oxidizing conditions yielding the oxidized thiolate and thioether metal cluster models **141Oa** and **141Ob** (Fig. 44B).[216] Such oxidations were also reported for the Fe$_2$(edt)(CO)$_6$ models using *m*-chloroperbenzoic acid.[217] Chemical oxidation of Fe$_2$(pdt)(CO)$_{(6-n)}$L$_n$ (L = CO, PPh$_3$, PMe$_3$) also shed light into the site specificity of the oxygenation. DFT calculations suggested that oxidation of the Fe–Fe bond is thermodynamically favoured resulting in μ-oxo species. Contrastingly, the experimental studies revealed oxygenation at the dithiolate sulphur resulting in S-oxygenate products which were crystallographically ellucidated.[215] Recently, Berggren, Hammerström and coworkers conducted oxidative degradation studies on Fe$_2$(adt)(CO)$_6$ and Fe$_2$(pdt)(CO)$_6$ complexes.[218] They showed that the interaction of Fe$_2$(adt)(CO)$_6$ with molecular oxygen in presence of chemical reductants leads to a transient degenerated state. Although Fe$_2$(pdt)(CO)$_6$ showed similar oxygen reactivity as compared with the above-mentioned complexes, the reaction speed was slow. The experiments thus highlight the importance of the secondary sphere on oxidative degradation pathways. The final steps of the oxidative cofactor degradation, however, are still unknown and further experiments are required to pinpoint this important aspect. Likewise, the influence of the cyanides is not understood yet.

4.2.6 Benzenedithiolate (BDT) models. The unsubstituted Fe$_2$(bdt)(CO)$_6$ (**149**, bdt = 1,2-benzenedithiolate) model can be synthesized from Fe$_2$(CO)$_9$ and 1,2-benzenedithiol.[219,220] Although it was at first not intended as a [FeFe]-hydrogenase mimic, the synthesized complex had significant similarities with the enzyme's active site. The IR spectrum in hexane shows only slightly shifted CO bands of 2079, 2044, 2006, 1967 and 1958 cm^{-1} compared to **2** which shows its respective bands at 2076, 2036, 2008, 1989 and 1979 cm^{-1}. This shift of the CO-frequencies is indicative for a reduced electron density at the iron core of the **149** and manifests also in the its redox potentials. According to Capon *et al.*, **149** undergoes a 2e$^-$-reduction at −1.35 V *vs.* Fc/Fc$^+$, which clearly distinguishes this model from all other [FeFe]-hydrogenase models.[221] These remarkable redox properties stem from an interaction between the sulphur and benzene p$_\pi$ orbitals that balance the electron count on the iron centres and reduce the energy changes upon reduction of the complex.[222]

These factors stimulated synthetic efforts and led to dedicated research to elucidate the influence of rigid and aromatic bridges on reactivity and electrochemical properties of such [FeFe]-hydrogenase model compounds. Strikingly, **149** was also reported to catalyse the reduction of CO$_2$ to formate.[223]

A recent review[224] on [FeFe]-hydrogenase mimics with aryldithiolate ligands covers many aspects of the design and application of these complexes as electro- or photocatalysts. Moreover, also monometallic bdt complexes are discussed, while we strictly focused on complexes with a [2Fe–2S]-core.

The electron withdrawing effect of the benzene moiety in $Fe_2(bdt)(CO)_6$ was the starting point of several additional studies, aiming at introducing further electron withdrawing groups to shift the reduction potential to more anodic potentials. Hence, the $Fe_2(S_2C_6H_{4-x}Cl_x)(CO)_6$ type complexes **150** to **152** (X = 2 to 4) were investigated in-depth and compared with $Fe_2(bdt^{4Me})(CO)_6$ (**153**, bdt^{4Me} = 4-methylbenzene-1,2-dithiolate).[222,225–227] While the methyl group causes a +I effect, the chlorines possess a strong −I effect.[226] As expected, **152** shows a strongly shifted CO IR pattern (approx. +10 cm^{-1}) compared to the methyl-substituted derivative. This observation reveals a decreased electron density at the diiron centre. Likewise, the reduction potential shifts towards more anodic values from −1.34 V (**153**) to reach −1.13 V (**152**).[226] Other substituents at the benzene ring, e.g. hydroxy-moieties, or electron deficient heteroaromatic rings, e.g. pyrazine, were also tested and shown to facilitate the reduction of the diiron centre.[228,229]

Models **154R** were synthesized via reaction of substituted 1,4-benzoquinones with $Fe_2(SH)_2(CO)_6$ in the presence of piperidine (Fig. 45).[230] These models were expected to undergo facile reduction, as it was proposed that hydroxyl substituents would aid in the stabilization of the accumulated negative charge on sulphur upon Fe–S bond cleavage. Electrocatalytic investigations of these analogues revealed that these models conduct catalysis at 44 mV lower overpotentials than $Fe_2(bdt)(CO)_6$. However, these hydroquinone models were also found to be less active for proton reduction from weak acids due to internal hydrogen bonding.[228] The hydroquinone was further functionalised with pyridine carboxylic acid chloride to introduce a basic proton relay[231] or with ferrocenoyl chloride to afford **155**. This model exhibits three isomers depending on the orientation of the Fc moieties.[232] The ferrocene unit, however, did not possess any interaction with the diiron core.

Another option to alter the properties of the hydroquinones **154R** was demonstrated by the oxidation with DDQ (2,3-dichloro-5,6-dicyano-1,4-benzoquinone). The respective models

156R possessing non-innocent quinones as ligands were compared to models **157** (1,4-naphthoquinone) and **158** (1,4-anthraquinone) with increased π-systems.[230] It was anticipated that the extended π-systems would favour the electron transfer to the [2Fe–2S]-centres and further anodically shift the reduction potential. However, protonation occurs at the quinone oxygen rather than the metal centre and consequently no H_2 evolution was observed.[230]

Similarly, functionalization of the carboxylic acid in the cbdt ligand of complex **159** allows for the introduction of a phosphine ligand tethered to the bridging dithiol, exemplarily shown in complex **160** (Fig. 46). This linkage was shown to increase the rotation barrier of the rotation of the respective $Fe(L)_3$ fragment. Thereby, kinetically labile, terminal hydrides were proposed to be stabilised.[233]

The effect of increased π-systems, as performed in case of 1,4-quinones, was also investigated for N-heterocycles **161** (quinoxaline-6,7-dithiol), **162** (2,3-diphenyl-6,7-quinoxaline dithiol) and **163** (2,1,3-benzothiadiazole-5,6-dithiol) (Fig. 47). These heterocycles withdraw electron density from the metal centres and thereby cause an anodic shift of the reduction potentials (E_{161} = −1.23 V, E_{162} = −1.24 V, E_{163} = −1.25 V vs. E_{149} = −1.33 V vs. Fc/Fc$^+$). Despite related structures, the models **162** and **163** follow different catalytic mechanisms. Due to the electron delocalisation within **161** caused by the additional S-atom, the nitrogen is unable to act as basic site and hence the complex follows an EC mechanism during proton reduction. Due to the absence of such an electron delocalization,
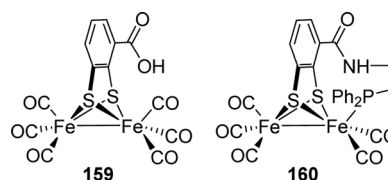
Fig. 46 Complexes **159** and **160**.
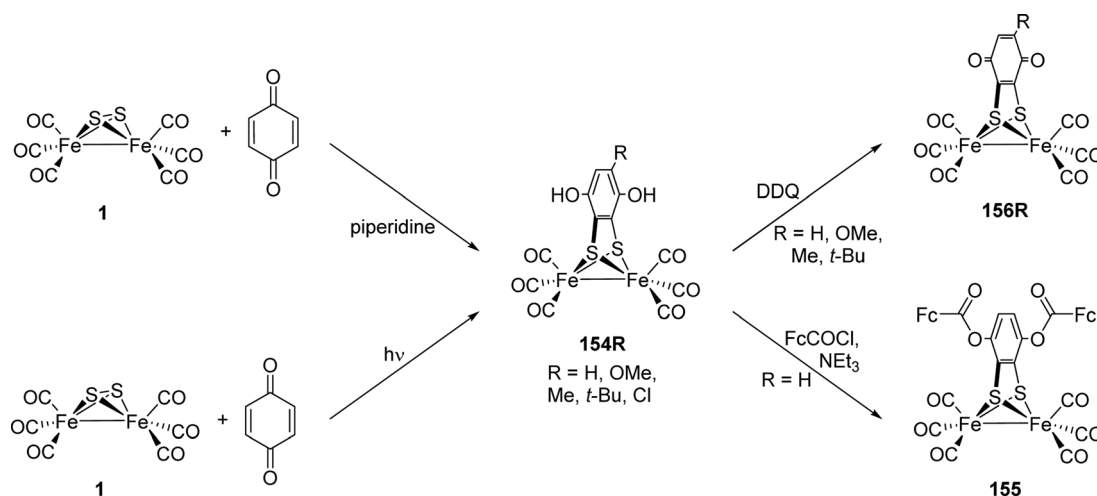
Fig. 45 Functionalized hydroquinone models **154R** to **156**.

This journal is © The Royal Society of Chemistry 2021

Chem. Soc. Rev., 2021, **50**, 1668–1784 | **1705**

Fig. 47 Multi-heteroaryl containing mimics.

Fig. 48 Multimetallic bdt-derived complexes **164** to **166**.

protonation at the ring nitrogen of **162** occurs and leads to a CEEC mechanism.[234]

Chen *et al.* designed tetra- and hexametallic clusters (**164** to **166**, Fig. 48) that undergo two or three consecutive two-electron reduction reactions and can act as stable multi-electron relays. The multi-electron reduction steps take place in the range of -1.33 to -1.81 V *vs.* Fc/Fc$^+$. Such consecutive reductions are relevant to natural systems, hence these models were suggested to be valuable templates to design robust catalyst systems.[235,236] Further experiments to investigate the potential of such models are, however, still missing.

4.2.6.1 BDT models with secondary sphere modifications. To improve the water solubility and to overcome the oxygen sensitivity and high overpotential the hydroquinone **167** was modified to afford the bis(2-bromo-2-methylpropionate) species **168** (Fig. 49). This complex was then co-polymerized with methyl methacrylate (MMA) and 2-(dimethylamino)ethyl methacrylate (DMAEMA) *via* atom transfer radical polymerization (ATRP). Here, The flexible –NMe$_2$ side chains at the DMAEMA monomer,

along with improving the water solubility and stability of the model, also enhance the complexes' catalytic activity and overcome the aforementioned challenges of water solubility and oxygen-sensitivity.[237]

Another polymerization technique to produce metallo-polymers is the copper-catalysed click-reaction between azides and alkynes (Fig. 50).[238] Depending on the azide used, the general properties of the obtained polymer can be adjusted. Thus, polymer **169Pb** bearing an acetate-substituted backbone, reveals an improved catalytic activity compared to complexes **169Pa** and **169Pc**. The different activity can be explained by enhanced proton shuttle properties of the acetate in **169Pb**.[238] This example shows, that in complex systems not only the catalyst itself is decisive for the overall HER performance, but also the network in which the catalyst is embedded.

4.2.7 Other arenedithiolate models. The different binding motif created by the naphthalene moiety as compared to Fe$_2$(bdt)(CO)$_6$ derivatives causes an increased S–S distance and a larger S–Fe–S angle (*e.g.* 84.1° in the anthracene derivate *vs.* 80.7° in bdt). Regarding the electron density at the diiron
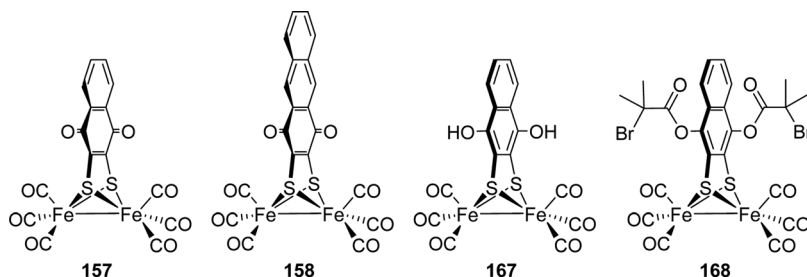
Fig. 49 Representative multiaryl diiron complexes.

1706 | *Chem. Soc. Rev.*, 2021, **50**, 1668–1784

This journal is © The Royal Society of Chemistry 2021
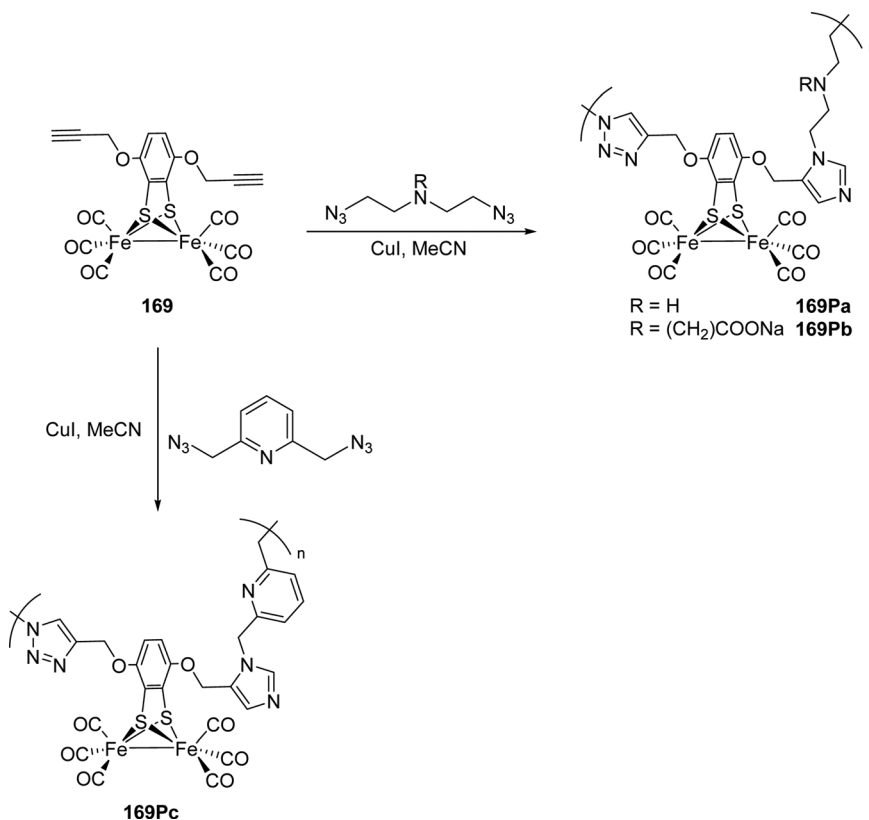
Fig. 50 Incorporation of bdt-derived complexes into polymers.

site, the naphthalene moiety in $Fe_2(1,8-S_2C_{10}H_6)(CO)_6$ (**170**) is less electron-withdrawing compared to its benzene congener. The naphthalene derivative shows CO-frequencies that are shifted by 5 cm^{-1} to lower wavenumbers as compared to $Fe_2(bdt)(CO)_6$.[220,239] Likewise, the reduction potential of **170** is 40 mV more cathodic.[221,240] Furthermore, naphthalene bridged [2Fe–2S]-mimics exhibit a reversible reduction and stabilise the monoanionic intermediate species obtained upon the first reduction and triggered considerable interest.[239–247] The facile synthetic route, reacting $Fe_3(CO)_{12}$ and naphthalene 1,8-disulphide, allows for easy manipulation of the naphthalene moiety and a series of modified naphthalene 1,8-disulphide models with chloride,[239] alkyl,[239,240] alkoxide,[240] amide and imide substituents were reported.[244,248,249] As already observed for the bdt model, the chloride substituted **171** shows a anodically shifted but irreversible reduction, which was explained with the subsequent loss of chloride.[239] Along this line, electron-donating groups such as OMe and ^{t}Bu shift the reduction potential cathodically.[239,240]

Besides iron–sulphur clusters, iron–selenium clusters were reported with a naphthalene bridge as well. Figliola et al. reported an extensive study of such naphthalene and phenanthrene modified dichalcogenide models (**170**, **172** to **175**, Fig. 51).[240] The selenium substituted models displayed catalysis at lower overpotentials as compared to their sulphur congeners.[239,250] Likewise, the synthesis and investigation of series comprising naphthalene modified systems with an imide
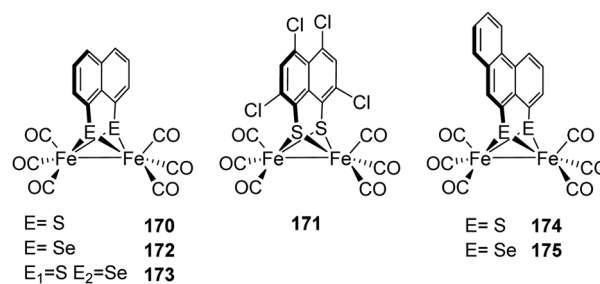
Fig. 51 1,8-Naphthalenedithiolate bridged model complex and derivatives.

functionality in *para*-position were reported by Weigand and coworkers (**176a–c** and **177a–c**, Fig. 53).[244] The modifications increased the stability of the reduced monoanion. Increasing the aromatic system by a further naphthalene moiety resulted in the formation of perylene monoamide-bridged hydrogenase models **178a–c**.[247] These analogues show an anodically shifted reduction potential due to the increased π-system. The first reduction potentials ($Fe^IFe^I \rightarrow Fe^IFe^0$) of these species are in the range −0.99 V to −1.04 V and the shift can be attributed to an increased electron withdrawing nature of the perylene linker and an enhanced stability of the reduced species.[247]

Another increased π-system was reported by Topf et al. who designed the acenaphthylene-based complex **179** (Fig. 52) which acts as redox relay for accelerated electron transfers to

This journal is © The Royal Society of Chemistry 2021

Chem. Soc. Rev., 2021, **50**, 1668–1784 | **1707**
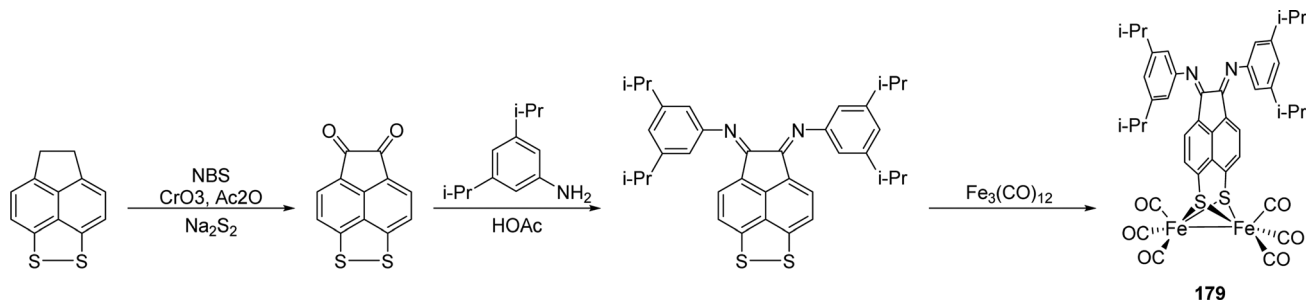
Fig. 52 Synthesis of the BIAN-R model **179**.

the diiron site.[241] By modification of the varying linker substituents, the bis(arylimino)acenaphthene (BIAN-R) models allow for tuneable electronic properties and solubility.

The robust naphthalene derivatives of the diiron dithiolates can be considered a major example of photocatalytically active mimics. Herein, the functionalization of the naphthalene ring with *e.g.* imides (**180**) or amines (**181**) provides a useful method to attach a photosensitizer.[248,251–253]

Instead of increasing the naphthalene π-system, a change to an intrinsically larger aromatic system such as phenanthrene likewise enables the modification of the electronic properties of the [FeFe]-hydrogenase models. Thus, oxidative addition of phenanthro[4,5-cde][1,2]dithiin to $Fe_2(CO)_9$ gave the phenanthrene-bridged model **182** (Fig. 53).[250] Compared to analogous naphthalene counterparts, the reduction potential was found to be more anodic due to the larger electron withdrawing ability of the dithiolate linker along with better stabilization of the anionic species.[250]

4.3 H-cluster models lacking the dithiolate bridge

Already in 1928, Reihlen *et al.* first described the synthesis of $Fe_2(SEt)_2(CO)_6$ (**183**) without any knowledge on [FeFe]-hydrogenases.[254,255] Also, in late 1930s Hieber *et al.* reported on the complex of the type $Fe_2(SR)_2(CO)_6$ (R = Ph (**184**), Et (**183**)) by refluxing $Fe_2(CO)_9$ and the respective dithiol.[256,257] Further,

the synthetic organometallic chemistry flourished and lead to various diiron(I) dithiolate complexes starting from $Fe_2S_2(CO)_6$ (**1**).[258] As illustrated in Fig. 54, **1** can be modified to obtain a variety of derivatives.

These complexes are commonly low spin, diamagnetic complexes which exist in three isomeric forms *aa*, *ae* and *ee* (Fig. 55) depending on the orientation of the R substituents on sulphur. Contrary to the chemistry displayed in the previous sections, the chelating thiolates lack such steric freedom and hence exist in the *aa* form.

Owing to the significant role of the cysteinyl ligands in both [NiFe]-hydrogenases and [FeFe]-hydrogenases, the introduction of cysteine as a bridging thiolate was pursued. However, unlike most other derivatives, this model could not be obtained through refluxing cysteine (or its methyl ester) with $Fe_3(CO)_{12}$. Employing the Boc-protected methyl ester of cysteine afforded the target product **185**. When **185** was refluxed in MeOH or in toluene containing CH_3COOH, intramolecular cyclization occurred leading to the EDT-like model **186** (Fig. 56).[259]

Furthermore, **185** was attached to α-helical peptides resulting in a prototype to replicate the second coordination sphere of the active site.[260] Furthermore, a ferrocene was incorporated and linked the two cysteinyl arms in **187** (Fig. 57).[261]

Since H-bonding interactions between NH and S are crucial for electron transfer processes in the metalloenzymes such as
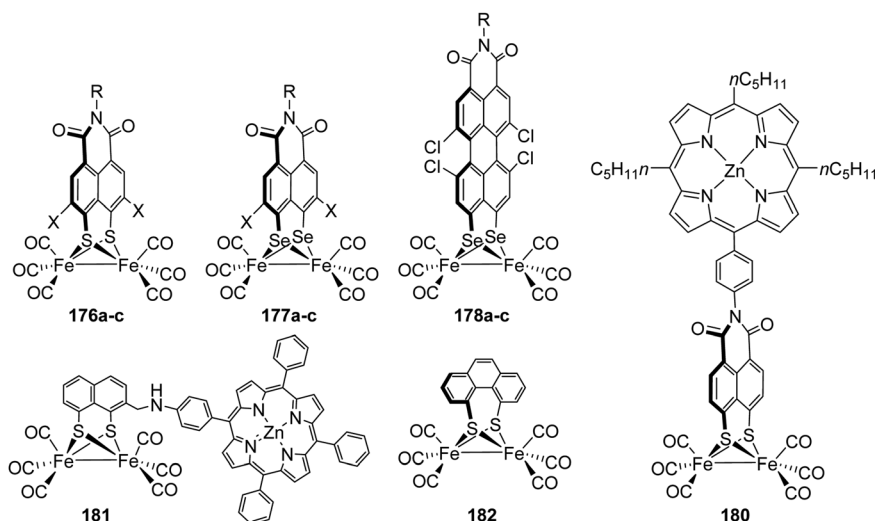
Fig. 53 Different naphthalene-derived model complexes.

Fig. 54 Modification possibilities of **1**.

Fig. 55 Isomers of unbridged $Fe_2(SR)_2(CO)_6$ complexes.

Fig. 56 Intramolecular cyclization of **185** resulting in **186**.

Fig. 57 Representative models lacking a dithiolate linker.

rubredoxin[262] and ferredoxins[263] and also influence their redox behaviour, complexes **188R** (R = CH_3, CF_3, C_6H_5, p-C_6H_4F) were synthesised revealing NH···S interactions. This interaction decreased the electron donating capability of the S atom and is visible by an anodic potential shift of 370 and 470 mV as compared to $Fe_2(pdt)(CO)_6$ and $Fe_2(SPh)_2(CO)_6$.[264]

As described earlier, complexes with aromatic dithiolate linkers conduct proton reduction at more positive potentials. Therefore, the models **189R** (R = o-OMe, p-OMe, p-Cl) were synthesized with varying ligand substitution patterns and showing varying electron donating capacities (see Section VI).[265]

In addition, models **190** to **192** were synthesized comprising pendant pyridine and quinoline groups and were supposed to facilitate an internal proton transfer. Notably, the N-heterocyclic groups were shown to dynamically coordinate to an iron atom. When a solution of these models is subjected to CO, the Fe–N bond is cleaved giving the hexacarbonyl complexes.[266]

4.4 Metal exchange in H-cluster models

Although numerous synthetic models of the active site have been synthesized and studied, less efforts have been directed towards development of mimics with different transition metals.

Indeed, inspiration to realize this goal can be taken from natural systems, wherein a mixed-metal hydrogenase, *i.e.* the [NiFe]-hydrogenase exists. Some synthetic studies described organometallic clusters with structural similarities to the active site of [FeFe]-hydrogenases, which will be discussed in this section.

4.4.1 Incorporation of group 8 elements. Organometallic complexes of heavier analogues of iron *i.e.* ruthenium and osmium have been reported by Cabeza *et al.* in 1998.[220] In that work, the synthesis of bimetallic organometallic centres bearing the aromatic benzenedithiolate linker (**193** and **194**, Fig. 58) is described. These complexes can be synthesised by refluxing the respective metal carbonyls ($Ru_3/Os_3(CO)_{12}$) with 1,2-benzenedithiol in toluene.[192]

Subsequently, Ru models with pdt (**195**) and adt (**196**) bridges were reported (Fig. 58). Thereby, $RuCl_3 \cdot nH_2O$ was carbonylated and *in situ* reacted with the dithiol as well as zinc.[33,267] In the case of adt, the secondary amine was protected
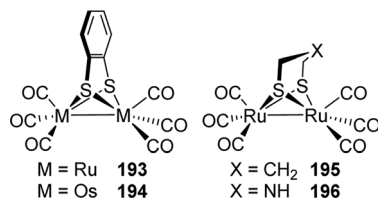
Fig. 58 Iron substitution by heavier homologues.

with a carbamate (CBz) protecting group (Fig. 59) when introduced as a dithiol (**197**).[33] In 2015, Wu *et al.*[268] reported the synthesis of the diruthenium complex *via* reaction of 1,3-propanedithiol and $Ru_3(CO)_{12}$. $Ru_2(pdt)(CO)_6$ was obtained as major product along with the multimetallic side product $\{(\mu-H)Ru_3(CO)_{10}\}_2(pdt)$. The $Ru_2(pdt)(CO)_6$ model along with tri(*o*-tolyl)phosphine in the presence of formic acid and triethylamine reports photocatalytic H_2 production activity with turnover frequencies of 5500 h^{-1} and a turnover number over 24 700 h^{-1}.[268]

The ligand exchange properties of the ruthenium models are very similar to those of the corresponding iron complexes (see Section 4.6). Phosphines and cyanides are likewise easily incorporated.[220,267–269] Still, it was reported that the cyanation reaction proceeds at faster rates as compared to the [FeFe]-analogues due to increased electrophilicity of the Ru–Ru bond.[269] In contrast, the protonation chemistry of the heavier homologues is distinctly different (see Section 5.3 for a detailed discussion of the protonation chemistry of the iron complexes). While the Os and Ru models (**193** and **194**) form a bridging hydride upon treatment with HBF_4, the corresponding Fe complex remains unaffected.[192]

Along this line, Rauchfuss and coworkers studied the photo-hydrogenation of $Ru_2(pdt)(CO)_4(PCy_3)_2$ (**198**). Notably, a terminal as well as a bridging hydride were observed in the very same complex, $HRu_2(pdt)(\mu-H)(CO)_3(PCy_3)_2$ (**198-μHtH**).[270] Contrarily, when a solution of **198** was subjected to HOTs, only the bridging hydride $[Ru_2(pdt)(\mu-H)(CO)_3(PCy_3)_2]^+$ ($[\textbf{198-μH}]^+$) was observed.[270]

Interestingly, the non-inertness of the conjugated acid $[Ru_2(pdt)(\mu-H)(CO)_4(CN)_2]^-$ (**199**) of the dicyanide model was shown in terms of ligand substitution and the complex readily undergoes decarbonylation when reacted with PMe_3. Although showing a labile ligand binding, **199** reveals a hampered H_2 evolution activity as compared to the diiron analogues (−1.6 V *vs.* −1.0 V for $Fe_2(pdt)(\mu-H)(CO)_4(CN)(PMe_3)$, both values referenced *vs.* Ag/AgCl).[269]

The successful synthesis of the $[2Ru]_H$-precursor $[Ru_2(adt)(CO)_4(CN)_2]^{2-}$ (**5**) shed light on the proton reduction mechanistic pathways in the enzyme and was successfully incorporated into apo-HydA1. Interestingly, the apoenzyme could be cleanly matured also with the bridging hydride. Spectroscopic data reveals that the protein environment affects the structure of these models, as the bridging hydride species, upon maturation, converts to the terminal hydride.

4.4.2 Incorporation of other metals – mixed-metal dithiolates. Inspired by the heterobimetallic centre of [NiFe]-hydrogenases, chemists investigated hetero- as well as homometallic derivatives of the FeFe-, MnFe-, NiFe- and CoFe-type.[271,272] The starting complex Fe(dithiolate)(CO)$_2$(diphos) can be synthesised by reaction of $FeCl_2$ with a corresponding dithiolate and chelating phosphines (Fig. 60). Treatment of $Fe(pdt)(CO)_2(dppe)$ (**200**) with $[(C_{12}H_{10})Mn(CO)_3]BF_4$ gave two isomeric Fe–Mn bimetallic complexes (*unsym*-**201** and *sym*-**201**). The asymmetric isomer slowly converts to the symmetric as is depicted in Fig. 61.[271]

This synthetic scheme was further extended to obtain the analogous ethanedithiolate models as well.[271] In the case of edt models, the asymmetric to symmetric isomer interconversion did not occur even at a longer time scale. Upon protonation, $[(CO)_3MnFe(pdt)(CO)_2(\kappa^2\text{-dppe})]^+$ converts to $[(CO)_3MnFe(pdt)-(\mu-H)(CO)_2(\kappa^2\text{-dppe})]$, whereas it undergoes decarbonylation upon reduction and affords $[(CO)_3MnFe(pdt)(CO)(\kappa^2\text{-dppe})]$.

For the mixed CoFe complex, $Fe(pdt)(CO)(\kappa^2\text{-dppe})$ was reacted with $CpCoI_2(CO)$ to give **202** followed by reduction with $CoCp_2$ to give the targeted complex **203**. This method was found to be more reliable than the direct synthesis using $CpCo(CO)_2$ in refluxing toluene/THF. Moreover, to generate the protonated complex, the precursors were treated with $HBF_4 \cdot Et_2O$ giving rise to the bridging hydride species at room temperature.[271,273]

The synthesis of such mixed metal complexes is not restricted to first row transition metals. In 2003 Adam *et al.* reported on the MoMn complex **204** which was obtained by refluxing $Mn_2S_2(CO)_7$ with $(MoCp(CO)_3)_2$. $CpMoM(\mu-S)_2(CO)_5$ reacts with various substrates to give the diverse derivatives **205** to **210** (Fig. 62).[274,275] Similar to the synthesis routes reported for **201** and **202**, the reaction of $Mo(bdt)(CO)_2$-$(PMe_3)_2$ with $Fe(CO)_5$ afforded the MoFe complex **211** (Fig. 61).[276]

4.5 Substitution of carbonyl ligands in H-cluster models

Regarding the native H-cluster, the introduction of two cyanide ligands is the first transformation that comes into mind. However, the generated dianions are unsuitable for modelling the active site in many cases, *e.g.* because of undesired N-protonation of cyanides[150,153,277,278] or the instability of the oxidised species.[279,280] Therefore, the cyanide ligands are often replaced by phosphines exhibiting similar electron-donating properties without a negative charge.[277,278] Other attempts to
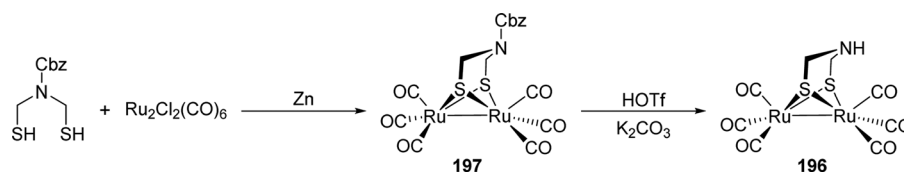
Fig. 59 Synthesis of **196** *via* the protected amine intermediate.

1710 | *Chem. Soc. Rev.*, 2021, **50**, 1668–1784

This journal is © The Royal Society of Chemistry 2021
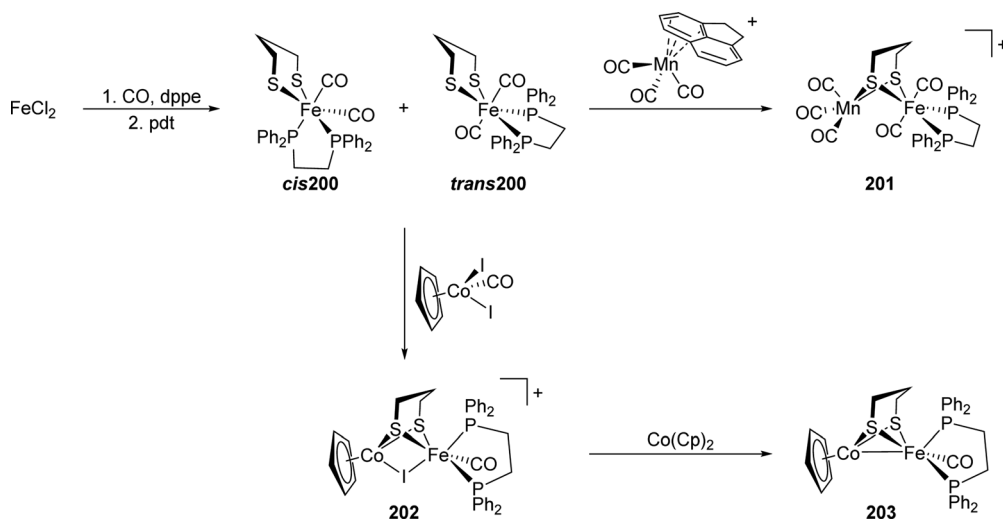
Fig. 60   Synthesis of FeMn and FeCo models.

Fig. 61   Isomerisation of **201** and structure of complex **211**.

modify the mimics involve the usage of N-heterocyclic carbenes (NHCs), isocyanides, or nitrosyls. The reaction pathways summarised in the following section are generally applicable and not limited to the herein described adt or pdt complexes.

4.5.1   Remarks on structural aspects. The ligands are denoted as apical (ap) or basal (ba) with respect to their position in the (idealised) square pyramidal coordination environment of the iron centres (Fig. 63). In some compounds only a single conformation is found, while others exhibit rapid exchange between almost energetically equal conformations at room temperature. This exchange is often referred to as turnstile rotation[281–283] – though there has been a debate, if turnstile rotation differs from a combination of Berry pseudo-rotation and other isomerisation mechanisms on a molecular level.[284–287] The dithiolate bridge was shown to also influence the position of the ligand beyond steric effects, at least in the solid state. For example, based on molecular structures, Rauchfuss and coworkers reported an apical/basal conformation of the cyanide ligands in $[Fe_2(pdt)(CO)_4(CN)_2]^{2-}$ (**212**),[279] in contrast to an apical/apical conformation in the corresponding adt and adt^{Me} complexes.[17,168]

4.5.2   H-cluster models with cyanide ligands. In 1999, shortly after the crystal structures of [FeFe]-hydrogenases revealed the presence of two cyanide ligands and a bridging dithiolate ligand in the active site, the groups of Darensbourg,[288] Pickett,[289] and Rauchfuss[279] independently described the synthesis of the $[Fe_2(pdt)(CO)_4(CN)_2]^{2-}$ dianion (**212**, Fig. 64). As observed

in the hexacarbonyl complexes, fast isomerisation of apical and basal positions is observed at room temperature.[283] Following an associative mechanism,[282] complexes of this type are easily accessible in yields over 90% by addition of NEt_4CN to solutions of the corresponding hexacarbonyl complex in MeCN.[279,288,289] The cyanation can also be accomplished using KCN, but this case requires either solubilising crown ethers[283,288] or elevated temperatures along with extended reaction times.[290] The reactions to the dicyanides exclusively yield complexes in which one CO molecule on each iron atom is substituted. As observed for the incorporation of every (monodentate) electron donating ligand,[168,277,278,291] this regioselectivity can be explained by the increased $Fe–C_{CO}$ bond strength due to an increased π-back bonding upon binding of the electron-rich cyanides. The increased bond strength is indicated by a shortened $Fe–C_{CO}$ bond length in the crystal structure of the cyanide complexes[279] and a shift of the carbonyl IR modes to higher wavenumbers.[279,288,289] It is worth mentioning, that for the hexacarbonyl complex with an o-xyloldithiolate (o-xyldt) ligand substantially larger reaction rates for the dicyanation than for the pdt complex were observed. This led to the conclusion that the rotation of the $Fe(CO)_3$ group, facilitated due to steric repulsion in the o-xyldt complex, is the first step of the cyanation in an associative pathway.[282,292] While many hexacarbonyl complexes are sufficiently oxygen-stable to be handled under ambient air, the cyanide complexes are generally less stable in the presence of oxygen – especially in solution.[279,289]

This journal is © The Royal Society of Chemistry 2021

Chem. Soc. Rev., 2021, **50**, 1668–1784 | 1711

Fig. 62 Synthetic pathways towards various MnMo complexes.
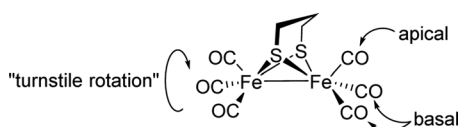
Fig. 63 Apical and basal ligands and "turnstile rotation".

Using only one equivalent of NEt$_4$CN, the monocyanide [Fe$_2$(pdt)(CO)$_5$(CN)]$^-$ (**213**) is unintuitively only formed in low yields up to *ca.* 15%. On the contrary, the dicyanide **212** is observed as the main product.[283] This observation led to the conclusion that the monocyanide complex reacts more rapidly with cyanide ions than the hexacarbonyl complex.[282] Indeed, kinetic measurements revealed that the intermediate formed upon mixing the hexacarbonyl complex and cyanides reacts more rapidly with additional cyanides than the hexacarbonyl complex.[282,283] Darensbourg and coworkers calculated a larger rate constant for the substitution reaction for the isolated monocyanide complex than for the hexacarbonyl.[282] In contrast, a competition experiment by the Rauchfuss group investigating the reaction of a mixture of hexacarbonyl and monocyanide complex revealed a slower CO/CN$^-$ substitution in the monocyanide complex[283] and DFT calculations supported this

observation.[292] Moreover, the isolated monocyanide complex, as well as the hexacarbonyl complex **20** were shown to react only slowly with phosphines, while the intermediate rapidly reacts with these nucleophiles. Accordingly, the monocyanide was suggested as an implausible intermediate for the formation of the dicyanide by the authors.[283] As an alternative intermediate, a structure with a (semi-)bridging carbonyl was proposed.[282,292] To the best of our knowledge, neither theoretical nor spectroscopic studies that further investigate the formation of the dicyanide without assuming the monocyanide as an intermediate were reported in literature. The reaction of the unidentified intermediate with nucleophiles is a useful method for synthesising asymmetric [(CO)$_2$(CN)-Fe(pdt)Fe(CO)$_2$(L)]$^-$ (L = *e.g.* PMe$_3$ (**214**)).[283] In contrast, using KCN under reflux conditions, the monocyanide was found to be an isolatable intermediate.[290]

Still, monocyanide complexes are accessible in good yield (*ca.* 75%) by converting one of the carbonyl ligands into a cyanide ligand using NaN(SiMe$_3$)$_2$.[282,288] Following a nucleophilic attack of the amide at the carbonyl carbon atom, the corresponding siloxane (SiMe$_3$)$_2$O is released. The increased electron density after the introduction of the cyanide hampers a second nucleophilic attack and accordingly a second CO

1712 | *Chem. Soc. Rev.*, 2021, **50**, 1668–1784

This journal is © The Royal Society of Chemistry 2021

Fig. 64 Synthesis routes towards mono- and disubstituted cyanide and phosphine complexes.

conversion is inhibited. This holds true even if an excess of NaN(SiMe$_3$)$_2$ is used.

The obtained sodium salt Na[Fe$_2$(pdt)(CO)$_5$(CN)] was reported to be unstable at room temperature even as a solid under inert atmosphere.[282] The sufficiently stable compound NEt$_4$[Fe$_2$(pdt)(CO)$_5$(CN)] was obtained in similar yields by the use of the decarbonylation agent trimethylamine *N*-oxide (Me$_3$NO) and subsequent addition of NEt$_4$CN to the solution. Widely applied for the selective substitution of one carbonyl ligand, Me$_3$NO oxidises a single carbonyl ligand to carbon dioxide, followed by dissociation from one iron centre. The vacant coordination site is presumably occupied by a coordinating solvent molecule (or NMe$_3$) to form a Fe$_2$(pdt)(CO)$_5$L (L = MeCN (**215**), NMe$_3$) species, that can be observed by IR spectroscopy with a significant lifetime in solution.[283] Further support for this claim was provided by Rudolph, Ishii, Weigand and coworkers who were able to crystallize the corresponding acetonitrile-coordinated intermediate.[293] The decarbonylated species can afterwards be attacked by nucleophiles, in this case cyanide. Similar to the attack of NaN(SiMe$_3$)$_2$, a second Me$_3$NO induced substitution is unfavourable.[283]

4.5.3 H-cluster models with phosphine ligands. While the cyanide ligands closely resemble the ligand environment in the native [2Fe]$_H$, the use of these ligands is accompanied by several drawbacks. First of all, the stability of the complexes – especially towards oxygen – is dramatically decreased. Moreover, protonation studies (*vide infra*) revealed undesired protonation of the cyanide ligands.[277,278] This protonation, however, does not occur natively due to encapsulation in the enzyme's binding pocket and H-bonding to the protein.[294] On the contrary, phosphine complexes cannot be protonated at the phosphorous atoms under the typical H$_2$ formation conditions but at the same time show similar electronic characteristics. The formal exchange of two cyanide ligands by electron-rich trimethyl phosphine ligands shifts the IR bands to higher wavenumbers

by only 15 cm^{-1} to 20 cm^{-1} still being shifted the opposite way by *ca.* 100 cm^{-1} compared to the hexacarbonyl complexes.[277,278]

The special coordination environment in the enzyme does not only change the reactivity of the system, but also its structure. Phosphines certainly are the most important group of ligands in the field of hydrogenase research due to the same reasons frequently discussed in other fields of homogenous catalysis.[295–297] Due to the strong metal phosphorous bonds, low valent metal complexes are stabilised. In addition, their electronic and steric properties can be easily controlled by their organic substituents and quantified *e.g.* by the Tolman electronic parameter,[298,299] the ligand cone angle,[300] and the percent buried volume.[301] The use of chelating bi- or tridentate phosphine ligands permits additional flexibility in the coordination sphere. Phosphine ligands also allow for a covalent linkage to groups with further functionalities and were used to increase the water solubility,[129,130,302] provide an internal proton relay,[303–305] or link the active site mimic to proteins,[306] photosensitisers,[307,308] redox-active ferrocenes[204,209,213,309–312] or other redox-active ligands.[313,314]

Notably, the reactivity of mono- and bidentate phosphines towards unbridged complexes Fe$_2$(SR)$_2$(CO)$_6$ is already known since the 1970s and many results from extensive studies of Haines, Greenwood and coworkers accord with the reports on the dithiolate derivates.[315,316]

4.5.3.1 Monodentate phosphines. The synthesis of hydrogenase model complexes substituted with monodentate phosphines is generally straightforward (Fig. 64). Typically, at room temperature the hexacarbonyl complexes undergo direct substitution of one carbonyl ligand by the phosphines more slowly than cyanides.[283] Still, within hours the monosubstituted complexes of less bulky phosphines (*e.g.* PMe$_3$, PMe$_2$Ph) are formed. Disubstituted byproducts are also regularly detected. For the reaction of more bulky phosphines (*e.g.* PPh$_3$, P(OEt)$_3$),

often elevated temperatures are needed.[170,317] By prolonged reaction times and elevated temperatures likewise disubstituted complexes are accessible in good yields for less bulky phosphines,[277,278,318] while for more bulky phosphines the yields range from moderate to low.[129,317,319] As observed for the cyanide complexes, the second substitution always occurs on the remaining $Fe(CO)_3$-fragment.[277,278,317,318] The monosubstituted complexes are also easily available by decarbonylation with Me_3NO in the presence of the desired phosphine.[275,283,303] A second substitution using this method only gives low yields, while thermolysis and photolysis are useful tools and afford high product yields ($>90\%$) also for bulky phosphines.[180] In neat PMe_3, photolysis of the edt, pdt and adt hexacarbonyls slowly yields the tetrasubstituted electron-rich complexes $Fe_2(xdt)(CO)_2(PMe_3)_4$ (**216xdt**) in a yield of *ca.* 60%.[320]

If the model complex is synthesised starting from $Fe_2S_2(CO)_6$, addition of the phosphine to the intermediate $Fe_2(SH)_2(CO)_6$, generated at dry ice temperature, also allows for the selective substitution of one carbonyl ligand (**217**) upon warming to room temperature.[321] $Fe_2(SCH_2OH)_2(CO)_6$ (**85**) can be substituted analogously and afterwards condensed to the oxa- or azadithiolate complexes $Fe_2(xdt)(CO)_5(PR_3)$ (*e.g.* R = Me **218xdt**).[185]

Mono- and disubstituted phosphine complexes, compared to their cyanide analogues, are typically more stable. The conformations of disubstituted phosphine derivatives are briefly discussed using the example of $Fe_2(xdt)(CO)_4(PMe_3)_2$ (xdt = edt, pdt; *e.g.* R = Me **219xdt**). In the solid state, a transoid basal–basal arrangement of the phosphine ligands is found for the pdt derivative, while the edt complex features a apical–basal arrangement.[277,278] This arrangement for edt is also found in acetone at $-60\ ^\circ C$, while NMR spectra reveal high fluxionality of the $Fe(CO)_2(PMe_3)$ units at room temperature.[278] The same interconversion is found for pdt, however, the conformation in solution was found to be highly dependent on the solvent. A comparison of calculated IR spectra with those obtained in different solvents revealed that the transoid basal–basal conformer is almost entirely found in heptane (90%) and hexane, while in acetonitrile and methanol significant amounts of the apical–basal (up to 40%) isomers are found.[322,323] In accordance with the increased amount of the more polar apical–basal isomer in polar solvents is the finding that the apical–basal isomer is predominant in acetone.[278,324,325] The cisoid basal–basal and the apical–apical conformers are not observed.

While monodentate phosphines exclusively give Fe, Fe′-disubstituted complexes, the use of bidentate phosphines makes other coordination modes accessible. By chelation of one iron atom by bidentate phosphines, strongly electron-rich iron centres can be synthesised and an asymmetry between both iron centres can be introduced. However, the different accessible coordination modes render the introduction of bidentate phosphines more complicated. The favourable coordination mode is not only determined by the applied reaction conditions but also by the linker of two phosphines moieties (backbone).

4.5.3.2 Bis(diphenylphosphino)methane (dppm). As κ^2-chelate complexes with dppm suffer from steric strain of the four-membered ring, the ligand is known to bridge bimetallic complexes preferably in a κ^1,κ^1,μ-geometry in favour of less strained five-membered cycles. In [FeFe]-hydrogenase mimics this coordination mode is likewise the most prominent (Fig. 65). Complexes $Fe_2(xdt)(CO)_4(\mu\text{-dppm})$ (**220xdt**, xdt = *e.g.* edt, pdt, adt^{alkyl}, odt) with two symmetric iron centres are readily prepared ($>70\%$ yield) from the hexacarbonyl complexes in refluxing toluene.[183,208,326,327] Contrary, the use of Me_3NO and the phosphine was reported to reduce the yield.[183,326] The chelate complex $Fe_2(pdt)(CO)_4(\kappa^2\text{-dppm})$ (**221pdt**) was observed as a crystalline side product but could not be isolated in the bulk.[183,326] Similar results were reported for $Fe_2(pdt)(CO)_4(\mu\text{-dcpm})$ (**222pdt**, dcpm = bis(dicyclohexylphosphino)methane).[326] The photolytic introduction of dppm into $Fe_2(odt)(CO)_6$ was also reported but gave lower yields.[208] In contrast to complexes with two monodentate phosphine ligands, the bidenatate phosphine ligands cannot adopt the apical position in these complexes and always adopt a cisoid basal–basal arrangement, which is otherwise sterically unfavourable.

The stable complexes $Fe_2(xdt)(CO)_5(\kappa^1\text{-dppm})$ (**223xdt**) with a monodentate dppm ligand can also be isolated; in the case of pdt from the reaction of the hexacarbonyl diiron complex and dppm in acetonitrile in the presence of Me_3NO. In case of adt$^{n\text{-propyl}}$ the reaction time has to be shortened from 60 min to 30 min. Both, the pdt and adt complexes can also be converted into to the corresponding μ-dppm compounds by thermolysis.[183,326] In an attempt to synthesize the κ^1-dcpm complex (**224**), the oxygen-sensitive ligand was partially oxidised by Me_3NO at both phosphine moieties (Fig. 66).[326]

In addition, asymmetric κ^2-chelate complexes can be synthesised if steric bulk is introduced to the backbone carbon atom as displayed by $C(Me)_2(PPh_2)_2$ *i.e.* Me_2dppm. The room temperature reaction of the hexacarbonyl complex **20**, Me_2dppm, and Me_3NO gives the κ^2-chelate complex **225** in 63% yield. While in solution the apical/basal and basal/basal isomers were detected in a 2:1 ratio by ^{31}P-NMR, only a dibasal arrangement was observed in the crystalline form. In refluxing toluene, the chelate complex slowly rearranges to the bridged complex with a $\mu\text{-Me}_2dppm$ ligand.[328]

A similar ligation behaviour as observed for Me_2dppm was reported for aminodiphosphine-ligands $(R_2P)_2NR'$ (PNP). The amine in the backbone of the ligand was proposed to enable a similar reactivity as the adt-amine and allowing PCET mechanisms. The thermodynamically favoured μ-PNP geometry comprising a five-membered ring is accessible by the direct reaction of the hexacarbonyl complexes with the PNP ligands in high boiling solvents, *e.g.* toluene or xylene.[130,308,329,330] In an alternative synthesis route, $Fe_2(CO)_6(\mu\text{-CO})(\mu\text{-PNP})$ (**226**) can be prepared photochemically from $Fe_2(CO)_9$, and subsequent reaction with the bridging dithiol.[331] By this route, the first dppm complex, $Fe_2((\mu\text{-S})_2CNR)(CO)_4(\mu\text{-dppm})$ (**227**), with a bridging dithiocarbamate ligand was synthesised.[332]

In contrast to dppm, κ^2-chelate complexes (**228xdt**) comprising PNP ligands can be isolated in moderate to high yields

1714 | *Chem. Soc. Rev.*, 2021, **50**, 1668–1784

This journal is © The Royal Society of Chemistry 2021
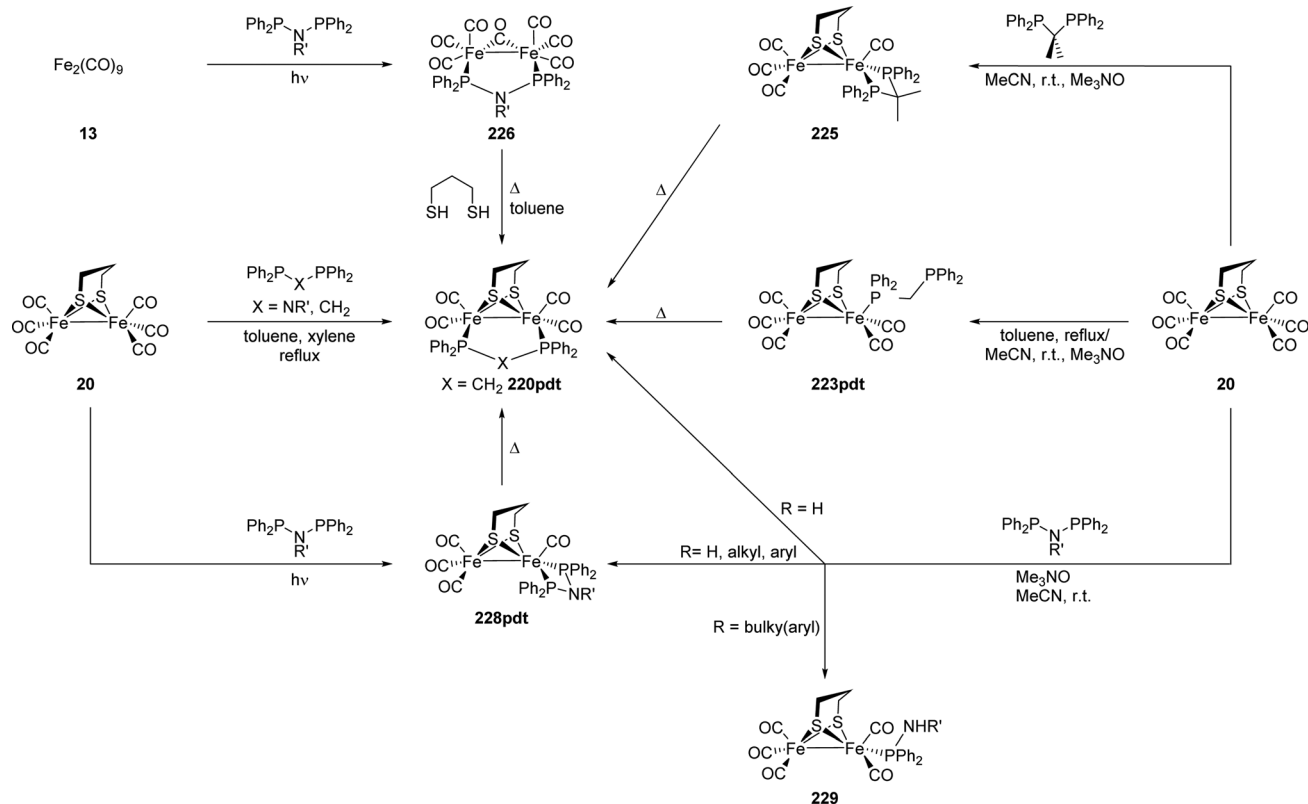
Fig. 65 Different synthetic pathways for the incorporation of dppm and derived ligands as well as PNP ligands into hydrogenase mimics.
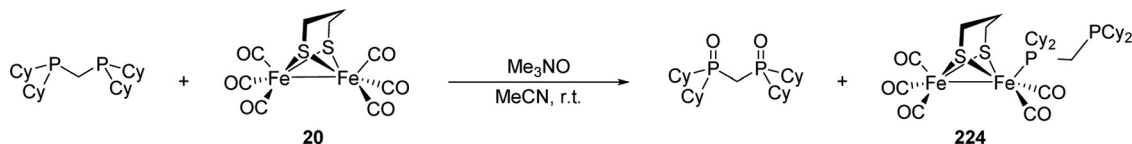
Fig. 66 Reaction of dcmp with complex **20** in the presence of Me₃NO.

(33% to 90%). The small PNP bite angle ligands favour a dibasal geometry in solution and solid state.[330,331] The substitution behaviour of PNP ligands in acetonitrile after decarbonylation with Me₃NO also strongly depends on the substituent R′ on the amine. For R′ = H, the obtained chelate complex was always formed together with the bridged μ-PNP complex in a 2 : 1 ratio and could not be isolated in pure form.[330] PNP ligands with sterically less demanding substituents (*e.g.* R′ = Me, Bu, (CH₂)ₙNMe₂ (*n* = 2, 3), *etc.*) smoothly react to the desired chelate complexes (55% to 90% yield).[130,330,331,333] With increasing steric bulk on nitrogen, the formation rate of the chelate complex slows down and for aryl-substituted amines often very low yields (<10% yield) were reported. Herein, the major product is the mono-substituted complex Fe₂(pdt)(CO)₅(κ¹-PPh₂NHR′) (**229**), in which the second P–N bond was hydrolysed.[330,333,334] A more general route towards the chelate complexes is provided by irradiation of the hexacarbonyl precursor with UV light in toluene.[333] The PNP chelate complexes also rearrange slowly to the thermodynamically favoured bridged isomers if solutions in toluene are heated to reflux.[130,330,331]

4.5.3.3 Bis(diphenylphosphino)ethane (dppe) and bis(diphenyl-phosphino)ethene (dppv). In contrast to dppm, the chelation of one iron centre is the most common coordination mode for dppe (Fig. 67) and its unsaturated analogue *cis*-bis(diphenyl-phosphino)ethene (dppv, Fig. 68). The formed five-membered rings are thermodynamically more favourable than the analo-gous four-membered rings in the case of dppm. Thereby, asymmetric complexes Fe₂(xdt)(CO)₄(κ²-diphosphine) are accessible. Another effect of the increased bite angle is that the basal-apical geometry of the chelate complexes becomes more favourable.[335–337] The chelate complexes **230xdt** (dppe) and **231xdt** (dppv) form upon decarbonylation of the hexa-carbonyl complexes in the presence of the phosphine ligand within hours.[154,210,326,336–338] Because of its rigidity, dppv (Fig. 68) forms the chelate complexes at room temperature,[154,210,326,337] while dppe (Fig. 67) requires elevated temperatures.[336,338] The reported yields vary significantly in the range of 26% to 90% for dppv and 23% to 47% for dppe. The thermal reaction without Me₃NO is also feasible but requires considerably extended reaction times,[326] gives lower yields,[326,339] or demands the use of the more

This journal is © The Royal Society of Chemistry 2021

Chem. Soc. Rev., 2021, **50**, 1668–1784 | **1715**
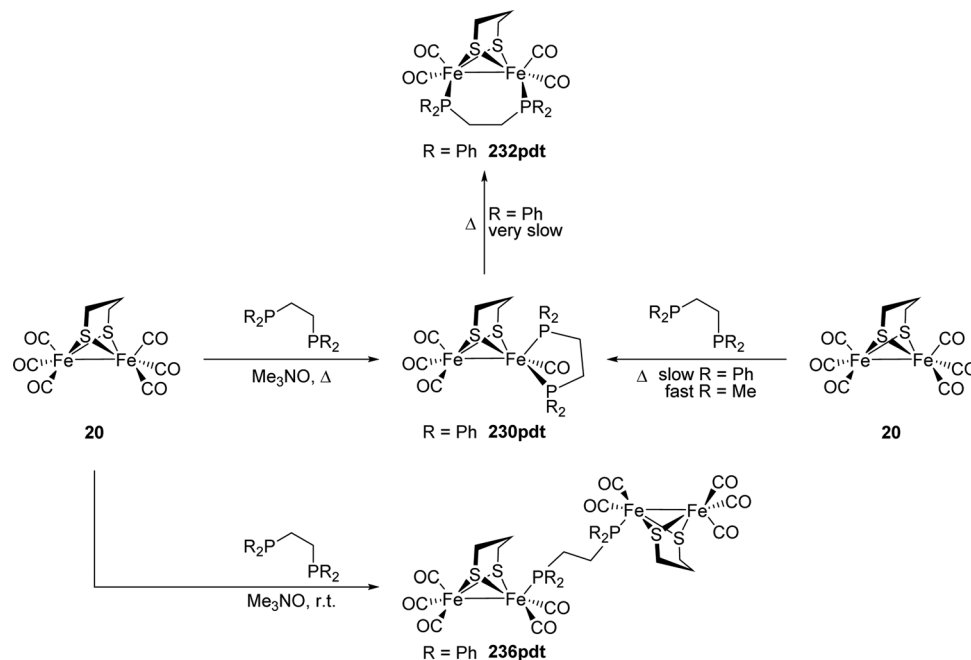
Fig. 67 Complexes with dppe ligands comprising different binding modes and their selective synthesis.
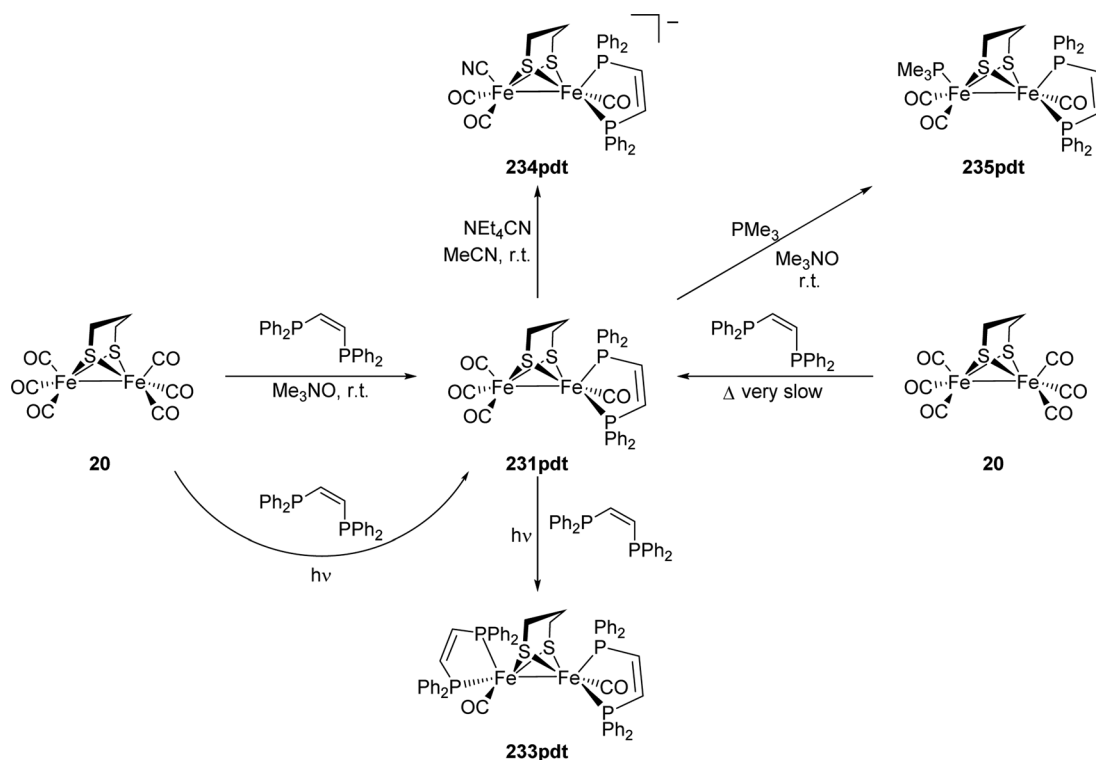
Fig. 68 Complexes bearing dppv ligands comprising different binding modes and their selective synthesis.

electron-rich and sterically less demanding bis(dimethylphos-phino)ethane (dmpe) ligand (Fig. 69).[159,340,341] Upon elongated heating the κ²-dppe complexes rearrange to afford the thermo-dynamically even more favourable μ-dppe complexes (**232xdt**).[342,343] For dppv the light-induced substitution of the hexacarbonyl

complexes was also reported;[344] however, this method is more often applied for the introduction of a second dppv ligand on the other iron centre to give the very electron-rich complexes **233xdt** of high symmetry.[53,154,210] Interestingly, while Fe,Fe′-disubstituted com-plexes [L(CO)₂Fe](xdt)[Fe(CO)₂(L)] (L = PR₃, CN⁻) are unreactive

1716 | *Chem. Soc. Rev.*, 2021, **50**, 1668–1784

This journal is © The Royal Society of Chemistry 2021
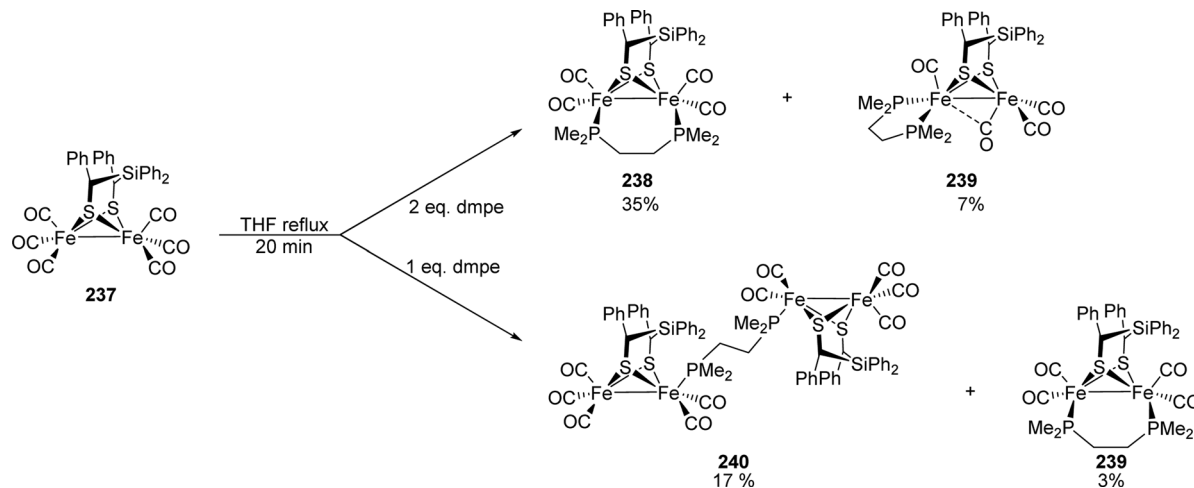
Fig. 69 Incorporation of dmpe into complex **237** yielding three different complexes.

towards further substitution under various conditions, additional electron donating substituents can be introduced into the complex Fe$_2$(CO)$_4$(edt)(κ^2-dppv). Cyanide (MeCN, r.t., **234xdt**), PMe$_3$ (Me$_3$NO, toluene, r.t., **235xdt**) and the bulkier phosphines PCy$_3$ and P^{i}Pr$_3$ ($h\nu$) replace a carbonyl ligand on the unfunctionalised iron centre under the same conditions known for the corresponding monosubstituted complexes. The pdt analogue shows similar reactivity but the substitution processes proceeds more slowly (Fig. 68).[337,345]

Dppe is also capable of linking two [2Fe–2S]-units giving "intermolecular" bridged complexes of the type [Fe$_2$(xdt)-(CO)$_5$]$_2$(μ-dppe) (**236xdt**) with half a dppe ligand per [2Fe–2S]-unit. This coordination mode is favoured if only one equivalent of dppe is added after decarbonylation with Me$_3$NO and the reaction mixture is stirred at room temperature.[145,183,339,346] In addition, this coordination mode was also observed for dmpe complexes containing the sterically crowded dithiol (Ph)$_2$Si(CHPh(SH))$_2$. From the reaction of the corresponding hexacarbonyl diiron complex **237** with one equivalent of dmpe predominantly the [4Fe–4S]-compound **238** is formed (Fig. 69). If two equivalents of dmpe are used, the chelate complex **239** is only a side product (7% yield) while the bridged complex Fe$_2$((μ-SCHPh)$_2$SiPh$_2$)(CO)$_4$(μ-dmpe) (**240**) is the main product (35% yield).[159] Interestingly, complex **239** features the unusual rotated geometry, which will be discussed in Section 5.1.

Complexes of the type Fe$_2$(xdt)(CO)$_4$(κ^2-diphosphine) can also be synthesised starting from iron(II) chloride and Fe(bda)(CO)$_3$ (bda = benzylideneacetone) (Fig. 70, compare Section 4.4.1). Thereby, the

selective labelling with Mössbauer-active ^{57}Fe is possible. Here, iron chloride reacts with the diphosphine under one atmosphere of carbon monoxide at room temperature and (the dilithium salt of) the dithiol bridge to give the monometallic precursor.[271,347] The formed Fe(xdt)(CO)$_2$(κ^2-diphosphine) complex then reacts with Fe(bda)(CO)$_3$ as the source for the Fe(CO)$_3$ fragment to give the asymmetric complex Fe$_2$(xdt)(CO)$_4$(κ^2-diphosphine) (*e.g.* **231pdt**).[271,348] Using ^{57}FeCl$_2$, the subsequent introduction of a second equivalent of dppv to afford the symmetric complex ^{57}FeFe(pdt^{Me})(CO)$_2$(κ^2-dppv)$_2$ (**233pdt^{Me}**, pdt^{Me} = 2,2-dimethyl-1,3-propanedithiol) was enabled.[348] Rauchfuss and coworkers were also able to synthesize mixed-metal mimics by exchanging the Fe(CO)$_3$ source by a Mn(CO)$_3$ or a Co(Cp) precursor (see Section 4.4.2).[271]

4.5.3.4 1,1′-Bis(diphenylphosphino)ferrocene (dppf). Redox-active ferrocene ligands were used to mimic the function of the [4Fe–4S]-cluster providing electrons to the [2Fe–2S]-cluster. While the monodentate, ferrocene substituted phosphines feature the same behaviour as other monodentate phosphines,[213,310,349] dppf shows coordination modes known from dppm and dppe. The connection of two [2Fe–2S]-units is common for the dppf ligand and is accessible *via* reaction of the hexacarbonyls with 0.5 equiv. of dppf in the presence of Me$_3$NO at room temperature in varying yields between 24% and 90%.[204,209,213,309,312,343] With toluene-3,4-dithiolate as the bridging ligand, also monodentate dppf in Fe$_2$(bdt^{Me})(CO)$_5$(κ^1-dppf)
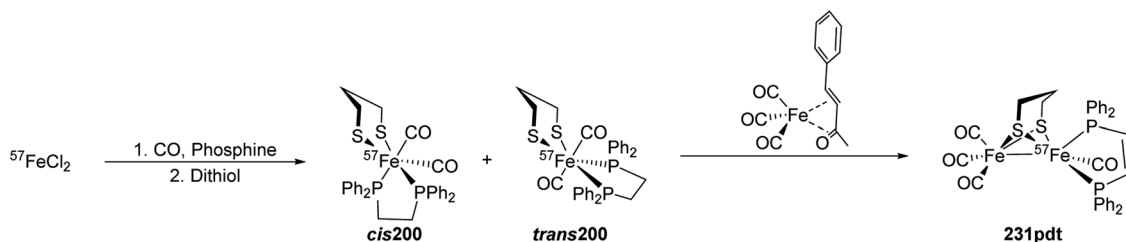
Fig. 70 Synthesis of selectively ^{57}Fe-labelled complex **231pdt**.

This journal is © The Royal Society of Chemistry 2021

Chem. Soc. Rev., 2021, **50**, 1668–1784 | **1717**

(**241**) was observed. If **20** is refluxed in toluene in the presence of dppf for an elongated time, the "intramolecular" bridged complex $Fe_2(pdt)(CO)_4(\mu\text{-dppf})$ (**242**) is formed.[311]

4.5.3.5 Other phosphines. Other bi- or tridentate phosphine ligands follow similar trends in terms of their substitution behaviour. For 1,2-bis(diphenylphosphino)benzene – as observed for dppv – the Me_3NO-induced substitution is more convenient than the thermal reaction in refluxing toluene.[326] The introduction of the electron-poor and thus, less reactive 4,5-bis(diphenylphosphino)-4-cyclopenten-1,3-dione with electron-withdrawing carbonyl-groups requires additional heating under refluxing conditions in toluene.[314] Notably, the related compound 2,3-bis(diphenylphosphino)maleic anhydride is prone to decomposition under these conditions, but can be incorporated into the [2Fe–2S]-framework by photolysis, which is also a known alternative method for the introduction of dppv ligands.[313]

In accordance with the stability of five- and six-membered chelate rings, the propane-analogue of dppe, 1,3-bis(diphenylphosphino)propane (dppp) also forms chelate complexes upon CO-substitution. Under the latter conditions the complex slowly rearranges to afford the bridged μ-dppp complex.[342] The 2-(n-alkyl)aza-analogues also form the expected chelate complexes as the major product in refluxing toluene together with small amounts of the intramolecular bridged complex and the tetranuclear cluster.[204,350,351] The latter can be synthesised selectively by decarbonylation with Me_3NO. The N-phenyl substituted phosphine gives the "intermolecular" bridged complex either with Me_3NO induced decarbonylation or in refluxing toluene.[351] Decarbonylation and subsequent prolonged heating in toluene allowed for the isolation of the respective chelate complex.[352] The additional methylene group in the backbone of 1,3-bis(diphenylphosphino)butane (dppb) renders the formation of the chelate compound unfavourable and the "intramolecular" bridged compound is formed under both conditions. As observed for dppe, the ligands with longer carbon chains in the backbone initially form the linked [4Fe–4S]-complexes. This coordination mode can be exclusively obtained if *trans*-bis(diphenylphosphino)ethene is used.[342]

Similarly, *meta*-substituted pyridyl and pyrimidyl phosphines also adopt this coordination mode if 0.5 equiv. are used. In the presence of one equivalent of the phosphine ligand mono-substituted complexes $Fe_2(xdt)(CO)_5(\kappa^1\text{-L})$ are formed.[305] The tridentate phosphine bis(diphenylphosphinoethyl)phenyl-phosphine can be introduced in refluxing toluene and adopts a μ,κ^1,κ^2-coordination mode showing both features of the chelate and the bridged complexes. The constraints of this coordination mode distort the square pyramidal coordination environment around the iron centres and lead to complexes with 'rotated state' character.[353,354]

4.5.4 H-cluster models with other ligands

4.5.4.1 Isocyanides. Especially in the early days of [FeFe]-hydrogenase research, isocyanide ligands gained interest. With a similar Fe–C≡N framework, but without a reactive nitrogen centre, isocyanide complexes were shown to give more stable hydrides as well as oxidised species (*vide infra*) as compared to the cyanides.[355–357] The substitution of the carbonyl ligands (Fig. 71) occurs slowly at room temperature. However, after twenty hours to two days at room temperature the single- or double-substituted complexes can be obtained.[213,355,358] For example, at 70 °C, isocyanomethane (CNMe) gives the double-substituted complex $Fe_2(pdt)(CO)_4(CNMe)_2$ (**243**) after two hours in acetonitrile.[356] Prolonged heating gives the three- and four-times substituted complexes (**244** and **245**) (Fig. 71).[356,357] If Me_3NO is applied, the double-substituted complex is also accessible selectively at room temperature within hours.[213,283] Notably, 1,4-diisocyanobenzene was also highlighted to enable bridging of two [2Fe–2S]-subunits (**246**).[204,213]

4.5.4.2 N-heterocyclic carbenes (NHCs). Like phosphines, N-heterocyclic carbenes (NHCs) are strong σ-donor ligands with tuneable steric properties. Their similar donor strength, stability of the corresponding complexes as well as their more convenient handling, *e.g.* compared to PMe_3, raised the interest in exchanging phosphine ligands by NHCs.[359,360] Accordingly, NHCs were also applied for the generation of electron-rich (mono)substituted active site mimics. The substitution of the carbonyl ligands by NHCs in the hexacarbonyl complexes

Fig. 71 Substitution of carbonyl ligands by isocyanides.

1718 | *Chem. Soc. Rev.*, 2021, **50**, 1668–1784

This journal is © The Royal Society of Chemistry 2021

Fig. 72 Synthesis of NHC-substituted models and further functionalisation.

occurs at room or moderately elevated temperatures (up to 60 °C) (Fig. 72). The sterically less demanding ligand 1,3-dimethyl-imidazol-2-ylidene (IMe) solely forms the monosubstituted complex at room temperature in high yields (83% for pdt),[361] while at 60 °C the disubstituted complex $Fe_2(pdt)(CO)_4(IMe)_2$ (**247**) is preferably formed (50% yield compared to 12% of the mono-substituted complex).[291] With sterically more demanding NHCs (e.g. 1,3-dimesitylimidazol-2-ylidene (IMes)) only the monosubstituted complex **248** is observed in high yields (>70%).[181,362–364] Under reflux conditions in toluene, PMe_3 can be introduced into the monosubstituted complexes on the $Fe(CO)_3$ fragment to give very electron-rich asymmetric mimic $Fe_2(pdt)(CO)_4(IMes)(PMe_3)$ (**249**, Fig. 72).[361,365] The substituents at the nitrogen atoms have also been functionalised with additional donor groups. While thioethers and amines were shown not to coordinate the iron atom even in the presence of Me_3NO,[363] the pyridine nitrogen in 1-methyl-3-(pyridylmethyl)-imidazol-2-ylidene binds to the iron centre immediately (**250**).[364] Interestingly, if the symmetric, N,N'-disubstituted 1,3-bis(pyridylmethyl)-imidazol-2-ylidene ligand is used, only the carbonic carbon atom and none of the pyridines coordinates to the iron centre in **251** at room temperature and even at 60 °C only 20% yield of complex **252** with a κ^2-NHC ligand was obtained. However, one of the pyridine nitrogen atoms can be coordinated upon addition of Me_3NO to the monodentate complex. By this method the κ^2-complex is obtained in 90% yield. The coordination of the other pyridine moiety or a ligation of the second iron atom are not observed.[364] Similar to bidentate phosphines, bis-carbene ligands with different alkyl linkers were introduced. With these ligands monosubstituted complexes,

chelate complexes (**253**), intermolecular bridged complexes (**254**) and mixtures thereof were obtained in low to moderate yields (up to 50%).[181,363]

Like mono-substituted phosphine complexes, NHC com-plexes are reasonably stable under ambient conditions even in solution. Carrying an additional phosphine ligand, the stability of the complexes towards air is massively reduced in solution, however the solids can be handled under air.[361]

4.5.4.3 Thioethers and sulfoxides. In contrast to cyanides and carbonyls, the third ligand observed in the active site – (metallo-)thioethers – gained considerably less interest as dis-crete ligands. However, thioethers and sulfoxides can also be introduced as terminal ligands by decarbonylation with Me_3NO and subsequent addition of the ligand at room temperature (**255**, Fig. 73).[366–368] In an alternative route, thioethers can be incorporated after one of the carbonyl ligands is converted to a Fischer-type carbene (**256b**) with n-BuLi and $[Et_3O]BF_4$.[367] The organometallic equivalent of a thioether $Cp(CO)_2FeSPh$ or $Cp(CO)_2Fe(Cys-\kappa S)$, mimicking the native cysteine link to the [4Fe–4S]-cluster, can also be incorporated by the former method.[178,204,209] The chemistry of [2Fe–3S]-assemblies is also part of Section V.

4.5.4.4 Amines and pyridines. By heating $Fe_2(pdt)(CO)_6$ to reflux in propylamine, the complex $Fe_2(pdt)(CO)_5(NH_2Pr)$ was obtained. This complex was shown to be stable in non-coordinating solvents. However, in coordinating solvents, e.g. acetonitrile, the amine ligand is replaced by the solvent molecule.[369] In contrast,

This journal is © The Royal Society of Chemistry 2021

Chem. Soc. Rev., 2021, **50**, 1668–1784 | **1719**

Fig. 73 Two methods for the incorporation of thioethers into [2Fe]$_H$-mimics.

focused on an exact representation of the ligands on the iron centre and the incorporation of different bridgehead atoms. Aiming at both structural and functional mimics, more complex alterations of the active site were pursued. By now, numerous protocols for the incorporation of different (functionalised) dithiolate bridges as well as many classical organometallic ligands and a combination thereof are available. The Fe(CO)$_3$ platform enables versatile ligand substitutions by associative or after thermal, photochemical or chemical decarbonylation by dissociative pathways. Both, functionalised ligands and bridges can be used to achieve the desired electronic or structural properties of the mimic and allow for the attachment of photosensitizers, redox active groups, or proteins. Much of the progress, in the development of synthetic protocols was driven by the aim to understand the relationship of structure and function of the [2Fe]$_H$-cluster. The most prominent example in this regard is the amine in the dithiolate bridge. Even before its presence in the active site was confirmed, the proposed function as a proton relay was confirmed in e.g. protonation experiments and gave strong evidence for its utmost importance. In the next sections, we will present how the synthetic progress gave rise to complexes that were able to mimic almost all relevant features (e.g. rotated structure, CO-binding, protonation behaviour, proton reduction, hydrogen oxidation, etc.) observed in the protein. Although there is no mimic known that is alone capable to display all properties of the natural active site, the variety of model complexes together is able to cover all aspects of [FeFe]-hydrogenases' activity.

V Structural models of the active site

In this section, we will present how by combination of different ligands and dithiolate bridges sophisticated structural or functional models of the active site were designed.

5.1 H-cluster models mimicking the rotated state

The distal iron atom in the native H-cluster features an unusual coordination environment, which is referred to as the 'rotated state'. Namely, the square pyramidal geometry is inverted compared to the hexacarbonyl and dicyanide complexes. One of the formerly terminal carbonyl ligands subsequently adopts a semi-bridging position. This unusual geometry is not found in the hexacarbonyl complexes, in which the carbonyl ligands of the two iron centres are eclipsed and many of the reported, substituted model complexes show the same unrotated geometry. However, due to steric interactions or other constraints deviations

complexes with pyridine donors and derivatives were found to be stable. The substitution with pyridine proceeds via decarbonylation with Me$_3$NO,[370] while the chelating ligands 2,2′-bipyridine[371] and 1,10-phenantroline[372] were introduced in refluxing toluene. The incorporation of an additional PMe$_3$ substituent was also shown to be feasible with Me$_3$NO for the latter one.[373] Adding two additional thiolate functions to 2,2′-bipyridine e.g. in 2,2′-([2,2′-bipyridine]-6,6′-diyl)bis(1,1-diphenylethane-1-thiolate) (= L^{N2S2}) yields the chelate complex 257 (Fig. 74) after adding NiCl$_2$ in THF at room temperature. Interestingly, changing the metal from nickel to iron, e.g. Fe(BF$_4$)$_2$, yields [Fe$_2$(L^{N2S2})$_2$H]$^+$ (258), a dimeric structure in which one thiolate is protonated.[374] Both complexes can be reacted with [CpFe(CO)(MeCN)$_2$]$^+$ yielding the respective NiFe- and FeFe-complexes (259 and 260).[375,376] Thus, the L^{N2S2} ligand closes the gap between [FeFe]- and [NiFe]-hydrogenase models, enabling both types of metal content.

4.6 Towards structural and functional H cluster models

The rich chemistry of Fe$_2$(SR)$_2$(CO)$_{6-n}$L$_n$ complexes, some of which developed almost a century ago, enabled the preparation of diverse synthetic mimics of the [2Fe]$_H$-cluster. The first and most simple model complexes bearing a dithiolate bridge were synthesised decades before the crystal structure was known. Based on the knowledge gained out of these studies, a variety of more accurate active site mimics were reported after the determination of the crystal structure. At first, the efforts

Fig. 74 Two methods for the incorporation of thioethers into [2Fe]$_H$-mimics.

from the idealised, eclipsed geometry were observed. Aiming at structural models of different enzyme states, more elucidated models featuring the special rotated geometry were developed and will be presented herein.

Already in 2003 Bruschi, Fantucci, and De Gioia[377] presented a DFT study on $Fe^{I}Fe^{I}$ complexes, which proposed stable energetic minima corresponding to a rotated state. In 2006, Tye, Darensbourg, and Hall[378] then investigated the influence of various substitution patterns on the stability of rotated structures with DFT calculations and showed that these structures become more favourable when altering the electron donating ligands (e.g. phosphines) from Fe,Fe'- to Fe,Fe-disubstituted complexes. In accordance with earlier reports on oxidised and reduced species with bridging carbonyl ligands,[357,379,380] the calculations also affirmed the increased stability of the rotated structures upon oxidation/reduction. In addition, it was proposed that strongly electron donating ligands on one iron atom in combination with strongly electron accepting ligands on the adjacent iron centre is another promising strategy towards "rotated models" – a strategy which is brought to an extreme by the use of NO^+ ligands in synthesis.[381–383] With one exception, in which one carbonyl ligand is forced into a bridging position by binding to strong Lewis acids,[53] at least one of these three strategies, is found in every active site mimic featuring a rotated geometry.

5.1.1 Remarks on the rotated geometry. Three criteria are used to describe and quantify the rotation of the iron centre denoted as Fe_d in analogy to the enzyme. First, the coordination environment around the rotated iron centre is evaluated – ideally being square pyramidal (Fig. 75). Upon distortion, the coordination is better described as trigonal bipyramidal. Although the Fe_p–Fe_d–C_b angle Ψ, where Fe_p is the unrotated iron centre and C_b is the carbon atom of the semi-bridging carbonyl ligand, is reduced for the formerly basal carbonyl ligand, now in equatorial position, the models are still regarded as unrotated. Contrary, in rotated complexes again a square pyramidal conformation is found. In this case, the coordination around the iron is inverted. The Addison τ parameter is used to quantitatively distinguish between a trigonal bipyramidal and a

square pyramidal coordination environment. The value is, according to eqn (1), determined by the difference between the two angles formed by opposing Fe_d–S and Fe_d–C_{CO} bonds divided by 60°.

$$\tau = \frac{\sphericalangle_{S_2Fe_dC_2} - \sphericalangle_{S_1Fe_dC_1}}{60°} \qquad (1)$$

In a square pyramidal environment, the four involved bonds span a basal plane. Accordingly, both angles equal 180° giving $\tau = 0$. In reality, for unrotated as well as rotated complexes, the iron atom is distorted out of the basal plane towards the apical ligand, so that both angles adopt values smaller than 180°, e.g. 156° and 160°, in the case of the pdt hexacarbonyl complex.[288] Still, in a symmetrical coordination environment τ is almost equal to zero. If the ligands around the iron form a trigonal bipyramid, a carbonyl ligand and a thiolate are in axial positions, while the other two ligands span the trigonal plane together with the third carbonyl ligand. This arrangement corresponds to an angle of 180° between the axial bonds, respectively 120° between the equatorial bonds. Hence, in trigonal bipyramidal environments $\tau = 1$. However, values of $\tau = 1$ are not observed in real structures for two reasons, which will be explained at the example of $Fe(pdt^{Et})(CO)_4(PMe_3)_2$ (**261**, pdt^{Et} = 2,2-diethyl-1,3-propanedithiolate, Fig. 76).[382] In this complex, the coordination environment of one iron centre can be described as trigonal bipyramidal. The iron, one of the sulphur atoms and both carbonyl atoms span the equatorial plane with only small deviations. Still, the angles between the ligands at the iron centre do not all equal 120°. The two S–Fe–C angles have values of 128° and 129° and the angle between the carbonyl ligand equals 102°, which is at the upper end observed for such complexes. Accordingly, in none of the severely distorted complexes reported in literature the largest angle in this plane $\measuredangle(S_1$–Fe_d–$C_1)$ is smaller than 127°.[381] In addition, the axial ligands almost never adopt positions, in which the angle $\measuredangle(S_2$–Fe_d–$C_2)$ between them is 180°, i.e. because of the constraint S–Fe–S angle. Typical values are 167° to 170°, 169° in the case of **261**, with various examples below this range and only two examples[159,382] above a value of 173°, both of which with
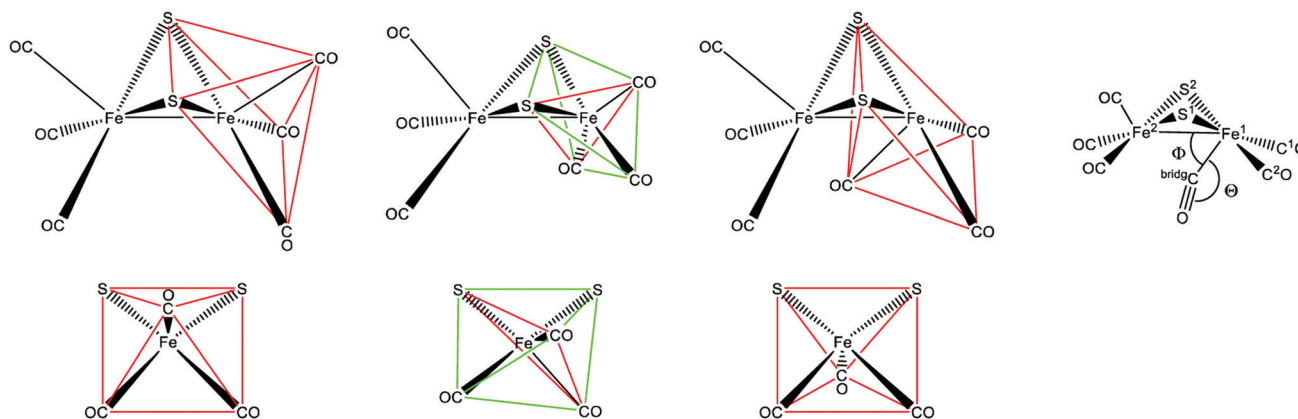
Fig. 75 Left: Two views of the unrotated (left), a distorted, trigonal-bipyramidal (middle) and a rotated (right) geometry from two perspectives. For clarity, bond lengths are exaggerated and all ligands are omitted. Right: Rotated complex, in which the angles Ψ and Θ are indicated.

This journal is © The Royal Society of Chemistry 2021

Chem. Soc. Rev., 2021, **50**, 1668–1784 | **1721**
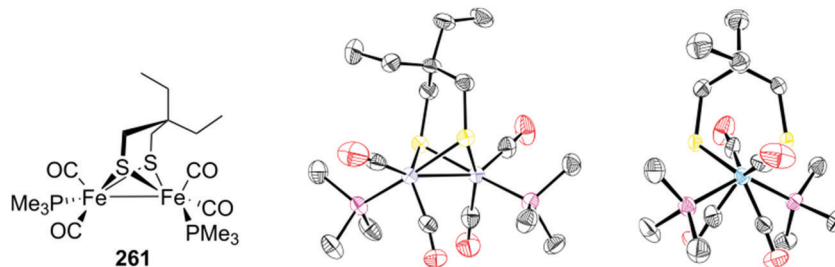
Fig. 76 Molecular structure of complex **261**. CCDC ID: PEGCOV.[382]

Fig. 77 Nitrosyl substituted complexes **262xdt** and **263xdt**.

smaller τ values (0.48 and 0.17) and sterically crowded dithiolates. Due to these deviations from an idealised trigonal bipyramidal environment Addison's τ-parameter is always considerably smaller than $\tau = 1$. For **261**, a value of $\tau = 0.67$ is obtained and with the limits of $\angle(S_1–Fe_d–C_1) = 127°$ and $\angle(S_2–Fe_d–C_2) = 173°$ described above an estimated maximal value of $\tau = 0.77$ can be extrapolated. Considering this behavior, complexes for which τ is about 0.75 can be considered trigonal bipyramidal and represent the transition from an unrotated to a rotated geometry. This upper limit should be considered when using Addisons' τ parameter to quantify the rotation of the iron centre. Moreover, the value is influenced by the position of four out of five ligands and therefore, sensitive to small changes in their position, *e.g.* due to steric effects, which can complicate the comparison of different complexes.

As a second aspect, the torsion angles between the apical ligand on the unrotated iron centre and the ligands on the rotated iron centre can be evaluated. Especially, the largest – including the (semi-bridging) carbonyl – and the smallest angle that can be regarded as the distortion of the eclipsed unrotated complex are of interest. Being the most intuitive values, care must be taken as the apical ligand on the unrotated iron can also be distorted from its idealised position (up to 20°) most often due to steric repulsion with the dithiolate bridge. In this context, **261** is again a useful example. Torsion angles of 75° (regarding C^1) and 176° (regarding C_b) are observed indicating a fully rotated complex. However, the apical ligand on the less distorted iron centre does not lie symmetrically between both sulphur atoms. If instead of the apical ligand, the pdt bridgehead carbon, which adopts an almost symmetric position, is used for the calculation, more realistic torsion angles of 56°,

respectively 157° are obtained. Even though the idealised torsion angles are useful quantifiers for the rotation of the iron centre, the described distortion can render these values meaningless, without careful evaluation of the complete complex.

The third aspect is the (semi-)bridging character of the "inverted" carbonyl ligand. The four relevant structural values discussed in the literature to distinguish between terminal, semi-bridging and bridging carbonyls are the $Fe_p–Fe_d–C_b$ angle Ψ, the $Fe_d–C_b–O_b$ angle Θ and both $Fe–C_b$ distances. Crabtree and Lavin[384] examined the correlation between these structural parameters in (semi-)bridging carbonyl ligands of different iron carbonyl complexes. In this discussion, structural parameters of different classes of iron carbonyl ligands were used, and even though, all of the complexes herein belong to a single class in different oxidation states, with different ligands, and different steric strain these values and their correlations are astonishingly valid. For terminal carbonyl ligands Ψ is about 100° in hexacarbonyl complexes and substituted complexes without steric bulk, *e.g.* $Fe_2(pdt)(CO)_4L_2$ (L = CO, CN^-, PMe_3).[277,279,288] If carbonyl ligands adopt positions with a higher bridging character, this value decreases. While for semi-bridging carbonyls this decrease correlates linearly with a decrease of Θ, in the case of terminal carbonyls, uncorrelated values of $\Theta > 170°$ corresponding to almost linear carbonyl ligands are observed. Based on the extrapolation of Ψ for which $\Theta = 180°$, Crabtree and Lavin suggested $\Psi = 75°$ as the frontier between terminal and semi-bridging carbonyl ligands. Even though Θ is not smaller than for terminal carbonyl ligands for Ψ values between 70° and 75°, there is a distinct difference between these ligands. While for values $\Psi < 75°$ the oxygen atom is bent away from Fe^2 corresponding to semi-bridging carbonyls, the orientation of the ligands is governed by steric effects for increased values. For $\Psi = 75°$ a distance $Fe_p–C_b$ of 2.69 Å was extrapolated, almost in the middle between the sum of the covalent radii (1.94 Å) and the sum of the van der Waals radii (*ca.* 3.5 Å). Accordingly, this distance is also a useful criterion for the evaluation of the bridging character. The length of the actual M–CO bond can also be considered. Below an angle Ψ of 70°, the bonds are lengthened due to a diminished π-backbond and correspond to a regular single bond in the symmetrically bridging case. As described above, the π-backbond strengthens and the M–CO bond shortens upon binding of electron rich ligands. The different bond lengths have to be considered, when comparing different complexes, which

1722 | *Chem. Soc. Rev.*, 2021, **50**, 1668–1784

This journal is © The Royal Society of Chemistry 2021

Fig. 78   Left: Addisons' τ parameter against $\Psi/°$ for the nitrosyl complexes **262edt**, **263edt** and **263pdt**. **263pdt.1** refers to the ba/ap rotamer and **263pdt.2** to the ba/ba rotamer. The ′ denotes different independent molecules in the asymmetric unit. Both **263pdt.2** molecules are weakly disordered, but the angles vary only by 1°. For all molecules of **263pdt** τ was calculated with the semi-bridging carbonyl in apical position. Right: Addisons' τ parameter against $\Psi/°$ for different rotated complexes.

makes the other values Ψ, Θ, and $Fe_p–C_b$ more robust in the context of this evaluation.

In Fig. 78, the values Ψ and τ of the nitrosyl substituted complexes $[Fe_2(xdt)(CO)_{4−n}(PMe_3)_{1+n}(NO)]^+$ (xdt = edt, pdt) (Fig. 77) are plotted. The unrotated complex **262edt** is characterised by a low τ value and a large angle Ψ. With increasing degree of rotation, Ψ decreases while τ increases initially. The strongly distorted molecule **263edt** and the rotamer **263pdt.1** are characterised by high τ values and angles Ψ at the edge of terminal to semi-bridging carbonyls. Both values decrease hereafter to characterise the rotamer **263pdt.2** with a rotated structure.

As an additional aspect in this regard, the carbonyl IR stretching frequencies are useful to evaluate their bridging character especially if no crystal structure is available. Similar to the M–CO bond length, the frequencies are also sensitive to the electron-donating abilities of other ligands, as well as oxidation states of the iron centres and accordingly, have to be assessed carefully. Still, in comparison of similar compounds carbonyl stretching frequencies and Ψ match well. More importantly, the observation of the band of the semi-bridging CO ligand by IR spectroscopy provides an easy, but powerful tool to assess the structure of the complexes in solution, which can differ strongly from the solid state (*vide infra*). Table 6 summarises various structural and spectroscopic parameters of complexes featuring a rotated or distorted geometry.

5.1.2   Fe^{I}Fe^I models displaying the rotated geometry. Already in 2001, Pickett and coworkers reported a metastable intermediate of the cyanation of $Fe_2(\kappa^3-pdt^{MeSMe})(CO)_6$ (**53**, pdt^{MeSMe} = 2-methyl-2-((methylthio)methyl)propane-1,3-dithiolate) bearing a bridging carbonyl ligand. This complex has no open coordination site as the H_{ox} or H_{red} states, but more closely resembles the H_{ox}-CO state (see Section 5.2).[138,139,385] Until 2007,

no complex with a bridging carbonyl ligand and an open coordination site was known. Thereafter, Justice, De Gioia and Rauchfuss[53] showed that a rotated geometry is indeed accessible outside the protein. They reported on model complexes **264xdt** (xdt = edt, pdt), in which the bridging CO ligand is stabilised by binding to strong Lewis acids (AlBr$_3$, B(C$_6$F$_5$)$_3$) (Fig. 79). Initial experiments with AlBr$_3$ showed, that strongly Lewis basic carbonyl ligands are required for a sufficient binding strength, accessible by the ligation of the iron centres by electron-donating groups. While $Fe_2(edt)(CO)_4(\kappa^2-dppv)$ and $Fe_2(edt)(CO)_3(\kappa^2-dppv)(PMe_3)$ were shown not to be sufficiently Lewis basic, in cyanide substituted complexes, those ligands would be the preferred binding site for the Lewis acid. Therefore, $Fe_2(xdt)(CO)_2(\kappa^2-dppv)_2$ (**233xdt**, xdt = edt, pdt) with four electron donating phosphine ligands were chosen for this study. Indeed, IR- and NMR-data are in line with calculated DFT spectra and indicated the formation of the rotated complexes $Fe_2(xdt)(\mu-COAlBr_3)(\kappa^2-dppv)_2(CO)$ in solution. Unfortunately, no structural data is available for a comparison with other rotated complexes, in which fundamentally different effects cause the rotation. Notably, the binding of the Lewis acids to the pdt derivative is stronger compared to the edt complex. This was explained by the destabilisation of the apical CO ligand by steric interactions with the methylene group. Thus, the Lewis acid-bound conformation with the bridging carbonyl ligand becomes more favourable.

This effect that is caused by steric repulsion between the bridge and the apical ligand is also an integral part of other rotated Fe^{I}Fe^I models. Moreover, all complexes feature, as proposed by Tye, Darensbourg and Hall, an asymmetric ligand environment on the [2Fe–2S]-core, rendering one iron atom strongly electron-rich due to two donating phosphine ligands. The very similar complexes **265**[341] and **266**,[344] reported in 2013, were the first rotated Fe^{I}Fe^I complexes characterised by X-ray

Table 6 Structural parameters of distorted and rotated active site mimics

Complex	Dithiolate	Ox. State Fe$_d$/Fe$_p$	Ligands Fe$_d$	Fe$_p$	Ψ/°	Θ/°	τ	Bond length Fe$_d$–C$_b$	Fe$_p$–C$_b$	μ-CO ν/cm^{-1}	CCDC ID	Ref.
265	adt^{Bn}	I/I		dmpe	57	146	0.12	1.815	2.179	1777^a	YIJDEC	341
266	pdt^{Et}	I/I		dppv	65	158	^{b}	1.744	2.499	1818^a		344
239	Ph$_2$Si(C(Ph)HS$^-$)$_2$	I/I		dmpe	64	156	0.48	1.789	2.379	1801^a	KOYKAM	159
235edt$^+$	edt	I/II	dppv	PMe$_3$	72	170	0.00	1.781	2.628	1883	XIGFEZ	386
235pdt$^+$	pdt	I/II	dppv	PMe$_3$	73	170	0.00	1.786	2.678	1889	AGEHIE	345
268P^{i}Pr$_3$$^+$	pdt	I/II^c	dppv	P^{i}Pr$_3$	79	178	0.00	1.785	2.833	1870^c	AGEHOK	345
249$^+$	pdt	I/II	I$_{Mes}$	PMe$_3$	57	152	0.20	1.864	2.196	1861	LIHCAH	365
270^{+d}	pdt^{Me}	I/II	PMe$_3$	PMe$_3$	58	152	0.03	1.813	2.204	1859	NONFEC	387
261$^+$	pdt^{Et}	I/II	PMe$_3$	PMe$_3$	58	153/146	0.17	1.839	2.222	1874	PEGCUB	382
233pdt$^+$	pdt	I/II	dppv	dppv	71	170	0.05	1.786	2.618	1884	RIXQAS	388
233pdt^{Me+e}	pdt^{Me}	I/II	dppv	dppv	65	163	0.00	1.793	2.460	1.854	HELPOG	348
271$^+$	adt^{Bn}	I/II	dppn		68	167	0.10	1.769	2.516	1896	AVUSAM	389
278	SCR$^-$	I/II^f	NO, PPh$_3$		70	168	0.08	1.783	2.570	1875^a	GICRUF	390
262edt	edt	I/II^f	NO, PMe$_3$		91	177	0.25	1.821	3.170		NOJVUE	381
262edt'	edt	I/II^f	NO, PMe$_3$		91	179	0.28	1.827	3.162		NOJVUE	381
263edt	edt	I/II^f	NO, PMe$_3$	PMe$_3$	81	173	0.62	1.792	2.872		NOJWEP	381
263pdt.1	pdt	I/II^f	NO, PMe$_3$	PMe$_3$	76	172	0.67	1.794	2.479		NOJWIT	381
263pdt.2^d	pdt	I/II^f	NO, PMe$_3$	PMe$_3$	66	160	0.52	1.813	2.472		NOJVOY	381
263pdt.2'^{d}	pdt	I/II^f	NO, PMe$_3$	PMe$_3$	62	154	0.38	1.780	2.325		NOJVOY	381
280	pdt	I/II^f	NO, I$_{Mes}$	PMe$_3$	51	136	0.12	1.747	2.028		UGOGUU	383
263pdt^{Me}	pdt^{Me}	I/II^f	NO, PMe$_3$	PMe$_3$	58	148	0.30	1.802	2.182	1877	PEGDEM	382
263pdt^{Et}	pdt^{Et}	I/II^f	NO, PMe$_3$	PMe$_3$	59	153	0.35	1.797	2.234	1874	PEGDAI	382
261	pdt^{Et}	I/I	PMe$_3$	PMe$_3$	82	172	0.67	1.747	2.873	1899	PEGCOV	382

$'$ second molecule in asymmetric unit, .1/.2 are rotamers. ^{a} Only observed in solid state. ^{b} Not all crystallographic data are reported. ^{c} Geometric and electronic situation is different in solution. ^{d} Disordered, values given for the stronger rotated molecule. ^{e} Second molecule in the asymmetric unit with negligible structural deviations. ^{f} Regarding the non-innocent NO-ligand other assignments are also reasonable.
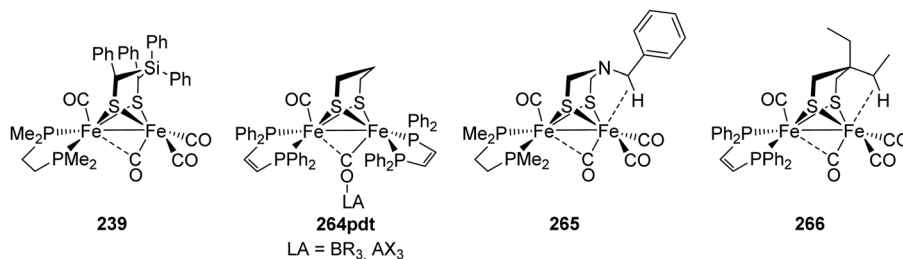
Fig. 79 Fe^{I}Fe^I models of the [2Fe–2S]-cluster exhibiting a rotated geometry.

crystallography (Fig. 79). Both complexes feature an additional stabilisation of the free coordination site on the rotated iron site through an agostic interaction. This interaction, although being weak, was identified by DFT calculations as crucial feature for obtaining the rotated geometry in the crystalline state. Notably, the asymmetric unit of the crystals of **266** feature two independent molecules one of which is rotated while the other is unrotated. This indicates a small energy difference between both confirmations. Likewise, it suggests that packing effects in the crystal also play an important role for stabilising the rotated conformation.

The coordination geometry of complex **239**[159] with a sterically heavily crowded dithiolate ligand shows a distorted, inverted square pyramidal geometry in the molecular structure. Nevertheless, the coordination environment also has a considerable trigonal bipyramidal character (τ = 0.48). The Fe(CO)$_3$ unit is rotated out of an idealised square pyramidal environment by about 10°–15°. The authors denoted this geometry as

semi-rotated and concluded that the missing agostic interaction, compared to **265** and **239**, prevents full rotation. By examination of other geometric parameters, a different conclusion can be proposed. One of the carbonyl ligands has considerable semi-bridging character (Ψ = 64°, Θ = 156°, Fe$_p$–C$_b$ = 2.379 Å), less than in **265** but slightly higher than in **266**. In addition, the angle $\angle$(S$_1$–Fe$_d$–C$_1$), which is used for the calculation of τ, is unusually large. The value of 175° is at least 5° larger than usual for rotated as well as unrotated complexes leading to an unusual linear arrangement, which could be caused by the high steric strain. Assuming a typical value of 170° for this angle, τ would equal 0.4 in accordance with a less distorted complex. Regarding the positions of C$_1$O and the phenyl group, that shields the open coordination site, in the crystal (Fig. 80) the distortion may be attributed to steric repulsion between the two groups. Accordingly, it can be proposed that the complex is a fully rotated complex that is distorted due to steric strain. Due to the low number of comparable complexes and the small energy
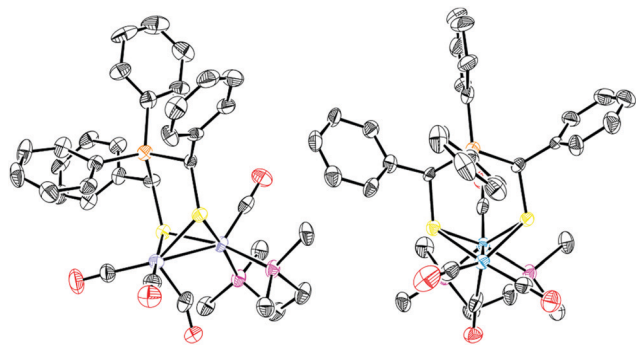
Fig. 80 Molecular structure of complex **239** featuring a rotated geometry. CCDC ID: KOYKAM.[159]

differences in the DFT calculations regarding this complex this explanation was not investigated further.

Even though all three complexes **239**, **265** and **266** were crystallised in the rotated state and μ-CO bands were detected in the IR spectra of the solids, the solution IR spectra show no bands for bridging carbonyl ligands. Accordingly, for none of the three complexes the rotated geometry is preserved in solution. Rotated complexes in solution were, except from **264xdt**, only observed for oxidised or NO$^+$-bound complexes. A very important feature of the three complexes **239**, **265** and **266** is that in each complex the Fe(CO)$_3$ unit is rotated. This is in accordance with the calculations of Tye, Darensbourg and Hall,[378] but no mimic in other oxidation states with a rotated Fe(CO)$_3$ unit has been crystallised.

These four examples indicate that for Fe^{I}Fe^I complexes a rotated geometry can be obtained by following the following strategies:

(1) Destabilisation of the apical ligand through steric bulk on the dithiolate.

(2) Stabilisation of the bridging carbonyl ligand.

(3) Stabilisation of the vacant coordination site through weak intramolecular interactions.

(4) Introduction of an electronic asymmetry on the two iron centres.

5.1.3 H$_{ox}$-models displaying the rotated geometry

5.1.3.1 Fe^{I}Fe^{II} H$_{ox}$-models. Since the structure of the active **H$_{ox}$** state was identified, dedicated efforts in modelling its key feature – the rotated geometry – were invested. The formation of a bridging CO ligand in Fe^{I}Fe^{II} H$_{ox}$-models was first reported

for the very same system as for the Fe^{I}Fe^I-complexes by Best, Pickett and their coworkers in 2002. *In situ* IR measurements of (electro-)chemically oxidized [Fe$_2$(pdt^{MeSMe})(CO)$_4$(CN)$_2$]$^{2-}$ (**267**) revealed a μ-CO band (see Section 5.2).[379] In 2007, the groups of Rauchfuss[386] and Darensbourg[365] independently presented the mixed valent Fe^{I}Fe^{II} complexes **235edt$^+$** and **249$^+$** showing a rotated geometry (Fig. 81). Both complexes were prepared by oxidation of asymmetrically substituted, not rotated model complexes with ferrocenium in non-coordinating solvents and isolated as their [BF$_4$]$^-$, respectively [PF$_6$]$^-$ salts. A crucial feature of both complexes is a sterically demanding and strongly electron donating ligand on the rotated iron atom. While Rauchfuss and coworkers applied a dppv ligand on the rotated iron centre, Liu and Darensbourg installed an I$_{Mes}$ ligand. In both cases, the unrotated iron atom is substituted with a PMe$_3$ ligand, which stabilises the oxidised Fe^{II} centre. In these complexes, the rotated geometry is not only present in the solid state, as observed for the rotated Fe^{I}Fe^I models, but also can be detected in solution, as indicated by bands for (semi-)-bridging CO ligands in the IR spectra. Complexes with other dithiolates **235xdt$^+$** (pdt, adt, adt^{Bn}, odt)[391] and phosphines [Fe$_2$(pdt)(CO)$_3$(κ^2-dppv)(PR$_3$)]$^+$ (**268PR$_3^+$**, PR$_3$ = PCy$_3$, P^{i}Pr$_3$)[345] were also reported by Rauchfuss later on. The exchange of PMe$_3$ by dppv also afforded rotated complexes **233pdt^{R+}** with pdt[388,392] and pdt^{Me} bridges.[348] By using the redox active phosphine PEt$_2$Fc* instead of PMe$_3$, Camara and Rauchfuss presented elaborate, functional model complexes **269adt^{R+}** with adt^R bridges (R = Bn, H). The IR spectra of these complexes also indicate a rotated complex geometry.[349] In addition, Darensbourg and coworkers reported that less bulky NHCs lead to less stable complexes that could not be characterised by X-ray diffraction. The bands assigned to μ-CO are strongly blue-shifted by 68 cm^{-1} compared to **249+** in the solution IR spectra of these complexes and indicate a greatly reduced or no semi-bridging character of the carbonyl ligand. Thus, steric bulk was identified as a key feature of rotated complexes.[361] Interestingly, it could be shown that the introduction of steric bulk on the dithiolate bridge (pdt^{Me} and pdt^{Et}) allows for rotated complexes **270$^+$** and **261$^+$** even with two small PMe$_3$ ligands. The authors highlighted that, in contrast to **249$^+$** and **270$^+$**, the higher thermal stability of **261$^+$** allows for room temperature EPR measurements.[382,387] Rauchfuss and coworkers reported later that the limited thermal stability of their compounds can be avoided by using [BAr$^F_4$]$^-$ instead of [BF$_4$]$^-$ as the counterion.[393]

Fig. 81 Structures of selected mixed-valence Fe^{I}Fe^{II} complexes showing a rotated geometry.

This journal is © The Royal Society of Chemistry 2021

Chem. Soc. Rev., 2021, **50**, 1668–1784 | **1725**

Fig. 82 Rotated, mixed-valence complexes bearing an adjacent amine.

The corresponding complexes showed no decomposition in solution at room temperature for days. The instability of the $[BF_4]^-$ anion towards electrophilic iron complexes has been reported earlier – interestingly also in the context of complexes for hydrogen activation/generation.[394]

Without doubt, all these complexes can be regarded as rotated state mimics (τ, torsion angles, crystal structure). Upon closer inspection of the structural features, some distinct differences are obvious. While the models with the NHC ligand and the bulky bridges all show carbonyl ligands with a high semi-bridging character ($\Psi < 60°$), in the dppv substituted complexes the carbonyl ligands are on the edge between terminal and semi-bridging ($\Psi = 71°–79°$). Only in the complex with the bulky pdt^{Me} bridge, the carbonyl ligand has considerably higher semi-bridging character ($\Psi = 65°$) attributed to the steric repulsion between dppv and the dithiolate. Remarkable in this regard is also the structure of complex $268P^iPr_3^+$, as the low-energy μ-CO band (1870 cm^{-1}) in the solution IR spectrum indicates a higher bridging character of the semi-bridging carbonyl ligand but the opposite is found in the crystal ($\Psi = 79°$).

Supported by additional DFT calculations,[382,387,395] in most complexes the iron centres were accordingly attributed the oxidation states $Fe_p^{II}Fe_d^I$.[345,361,382,387] This is especially interesting, as the same assignment is assumed in the active H_{ox} state (see Section 3.2). The EPR measurements of the P^iPr_3 and PCy_3 substituted complexes $268P^iPr_3^+$ and $268P^iCy_3^+$ indicate another assignment despite the similar crystal structure of $268P^iPr_3^+$ compared to complexes $235edt^+$ and $235pdt^+$.[345] While for all other complexes the spin ($S = 1/2$) is mainly localised on the rotated iron centre, and in some cases partially on the dithiolate,[382] in the complexes substituted with bulky phosphines ^{31}P hyperfine coupling constants indicate that the spin is localised on the other iron centre. Comparing the solution IR spectra to spectra of a rapidly precipitated solid and grown single crystals, in the latter of which no μ-CO band is detected. The authors concluded that in solution the other iron centre Fe(CO)$_2$(PR$_3$) is rotated exhibiting a stronger semi-bridging carbonyl ligand. In this case, the spin resides on the rotated iron centre also in solution.

In order to synthesise a more electrophilic H_{ox}-model for hydrogen oxidation experiments, Camara and Rauchfuss[389] synthesised the tetracarbonyl complex Fe$_2$(adt^{Bn})(CO)$_4$(κ^2-dppn) 271 (dppn = 1,8-bis(diphenylphosphino)naphthalene). Its cation 271$^+$ is, in contrast to other adt tetracarbonyl cations, stable at room temperature in solution for at least 24 h.

Its structure, the first crystallographically confirmed of a rotated adt complex, is very similar to the dppv complexes reported by Rauchfuss with a higher semi-bridging character ($\Psi = 68°$) of the carbonyl ligand on the rotated Fe(μ-CO)(dppn) unit. The complexes Fe$_2$(xdt)(CO)$_4$(κ^2-L)$^+$ (272xdt$^+$, xdt = adt^{Bn}, edt, pdt, bdt^{3Me}; L = ^{n}PrN(CH$_2$PPh$_2$)$_2$) also feature the rotated geometry and an enzyme-like proton relay.[396,397] These complexes resemble the only examples of rotated [FeFe]-hydrogenase mimics, in which the unrotated iron centre is unsubstituted. By EPR measurements, the same $Fe_p^{II}Fe_d^I$ electronic structure was identified.

If the oxidation of the electron-rich precursors is conducted in coordinating solvents, e.g. acetonitrile, the coordination of a solvent molecule promotes the oxidation to the diferrous complexes.[337,345,386,398] Likewise, in the presence of phosphines,[398–400] cyanides,[399] isocyanides,[356,357] or even the adt amine[391,401] oxidation to the Fe^{II}Fe^{II} complexes occurs. A bridging carbonyl ligand is a prominent feature of many of the obtained complexes. Moreover, the diferrous complexes are labile towards further substitution to give highly substituted complexes. An overview over these oxidatively induced ligand substitutions is given in Fig. 83.

5.1.3.2 Hydrogen oxidation by H_{ox}-models. Despite the high activity of [FeFe]-hydrogenases for the dihydrogen oxidation,[402,403] the application of mimics as proton reduction catalysts always dominated research and dihydrogen activation is rare with mimics. Still, H/D exchange reactions catalysed by bridging hydride complexes indicated heterolytic dihydrogen activation.[277,278,355,404] The photolytic oxidative addition of dihydrogen to Ru$_2$(pdt)(CO)$_4$(PCy$_3$)$_2$ (198) reported in 2004, gave the dihydride complex HRu$_2$(pdt)(μ-H)(CO)$_3$(PCy$_3$)$_2$. In the presence of coordinating solvents or counterions hydrogen is released upon protonation, while in CH$_2$Cl$_2$ with [H(OEt$_2$)][BAr$^F_4$] (Ar^F = 3,5-bis(trifluoromethyl)phenyl) a dihydrogen σ-complex is formed.[270] For the iron complex 231edt, the photolytic oxidative addition to a similar dihydride complex was also reported. In the presence of B(C$_6$F$_5$)$_3$ heterolytic dihydrogen activation yields a complex bearing a bridging hydride.[405] The ruthenium and the iron complexes are both capable of oxidatively adding other E–H (E = Cl, O, S, Si) bonds.

The first, actual biomimetic dihydrogen activation was reported for the rotated H_{ox}-models 235adt^{R+} [Fe$_2$(adt^R)(CO)$_3$(P-Me$_3$)(κ^2-dppv)][BAr$^F_4$] (R = H, Bn) (Fig. 82).[393] The corresponding pdt and odt complexes are incapable of performing this reaction, again highlighting the importance of the internal

1726 | Chem. Soc. Rev., 2021, 50, 1668–1784

This journal is © The Royal Society of Chemistry 2021

Fig. 83 Top: Oxidation of complex **235xdt** in the presence and absence of coordinating solvents. Middle: Substitution of a carbonyl ligand in a diferrous complex. Bottom: Exemplary complexes obtained by oxidatively induced ligand substitution.

proton shuttle for any hydrogenase-like activity. However, the reaction was reported to be slow and required high H_2 pressures (12.4 MPa). In the presence of additional oxidants (*e.g.* substituted ferrocenium) the reaction rate is strongly increased.[389] This observation was explained with the mechanism shown in Fig. 84. Similar to a PCET, the heterolytic cleavage of dihydrogen is proposed to occur simultaneously to the oxidation of the complex by the additional oxidant, which is incapable of oxidising **235adt**$^{R+}$. Without ferrocenium present in solution a second molecule of **235adt**$^{R+}$ is oxidised, which limits the reaction rate. The rate limiting step in the presence of an oxidant is the binding of H_2 to the open coordination site. The formed, but not observed double-protonated intermediate is then most likely deprotonated, either by an additional base *e.g.* P(*o*-tolyl)$_3$ or by reduced **235adt**$^{R+}$, yielding the bridging hydride. At some point during the mechanism, the formed terminal hydride isomerizes to a bridged hydride. Thus, in the absence of additional oxidants and bases only half of the bridging hydride is directly formed from the heterolytic dihydrogen cleavage, while the other half is formed by reduction and subsequent protonation. Contrary, in the presence of excess oxidant and base, more realistic for the situation in the enzyme, the bridging hydride is formed

quantitatively from heterolytic H_2 activation. The more electrophilic complex **271**$^+$ shows an even higher reaction rate. Still, both complexes do not show any catalytic activity, which is attributed to the fact that deprotonation of the bridging hydride is not feasible. Indeed, complexes **272xdt**$^+$, in which deprotonation of the bridging hydride is easily accessible, shows catalytic hydrogen oxidation activity.[396] For this complex, also the double-protonated intermediate is observed. Other models that show catalytic activity, though at low turnover numbers, are complexes **269adt**$^{Bn+}$ and **269adt**$^+$.[349] Here, the internal oxidant not only increases the rate of H_2 activation compared to **235adt**$^{R+}$, but increases the acidity of the bridging hydride upon oxidation. This allows for the deprotonation required for catalytic H_2 oxidation.

Subsequently, Hogarth, Holt and coworkers reported on the electrochemical H_2-oxidation catalysed by Fe$_2$(pdt)(CO)$_4$(dppf) also featuring an internal oxidant in the presence of base. However, the mechanism in the absence of an internal proton shuttle remained unclear and the authors tentatively suggested an intermediary dihydride species.[311]

5.1.3.3 Nitrosyl substituted H$_{ox}$-models. Binuclear, nitrosyl substituted iron sulphur complexes are known for more than 150 years. In 1858, Roussin reported on the "red salt"

This journal is © The Royal Society of Chemistry 2021

Chem. Soc. Rev., 2021, **50**, 1668–1784 | 1727

Fig. 84 Hydrogen oxidation by complexes **235adt^{R+}**.
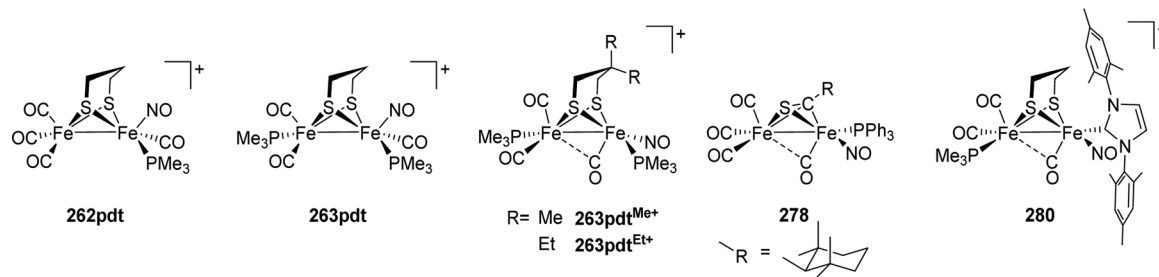
Fig. 85 Exemplary nitrosyl substituted complexes. Note: in the crystalline state **263pdt** shows different degrees of rotation.

$K_2[Fe_2S_2(NO)_4]$ and the corresponding "ester" $Fe_2(SR)_2(NO)_4$.[406,407] Interestingly, the first rotated diiron nitrosyl complex $[Fe_2(\mu,\eta^2\text{-SCR})(CO)_4(NO)(PPh_3)]$ (**278**) was already reported in 1988 by Behrens and coworkers (Fig. 85). In this complex, the iron centres are bridged by a thioacyl moiety and a semi-bridging carbonyl ligand, which is not observed in the absence of the phosphine.[390] Nitrosyl substituted hydrogenase mimics were firstly reported in 2008 by the groups of De Gioia and Rauchfuss.[381] Also in this first report, the authors showed that the substitution of carbonyl by nitrosyl ligands can lead to rotated complexes. Since assigning (formal) oxidation states in the presence of nitrosyl ligands can be difficult (NO^+ vs. $NO^•$), complexes with nitrosyl ligands are discussed separately.

Generally, NO^+ used as the $[BF_4]^-$ salt replaces a carbonyl ligand within several hours at room temperature or even 0 °C. The reaction is limited by the poor solubility of $NOBF_4$ in CH_2Cl_2, which is used to decrease the rate of decomposition of the products. The diamagnetic nitrosyl complexes are air-sensitive and temperature labile, but sufficiently stable at 0 °C.[381–383,408] Handling and storing the complexes under an atmosphere of CO was also reported to increase the stability of the complexes.[383] In literature, only nitrosyl complexes of electron-rich mimics are known. Not surprisingly, several studies showed that the nitrosyl cation attacks at the more electron-rich iron atom. Further substitution reactions with electron donating ligands (PMe_3, CN^-) were shown to occur on the nitroso substituted iron centre.[381,383] Apart from the very electron rich $Fe_2(pdt)(CO)_2(\kappa^2\text{-dppv})_2$ (**233pdt**), only mono-substituted nitrosyl derivatives are reported. Induced by the steric repulsion of the two dppv ligands, $[Fe_2(pdt)(CO)(\kappa^2\text{-dppv})_2(NO)]^+$ (**279pdt**) is also unusual as the NO^+ ligand adopts a basal site, whereas it is usually apical in unrotated complexes.[408]

Nitrosyl complexes gained interest after the first report of a rotated complex bearing a nitrosyl ligand. $[Fe_2(pdt)(CO)_3(PMe_3)_2(NO)]^+$ **263pdt** was shown to crystallise as an apical and

a basal rotamer referred to the PMe_3 on the $Fe(CO)_2(PMe)_2$ unit. In the apical rotamer **263pdt.1** the $Fe(CO)(NO)(PMe_3)$ unit has a high trigonal bipyramidal character ($\tau = 0.67$) and the carbonyl ligand little semi-bridging character ($\Psi = 76°$, Fe_p–$C_b = 2.479$ Å). In contrast, two independent molecules of the basal rotamer **263pdt.2** with higher square pyramidal character ($\tau = 0.52, 0.38$) and higher semi-bridging character of the carbonyl ligand ($\Psi = 67°, 62°$) were crystallised. This again emphasizes the importance of packing effects on the rotation of crystalline mimics. Also, in the complexes **263pdt^R** (R = Et, Me) and $[Fe_2(pdt)(CO)_3(NO)(I_{Mes})(PMe_3)]^+$ (**280**) rotation is induced upon binding of NO^+.[382,383] Complexes of these type are also rotated if the oxidized state lacks the NO ligand – however, $[Fe_2(pdt)-(CO)_2(\kappa^2\text{-dppv})(PMe_3)(NO)]^+$ (**281**) is in contrast unrotated.[408] The authors presumed that the nitrosyl ligand is not sufficiently electron-withdrawing to overcome the effect of two donating phosphines and induce electronic asymmetry.

The introduction of a NO^+ has effects similar to an oxidation, not only on the molecular but also on the electronic structure as indicated by DFT calculations and Mössbauer measurements.[381–383] Accordingly, the oxidation states should be assigned to $Fe(II)\{Fe(I)(NO^•)\}$ with an antiferromagnetic coupling to give diamagnetic complexes, though other assignments are also possible. Indeed, complexes **279pdt**, **281**, and $[Fe_2(pdt)(CO)_3(\kappa^2\text{-dppv})(NO)]^+$ (**282pdt**) were also prepared by first oxidising the corresponding precursors and a subsequent treatment with $NO^•$ under the substitution of a carbonyl ligand.[345,386,408]

5.1.3.4 Reactivity of H$_{ox}$-models towards CO. Within the enzyme the active site of [FeFe]-hydrogenases is reversibly inhibited by carbon monoxide affording the **H$_{ox}$-CO** state. A similar reactivity was also observed for some of the rotated complexes with an open coordination site. Though, the eclipsed complexes typically do not exchange carbonyl ligands between both iron centres and do not interact/exchange with

1728 | *Chem. Soc. Rev.*, 2021, **50**, 1668–1784

This journal is © The Royal Society of Chemistry 2021

extrinsic CO except after photodissociation of a carbonyl ligand.[282]

The reactivity of $\mathbf{H_{ox}}$ models towards CO is governed by their stability and basicity. At -78 °C under 1 atm of CO, $\mathbf{249^+}$ does not form a stable CO adduct. However, regioselective incorporation of ^{13}CO on the rotated iron centre is observed.[361,409] The same regioselectivity for ^{13}C-exchange albeit under different conditions (5 °C, $h\nu$) is found in the active site of *D. desulfuricans*.[56] At room temperature, ^{13}CO is also incorporated into the positions on the unrotated iron centre.[361,409] The corresponding, less stable complex $\mathbf{283^+}$ with an $\mathbf{I_{MesMe}}$ ligand instead of an $\mathbf{I_{Mes}}$ ligand incorporate ^{13}CO in all positions already at -78 °C. Moreover, in addition to the fully labelled complex, a CO adduct is observed. For $\mathbf{249^+}$, $\mathbf{283^+}$ and the $\mathbf{I_{Me}}$ substituted complex $\mathbf{283'^+}$ CO adducts are formed upon increasing the CO availability by sparging solutions at -78 °C with CO. While the more stable $\mathbf{249^+}$ reacts slowly and is in equilibrium with its CO adduct, the CO adduct formation is quantitative and fast for $\mathbf{283^+}$ and $\mathbf{283'^+}$. In all cases the starting material is recovered upon exposure of the solutions to vacuum or purging with Ar/N$_2$. Notably, the CO release of $\mathbf{283^+CO}$ and $\mathbf{283'^+CO}$ is considerably slower. DFT calculations on $\mathbf{283'^+}$, supported by the EPR spectrum of $\mathbf{283^+CO}$, indicated that in both complexes the extrinsic CO does not bind to the NHC substituted iron atom (which exhibits an open coordination site in the solid state of $\mathbf{249^+}$) but to the PMe$_3$ substituted one.[361]

Complexes $\mathbf{233edt^+}$,[392] $\mathbf{235edt^+}$,[386] $\mathbf{235pdt^+}$, and $\mathbf{268P^iPr_3^+}$[345] bind CO at -45 °C within seconds/minutes. $\mathbf{235edt^+}$ releases the bound CO upon purging with N$_2$ at 0 °C, while for $\mathbf{233^+}$ removal of the CO atmosphere was reported to be sufficient. The adduct *unsym*-$\mathbf{233^+CO}$[392] formed upon the reaction of $\mathbf{233^+}$ with CO shows the same orientation (ba/ba; ap/ba) of the dppv ligands as its precursor. Upon warming a solution of *unsym*-$\mathbf{233^+CO}$ to -30 °C or if $\mathbf{233}$ is oxidised at 0 °C in the presence of CO, the symmetric adduct *sym*-$\mathbf{233^+CO}$ is formed in which both dppv ligands adopt a basal/apical orientation. This adduct of the cation of the highly basic precursor $\mathbf{233}$ and CO is significantly more stable and was crystallised from a CO-saturated solution. The crystal structure confirms the results of computational studies on $\mathbf{283'^+CO}$ and $\mathbf{233^+CO}$, that predicted a symmetric carbonyl ligand and an unusually elongated Fe–Fe distance (2.70 Å in the crystal).[361,392] The high bridging character of the carbonyl ligand in $\mathbf{233^+}$, $\mathbf{235edt^+}$, $\mathbf{235pdt^+}$ and $\mathbf{268P^iPr_3^+}$ is also reflected in the strongly low-energy shifted μ-CO bands around 1790 cm^{-1}. DFT calculations and the EPR spectrum of $\mathbf{283^+CO}$ are in accordance with a delocalisation of the spin on both iron centres, which is distinctly different from the situation in the $\mathbf{H_{ox}}$ models, but again reflects the situation in the enzyme properly.[361] Worth mentioning, Silakov, Lubitz, and coworkers also observed spin delocalisation in the $\mathbf{H_{ox}}$-CO model $\mathbf{267^+}$.[410]

The nitrosyl complexes $\mathbf{263xdt}$ and [Fe$_2$(edt)(CO)(κ^2-dppv)$_2$(NO)]$^+$ ($\mathbf{279edt}$) bind CO reversible at low temperatures. In contrast to the complexes without a nitrosyl ligand, the bridging position is occupied by a nitrosyl ligand as indicated by IR spectroscopy.[381,408] The less basic complexes $\mathbf{262xdt}$, $\mathbf{282edt}$, and [Fe$_2$(pdt)(CO)$_4$(I$_{Me}$)(NO)]$^+$ ($\mathbf{284}$) are not sufficiently

basic to form stable adducts.[381,383,408] The latter incorporates ^{13}CO, but presumably *via* a dissociative pathway.[383]

5.1.4 Rotated state models – a highlight in biomimetic modelling. While the rotated geometry of the [2Fe]$_H$-cluster is not regularly observed in model complexes, the sophisticated design of some model complexes enables the rotated geometry outside the enzyme. This finding emphasises, that the rotation is an intrinsic feature of [2Fe–2S]-clusters and not a unique enzyme-only geometry. In this context, the value of DFT calculations for biomimetic modelling aspects also becomes evident. The relevant electronic features for rotation identified by quantumchemical calculations namely electronic asymmetry, mixed-valency and strongly electron-accepting ligands (NO$^+$) are all found in synthetic models.

Though rare in Fe^{I}Fe^I complexes, the rotated geometry is accessible in asymmetrically substituted and sterically crowded models. Agostic interactions were identified as a small but crucial contribution to obtain fully rotated complexes. In contrast, mixed-valence complexes obtained by external (Fc$^+$) or internal (NO$^+$) oxidants more regularly show a rotated geometry. These complexes show limited stability and high reactivity, *e.g.* towards BF$_4^-$. Interestingly, some of these complexes do not only mimic the structure but also the reactivity towards exogenous CO and H$_2$ oxidation in terms of a PCET. Accordingly, these complexes are very powerful models of the $\mathbf{H_{ox}}$ state and make this state the most exactly represented by biomimetic modelling.

5.2 [2Fe–3S]-assemblies as H-cluster models

The introduction of a third sulphur ligand allows for more elaborate structural modelling of the active site – *e.g.* thioether coordination induces significant changes in the molecular structure.

In 2001, models with an additional sulphur donor on the dithiolate bridge were presented by the groups of Pickett[139] and Rauchfuss (Fig. 86).[169] In case of $\mathbf{50}$ and $\mathbf{285}$, the coordination of the sulphur was observed after the introduction of the dithiol (*via* the thiol route). Contrary, Rauchfuss and coworkers isolated the hexacarbonyl complex $\mathbf{84}$ (*via* the salt-elimination) and induced sulphur coordination to form complex $\mathbf{286}$ by decarbonylation with Me$_3$NO.[366–368] A reasonable explanation

Fig. 86 [2Fe–3S]-assemblies carrying a thioether on the dithiolate bridge.

for the different behaviour of the adt- and pdt-derivatives is the enforced harsher conditions (90 °C (pdt) *vs.* −78 °C to r.t. (adt)), that could induce the thioether binding. Likewise, the different alkyl linkers between the bridgehead atom and the donor atoms as well as the different bridgehead atoms themselves, led to different binding behaviour due to different strain. Similar effects are also known from complexes comprising the Si/C exchange in tripodal ligands.[411] At last, the additional methyl group on the pdt-derivate renders the coordination more favourable and a comparable trend was observed for adt^{MeBH3} *vs.* adt^{BH3} complexes and attributed to the Thorpe–Ingold effect.[175]

The additional, hemilabile donor moiety in the bridging ligand has an immense effect on the substitution behaviour of the [2Fe–3S] assemblies (Fig. 87). In contrast to the hexacarbonyl complexes, the monocyanide complex is easily isolable from the reaction of **50** with cyanide. In fact, its formation is several orders of magnitude faster than in the unsubstituted complexes. Again, the thioether moiety is coordinated to an iron centre, but IR studies revealed that the complex [Fe$_2$(κ^3-pdt^{MeSMe})-(CO)$_5$(CN)]$^−$ (**287**) is formed initially. Similar results were reported for the introduction of P(OMe)$_3$ into complex **140**.[412] Herein, the pentacarbonyl intermediate is sufficiently stable to allow for its crystallisation. For the equilibrium between the two monocyanide complexes **287** and **288**, as well as for the initial attack of **50** by a cyanide, a transition state with a bridging CO was proposed. The iron centre bearing the thioether is attacked by additional cyanide to form a metastable species **289** with a bridging carbonyl ligand. Being stable at 0 °C, the complex slowly converts to complex **267** at room temperature. With large excess of cyanide present in solution, complex **267** is directly formed from **50**.[138,139,385,413]

Complex **299** closely resembles the **H$_{ox}$-CO** state in terms of the ligand environment of the iron centre but not in their oxidation states. Through transient IR and EPR spectroscopy of the product obtained upon chemical and electrochemical

electron oxidation of **267**, formation of [Fe$_2$(pdt^{MeSMe})(μ-CO)-(CO)$_3$(CN)$_2$]$^−$ was proposed.[379] With a comparable first coordination sphere, the same spin state and very similar IR bands with respect to the **H$_{ox}$-CO** state, this complex was the first close resemblance of an actual state of the [FeFe]-hydrogenases. These spectroscopic similarities affirmed the assignment of the (unusual) oxidation states (Fe^{I}Fe^{II}) in the active site. The spectroscopically and theoretically studies on [Fe$_2$(adt^{SMe})-(CO)$_4$(L)$_2$]$^{+/−}$ (adt^{SMe} = (methylthio)ethylbis(sulfidomethyl)-amine, L = PMe$_3$, CN$^−$) further supported the suggested structure – however, comprising a bridgehead nitrogen atom as an additional detail.[280,414,415]

Notably, Tard *et al.* reported on complex **291**, representing the hitherto only complete iron-sulphur framework of the H-cluster (Fig. 88).[416] Contrary to the natural H-cluster, the [2Fe–2S]- and the [4Fe–4S]-clusters are interconnected by an organic thioether moiety instead of a cysteine residue, completing the H-cluster framework. The formal exchange of the methyl group of **50** by a [4Fe–4S]-cluster results in a downshift of the IR bands of about 15 cm$^{−1}$. Electrochemical studies revealed that the [4Fe–4S]$^{2+}$-cluster is reduced at milder potentials, than the [2Fe–2S]-cluster (compare **H$_{red}$** *vs.* **H$_{red'}$**, though the oxidation states of [2Fe]$_H$ vary). While complex **291** revealed HER activity, despite its remarkable structural resemblance with the H-cluster, further in-depth studies on this model are quite limited due to the inherent instability of the H-cluster mimic.[416–418]

In general, the electronic influence of the connection of the thioether to the dithiolate bridge is apparently small. From pdt- and adt-hexacarbonyls to the thioether substituted models **50** and **286** the highest-energy IR frequency shifts by 26 cm$^{−1}$, respectively 21 cm$^{−1}$ to lower wavenumbers.[138,139,169,288] For the diethyl sulphide substituted pdt-complex a shift of 27 cm$^{−1}$ is observed.[366] For discrete and linked metallothioethers shifts of 30 to 38 cm$^{−1}$ are reported.[178,204,209,416,419]

If the unprotected trithiol CH$_3$C(CH$_2$SH)$_3$[420] and its sila-substituted derivative[157] are reacted with triiron dodecacarbonyl,

Fig. 87 Proposed mechanism for the dicyanation of **50**.[138,139,385,413]

1730 | *Chem. Soc. Rev.*, 2021, **50**, 1668–1784

This journal is © The Royal Society of Chemistry 2021
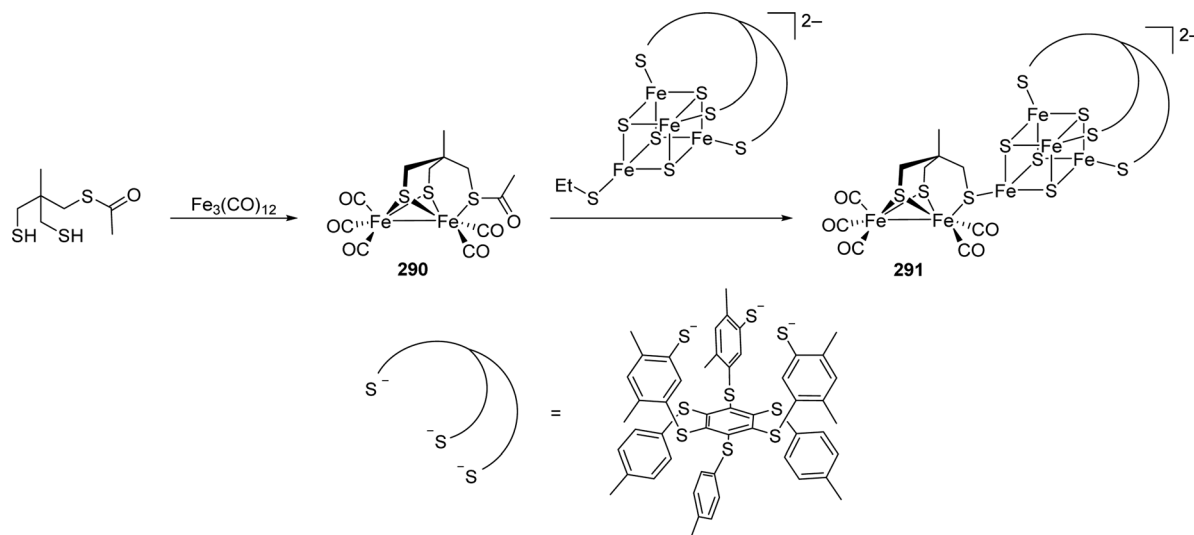
Fig. 88 Synthesis of the H-cluster model **291**.

E = C, Si **292E**

Fig. 89 Synthesis of complex **292E**.

the only isolable products are the tetra iron clusters **292E**, in which two [2Fe–2S]-units are bridged by the two thiolate arms (Fig. 89).[420–422]

All in all, as shown for **50**, an additional thioether strongly influences the reactivity of model complexes and enables the formation of the **H$_{ox}$-CO** mimic **267$^+$** with the complete first coordination sphere of the iron atoms in the enzyme.

5.3 Protonated H-cluster models

As a hydrogen forming catalyst, protonated states of the active site of [FeFe]-hydrogenases are an integral part of the catalytic cycle. Model complexes with bridging hydrides are readily formed upon protonation;[277,278,423,424] however, their relevance for the catalytic cycle was questioned and is still under discussion (Section 3.10). Terminal hydrides, though rare in mimics, are more appealing as key intermediates for rapid H$_2$ formation due to their lower reduction potential,[154] their higher hydridic character,[270] and the proximity to the amine proton shuttle by the adt-ligand.[30]

The reactivity of hydrogenase mimics towards other nucleophiles than protons and nitrosyls was also extensively studied. While giving bridged complexes for a variety of electrophiles,[425–435] terminal intermediates were reported as well.[433,434] In addition, other electrophiles, especially alkylation agents, also showed cyanide,[153,290] thiolate,[404,436] or carbonyl[53] centred reactivity as well.

5.3.1 Remarks on terminal and bridging hydrides. In terms of metal centred protonation reactions, mainly two different binding modes are observed, (apical) terminal hydrides and thermodynamically favourable bridging hydrides (Fe(μ-H)Fe). Notably, basal terminal hydrides also have been proposed as intermediates in isomerisation processes.[437] The two main binding modes are easily distinguishable by the hydride resonances in the ^{1}H-NMR spectra. Terminal hydrides cause a signal at *ca.* −5 ppm,[438] whereas bridging hydrides show resonances in a range of −12 ppm to −20 ppm.[423,424] These signals feature a characteristic coupling to the ^{31}P nuclei of phosphine ligands. In the case of terminal hydrides, strong coupling ($J_{PH} \approx$ 75 Hz chelating phosphines, 50 to 100 Hz monodentate) to phosphines ligated to the same iron centre is detected,[154,210,320,336,438] while bridging hydrides couple to phosphines in basal positions on both iron centres ($J_{PH} \approx$ 25 Hz) and only weakly (5 Hz) to the apical phosphines.[277,278,423,424,438] Protonation of the iron core to give hydrides is accompanied by an average upshift of the IR bands by 60–110 cm^{-1}.[140,150,153,278,363]

It is worth to mention that in the case of terminal hydrides, a μ-CO band is detected.[438] The spectroscopic properties of many protonated complexes have been summarised by Tschierlei *et al.* and we would like to direct the reader to this review for more detailed information.[439]

The structure of the bridging hydride complexes is very similar to the unprotonated complexes. The metal–metal distance is only slightly elongated (0.02 Å to 0.05 Å) upon protonation despite the loss of the Fe–Fe bond. In the face-sharing octahedrons the iron atoms are less displaced from the equatorial S$_2$(CO)L planes compared to the displacement form the basal plane in the neutral complexes.[153,277,278,440,441] Importantly, the high fluxionality of the FeL$_3$ units is lost upon protonation consistent with higher site exchange barriers in the octahedral coordination environment.[153,278]

5.3.2 Iron-centred protonation of H-cluster models. The hexacarbonyl complexes are not basic enough to be protonated

by strong acids, *e.g.* HBF$_4$·Et$_2$O, but require harsh, super-acidic conditions (*e.g.* [SiEt$_3$][B(C$_6$F$_5$)$_4$] + HCl$_{(g)}$).[277,278,442,443] Contrary, the electron-donating abilities of a thioether in **50** are sufficient to allow for its protonation by HBF$_4$·Et$_2$O in dichloromethane.[140,444] In addition, protonation of dicyanide complexes gives several complexes with resonances corresponding to bridging hydrides in the ^{1}H-NMR spectrum, but cyanide ligand protonation and their intrinsic instability render these complexes unsuitable for protonation studies.[277–279] However, the pdt dicyanide complex **212** reduced protons from strong acids under decomposition to sub-stoichiometric amounts of dihydrogen.[279] Using only a small excess of acid, Pickett and coworkers were able to reveal the protonation process and suggested an initial protonation of the cyanide ligand with a subsequent rearrangement to afford a bridging hydride.[324,325] Notably, protection of the cyanides by boranes allows for the formation of stable protonated species bearing a bridging hydride.[290] The formal exchange of one cyanide ligand by PMe$_3$ to give the complex [Fe$_2$(pdt)(CO)$_4$(CN)(PMe$_3$)]$^-$ (**214**) also allows for the isolation of a stable bridging hydride, while the corresponding P(OMe)$_3$ complex and the unsubstituted monocyanide are protonated at the cyanide. For the phosphine and the phosphite complex double protonation is observed with very strong acids.[150,153]

Stable diphosphine complexes with bridging hydrides are known since the 1970s from early studies by Poilblanc, Mathieu and coworkers.[423,424,440] The protonation of Fe$_2$(pdt)(CO)$_4$-(PMe$_3$)$_2$ (**219pdt**) gave the first and representative example for a bridging hydride [**219pdt-μH**]$^+$ with a dithiolate bridge (Fig. 90).[277,278] Subsequently, stable bridging hydrides were obtained by protonation of a variety of electron-rich cofactor mimics.[270,278,326,342,353–355,445,446] The protonation behaviour of diphosphine bridged complexes Fe$_2$(pdt)(CO)$_4$(μ-diphosphine) shows remarkable dependence on the nature of the diphosphine. While the complexes with electron-poor, small-bite-angle phosphines dppm, dppe and (Ph$_2$P)$_2$NR are sluggishly protonated to give unstable bridging hydrides, complexes with the electron-rich

dcpm and the more flexible chelating phosphines form stable bridging hydrides.[326,342,353,354]

Bridging hydride complexes are either not, or only slowly deprotonated by amine bases.[278,283,342] However, the less basic but smaller chloride ion deprotonates bridging hydrides and can also increase the deprotonation rate by amine bases when added sub-stoichiometrically (Fig. 93).[278,283,447]

Protonated disubstituted phosphine and isocyanide complexes enable H/D exchange reactions between D$_2$, D$_2$O, alkenes, and Fe(μ-H)Fe under photolytic conditions. The reaction was proposed to proceed after dissociation of a carbonyl ligand, or a hydride shift to a single iron centre to provide a binding site for the substrate. This assumption is supported by the inhibition of the scrambling reactions by CO, acetonitrile, and in the case of D$_2$/D$_2$O by alkenes.[277,278,355,404]

After the first detection in the electrocatalytic proton reduction with a [2Fe–2P]-complex,[448] the first terminal hydride [**216edt-tH**]$^+$ observed in a [2Fe–2S]-complex was synthesised in 2005 by Rauchfuss and coworkers.[438] In contrast to earlier studies, the complex was prepared by addition of a hydride source to the diferrous complex [Fe$_2$(edt)(CO)$_2$(PMe$_3$)$_4$(MeCN)]-(PF$_6$)$_2$ ([**274edt**]$^{2+}$, Fig. 90). At low temperatures (−25 °C), this reaction yields a terminal hydride that was studied by NMR and IR spectroscopy and structurally characterised by X-ray diffraction. The isomerisation to the favourable bridging hydride [**216edt-μH**]$^+$ occurs slowly at these temperatures (as well as in the solid state) but proceeds rapidly at room temperature. Notably, the corresponding complex with only three phosphine ligands showed no terminal hydride complex. Complexes [**216xdt-tH**]$^+$ are also accessible by protonation of the corresponding complexes **216xdt**.[320] The protonation of the edt and pdt analogues yields a mixture of bridging and terminal hydrides, while the protonation of **216adt** only yields the terminal hydride. Though the terminal hydrides [**216xdt-tH**]$^+$ isomerise to the bridging hydrides [**216xdt-μH**]$^+$ at room temperature, terminal hydrides are no intermediates in the initial formation of the bridging hydride in the case of the edt

Fig. 90 Schematic structure of typical hydride complexes and their precursors.

X = -   **219edt**
X = CH$_2$ **219pdt**
X = NBn **219adt^{Bn}**

274^{2+}

X = -   **216edt**
X = CH$_2$ **216pdt**
X = NH **216adt**

X = -   [**219edt-μH**]$^+$
X = CH$_2$ [**219pdt-μH**]$^+$
X = NBn [**219adt^{Bn}-μH**]$^+$

X = -   [**216edt-tH**]$^+$
X = CH$_2$ [**216pdt-tH**]$^+$
X = NH [**216adt-tH**]$^+$

X = -   [**216edt-μH**]$^+$
X = CH$_2$ [**216pdt-μH**]$^+$
X = NH [**216adt-μH**]$^+$

1732 | *Chem. Soc. Rev.*, 2021, **50**, 1668–1784

This journal is © The Royal Society of Chemistry 2021

and pdt complexes. For the initial formation of the bridging hydride an intermolecular reaction from an S-protonated intermediate was proposed. Interestingly, [**216edt**-tH]$^+$ releases hydrogen upon treatment with strong acids, which is not always observed for terminal hydrides, *e.g.* [**216adt**-tH]$^+$ and [HFe$_2$(pdt)(CO)$_2$(κ^2-dppe)$_2$]$^+$ ([**233pdt**-tH]$^+$) and generally not observed for bridging hydrides.[320,438,449]

In contrast to the symmetric complexes **216xdt** and **219xdt** (xdt = edt, pdt),[320,324,325] terminal hydrides were proposed to be intermediates in the protonation of the asymmetric complexes Fe$_2$(xdt)(CO)$_4$(κ^2-L) (κ^2-L = dppe, dmpe, dppv, phen, bis(NHC), NHC–PPh$_3$; xdt = edt, pdt), Fe$_2$(pdt)(CO)$_3$(PMe$_3$)(κ^2-dppv), as well as in the sterically demanding complexes Fe$_2$(xdt)(CO)$_2$(κ^2-dppv)$_2$ (xdt = edt, pdt, adt, odt).[154,210,336,340,363,372,437,450] In contrast, the protonation of Fe$_2$(xdt)(CO)$_4$(κ^2-dppp)[342] at −70 °C mainly yields bridging hydrides and for Fe$_2$(edt)(CO)$_{4-x}$(PMe$_3$)$_x$(κ^2-dppv) (x = 0, 1)[437] no terminal hydride is observed. Not only the dithiolate bridge but also the strength of the acid were reported to influence the occurrence of terminal hydride intermediates.[373,451] Admittedly, especially in cases where bridging hydrides isomerise quickly, distinguishing between a terminal hydride as a necessary intermediate and a terminal hydride as a (side) product that isomerises quickly is not trivial and requires elaborated experiments.

While the asymmetric terminal hydride complexes isomerise quickly at low temperatures (−30 °C to −90 °C),[336,340,363,372,437] the sterically crowded terminal hydrides [HFe$_2$(xdt)(CO)$_2$(κ^2-dppv)$_2$]$^+$ [**233xdt**-tH]$^+$ are reasonably stable at −20 °C.[154,210,437] Unintuitively, protonation of the less electron-rich Fe(CO)$_3$ unit in the asymmetric complexes is regularly observed under these conditions.[336,340,363,437] A stable terminal hydride was reported for (Cp*)Fe(pdt)(μ-CO)Fe(κ^2-dppe)H (**293**-tH), which only isomerises upon oxidation. Interestingly, the corresponding reduced bridging hydride partially isomerises to the terminal hydride – a process which is not observed for any other bridging hydride in context of hydrogenase mimics (Fig. 91).[452]

Fig. 91 Redox-Isomerisation of the terminal hydride [**293**-tH].

5.3.3 Influence of adjacent amines on the protonation of H-cluster models.
The formal exchange of the bridgehead atom from pdt- to the basic adt-complex has, in contrast to the small influence on electronic and structural properties, an enormous influence on the protonation behaviour of hydrogenase mimics. Experimental observations highlight the advantages of the unique adt-ligand for the reversible proton reduction and, in this context, the relevance of nature's choice for the adjacent amine becomes obvious.

The adt^R amine is protonated by strong acids (*e.g.* HOTf, HBF$_4$/Et$_2$O),[151,168,177,183,196,203,346,354,447,453–459] while weaker acids (*e.g.* CF$_3$COOH, HOAc) are not sufficiently acidic to protonate the hexacarbonyl complexes in organic media.[195,343,460] Electron donating ligands on the iron core were reported to increase the basicity of the amine and allow for protonation with weaker acids,[210,320,451,459] while some hexacarbonyl complexes are only partially protonated by triflic acid or deprotonated in neutral solution.[454,459] Amine-functionalised phosphines show a similar protonation behaviour as the adt-bridge.[152,302,303,350–352,461] In the IR spectrum of the N-protonated complexes, the bands are shifted by *ca.* 15 cm^{-1} under retention of the band structure.[459] The reversibility of the N-protonation was demonstrated with amine bases.[151,183,350,453–455] In electron-rich complexes bearing an adjacent amine, metal centred protonation is likewise observed. Importantly, in some cases the corresponding complexes lacking the amine are very slowly protonated or are only protonated by stronger acids.[210,320,351] In accordance with similar basicities, this effect is attributed to reduced kinetic barriers and is crucial for rapid H$_2$ formation.[154,210,350,351] Due to two basic sites, the protonation behaviour of these mimics can be complex and is affected by several parameters. While in some cases the amine only facilitates the protonation of the iron centre by decreasing the kinetic barrier and itself remains unprotonated,[154,462] mixtures of N- and Fe-protonated species[152,350,351] as well as solely N-protonated complexes were obtained.[151,447,455,459] The latter is observed if the amine is not in proximity to the site of metal protonation and can represent a metastable intermediate that slowly coverts to the bridging hydride.[151,455,459] This tautomerization can be accelerated by chloride.[455,459] Still, in some cases metal protonation is not observed at all.[447,463] Both amine and iron can be the more basic site and accordingly be the thermodynamically favourable site for protonation. If the basicities of both sites are similar, the equilibrium between the ammonium and the hydride tautomer is influenced by the solvent,[152,154,351,451] the used acid/counterion,[351,451] and the basicity of the amine.[225,352]

In general, more polar solvents stabilise the ammonium tautomer as well as the ability of the counterion to form hydrogen bonds. With strong acids double-protonated species are accessible, where the hydride can occupy a terminal or a bridging position.[151,154,320,447,451,455] It was shown that decreasing the basicity of the amine in Fe$_2$(pdt)(CO)$_4$((Ph$_2$PCH$_2$)NR) (**294R**) from **294Me** to **294Ph** is sufficient to prevent double-protonation by triflic acid (Fig. 92). This behaviour exemplifies the high acidity of the double-protonated complexes, which are sensitive to weak bases *e.g.* methanol, water or even

This journal is © The Royal Society of Chemistry 2021

Chem. Soc. Rev., 2021, **50**, 1668–1784 | 1733
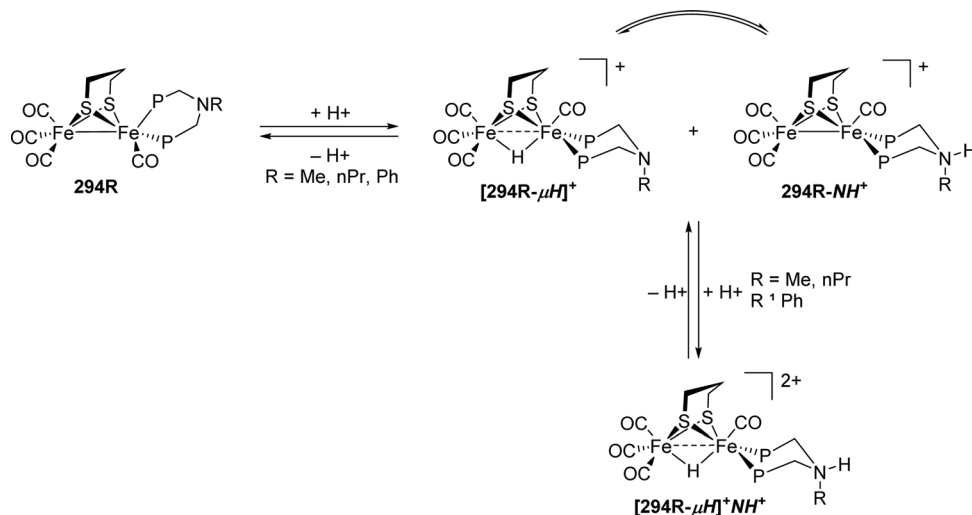
Fig. 92 Protonation and deprotonation pathways of the complexes **294R**.
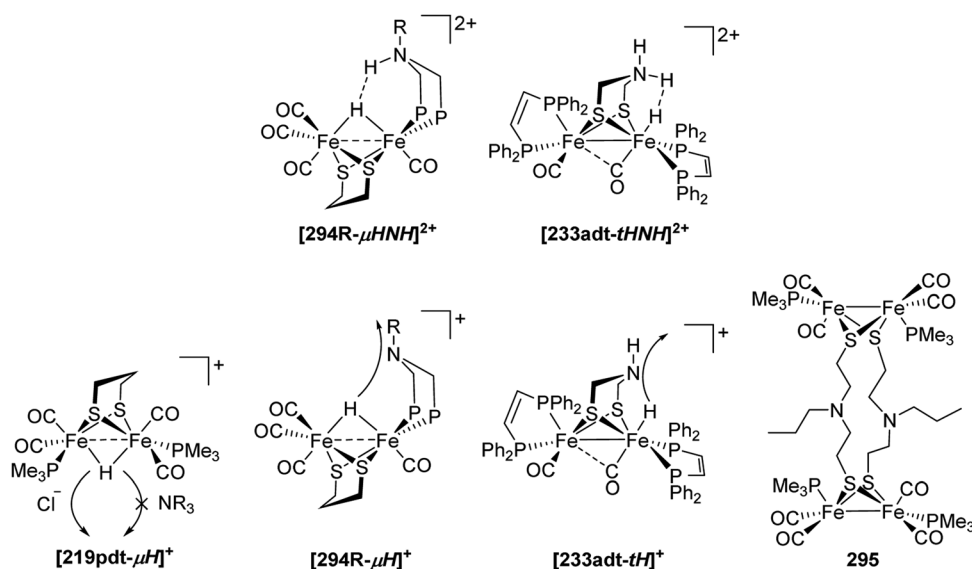
Fig. 93 Top: H−H interaction in double-protonated complexes. Bottom: Deprotonation of hydride complexes and structure of complex **295** (Note: P = PPh$_2$ in **294R**).

acetonitrile.[151,154,320,454,455] By NMR spectroscopy and single-crystal XRD hydrogen–hydrogen interactions were suggested in these complexes (Fig. 93).[351,451]

The deprotonation of the ammonium proton is typically fast, while the deprotonation rate of the hydride is dependent on the structure of the complex and the base used. In the complexes [**294R**-μH]$^+$ and [**233adt**-tH]$^+$ where the amine is in close proximity to the hydride, the deprotonation of the hydride can be accomplished with amine or phosphine bases (Fig. 93). The formal exchange of the NH groups by CH$_2$ groups prohibits any deprotonation,[210,351,464,465] while an oxygen atom showed a decreased, yet existent proton relay ability.[210] In the case of **295** (Fig. 93), the iron protonated tautomer is metastable and rearranges to the N-protonated tautomer. If the hydride and the amine are spatially separated, the amine does not function

as a proton relay and deprotonation by amine bases is prohibited.[151,455] However, selective deprotonation by chloride was reported to be efficient.[447]

To emphasize the importance of the adjacent amine, we briefly summarize the different reactivities of the complexes shown in Fig. 94. The initial product of the protonation of **219adt** is the ammonium salt and not the bridging hydride as for **219pdt**[151,277,278,324,325,455] and in contrast to **294R**, **294C** is only protonated by H(Et$_2$O)BF$_4$ if used in large excess.[342,351] While the protonation of **216adt** and **233adt** is feasible with medium strength acids as ammonium or phosphonium salts, the protonation of their pdt analogues requires strong acids.[210,320] Accordingly, in the cases where the protonation site is in close proximity to the amine (**216adt**, **233adt**, **294R**), the protonation rate of the iron centre is accelerated. The same

1734 | *Chem. Soc. Rev.*, 2021, **50**, 1668–1784

This journal is © The Royal Society of Chemistry 2021
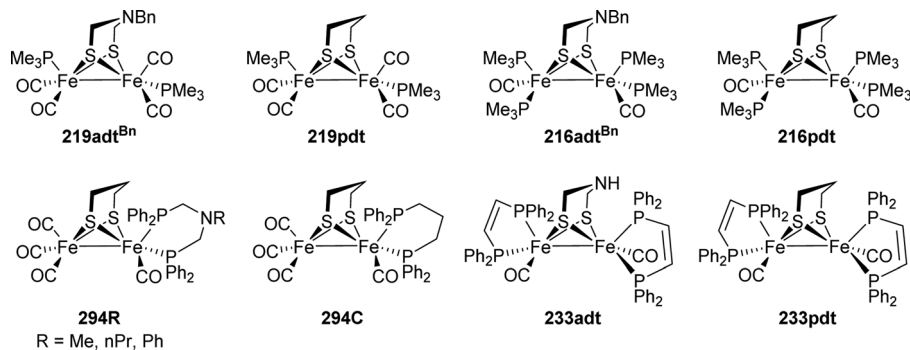
Fig. 94   Exemplary complexes, whose reactivity towards protons is strongly altered by the adjacent amine.

was observed for the deprotonation of the terminal hydride in [**233adt**-tH]$^+$ and the bridging hydride in [**294Me**-μH]$^+$, but not for [219adt-μH]$^+$, where the bridging hydride and the amine are spatially separated.[210,351,455] At last, all amine containing complexes except from **294Ph** allow for double-protonation to give a complex bearing an ammonium proton and a hydride.

5.3.4   Significance of the adjacent amine revealed by protonation studies. Protonation of electron-rich [2Fe]$_H$-mimics efficiently yields bridging hydrides accompanied by very small changes in the geometry of the [2Fe–2S]-core. However, their reactivity along with spectroscopic features on the enzyme questioned their relevance for rapid H$_2$ formation. The more relevant terminal hydrides are formed as intermediates or metastable products both converting to the thermodynamically more stable bridging hydrides. In protonation experiments, the adjacent amine proved crucial for rapid proton transfer to and from the metal centre as well as for protonation with weak acids. These findings highlight the importance of the unprecedent adt-bridging ligand for the activity of the enzyme and fully explain the loss of activity upon incorporation of bridgehead-altered [2Fe]$_H$-models.

VI Electrochemistry of H-cluster models – redox and catalytic properties

6.1   Redox chemistry of H-cluster models

Due to the mild potentials at which the native enzyme operates the hydrogen conversion/formation, models of its active site were extensively studied as noble-metal-free catalysts for the hydrogen evolution reaction. In order to evaluate potential catalysts, the redox behaviour of numerous complexes described in the previous sections was intensively investigated. In general, the interplay of the reduction potentials and the basicity of these clusters heavily influences the proton-coupled electron transfer processes that are crucial for HER.

Before describing the electrocatalytic capabilities of the active site models to serve as potent HER catalysts and the specific mechanisms involved, a short discussion on the non-catalytic redox behaviours of the diiron subsite models is advisable. Subsite models are generally in the Fe^{I}Fe^I resting state and undergo reversible or quasi-reversible (stepwise)

reductions. Therefore, the complexes act as precatalysts and form the actual catalyst upon reduction. In the anodic scan, the mimics commonly display a one-electron oxidation resulting in a Fe^{II}Fe^I state followed by another electron oxidation resulting in a Fe^{II}Fe^{II} state. Herein the four most discussed complexes *i.e.* Fe$_2$(pdt)(CO)$_6$, Fe$_2$(adt)(CO)$_6$, Fe$_2$(odt)(CO)$_6$ and Fe$_2$(sdt)(CO)$_6$ will be considered. However, the oxidation only plays a minor role in the chemistry of hydrogenases and we will thus mainly focus on their reduction properties. In the following, all given potentials are referenced *versus* the ferrocene/ferrocenium couple if not otherwise specified.

Fe$_2$(pdt)(CO)$_6$ (**20**) displays a quasi-reversible single-electron reduction at $E_1 = -1.74$ V (-1.34 V *vs.* NHE) in MeCN and a second irreversible reduction is observed at a more negative potential of -2.35 V (-1.95 V *vs.* NHE).[466] Notably, the reduction potential (E_1) for **20** has been reported with an averaged value of -1.66 V.[283,289,302,317,329,367] The azadithiolate model Fe$_2$(adt)(CO)$_6$ (**2**) is reduced from a Fe^{I}Fe^I to a Fe^{I}Fe^0 state at -1.58 V.[170] This value is slightly less negative than the reduction potential of **20**, which is reasonable due to the higher electronegativity of nitrogen compared to carbon and therefore a decreased electron density at the diiron core. Likewise, Fe$_2$(odt)(CO)$_6$ (**136**) undergoes a single-electron quasi-reversible reduction at -1.59 V and a further irreversible reduction at -2.1 V.[204] Furthermore, the sulphur analogue Fe$_2$(sdt)(CO)$_6$ (**139**) is reduced to the Fe^{I}Fe^0 stage at -1.51 V followed by reduction at -1.94 V to the Fe^{0}Fe^0 state.[211] Thus, the bridgehead atom exerts only a small influence on the non-catalytic reduction behaviour of these models. Comparatively, models with aromatic thiolate linkers, especially Fe$_2$(bdt)(CO)$_6$ (**149**), are reduced at milder potentials (about -1.3 V).[221,467,468] The reduction comprises two overlapping single-electron processes. It is worth mentioning that the reduction of **149** proceeds with structural changes wherein one of the Fe–S bonds is cleaved, and a CO ligand transforms from a terminal to a bridging position. This geometric transformation causes a potential inversion, making the second reduction more feasible than the first one (Fig. 95).[468–471]

6.2   Influence of modified thiolate bridges on the redox behaviour of H-cluster models

A common method to alter the redox-properties of metal centres is manipulation of their ligand environment and hence
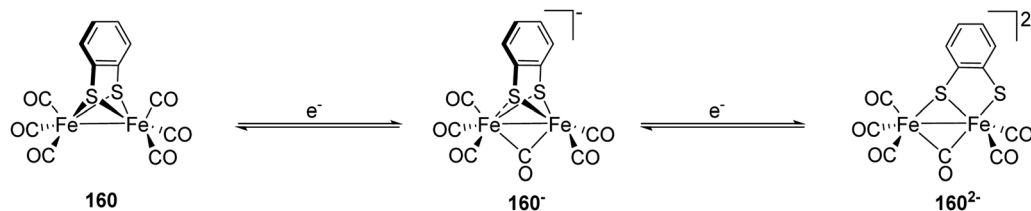
Fig. 95 Scheme depicting the reduction of $Fe_2(bdt)(CO)_6$ based on spectroscopic data and DFT studies.[470–472]

their electron density, which influences thermodynamics and kinetics of the redox-event. For C_2-substituted $Fe_2(pdt)(CO)_6$-like models, the inductive effect of the substituent is therefore decisive for the potential shift. Alkyl chains, that exhibit a +I effect, are expected to negatively shift the reduction potential due to the increasing electron density. However, models $Fe_2((SCH_2)_2CR_1R_2)(CO)_6$ ($R_1 = R_2 = Me$ (**296**); $R_1 = R_2 = Et$ (**297**); $R_1 = Et$, $R_2 = Bu$ (**298**)), bearing methyl-, ethyl- or butyl-groups at the bridging position, undergo the first reduction at -1.61, -1.67 and -1.64 V, respectively.[473] These values are within the reported range for the reduction of **20**. Thus, inductive effects of alkyl-substituents at this specific position can be neglected. Contrary, substituents bearing an electron withdrawing group, should direct the reduction potential to more positive values due to the decreased electron density. Here, especially ketons,[137] carboxylates[133,137,141] and alcohols[134–136,474] are present in literature. For example, complexes **35** and **38** are functionalized by a hydroxy group in C_2 position and can be reduced at -1.61 and -1.60 V, respectively. Compared to the alkyl-substituted PDT-models and unsubstituted **20**, the reduction potential is barely shifted to more positive values, which again shows the limited influence of inductive effects at the C_2-position.[134,135] The same is true for ester bearing models **38**, **43c** and **43d** that show a reduction potential of approx. -1.59 V.[133,137] The strongest shift in reduction potential (-1.53 V) is observed for model **39**, which however, has kinetic reasons since the reduced state of this model is stabilized by an intermolecular H-bond between the hydroxy group and the reduced iron centre.[136] These few examples show that the influences of C_2-substituents on the reduction potential of $Fe_2(pdt)(CO)_6$-like models is generally low and highlights the electronic remoteness of this position within the mimics.

Along this line, substituted azadithiolate models likewise possess reduction potentials between -1.49 V to -1.59 V (Section 6.5.2). Contrary to the pdt-models, more pronounced shifts in the reduction potential are observed upon modifying the mimics at the nitrogen atom. For example, alkyl substituted models are generally reduced at more cathodic potential (-1.63 V to -1.68 V).[182,186,190] Furthermore, strongly electron withdrawing systems attached to a phenyl-ring such as in $Fe_2(adt^R)(CO)_6$ ($R = p$-$C_6H_4NO_2$, **120**) cause a reduction potential shift to -1.42 V.[194]

In contrast to $Fe_2(pdt)(CO)_6$ and $Fe_2(adt)(CO)_6$ models, the aryl-substituents of $Fe_2(bdt)(CO)_6$ have a severe influence on the redox potentials of the hydrogenase mimics (Section 6.5.6).[222,228,232,239,240,242] Notably, bdt-models comprising

ligands with +I effect are rare in literature and show only slightly increased electron density at the diiron centre. Complex **153** is a good example for such a system and possesses a single methyl group in m/p-position. The complex shows a reduction potential of -1.37 V compared to -1.36 V for **149**.[222] Attachment of electron withdrawing groups, especially chlorides, reduce the electron density at the diiron core to a significant extent. The most prominent effect can be observed in **152** with a *per*-chlorinated benzene ring and exhibits a reduction potential of -1.13 V in MeCN.[226] Moreover, models with N-heterocyclic substituents (*e.g.* 2,3-quinoxalinedithiolate) are more conveniently reduced owing to the decreased electron density on the diiron centre due to the electron withdrawing N-substituted aryl rings (Section 6.5.6).[222,228,229]

In contrast to $Fe_2(bdt)(CO)_6$ and its analogues, 1,8-naphthalenedithiolate models mainly undergo two single-electron reductions (Section 6.5.7).[239,242,244,247,251] The first reduction usually occurs at -1.52 V, which is approx. 200 mV more negative compared to $Fe_2(bdt)(CO)_6$.[239] Electron density manipulating groups alter the redox potential in the same way as described above for bdt-derivatives but to a somewhat lesser extent.

The biphenyl[475] as well as the *o*-carborane[476] modified Fe_2S_2 complex also undergoes two successive single step electron reductions. Moreover, due to the delocalisation of the negative charge on the aromatic ring and rigidity of the naphthalene-linker these models prove to generate more stable reduced states. In addition, the phenanthrene-4,5-dithiolate-bridged compound **182** is reduced at more positive potentials due to the enhanced electron delocalization of the phenanthrene system.[240]

Despite of the increased electron density at the diiron centre in chalcogenide-substituted complexes, anodically shifted reduction potentials upon sulphur to chalcogenide exchange were observed (*e.g.* **39** *vs.* **40**).[133,136,145,146,204,205,211,239,240,251,477] This positive shift is overall < 50 mV and can be rationalised by the improved stabilization of the reduced species. Furthermore, Weigand and coworkers further reported decreasing reorganization energies for the reduction to a Fe^IFe^0-species within the S, Se and Te series that partially counteracts the trend of increasing electron density at the diiron centres.[146]

In contrast, $Fe_2((ECH_2)N$-p-$C_6H_4R)(CO)_6$ derivatives show almost no shift in the reduction potentials for the respective selenium containing models ($R = H$, $E_{128} = -1.57$ V *vs.* $E_{128} = -1.58$ V; $R = NO_2$ $E_{130} = -1.48$ V *vs.* $E_{120} = -1.49$ V).[198] Along this line, it is worth to mention that the reduction of **2** (adt) and **96**

(adSe) occurs at almost same potentials of approx. -1.2 V *vs.* SHE.[32] Thus, the experimentally observed shifts are depending on the interplay of the electron density modulating properties of the headgroup and the chalcogenide as well as the counteracting change of reorganisation energies for the reduction.

6.3 Influence of CO-ligand substitution on the redox behaviour of H-cluster models

While the carbonyl to cyanide replacement aims at replicating systems that resemble the natural subsite more closely, the complicated electronic behaviour of the cyanide restricts their investigations; in this regard many studies adopted phosphines and carbenes as non-native ligand systems. Herein, it is necessary to highlight that the redox behaviour of the metal centres are considerably affected by the nature of the binding ligand as the LUMO has major contributions of metal–metal and metal–ligand anti-bonding orbitals.[138]

6.3.1 Cyanide and isocyanide substituted models. The first irreversible reduction of the dianionic dicyanide model $[Fe_2(pdt)(CO)_4(CN)_2]^{2-}$ (**212**) takes place at -2.73 V and the irreversible oxidation takes place at -0.51 V.[289] Contrarily, $[Fe_2(pdt)(CO)_5(CN)]^-$ (**213**) displays its first irreversible reduction at -2.17 V and the oxidation takes place at $+0.13$ V.[283] Therefore, compared to $Fe_2(pdt)(CO)_6$ (**20**), successive CO to CN^- exchange causes a 0.51 V to 0.59 V cathodic shift of E_{pc} due to the increasing electron density at the metal centres owing to the strong electron donating nature of the CN^- ligand and thereby making them harder to reduce.[138,283,289,478] Replacement of CN^- ligands with weaker electron donating ligands such as methyl isocyanide results a moderate ΔE_{pc} of -0.15 V upon single CO-replacement. Along this line, the second substitution proceeds with a further shift of -0.27 V.[283]

6.3.2 Phosphine or phosphite substituted models. As a general trend, the replacement of one CO ligand by a phosphine or phosphite results in cathodic shifts of the reduction potential E_{pc} of about 0.12 to 0.3 V. Herein, the electron density at the metal centre is severely increased due to σ-donation and decreased back donation of the phosphine or phosphite.[121,170,195,215,222,229,317,473,479–481] Comparing PPh_3 and PMe_3 substituted mimics, the former are reduced at less cathodic potentials (Table 7), which can be attributed to the weaker electron donating capability of the PPh_3 ligand.[170,302,317] Notably, when a second CO ligand is replaced, E_{pc} further shifts by approx. 0.2 V to 0.46 V to more negative

potentials.[170,182,191,195,317,454,479] Thus, the second ligand exchange results in in case of two PMe_3 ligands (**219pdt**) in a reduction potential of -2.31 V, which is notably 0.4 V less negative as for **212**. In case of monosubstituted phosphine models of **149**, the cathodic scan shows a stepwise two-electron reduction at more cathodic potentials, *e.g.* approx. 0.2 V for a single PPh_3 ligand in acetonitrile and contradicts the concerted two-electron transfer found in the hexacarbonyl complexes. This behaviour was reasoned by slower electron transfer kinetics of the monoanion in the substituted models.[229,480,482]

The alteration of E_{pc} for chelating phosphine ligands is comparable to the shifts observed for mimics possessing two monodentate phosphines.[130,328,338,479] For example, the reduction potential of $Fe_2(pdt)CO_4(\kappa^2\text{-dppe})$ (**232pdt**) is with -2.33 V similar to that of $Fe_2(pdt)CO_4(PMePh_2)_2$ (**299**) with -2.30 V. Likewise, analogues with bridging phosphine ligands reveal comparable reduction potentials as their chelating counterparts.[130,328,338]

6.3.3 NHC substituted models. Much like phosphine substituted complexes, carbene substituted models show similar trends, *i.e.* cathodic shifts of the reduction potential. However, the influence of the carbene ligand is much stronger than reported for phosphines.[197,291,361,362,364,473] Herein, upon each CO to NHC exchange, potential shifts of up to 0.44 V are observed. For example, the E_{pc} of $Fe_2(pdt)(CO)_{6-n}(IMe)_n$ ($n = 1$ (**300**), 2 (**247**)) is observed at -2.06 V and -2.47 V, respectively, and is thus more cathodic as compared to the phosphine (PMe_3) analogues (**218pdt** & **219pdt**) that exhibit the respective reduction signals at -1.94 V and -2.31 V.[291,302] Aromatic *N*-substituents at the imidazole result in less negatively shifted reduction potentials of the respective mono-substituted complexes, *e.g.* -2.01 V in the IMes ligand. Interestingly, the potential change caused by the IMe and IMes ligand, is smaller than the difference observed for PPh_3 *vs.* PMe_3 substituted compounds. This difference shows that the effect of the additional substituents of imidazole based NHCs is not as significant as in phosphines (Table 8). As found for IMes substituted complexes, furan and pyridine modified disubstituted carbene models are reduced at potentials 0.95 V more cathodic than the hexacarbonyl models.[197]

6.3.4 Models substituted with other ligands. The natural [2Fe–2S]-cofactor is not only coordinated by two cyanide and four CO ligands, but also linked to the [4Fe–4S]-cluster *via* a cysteine that forms a thioether with the cubic cluster. Therefore,

Table 7 $E_{pc}(Fe^IFe^I/Fe^IFe^0)$ of phosphine/phosphite-substituted models

Complex	Ligand	$E_{pc,mono}$ [V] $n = 1$	$E_{pc,di}$ [V] $n = 2$	ΔE *vs.* CO [V]	Ref.
$Fe_2(pdt)(CO)_6$		-1.66			215, 283, 289, 302, 317, 329 and 367
$Fe_2(pdt)(CO)_{6-n}(L)_n$	PMe_3	-1.94	-2.31	0.28, 0.37	221, 467 and 468
$Fe_2(pdt)(CO)_{6-n}(L)_n$	PMe_2Ph	-1.90	-2.30	0.24, 0.40	283
$Fe_2(pdt)(CO)_{6-n}(L)_n$	PPh_3	-1.84		0.18	291
$Fe_2(pdt)(CO)_{6-n}(L)_n$	$P(OEt)_3$	-1.81	-2.27	0.15, 0.46	473
$Fe_2(pdt)(CO)_{6-n}(L)_n$	$P(OMe)_3$	-1.98	-2.30	0.32, 0.32	473
$Fe_2(pdt)(CO)_{6-n}(L)_n$	PTA	-1.94	-2.14	0.28, 0.20	473
$Fe_2[(SCH_2)_2(NH)](CO)_6$		-1.58			473
$Fe_2(adt)(CO)_{6-n}(L)_n$	PMe_3	-1.88		0.30	170
$Fe_2(adt)(CO)_{6-n}(L)_n$	PPh_3	-1.70		0.12	170

This journal is © The Royal Society of Chemistry 2021

Chem. Soc. Rev., 2021, **50**, 1668–1784 | **1737**

Table 8 $E_{pc}(Fe^IFe^I/Fe^IFe^0)$ of carbene, cyanide and isocyanide-substituted models

Complex	Ligand	$E_{pc,mono}$ [V] $n = 1$	$E_{pc,di}$ [V] $n = 2$	ΔE vs. CO [V]	Ref.
$Fe_2(pdt)(CO)_{6-n}(L)_n$		−1.66			215, 283, 289, 302, 317, 329 and 367
$[Fe_2(pdt)(CO)_{6-n}(L)_n]^{n-}$	CN^-	−2.17	−2.72	0.51, approx. 0.55	221, 467 and 468
$Fe_2(pdt)(CO)_{6-n}(L)_n$	CNMe	−1.81	−2.08	0.15, 0.27	283
$Fe_2(pdt)(CO)_{6-n}(L)_n$	IMe	−2.06	−2.47	0.40, 0.41	291
$Fe_2(pdt^{Me})(CO)_6$		−1.61			473
$Fe_2(pdt^{Me})(CO)_{6-n}(L)_n$	IMes	−2.01		0.40	473
$Fe_2(pdt^{Et})(CO)_6$		−1.67			473
$Fe_2(pdt^{Et})(CO)_{6-n}(L)_n$	IMes	−2.02		0.35	473

Table 9 $E_{pc}(Fe^IFe^I/Fe^IFe^0)$ and $E_{pa}(Fe^IFe^I/Fe^{II}Fe^I)$ of **50** and **285** and their respective cyanides[138]

Complex	E_{pc} vs. SCE (vs. Fc$^{+/0}$) [V]	E_{pa} vs. SCE (vs. Fc$^{+/0}$) [V]
$Fe_2(pdt^{MeSMe})(CO)_5$	−1.38 (−1.78)	+0.67 (+0.27)
$Fe_2(pdt^{MeSBn})(CO)_5$	−1.36 (−1.76)	+0.77 (+0.37)
$[Fe_2(pdt^{MeSMe})(CN)(CO)_4]^-$	−1.83 (−2.23)	+0.17 (−0.23)
$[Fe_2(pdt^{MeSBn})(CN)(CO)_4]^-$	−1.83 (−2.23)	+0.12 (−0.28)
$[Fe_2(\mu-CO)(pdt^{MeSMe})(CN)_2(CO)_3]^{2-}$	−2.40 (−2.83)	−0.10 (−0.03)
$[Fe_2(pdt^{MeSMe})(CN)_2(CO)_4]^{2-}$	−2.40 (−2.83)	−0.25 (−0.65)
$[Fe_2(pdt^{MeSBn})(CN)_2(CO)_4]^{2-}$	−2.40 (−2.83)	−0.26 (−0.66)

thioether and sulphoxide substituted models were synthesized to mimic the properties of the native cysteine.[138,139,367] Thioethers generally were shown to cause cathodic shifts of up to 100 mV for the reduction of Fe^IFe^I (Table 9). Contrary, sulphoxides induced no noteworthy shift of the respective potential due to the competing inductive effects of the oxide and alkyl chains.[367] Along this line, the incorporation of a strong electron accepting ligand, such as NO^+, lead to a 1 V cathodic shift of E_{pc} as compared to the related hexacarbonyl complexes.[150,153,381]

6.4 Remarks on the electrochemical oxidation of H-cluster models

As described above, the electron donating capabilities of the ligands effect the complexes reduction potentials. Analogously, the oxidation processes are likewise affected by ligand exchanges. Thus, strong donor ligands such as PMe_3 and CN^- e.g. cause a cathodic shift of E_{pa} (Table 10). Importantly, the influence of the ligand substitution is greater on the oxidation potentials than on the reduction potentials, a trend

that can be explained by different HOMO–LUMO participation. As oxidation involves removal of electrons from the HOMO, which usually has a strong contribution of the Fe–Fe bond, attaching strong donor ligands to the iron atoms directly eases this process. However, in case of any reduction, the less metal-centred LUMO with a significant Fe–S bond character is involved and renders this process comparatively less sensitive to ligand exchange.[138]

The first oxidation of [FeFe]-hydrogenase mimics leads to bivalent Fe^IFe^{II} species, which is related to the H_{ox} state of the native active site. The effect of the dithiolate bridge on the stability of the oxidised state was reported by Justice et al. investigating $Fe_2(xdt)(CO)_3(PMe_3)(dppv)$ (**235xdt**, xdt = edt, pdt, adt).[337] Upon chemical oxidation with Cp_2FePF_6 in MeCN, rotated states mimics with bridging CO and NCMe coordination at the "open site" resulting in $[Fe_2(xdt)(CO)_2(\mu-CO)(PMe_3)-(dppv)(NCMe)]^{2+}$ (**235xdt(MeCN)$^{2+}$**) was observed. Notably, the dicationic state of edt was found to be stable at room temperature, while the pdt bridged model decomposed within 30 minutes at −40 °C. Remarkably, no dicationic species was yet detected for any adt analogue. Based on these observations, it was concluded that bulky ligands, e.g. PMe_3 are not accommodated by pdt and adt linkers in the rotated state, due to steric limitations which are not present in edt-bridged derivative, thereby explaining the preference of nature to apply sterically less demanding CN^- and CO as ancillary ligands. Adding substituents to the amine bridgehead allows for the facile oxidation of such complexes as seen in e.g. $Fe_2(adt^{Bn})$-$(CO)_4(dmpe)$ (**265**).[483] The described reason for the stabilization of the rotated Fe^IFe^{II}-oxidation state is an anagostic interaction between the methyl group of the Bn substituent and the

Table 10 $E_{pa}(Fe^IFe^I/Fe^{II}Fe^I)$ and shift of the peak potentials compared to the corresponding hexacarbonyl ΔE vs. (CO)$_6$ of various substituted models

Complex	Ligand	E_{pa} [V]	ΔE vs. (CO)$_6$ [V]	Ref.
$Fe_2(pdt)(CO)_6$		+0.80		
$[Fe_2(pdt)(CO)_5(CN)]^-$	CN^-	+0.13	0.67	283
$[Fe_2(pdt)(CO)_4(CN)_2]^{2-}$	CN^-, CN^-	−0.52	0.66	289
$Fe_2(pdt)(CO)_5(CNMe)$	CNMe	+0.57	0.17	283
$Fe_2(pdt)(CO)_4(CNMe)_2$	CNMe, CNMe	+0.21	0.42	283
$Fe_2(pdt)(CO)_5(PMe_3)$	PMe_3	+0.23	0.57	317
$Fe_2(pdt)(CO)_4(PMe_3)_2$	PMe_3, PMe_3	−0.20, −0.14	0.43, 0.37	153 and 215
$Fe_2(pdt)(CO)_5(P(OEt)_3)$	$P(OEt)_3$	+0.44	0.36	317
$Fe_2(pdt)(CO)_4(P(OEt)_3)_2$	$P(OEt)_3$, $P(OEt)_3$	0.00	0.44	317
$Fe_2(adt)(CO)_6$		+0.59		170
$Fe_2[(adt)(CO)_5(CN)]^-$	CN^-	−0.043	0.63	478
$Fe_2(adt)(CO)_5(PPh_3)$	PPh_3	+0.19	0.40	170

1738 | Chem. Soc. Rev., 2021, **50**, 1668–1784

This journal is © The Royal Society of Chemistry 2021

Fig. 96 Structural reorganisation of **265** upon oxidation.

iron centre (Fe···H–C), which also allows its facile second oxidation. It was also observed that these weak interactions are lost under CO atmosphere. In this case, the $[Fe^{II}Fe^{I}(adt^{Bn})(CO)_4(dmpe)]^+$ is stabilized by binding of an additional carbonyl ligand to an iron centre, rather than an anagostic stabilisation (Fig. 96).

6.5 Redox potentials of selected H-cluster models

While the above-mentioned trends are explained on distinct examples, comparable trends can be observed for numerous synthetic mimics. The large number of mimics would certainly distract the reader from the actual message and trends observed. However, to present a full picture and allow the reader to obtain the formation without a detailed literature research, we subsequently present the redox properties of numerous complexes in tabular form (Tables 11–23).

6.5.1 PDT and derivatives thereof

The tabular section can be summarized as follows:

• Fe_2S_2 models undergo electrochemical reductions resulting in a Fe^0Fe^0 state which might be achieved in concerted two-electron transfer steps or require two single-electron potential-separated reductions.

• Functionalisation of the dithiolate bridge has only minimal influence on the redox potentials.

• Upon CO-replacement, electron donating ligands shift both, the reduction and oxidation potential, towards more cathodic values. The opposite is true for electron withdrawing ligands. However, the oxidation potential is more affected due to the nature of the HOMO and LUMO orbitals.

These investigations of the diiron models in the absence of acids give a fair idea about their respective redox properties, which can be mainly correlated to the basicity of the Fe–Fe bond. This basicity is an important factor for the catalytic mechanism of hydrogen evolution, which will be discussed in Section 6.6.

Table 11 Mono-substituted complexes

L_1	Solvent	$E_{pc}(Fe^IFe^I/Fe^IFe^0)$/V	$E_{pc}(Fe^IFe^0/Fe^0Fe^0)$/V	$E_{pa}(Fe^IFe^I/Fe^IFe^{II})^a$/V	Ref.
CO	MeCN	−1.65 to −1.74	−2.32	0.74 to +0.82	215, 283, 289, 302, 317, 329 and 367
CO	THF	−1.25^b			283

This journal is © The Royal Society of Chemistry 2021

Chem. Soc. Rev., 2021, **50**, 1668–1784 | **1739**
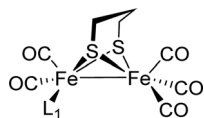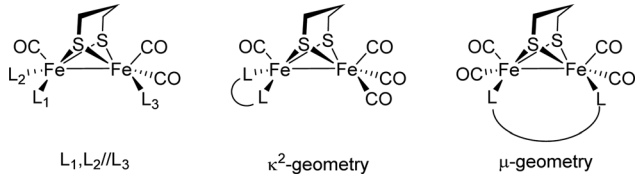
Table 11 (*continued*)

L$_1$	Solvent	$E_{pc}(Fe^IFe^I/Fe^IFe^0)$/V	$E_{pc}(Fe^IFe^0/Fe^0Fe^0)$/V	$E_{pa}(Fe^IFe^I/Fe^IFe^{II})^a$/V	Ref.
PTA	MeCN	-1.94^c		+0.34	302
P(NC$_4$H$_8$O)$_3$	MeCN	-1.86		$+0.27^d$	129
	MeCN/H$_2$O 10:1	-1.84			
	MeCN/H$_2$O 3:1	-1.80			
	MeCN/H$_2$O 2:1	-1.78			
(PPh$_2$)NH((CH$_2$)$_2$NMe$_2$)		-1.87		+0.348	303
(PPh$_2$)NH(o-C$_6$H$_4$NH$_2$)		-1.86		+0.259	303
PPh$_2$-(C$_6$H$_4$)-2CH$_2$N(Me)$_2$		-1.85			303
Val-Epa-Leu	MeCN	-1.93		+0.22	306
	MeCN/H$_2$O 3:1	ND			
	MeCN/H$_2$O 3:2	ND			
Val-Ipa-Leu	MeCN	-1.90		+0.26	306
	MeCN/H$_2$O 3:1	-1.78		+0.22	
	MeCN/H$_2$O 3:2	-1.74		+0.22	
Val-Ppa-Leu	MeCN	-1.82		+0.31	306
	MeCN/H$_2$O 3:1	-1.77		+0.29	
	MeCN/H$_2$O 3:2	-1.72		+0.32	
PPh$_2$(S(o-C$_6$H$_4$NH$_2$))	MeCN	-1.79	-2.06		307
PPh$_2$(p-C$_6$H$_4$NH$_2$)	MeCN	-1.85	-2.10		307
PPh$_2$(S(o-C$_6$H$_4$NH$_2$-L$_a{}^e$))	MeCN	-1.76		+0.34	307
PPh$_2$(p-C$_6$H$_4$NH$_2$-L$_a{}^e$)	MeCN	-1.83		+0.36	307
PMe$_3$	MeCN	-1.94^f		+0.31, +0.65	317
PMe$_2$Ph	MeCN	-1.90^f		+0.25, +0.66	317
PPh$_3$	MeCN	-1.84^f		+0.26, +0.62	317
		-1.87	-2.24	+ 0.27, +0.66	215
P(OEt)$_3$	MeCN	-1.81^f		+0.44, +0.63	317
PPh$_2$Py		-1.74		+0.46, +0.68	319
PPy$_3$		-1.66		+0.65	319
PPh$_2$NH(p-C$_6$H$_4$Br)	MeCN	-1.80			334
PPh$_2$NH(p-C$_6$H$_4$Me)	MeCN	-1.82			334
PPh$_2$(R$_1$)^g	DCM	-2.05			305
PPh$_2$(R$_2$)^g	DCM	-2.02	-2.17		305
PPh$_2$(R$_3$)^g	DCM/DMF 1:4	-1.83	-2.07		305
IMe	MeCN	$-2.06/-2.01$		+0.11	291 and 361
IMes	MeCN	-2.10		+0.11	361
IMes		-2.10^c		+0.11, +0.72	362
IMeMes	MeCN	-2.12		+0.23	361
IPic^h	MeCN	-2.07^f		+0.10	364
SEt$_2$	MeCN	-1.72^i			367
S(CH$_3$CH$_2$)((CH$_2$)$_2$Cl)	MeCN	-1.76^i			367
S(CH$_2$CH$_3$)(C$_6$H$_5$)	MeCN	-1.77^i			367
SO(CH$_2$CH$_2$CH$_3$)$_2$	MeCN	-1.65^i			367
SO(CH$_3$)$_2$	MeCN	-1.68^i			367
MeCN	MeCN	-1.68			369
NH$_2$n-Pr	MeCN	-1.80			369
PySEt^j	MeCN	-1.65^i	-2.22		370
P(piperidyl)$_3$	MeCN	-1.98		+0.18	484
P(OMe)$_3$	MeCN	-1.98	-2.29	+0.37	485
DAPTA^k	MeCN^l	-1.83^c			486
CNMe	MeCN	-1.81^i		+0.57	283
CN−	MeCN	-2.17^i		+0.13	283

^{a} Second oxidation corresponds to Fe^{I}Fe^{II}/Fe^{II}Fe^{II}. ^{b} Reported *vs.* Ag/AgCl. ^{c} Reported *vs.* NHE, converted. ^{d} Electron count not defined. ^{e} L$_a$ = CO(bpy)(ppy)$_2$Ir. ^{f} Reported *vs.* 0.01 M Ag/Ag(NO$_3$), converted. ^{g} R$_1$ = 6-(diphenylphosphaneyl)pyridin-2-yl, R$_2$ = 6-(diphenylphosphaneyl)pyrimidin-4-yl, R$_3$ = 6-(*tert*-butyl)pyrimidin-4-yl. ^{h} 1,3-Bis(2-picolyl)imidazol-2-ylidene. ^{i} Reported *vs.* Ag/AgCl, converted. ^{j} 4-(Ethylthio)pyridine. ^{k} DAPTA = 3,7-diacetyl-1,3,7-triaza-5-phosphabicyclo[3.3.1]nonane. ^{l} Reference for redox potentials in different H$_2$O:MeCN ratios.

1740 | *Chem. Soc. Rev.*, 2021, **50**, 1668–1784

This journal is © The Royal Society of Chemistry 2021

Table 12 Multi-substituted complexes

| | $L_1,L_2//L_3$ | κ^2-geometry | μ-geometry |

Ligands: $Fe_1//Fe_2$	Solvent	$E_{pc}(Fe^IFe^I/Fe^IFe^0)$/V	$E_{pc}(Fe^IFe^0/Fe^0Fe^0)$/V	$E_{pa}(Fe^IFe^I/Fe^IFe^{II})^a$/V	Ref.
PTA//PTA	MeCN	-2.18^b		$+0.00$	302
P(NC$_4$H$_8$O)$_3$//P(NC$_4$H$_8$O)$_3$	MeCN	-2.08		$+0.01^c$	129
κ^2-(PPh$_2$)$_2$N-(CH$_2$)$_2$NMe$_2$BzBr	MeCN^d	-2.10		$+0.06$	130
	MeCN:H$_2$O (3:2)	-1.92		$+0.06$	
μ-(PPh$_2$)$_2$N-(CH$_2$)$_2$NMe$_2$BzBr	MeCN^d	-2.09		$+0.40$	130
	MeCN:H$_2$O (3:2)	-1.93		$+0.42$	
μ-dppf^e	MeCN	-2.10	-2.19	$+0.05$	311
PMe$_2$Ph//PMe$_2$Ph	MeCN	-2.30^f		$-0.14, +0.20$	317
P(OEt)$_3$//P(OEt)$_3$	MeCN	-2.27^f		$+0.00$	317
P(Ph$_2$Py)$_3$//P(Ph$_2$Py)$_3$		-1.92		$+0.32, +0.72$	319
P(Py)$_3$//P(Py)$_3$		-1.70		$+0.62$	319
μ-dppm	MeCN	-2.28^f		$+0.22, +0.60$	183
κ^2-Me$_2$dppm	MeCN	-2.16^g	-2.23	$-0.19, +0.04$	328
μ-Me$_2$dppm	MeCN	-2.50		$+0.74$	328
μ-(PPh$_2$)$_2$NPr	MeCN	-2.17	-2.46	$+0.33$	329
κ^2-(PPh$_2$)$_2$N(allyl)	MeCN	-2.19		-0.11	330
	DCM	-2.23		$+0.07$	
μ-(PPh$_2$)$_2$N(allyl)	MeCN	-2.15		$+0.31$	330
	DCM	-2.23		$+0.65$	
κ^2-(PPh$_2$)$_2$N(p-C$_6$H$_4$Me)	MeCN	-2.21			334
κ^2-dppe	MeCN	-2.07^g			338
	THF	-2.12			
μ-dppe	MeCN	-2.23			338
	THF	-2.37			
IMe//IMe	MeCN	-2.47			291
IMes//PMe$_3$	MeCN	-2.36		-0.47	361
IMeMes//PMe$_3$	MeCN	-2.52		-0.33	361
IMe//PMe$_3$	MeCN	-2.53		-0.24	361
κ^2-IMe-CH$_2$-IMe	MeCN	-2.42^h		-0.41	363
κ^2-NHCMePy^i	MeCN	-2.16^f	-0.16		364
κ^2-bpy	MeCN	-2.06			371
	DCM		-0.25		
P(OMe)$_3$//P(OMe)$_3$	MeCN	-2.30		$+0.12^j$	485
PMe$_3$//PMe$_3$	MeCN	$-2.31,^k -2.37$		$-0.20, -0.14$	153 and 215
PMe$_3$,NO$^+$	DCM	-0.36^g	-1.03		381
PMe$_3$, NO$^+$//PMe$_3$	DCM	-0.64	-0.98		381
κ^2-(Ph$_2$PCH$_2$)$_2$NCH$_3$	DCM	-2.3		-0.17	152
PMe$_2$Ph//PMe$_3$	MeCN^l	-2.20^f		-0.08	487
PMe$_2$Ph//PPh$_3$	MeCN^l	-2.09^f		$+0.03$	487
PMe$_2$Ph//P(OEt)$_3$	MeCN^l	-2.17^f		$+0.01$	487
PMe$_3$//P(OEt)$_3$	MeCN^l	-2.16^f		$+0.03$	487
PPh$_3$//P(OEt)$_3$	MeCN^l	-2.06^f		$+0.13$	487
PCy$_3$//P(OEt)$_3$	Toluene/MeCN 1:3^l	-2.14^f		$+0.14$	487
PMe$_3$//PPh$_3$	MeCN^l	-2.12^f		$+0.02$	487
PMe$_3$//PCy$_3$	Toluene/MeCN 1:3^l	-2.15^f		-0.02	487
DAPTA//DAPTA	MeCN	-2.06^b			486
DAPTA//PTA	MeCN	-2.14^b			486
PMe$_3$//CN$^-$	MeCN	-2.58^k		-0.39	150
CNMe//CNMe	MeCN	-2.08^k		$+0.21$	283
CN$^-$//CN$^-$	MeCN	-2.72^m		-0.50	289
CN$^-$//CN$^-$	MeCN	-2.72^k		-0.52	283

^{a} Second oxidation corresponds to- Fe^{I}Fe^{II}/Fe^{II}Fe^{II}. ^{b} Reported *vs.* NHE, converted. ^{c} Electron count not defined. ^{d} Reference for redox potentials in different H$_2$O:MeCN ratios. ^{e} dppf = 1,10-bis(diphenylphosphino)ferrocene. ^{f} Reported *vs.* 0.01 M Ag/Ag(NO$_3$), converted. ^{g} Reported *vs.* Ag/AgCl. ^{h} Fe^{I}Fe^I/Fe^{0}Fe^0. ^{i} 1-Methyl-3-(2-pyridyl)imidazol-2-ylidene. ^{j} Fe^{I}Fe^I/Fe^{II}Fe^{II}. ^{k} Reported *vs.* Ag/AgCl, converted. ^{l} Under CO. ^{m} Reported *vs.* SCE, converted.

Table 13 Alternative dithiolate bridges
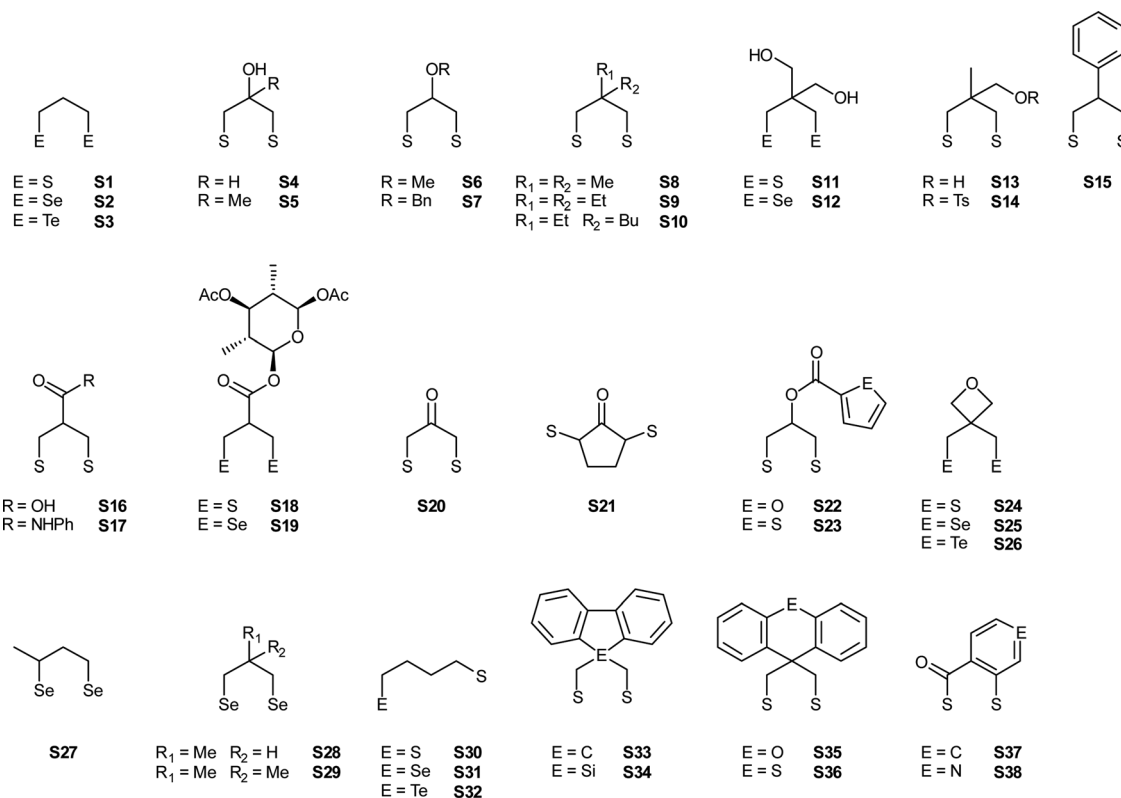
E = S **S1**
E = Se **S2**
E = Te **S3**

R = H **S4**
R = Me **S5**

R = Me **S6**
R = Bn **S7**

R₁ = R₂ = Me **S8**
R₁ = R₂ = Et **S9**
R₁ = Et R₂ = Bu **S10**

E = S **S11**
E = Se **S12**

R = H **S13**
R = Ts **S14**

S15

R = OH **S16**
R = NHPh **S17**

E = S **S18**
E = Se **S19**

S20

S21

E = O **S22**
E = S **S23**

E = S **S24**
E = Se **S25**
E = Te **S26**

S27

R₁ = Me R₂ = H **S28**
R₁ = Me R₂ = Me **S29**

E = S **S30**
E = Se **S31**
E = Te **S32**

E = C **S33**
E = Si **S34**

E = O **S35**
E = S **S36**

E = C **S37**
E = N **S38**

Dithiolate	Ligands: Fe_1//Fe_2	Solvent	$E_{pc}(Fe^IFe^I/Fe^IFe^0)$/V	$E_{pc}(Fe^IFe^0/Fe^0Fe^0)$/V	$E_{pa}(Fe^IFe^I/Fe^IFe^{II})^a$/V	Ref.
S16		MeCN	-1.64^b	-2.40		141 and 144
S16		MeCN^c	-1.64	-2.51		
S16	PMe₃//PMe₃	MeCN	-2.42			141
S17		MeCN^c	-1.67	-2.60		141
S18		MeCN	-1.58^d	-1.97	$+1.01$	133
S19		MeCN	-1.54^d	-2.10	$+0.89$	133
S4		MeCN	-1.61^d	-2.23	$+0.77$	134
S5		MeCN	-1.60^d	-2.26	$+0.70$	135
S6		MeCN	-1.60^d	-2.17	$+0.79$	135
S15		MeCN	-1.61	-2.17	$+0.75$	479
S15	PPh₃	MeCN	-1.78		$+0.39$	479
S15	κ¹-dppm	MeCN	-1.80	-2.16	$+0.19$	479
S15	μ-dppm	MeCN	-2.22			479
S7		MeCN	-1.61	-2.12	$+0.70$	339
S7	PPh₃	MeCN	-1.63	-2.41	$+0.40$	339
S7	PPh₃//PPh₃	MeCN	-1.96	-2.26	$+0.07$	339
S21	PMe₃//PMe₃	DCM			$+0.04, +0.29$	474
S11		MeCN	-1.53		$+0.67^e$	136
S12		MeCN	-1.49		$+0.58^e$	136
S13	μ-(PPh₂)₂NCH₂-pyridin-2-yl	THF^c	-2.25	-2.34		488
			-2.27	-2.38		
S13	μ-(PPh₂)₂NBn	THF^c	-2.27	-2.36		488
		THF^c	-2.21	-2.31		
S14	μ-(PPh₂)₂NCH₂-pyridin-2-yl		-2.19	-2.41^f		488
			-2.12	-2.29^f		
S22		MeCN^c	-1.58	-2.21	$+0.85$	137
S23		MeCN^c	-1.59	-2.23	$+0.84$	137
S20		MeCN^c	-1.52	-2.39	$+1.01$	137
S9		MeCN^c	-1.67	-2.27	$+0.82$	473
S10		MeCN^c	-1.64	-2.27	$+0.78$	473
S8		MeCN^c	-1.61	-2.24	$+0.73$	473
S8	IMes	MeCN^c	-2.01		$+0.76, +0.05$	473
S8	PPh₃	MeCN^c	-1.79	-2.29	$+0.69, +0.35$	473
S9	IMes	MeCN^c	-2.02		$+0.73, +0.16$	473

1742 | *Chem. Soc. Rev.*, 2021, **50**, 1668–1784

This journal is © The Royal Society of Chemistry 2021

Table 13 (*continued*)

E = S **S1**
E = Se **S2**
E = Te **S3**

R = H **S4**
R = Me **S5**

R = Me **S6**
R = Bn **S7**

R$_1$ = R$_2$ = Me **S8**
R$_1$ = R$_2$ = Et **S9**
R$_1$ = Et R$_2$ = Bu **S10**

E = S **S11**
E = Se **S12**

R = H **S13**
R = Ts **S14**

S15

R = OH **S16**
R = NHPh **S17**

E = S **S18**
E = Se **S19**

S20

S21

E = O **S22**
E = S **S23**

E = S **S24**
E = Se **S25**
E = Te **S26**

S27

R$_1$ = Me R$_2$ = H **S28**
R$_1$ = Me R$_2$ = Me **S29**

E = S **S30**
E = Se **S31**
E = Te **S32**

E = C **S33**
E = Si **S34**

E = O **S35**
E = S **S36**

E = C **S37**
E = N **S38**

Dithiolate	Ligands: Fe$_1$//Fe$_2$	Solvent	E_{pc}(Fe^{I}Fe^I/Fe^{I}Fe^0)/V	E_{pc}(Fe^{I}Fe^0/Fe^{0}Fe^0)/V	E_{pa}(Fe^{I}Fe^I/Fe^{I}Fe^{II})^a/V	Ref.
S24		MeCN	−1.60		+0.81	146
S25		MeCN	−1.55		+0.78	146
S26		MeCN	−1.54		+0.71	146
S2		MeCN	−1.61	−2.15	+0.73^e	477
S2		MeCN	−1.90^{bg}		+0.95^e	145
S27		MeCN	−2.08^b		+0.32^g	145
S28		MeCN	−1.61			148
S29		MeCN	−1.55^h			148
S30		DCM	−1.66^i		+0.76	128 and 147
S31		DCM	−1.63^h		+0.72	128
S32		DCM	−1.64^h		+0.71	128
S3		MeCN	−1.58	−2.09	+0.64^e	149
S3	μ-(PPh$_2$)$_2$N-nPr	MeCN	−2.06	−2.45	+0.14	149
S33		DCM	−1.48^h			158
S35		DCM	−1.56^h			158
S36		DCM	−1.56^h			158
S34	PPh$_3$	DCM	−1.81			158
S38			−1.18			489
S37			−1.28			489
S37	PPh$_3$		−1.47			489

^{a} Second oxidation corresponds to- Fe^{I}Fe^{II}/Fe^{II}Fe^{II}. ^{b} Reported *vs.* Ag/AgCl, converted. ^{c} Under CO. ^{d} Reported *vs.* 0.01 M Ag/Ag(NO$_3$), converted. ^{e} Fe^{I}Fe^I/Fe^{II}Fe^{II}. ^{f} Additional unidentified process(es) involved. ^{g} Electron count not defined. ^{h} Fe^{I}Fe^I/Fe^{0}Fe^0. ^{i} ECE process.

This journal is © The Royal Society of Chemistry 2021

Chem. Soc. Rev., 2021, **50**, 1668–1784 | **1743**

6.5.2 ADT and derivatives thereof

Table 14 ADT and derivatives thereof
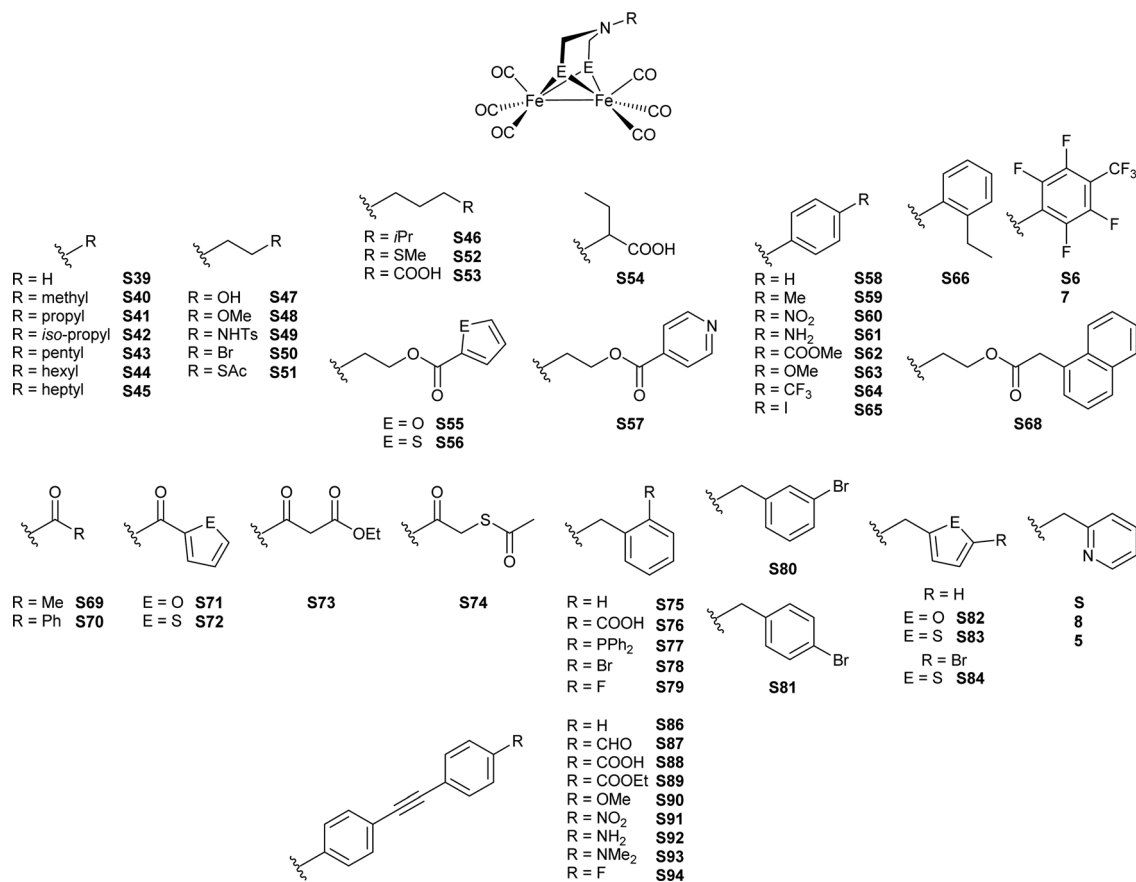
R = H **S39**
R = methyl **S40**
R = propyl **S41**
R = *iso*-propyl **S42**
R = pentyl **S43**
R = hexyl **S44**
R = heptyl **S45**

R = OH **S47**
R = OMe **S48**
R = NHTs **S49**
R = Br **S50**
R = SAc **S51**

R = *i*Pr **S46**
R = SMe **S52**
R = COOH **S53**

S54

R = H **S58**
R = Me **S59**
R = NO₂ **S60**
R = NH₂ **S61**
R = COOMe **S62**
R = OMe **S63**
R = CF₃ **S64**
R = I **S65**

S66

S67

E = O **S55**
E = S **S56**

S57

S68

R = Me **S69**
R = Ph **S70**

E = O **S71**
E = S **S72**

S73

S74

R = H **S75**
R = COOH **S76**
R = PPh₂ **S77**
R = Br **S78**
R = F **S79**

S80

S81

R = H, E = O **S82**
R = H, E = S **S83**
R = Br, E = S **S84**

S85

R = H **S86**
R = CHO **S87**
R = COOH **S88**
R = COOEt **S89**
R = OMe **S90**
R = NO₂ **S91**
R = NH₂ **S92**
R = NMe₂ **S93**
R = F **S94**

R	Ligands: Fe_1//Fe_2	E	Solvent	$E_{pc}(Fe^IFe^I/Fe^IFe^0)$/V	$E_{pc}(Fe^IFe^0/Fe^0Fe^0)$/V	$E_{pa}(Fe^IFe^I/Fe^IFe^{II})^a$/V	Ref.
S39		S	MeCN	−1.58		+0.59	170
S39		S	MeCN	−1.20^b			32
S39		Se		−1.20			32
S39	PPh₃	S	MeCN	−1.70		+0.19	170
S39	PMe₃	S	MeCN	−1.88		+0.51	170
S39	P(*p*-tol)₃^c	S	MeCN	−1.81		+0.26	321
S39	P(*m*-tol)₃	S	MeCN	−1.83		+0.33	321
S39	P(*p*-C₆H₄F)₃	S	MeCN	−1.77		+0.34	321
S39	P(*m*-C₆H₄F)₃	S	MeCN	−1.71		+0.39	321
S39	P(C₄H₃O)₃	S	MeCN	−1.80		+0.45	321
S39	PPh₂(OEt)	S	MeCN	−1.84		+0.40	321
S39	CN⁻	S	MeCN	−2.23		−0.043	478
S39	μ,κ¹,κ²-triphos^d	S	DCM			−0.45	354
S60		S	MeCN	−1.42^e	−1.79	+0.70	194
S61		S	MeCN	−1.56^e		+0.72	194
S49		S	MeCN	−1.57^e		+0.56	177
S47		S	MeCN	−1.66		+0.59	186
S57		S	MeCN	−1.65		+0.61	186
S74		S	MeCN	−1.49	−1.96	+0.86	192
S73		S	MeCN	−1.51	−2.00	+0.87	192
S71		S	MeCN	−1.54	−1.99	+0.81	192
S72		S	MeCN	−1.52	−1.97	+0.82	192
S62		S	MeCN	−1.54	−2.01	+0.55, +0.87	460
S62	PPh₃	S	MeCN	−1.67		+0.34, +0.61	343
S50		S	MeCN^f	−1.63	−2.33	+0.59	190
S51		S	MeCN^f	−1.62	−2.29	+0.56	190
S55		S	MeCN^f	−1.63	−2.10	+0.53	190

1744 | *Chem. Soc. Rev.*, 2021, **50**, 1668–1784

This journal is © The Royal Society of Chemistry 2021

Table 14 (*continued*)

R = H **S39**
R = methyl **S40**
R = propyl **S41**
R = *iso*-propyl **S42**
R = pentyl **S43**
R = hexyl **S44**
R = heptyl **S45**

R = OH **S47**
R = OMe **S48**
R = NHTs **S49**
R = Br **S50**
R = SAc **S51**

R = *i*Pr **S46**
R = SMe **S52**
R = COOH **S53**

S54

R = H **S58**
R = Me **S59**
R = NO₂ **S60**
R = NH₂ **S61**
R = COOMe **S62**
R = OMe **S63**
R = CF₃ **S64**
R = I **S65**

S66

S67

E = O **S55**
E = S **S56**

S57

S68

R = Me **S69**
R = Ph **S70**

E = O **S71**
E = S **S72**

S73

S74

R = H **S75**
R = COOH **S76**
R = PPh₂ **S77**
R = Br **S78**
R = F **S79**

S80

S81

R = H
E = O **S82**
E = S **S83**
R = Br
E = S **S84**

S85

R = H **S86**
R = CHO **S87**
R = COOH **S88**
R = COOEt **S89**
R = OMe **S90**
R = NO₂ **S91**
R = NH₂ **S92**
R = NMe₂ **S93**
R = F **S94**

R	Ligands: Fe₁//Fe₂	E	Solvent	$E_{pc}(Fe^IFe^I/Fe^IFe^0)$/V	$E_{pc}(Fe^IFe^0/Fe^0Fe^0)$/V	$E_{pa}(Fe^IFe^I/Fe^IFe^{II})^a$/V	Ref.
S56		S	MeCN^f	−1.64	−2.09	+0.56	190
S76		S	MeCN	−1.61		+0.62	191
S76	PMe₃//PMe₃	S	MeCN	−2.01		−0.23	191
S53		S	MeCN	−1.60		+0.62	191
S53	PMe₃//PMe₃	S	MeCN	−2.05		−0.27	191
S54		S	MeCN	−1.63		+0.64	191
S54	PMe₃//PMe₃	S	MeCN	−1.94		−0.12	191
S63		S	MeCN	−1.61	−2.10	+0.48, +0.81	195
S63	PHPh₂	S	MeCN	−1.78	−2.22	+0.26, +0.49	195
S66		S	MeCN	−1.55			193
S43		S	MeCN	−1.66	−2.22	+0.55, +0.88	182
S43	PMe₃//PMe₃	S	MeCN	−2.00	−2.32	−0.21, −0.09	182
S44		S	MeCN	−1.66	−2.24	+0.59, +0.92	182
S44	PMe₃//PMe₃	S	MeCN	−1.99	−2.29	−0.20, −0.08	182
S45		S	MeCN	−1.68	−2.21	+0.58, +0.90	182
S45	PMe₃//PMe₃	S	MeCN	−2.00	−2.35	−0.22, −0.078	182
S82		S	MeCN	−1.55		+0.71, +0.73	196 and 457
S82	IMe//IMe	S	MeCN	−2.53			197
S83		S	MeCN	−1.64		+0.65	196
S84		S	MeCN	−1.54		+0.72	196
S85							
S85	IMe//IMe	S	MeCN	−2.49			197
S60		Se	MeCN	−1.48^e	−1.79	+0.58	198
S58		Se	MeCN	−1.57^e	−2.10	+0.50, +0.78	198
S59		Se	MeCN	−1.58^e	−2.08	+0.49, +0.81	198
S69		Se	MeCN^f	−1.50	−1.97	+0.72^g	173
S70		Se	MeCN^f	−1.48	−1.95	+0.73^g	173
S77	PMe₃//PMe₃	S	DCM			−0.24, −0.02	318
S67		S	MeCN	−1.53	−2.02	+0.89	481
S67	PPh₃	S	MeCN	−1.74	−2.22	+0.44	481
S64		S	MeCN	−1.54	−2.02	+0.61	481

Table 14 (*continued*)
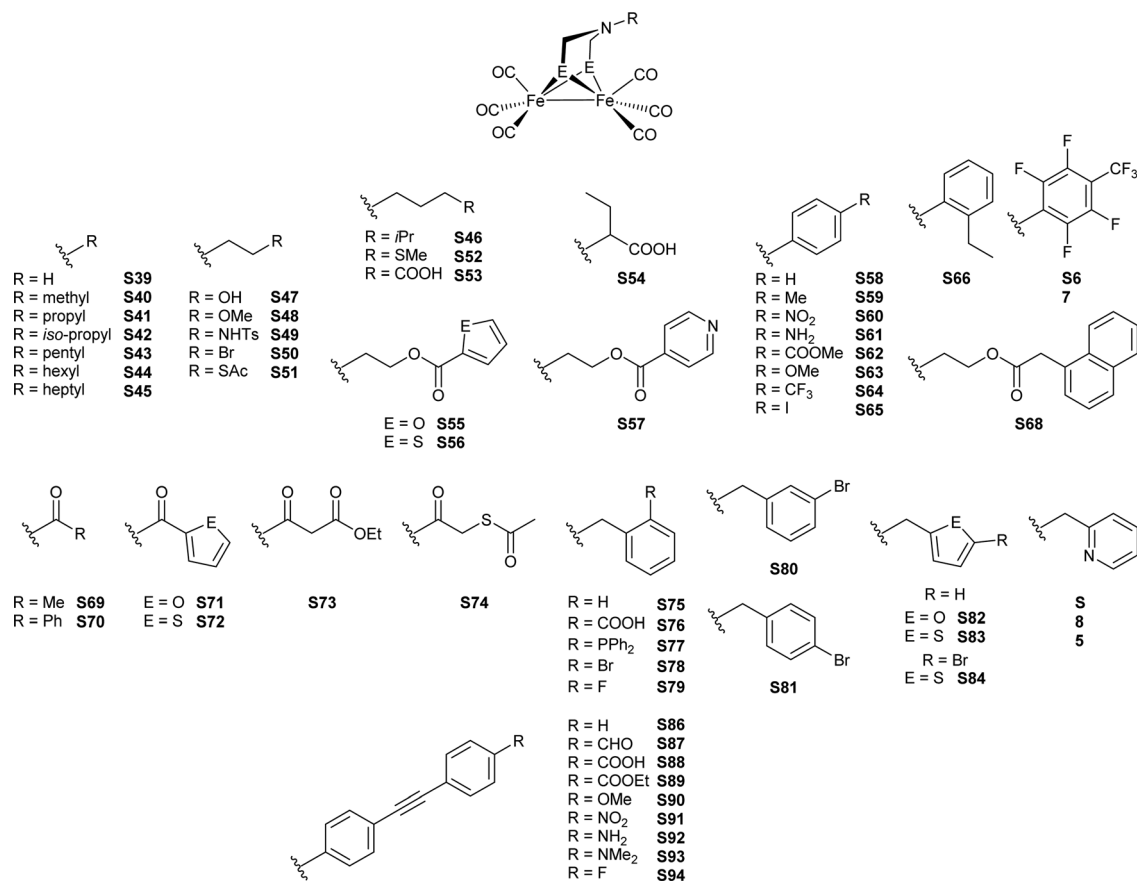
R = H   **S39**
R = methyl   **S40**
R = propyl   **S41**
R = *iso*-propyl   **S42**
R = pentyl   **S43**
R = hexyl   **S44**
R = heptyl   **S45**

R = OH   **S47**
R = OMe   **S48**
R = NHTs   **S49**
R = Br   **S50**
R = SAc   **S51**

R = *i*Pr   **S46**
R = SMe   **S52**
R = COOH   **S53**

S54

R = H   **S58**
R = Me   **S59**
R = NO₂   **S60**
R = NH₂   **S61**
R = COOMe   **S62**
R = OMe   **S63**
R = CF₃   **S64**
R = I   **S65**

S66   **S67**

E = O   **S55**
E = S   **S56**

S57

S68

R = Me   **S69**
R = Ph   **S70**

E = O   **S71**
E = S   **S72**

S73

S74

R = H   **S75**
R = COOH   **S76**
R = PPh₂   **S77**
R = Br   **S78**
R = F   **S79**

S80

S81

E = O   **S82**
E = S   **S83**
R = Br
E = S   **S84**

R = H

S85

R = H   **S86**
R = CHO   **S87**
R = COOH   **S88**
R = COOEt   **S89**
R = OMe   **S90**
R = NO₂   **S91**
R = NH₂   **S92**
R = NMe₂   **S93**
R = F   **S94**

R	Ligands: Fe₁//Fe₂	E	Solvent	$E_{pc}(Fe^IFe^I/Fe^IFe^0)$/V	$E_{pc}(Fe^IFe^0/Fe^0Fe^0)$/V	$E_{pa}(Fe^IFe^I/Fe^IFe^{II})^a$/V	Ref.
S64	PPh₃	S	MeCN	−1.73	−2.09	+0.41	481
S78		S	MeCN	−1.56^e	−2.05	+0.61	454
S78	PMe₃//PMe₃	S	MeCN	−2.18^e		−0.13	454
S79		S	MeCN	−1.56^e	−2.07	+0.67	454
S80		S	MeCN	−1.56^e	−2.06	+0.67	454
S59		S	MeCN	−1.55		+0.55	358
S59	CN-*p*C₆H₄I//CN-*p*C₆H₄I	S	MeCN	−1.70		+0.13	358
S65		S	MeCN	−1.67		+0.44	490
S65	P(*p*-tol)₃	S	MeCN	−1.79		+0.30	321
S65	P(*m*-tol)₃	S	MeCN	−1.75		+0.34	321
S65	P(*p*-C₆H₄F)₃	S	MeCN	−1.72		+0.38	321
S65	P(*m*-C₆H₄F)₃	S	MeCN	−1.67		+0.39	321
S65	P(C₄H₃O)₃	S	MeCN	−1.72		+0.33	321
S46							
S46	PPh₃	S	DCM	−2.04		+0.26	185
S46	PPh₂(*o*-py)^h	S	DCM	−2.08		+0.18	185
S46	P(*p*-tol)₃	S	DCM	−2.10		+0.22	185
S52							
S52	PPh₃	S	DCM	−2.05		+0.25	185
S52	PPh₂(*o*-py)	S	DCM	−2.06		+0.17	185
S52	P(*p*-tol)₃	S	DCM	−2.10		+0.23	185
S41							
S41	μ-dppm	S	MeCN	−2.25^i		+0.08, +0.42	183
S42							
S42	κ²-dppe	S	MeCN	−2.01			338
			THF	−2.22			
S42	μ-dppe	S	MeCN	−2.12			338
S42	κ²-1,10-phenantroline	S	MeCN	−2.22			463
S48							
S48	κ²-dppe	S	MeCN	−1.98			338
			THF	−2.16			

Table 14 (*continued*)

R	Ligands: Fe$_1$//Fe$_2$	E	Solvent	$E_{pc}(Fe^IFe^I/Fe^IFe^0)$/V	$E_{pc}(Fe^IFe^0/Fe^0Fe^0)$/V	$E_{pa}(Fe^IFe^I/Fe^IFe^{II})^a$/V	Ref.
S48	μ-dppe	S	MeCN	−2.10			338
			THF	−2.36			
S81		S	MeCN	−1.56			456
S91		S	MeCN	−1.56		+0.55	490
S91	PPh$_3$	S	MeCN	−1.67		+0.52	490
S87		S	MeCN	−1.56	−1.98	+0.61	490
S92		S	MeCN	−1.58	−2.06	+0.46	490
S88		S	DMF	−1.59	−2.49	+0.64	490
S89		S	MeCN	−1.56	−2.08	+0.60	490
S94		S	MeCN	−1.56	−2.08	+0.57	490
S86		S	MeCN	−1.54	−1.99	+0.55	490
S90		S	MeCN	−1.56	−2.03	+0.55	490
S93		S	MeCN	−1.55	−2.02	+0.50	490
S58	κ^2-(PPh$_2$)$_2$N(CH$_2$CHMe$_2$)	S	MeCN	−2.10			491

^{a} Second oxidation corresponds to- Fe^{I}Fe^{II}/Fe^{II}Fe^{II}. ^{b} Reported *vs.* SHE. ^{c} tol = methylphenyl. ^{d} Phenyl bis(diphenylphosphinoethyl)phosphine. ^{e} Reported *vs.* 0.01 M Ag/Ag(NO$_3$), converted. ^{f} Under CO. ^{g} Fe^{I}Fe^I/Fe^{II}Fe^{II}. ^{h} py = pyridyl. ^{i} Reported *vs.* 0.001 M AgNO$_3$, converted.

This journal is © The Royal Society of Chemistry 2021

Chem. Soc. Rev., 2021, **50**, 1668–1784 | **1747**

6.5.3 EDT and derivatives thereof

Table 15 EDT and derivatives thereof

R = H **S95**
R = Me **S96**

R = COOMe **S97**

R = H **S98**
R = OH **S99**
R = SO$_3^-$Na$^+$ **S100**

S101

Dithiolate	Ligands: Fe$_1$//Fe$_2$	Solvent	E_{pc}(Fe^{I}Fe^I/Fe^{I}Fe^0)/V	E_{pc}(Fe^{I}Fe^0/Fe^{0}Fe^0)/V	E_{pa}(Fe^{I}Fe^I/Fe^{I}Fe^{II})/V	Ref.
S95		MeCN	−1.63[a]			117
S95	PMe$_3$, NO$^+$	DCM	−0.45[b]	−0.95		381
S95	PMe$_3$, NO$^+$//PMe$_3$	DCM	−0.67[c]	−0.98		381
S95	κ^2-(PPh$_2$)$_2$N(CH$_2$CHMe$_2$)	MeCN	−2.23			491
S98		MeCN	−1.66			117
S96		MeCN	−1.68			117
S99		MeCN	−1.63			117
S99			−1.67[d]		+0.91	138
S99	CN$^-$//CN$^-$	MeCN	−2.75[d]		−0.47	138
S100		MeCN	−1.64[e]	−2.02		119
S100		H$_2$O	−1.07[f]			
S101		MeCN	−1.60	−2.11	+0.96	121
S101	PPh$_3$	MeCN	−1.74		+0.57	121
S101	dppm	MeCN	−1.75		+0.46	121
S97		DCM	−1.11	−1.25		492

[a] At fast scan rate (0.1 V s^{-1}). [b] Reported *vs.* Ag/AgCl at 0 °C. [c] Reported *vs.* Ag/AgCl. [d] Reported *vs.* SCE, converted. [e] Reported *vs.* NHE, converted. [f] Reported *vs.* NHE.

6.5.4 ODT and derivatives thereof

Table 16 ODT and derivatives thereof

X	E	Ligand L	Solvent	E_{pc}(Fe^{I}Fe^I/Fe^{I}Fe^0)/V	E_{pc}(Fe^{I}Fe^0/Fe^{0}Fe^0)/V	E_{pa}(Fe^{I}Fe^I/Fe^{I}Fe^{II})/V	Ref.
S	S	CO	MeCN	−1.51	−1.94	+0.79	211
S	S	CN-tBu	MeCN	−1.76	−1.98	+0.49	213
S	Se	CO	MeCN	−1.49	−1.97	+0.64[a]	205
O	S	CO	MeCN	−1.59	−2.10	+0.81[a]	204
O	Se	CO	MeCN	−1.55	−2.06	+0.71[a]	205

[a] Fe^{I}Fe^I/Fe^{II}Fe^{II}.

1748 | *Chem. Soc. Rev.*, 2021, **50**, 1668–1784

This journal is © The Royal Society of Chemistry 2021

6.5.5 XDT and derivatives thereof

Table 17 XDT and derivatives thereof

X	G//G	E	Ligands: Fe$_1$//Fe$_2$	Solvent	E_{pc}(Fe^{I}Fe^I/Fe^{I}Fe^0)/V	E_{pc}(Fe^{I}Fe^0/Fe^{0}Fe^0)/V	E_{pa}(Fe^{I}Fe^I/Fe^{I}Fe^{II})/V	Ref.
SiMe$_2$	CH$_2$//CH$_2$	S		DCM	−1.71	−1.84	+0.77	160
GeMe$_2$	CH$_2$//CH$_2$	S		DCM	−1.72	−1.85	+0.74	160
SnMe$_2$	CH$_2$//CH$_2$	S		DCM	−1.68	−2.20	+0.70	160
SnMe$_2$	CH$_2$//—	Se		DCM	−1.75^a			161
SnMe$_2$	CH$_2$//CH$_2$	Se		DCM	−1.63^a			161
SiPh$_2$	CHPh//CHPh	S		DCM	−1.57			159
				MeCN	−1.43			
SiPh$_2$	CHPh//CHPh	S	κ^2-dmpe	DCM	−2.21			159
				MeCN	−2.00	−2.30		
SiPh$_2$	CHPh//CHPh	S	μ-dmpe	DCM	−2.32			159
				MeCN	−2.14			
P(O)Me	CH$_2$//CH$_2$	S		MeCN	−1.41			202
P(O)(OEt)	CH$_2$//CH$_2$	S		MeCN	−1.42			202

^{a} Fe^{I}Fe^I/Fe^{0}Fe^0.

6.5.6 BDT and derivatives thereof

Table 18 BDT and derivatives thereof

Bridge	Ligands: Fe$_1$//Fe$_2$	Solvent	E_{pc}(Fe^{I}Fe^I/Fe^{I}Fe^0)/V	E_{pc}(Fe^{I}Fe^0/Fe^{0}Fe^0)/V	E_{pa}(Fe^{I}Fe^I/Fe^{I}Fe^{II})/V	Ref.
S102		MeCN^a	−1.35,^{b} −1.36			222 and 232
		MeCN	−1.36^b			232
		MeCN	−1.31			226

This journal is © The Royal Society of Chemistry 2021

Chem. Soc. Rev., 2021, **50**, 1668–1784 | **1749**

Table 18 (*continued*)

$E =$ CH **S123**
$E =$ N **S124**

$R =$ H **S125**
$R =$ Ph **S126**

Bridge	Ligands: Fe_1//Fe_2	Solvent	$E_{pc}(Fe^IFe^I/Fe^IFe^0)$/V	$E_{pc}(Fe^IFe^0/Fe^0Fe^0)$/V	$E_{pa}(Fe^IFe^I/Fe^IFe^{II})$/V	Ref.
		MeCN	-1.32^b			468
			-1.27^b			467
S102	PMe_3//PMe_3	MeCN	-2.09			222
S102	$PR_3{}^c$	DCM	-1.44^d	-1.64		493
S102	$P(OMe)_3$		-1.59		$+0.64$	482
S102	PPh_3	DCM	-1.82		$+0.58$	480
		MeCN	-1.57	-1.80		
S102	PPh_2Me	DCM	-1.89		$+0.60$	480
		MeCN	-1.59	-1.88		
S102	PPh_2H	DCM	-1.80		$+0.60$	480
		MeCN	-1.54	-1.76		
S102	PPh_3//PPh_3	DCM	-2.17		$+0.13$	480
		MeCN	-1.83			
S102	PPh_2Me//PPh_2Me	DCM	-2.21			480
		MeCN	-1.89			
S102	PPh_2H//PPh_2H	DCM	-2.02		$+0.21$	480
		MeCN	-1.74			
S102	Val-Ppa-Leu	MeCN	-1.62		$+0.47$	306
		MeCN/H_2O 3:1	-1.51		$+0.48$	
		MeCN/H_2O 3:2	-1.47		$+0.46$	
S106		MeCN	-1.28			228^e
S109		MeCN	-1.32			228
S107		MeCN	-1.28			228
S108		MeCN	-1.27			228
S110		MeCN	-1.22			228
S111		MeCN	-1.22			228
S112		DCM	-1.34			228
S106		MeCN^a	-1.34^b			232
		MeCN	-1.34^b			
S113		MeCN^a	-1.28^b			232
			-1.28^b			
S103		MeCN	-1.37			222
			-1.34^f			226
S103	PMe_3//PMe_3	MeCN	-2.08			222
S104		MeCN	-1.23			222
			-1.20			226

1750 | *Chem. Soc. Rev.*, 2021, **50**, 1668–1784

This journal is © The Royal Society of Chemistry 2021

Table 18 (*continued*)

Bridge	Ligands: $Fe_1//Fe_2$	Solvent	$E_{pc}(Fe^IFe^I/Fe^IFe^0)$/V	$E_{pc}(Fe^IFe^0/Fe^0Fe^0)$/V	$E_{pa}(Fe^IFe^I/Fe^IFe^{II})$/V	Ref.
S104	$PMe_3//PMe_3$		−1.91			222
S115		DCM	$−1.23^g$			230
S116		DCM	$−1.20^g$			230
S117		DCM	$−1.32^g$			230
S118		DCM	$−1.24^g$			230
S120		DCM	$−1.29^g$			230
S120	$PMe_3//PMe_3$	DCM	$−1.71^g$			230
S121		DCM	$−1.25^g$			230
S122		MeCN	$−1.17^b$			229
S122	PPh_3	MeCN	−1.38	−1.65		229
S124		MeCN	$−1.23^b$			229
S124	PPh_3	MeCN	−1.42	−1.70		229
S123		MeCN	−1.22			222
S123	PPh_3	MeCN	−1.41	−1.70		229
S123	$PMe_3//PMe_3$		−1.88			222
S125		MeCN	$−1.34^b$			234
S125	PPh_3	MeCN	−1.55	−1.85		494
S125	$P(OEt)_3$	MeCN	−1.58			494
S125	$P(OEt)_3//P(OEt)_3$	MeCN	−1.9			494
S126		MeCN	$−1.34^b$			234
S126	PPh_3	MeCN	−1.56	−1.80		494
S126	$P(OEt)_3$	MeCN	−1.57			494
S126	$P(OEt)_3//P(OEt)_3$	MeCN	−1.84			494
S127		MeCN	$−1.35^b$			234
S127	PPh_3	MeCN	−1.56	−1.83		494
S127	$P(OEt)_3$	MeCN	−1.60			494
S127	$P(OEt)_3//P(OEt)_3$	MeCN	−1.86			494
S105		DCM	$−1.68^b$			221
S114		MeCN	$−1.15^f$			226
S119		MeCN	$−1.13^f$			226

^{a} Under CO. ^{b} Fe^IFe^I/Fe^0Fe^0. ^{c} 2,2′-(2-Phenyl-4,5,6,7-tetrahydro-2*H*-isophosphindole-1,3-diyl)dipyridine. ^{d} Reduction associated with the ligand at −1.76 V. ^{e} For this reference, reported are E°_{ov} values, *i.e.* standard potential for overall 2e$^-$ reduction defined as $E^\circ_1 + E^\circ_2/2$. ^{f} Electron count not defined. ^{g} Reduction associated with quinone.

This journal is © The Royal Society of Chemistry 2021
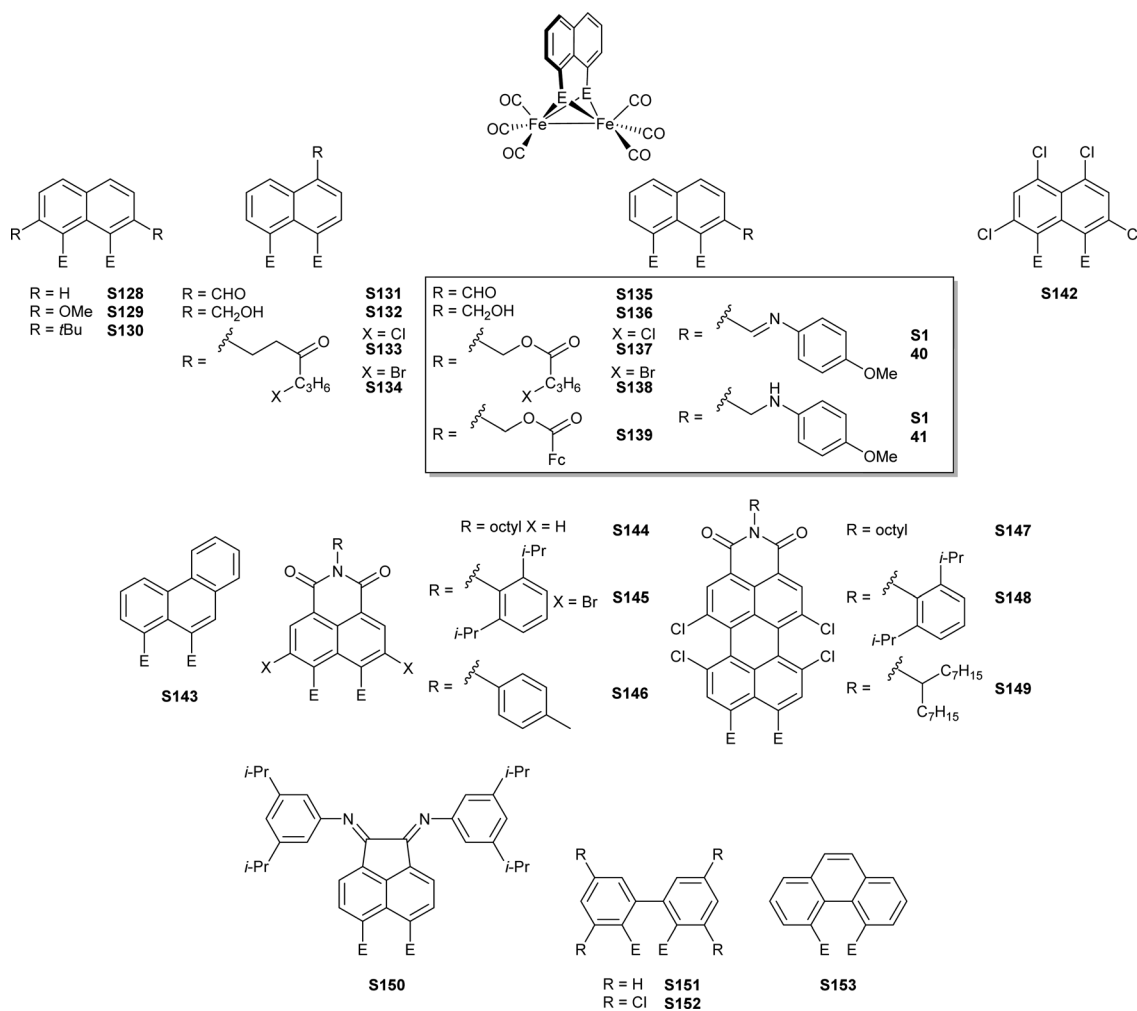
Chem. Soc. Rev., 2021, **50**, 1668–1784 | **1751**

6.5.7 1,8-Disulfidonaphtalene complexes and derivatives thereof

Table 19 1,8-Disulfidonaphtalene complexes and derivatives thereof

R = H **S128**
R = OMe **S129**
R = tBu **S130**

R = CHO **S131**
R = CH$_2$OH **S132**
X = Cl **S133**
X = Br **S134**

R = CHO **S135**
R = CH$_2$OH **S136**
X = Cl **S137**
X = Br **S138**
S139

S140
S141

S142

S143

R = octyl X = H **S144**
X = Br **S145**
S146

R = octyl **S147**
S148
S149

S150

R = H **S151**
R = Cl **S152**

S153

Bridge	E	Solvent	$E_{pc}(Fe^IFe^I/Fe^IFe^0)$/V	$E_{pc}(Fe^IFe^0/Fe^0Fe^0)$/V	$E_{pa}(Fe^IFe^I/Fe^IFe^{II})^a$/V	Ref.
S128	S	DCM	−1.76	−2.00		239
		MeCN	−1.52	−1.96	+0.87	
S142	S	DCM	−1.60		+1.00	239
S130	S	DCM	−1.84	−2.12		239
		MeCN	−1.59	−2.05	+0.78	
S135	S	DCM	−1.51		+0.86	242
S135	S	MeCN	−1.46	−1.60	+0.75	242
S135	S	DMF	−1.36	−1.63		242
S131	S	DCM	−1.54		+0.69	242
S131	S	MeCN	−1.45	−1.55	+0.77	242
S131	S	DMF	−1.37	−1.58		242
S136	S	DCM	−1.62	−1.88	+0.82	242
S136	S	MeCN	−1.53	−1.88	+0.79	242
S132	S	DCM	−1.65	−1.87	+0.82	242
S132	S	MeCN	−1.54	−1.87	+0.81	242
S137	S	DCM	−1.60	−1.93	+0.89	242
S137	S	MeCN	−1.51	−1.87	+0.85	242
S133	S	DCM	−1.63	−1.95	+0.90	242
S133	S	MeCN	−1.51	−1.89	+0.84	242
S138	S	DCM	−1.61	−1.93	+0.90	242
S138	S	MeCN	−1.51	−1.88	+0.82	242
S134	S	DCM	−1.63	−1.96	+0.89	242
S134	S	MeCN	−1.51	−1.90	+0.82	242

1752 | *Chem. Soc. Rev.*, 2021, **50**, 1668–1784

This journal is © The Royal Society of Chemistry 2021

Table 19 (*continued*)

R = H **S128**
R = OMe **S129**
R = *t*Bu **S130**

R = CHO **S131**
R = CH₂OH **S132**
X = Cl **S133**
X = Br **S134**

R = CHO **S135**
R = CH₂OH **S136**
X = Cl **S137**
X = Br **S138**
S139

R = **S140**
R = **S141**

S142

S143

R = octyl X = H **S144**
X = Br **S145**
S146

S147
S148
S149

S150

R = H **S151**
R = Cl **S152**

S153

Bridge	E	Solvent	$E_{pc}(Fe^IFe^I/Fe^IFe^0)$/V	$E_{pc}(Fe^IFe^0/Fe^0Fe^0)$/V	$E_{pa}(Fe^IFe^I/Fe^IFe^{II})^a$/V	Ref.
S139	S	DCM	−1.62	−1.92	+0.85	242 and 243
S144	S	DCM	−1.34	−1.68	+0.93	244
S144	Se	DCM	−1.39	−1.63	+0.89	244
S145	S	DCM	−1.12	−1.54	+1.11	244
S145	Se	DCM	−1.17	−1.55	+0.98	244
S129	S	MeCN	−1.65		+0.99, +1.20	240
S129	Se	MeCN	−1.64		+0.88, +1.13	240
S128	Se	MeCN	−1.54		+1.00	240
S128	S, Se	MeCN	−1.60		+0.68, +1.12	240
S130	Se	MeCN	−1.34		+0.55, +0.90	240
S130	S, Se	MeCN	−1.61		+1.07	240
S143	S	MeCN	−1.64		+0.87, +1.14	240
S143	Se	MeCN	−1.52		+0.98, +1.31	240
S140	S	MeCN	−1.51	−1.74	+1.00	251
S140	Se	MeCN	−1.45	−1.86	+0.96	251
S141	S	MeCN	−1.51	−1.85	+0.46, +0.76	251
S141	Se	MeCN	−1.51	−1.90	+0.52, +0.68	251
S148	S	DCM	−0.99	−1.23	+0.98	247
S147	S	DCM	−1.01	−1.24	+0.97	247
S149	S	DCM	−1.04	−1.25	+0.99	247
S150	S	DCM	−1.58			241
S146	S	MeCN	−1.1318	−1.49		248
S153	S	MeCN	−1.279		+0.42	250
S151	S	MeCN	−1.09	−1.30		475
S152	S	DCM	−1.05	−1.40		492

a Second oxidation corresponds to Fe^{I}Fe^{II}/Fe^{II}Fe^I.

This journal is © The Royal Society of Chemistry 2021

Chem. Soc. Rev., 2021, **50**, 1668–1784 | **1753**

6.5.8 Other models
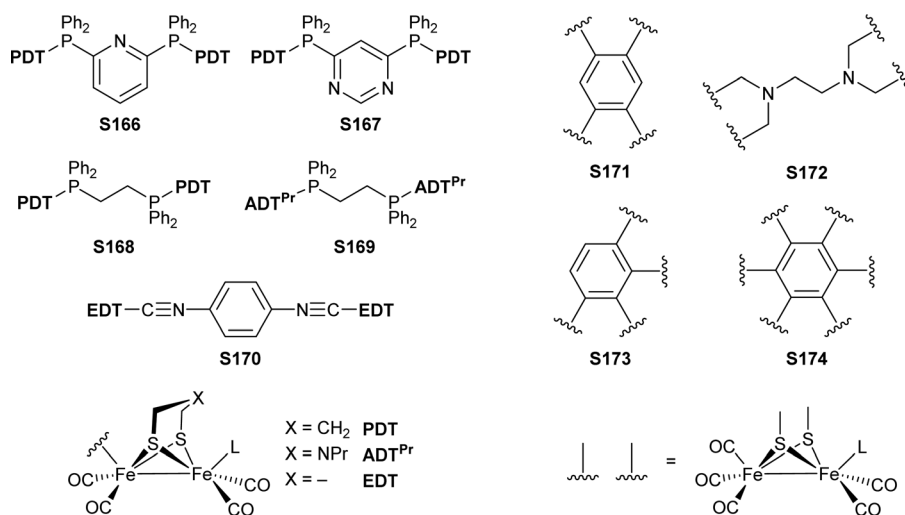
Table 20 Other models with monodentate thiolates

Thiolate	Ligands: Fe₁//Fe₂	Solvent	$E_{pc}(Fe^IFe^I/Fe^IFe^0)$/V	$E_{pc}(Fe^IFe^0/Fe^0Fe^0)$/V	$E_{pa}(Fe^IFe^I/Fe^IFe^{II})^a$/V	Ref.
S161		MeCN	−1.29	−1.73	+0.74	264
S162		MeCN	−1.22	−1.68	+0.88	264
S163		MeCN	−1.24	−1.71	+0.75	264
S164		MeCN	−1.19	−1.66	+0.77	264
S157		MeCN	−1.44	−2.26	+0.81	265
S158		MeCN	−1.51	−2.42	+0.93, +1.06	265
S159		MeCN	−1.35	−2.11	+0.79	265
S160		MeCN	−1.55	−2.29	+0.73, +1.08	265
S160	PMe₃//PMe₃	MeCN	−2.08	−2.45	−0.23, +1.03	265
S165		MeCN	−1.33		+0.61	495
S165	PMe₃	MeCN	−1.49		+0.31	495
S165	P(p-C₆H₄OMe)₃	MeCN	−1.66	−2.37	+0.29, +1.00	496
S156		MeCN^b	−1.73	−2.37		141
S154		DMF	−1.25^c	−1.64		497
S155		DMF	−1.20^{cd}	−1.60		497

^{a} Second oxidation corresponds to- Fe^{I}Fe^{II}/Fe^{II}Fe^{II}. ^{b} Under CO. ^{c} Reported *vs.* SCE. ^{d} Average for *syn* and *anti*-isomer.

Table 21 Other models with two or more [2Fe–2S] units

Unit	Ligands L	Solvent	$E_{pc}(Fe^IFe^I/Fe^IFe^0)^a$/V	$E_{pa}(Fe^IFe^I/Fe^IFe^{II})^e$/V	Ref.
S166	CO, CO	DCM	−2.06^b		305
S167	CO, CO	DCM	−2.04, −2.25^b		305
S168	CO, CO	DCM	−1.94^c	+0.67	183
S172	CO, CO	MeCN	−1.59^b	+0.58	177
S169	CO, CO	DCM	−1.93^c	+0.62	183

1754 | *Chem. Soc. Rev.*, 2021, **50**, 1668–1784

This journal is © The Royal Society of Chemistry 2021

Table 21 (*continued*)

Unit	Ligands L	Solvent	$E_{pc}(Fe^IFe^I/Fe^IFe^0)^a$/V	$E_{pa}(Fe^IFe^I/Fe^IFe^{II})^e$/V	Ref.
S170	CO, CO		$-1.65, -1.82$	$+0.50, +0.85$	204
S171	CO, CO	DCM	$-1.38,^d -1.66^d$		235
S171	CO, PPy$_3$	DCM	$-1.42,^d -1.70^d$		235
S171	PPy$_3$, PPy$_3$	DCM	$-1.47,^d -1.79^d$		235
S173	CO, CO	DCM	$-1.40,^d -1.66^d$		235
S174	CO, CO, CO	DCM	$-1.33,^d -1.56,^d -1.81^d$		236

^{a} More than one Fe^{I}Fe^I/Fe^{I}Fe^0 steps possible. ^{b} Involving ligand reduction. ^{c} Reported *vs.* 0.001 M Ag/AgNO$_3$. ^{d} All values involving 2e$^-$. ^{e} Electron count not defined.

Table 22 Oxidised models
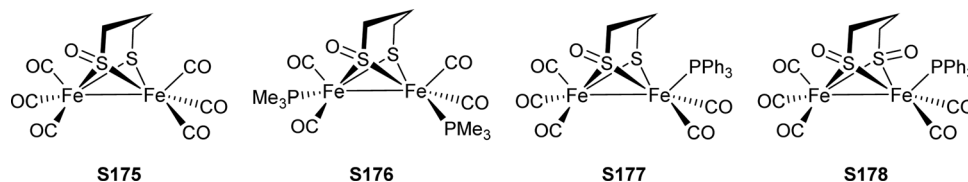
Complex	Solvent	$E_{pc}(Fe^IFe^I/Fe^IFe^0)$/V	$E_{pc}{}^a$/V	$E_{pa}(Fe^IFe^I/Fe^IFe^{II})$/V	Ref.
S175	MeCN	-1.58	$-1.70, -2.25$	$+0.95$	215
S176	MeCN	-2.21	-2.38	$+0.03$	215
S177	MeCN	-1.77	$-1.97, -2.3$	$+0.48$	215
S178	MeCN	-1.72	-1.98	$+0.65$	215

^{a} Further undefined reductions.

Table 23 Photocatalytic efficiencies of the diiron subsite models

Catalytic site	Sensitizer	Electron/proton source/solvent	TON	TOF	Ref.
105	ZnTPP	2-Mercaptobenzoic acid, CF$_3$COOH in CH$_2$Cl$_2$	0.16		528
91	Re(imidazo[4,5-*f*]-1,10-phenanthroline) (4-(phenylethynyl)pyridine) (CO)$_3$-Fc	Ascorbic acid CH$_3$CN	0.35		527
170	ZnPn$_3$PhP	*p*-Anisidine, CF$_3$COOH toluene	0.5		248
170	Modified ZnTPP	2-Mercaptobenzoic acid, CF$_3$COOH CH$_2$Cl$_2$	0.56		252
150	[Ru(bpy)$_3$]$^{2+}$	Ascorbic acid DMF/H$_2$O	200	2.7 h^{-1}	537
91	[Ru(bpy)$_3$]$^{2+}$	Ascorbic acid CH$_3$CN/H$_2$O	4.3		536

This journal is © The Royal Society of Chemistry 2021

Chem. Soc. Rev., 2021, **50**, 1668–1784 | 1755

6.6 Electrocatalytic proton reduction by H-cluster models

Besides the basic redox properties, the function of numerous diiron various complexes in the presence of a proton source was analysed. Although water is considered to be an ideal proton source and electrolyte, aqueous conditions are mostly not attainable for the catalysis tests due to the insolubility and instability of the mimics (Section 4.6). As a result, artificial Fe_2S_2 systems are commonly studied in various organic solvents (MeCN, DCM, THF, DMF) in presence of acids of varying strengths, *e.g.* organic acids (CH_3COOH, CF_3COOH, HOTs, Pivalic acid) or $HBF_4 \cdot OEt_2$. While native [FeFe]-hydrogenases catalyse the proton reduction starting from the $Fe^{II}Fe^{I}$ H_{ox} state (Section 3.1), the active site mimics mostly possesses an inactive $Fe^{I}Fe^{I}$ resting state and reveal HER activity only upon their reduction (Section 4.7). Studying the proton reduction mechanisms of the subsite models is thus important to develop an in-depth understanding of the underlying principles and to design an "ideal", optimized artificial catalytic system.

Although the specific mechanism varies between different complexes and depends upon various factors, the general pathways for the proton reduction by subsite analogues are present and highlighted in Fig. 97. Their combination depends on the applied complex as well as acid utilized. Also, it is to be noted that the $L_nFe_2^{x,x}H$ state does not specifically represent protonation at the metal centre, rather it represents unspecific protonation of the subsite model.

As discussed in the previous sections, hexacarbonyl mimics in their $Fe^{I}Fe^{I}$ state rarely undergo direct protonation. However, if the carbonyl ligands are substituted by electron donating ligands (phosphines (PMe_3, $P(OEt)_3$, dppe, dppm, dppv, carbenes (IMe, IMes), cyanide – Section 5.3.2), the Fe centre(s) becomes basic enough to undergo a direct protonation[150,151,154,454] resulting in $[L_nFe_2^{II,I}H]$ or $[L_nFe_2^{II,II}HH]$. Elsewise, models

undergo one- or two-electron reduction steps affording the $L_nFe_2^{I,0}$ or $L_nFe_2^{0,0}$ state. These states show greater affinity for protons due to their increased electron density/basicity at the metal centres and hence are readily converted to the hydride intermediates $L_nFe_2^{I,I}H$ or $L_nFe_2^{I,0}H$ even in the presence of weaker acids such as HOAc.[135,151,186,239,242,466] Further protonation of the hydride intermediates then results in the formation of dihydride intermediates $L_nFe_2^{II,I}HH$ or $L_nFe_2^{I,I}HH$ and hydrogen might then be released from a two-electron reduced double-protonated intermediate involving either a dihydrogen or dihydride species. Cleavage of H_2 then reforms the starting complex $L_nFe_2^{I,I}$.

Notably, the presence of an additional basic site (*e.g.* adjacent amines) within the subsite analogues was shown to affect the overall catalytic mechanism. In such cases, ligand protonation can be kinetically favoured and then dominantly occur. Usually, such a protonation is then followed by an intramolecular proton transfer to the metal centre and eases the catalytic progress through facilitated formation of the hydride state.

A detailed analysis of the proton reduction mechanism can be only derived from a combination of electrochemical, spectroscopic (IR, UV-vis), and spectroelectrochemical data. Notably, the proposed mechanisms were often supported or even forecasted by theoretical calculations that are therefore an anchor stone in these detailed analyses.

6.6.1 Mechanisms of proton reduction by unsubstituted H-cluster models. The electrocatalytic ability of **20** was studied in detail in the presence of HOTs utilizing electrochemical as well as spectroelectrochemical methods.[380,498] DFT calculations assisted in describing the plausible proton reduction.[499] As **20** in the $Fe^{I}Fe^{I}$ state is itself not protonable even by strong acids, the catalytic cycle herein was shown to begin with a $1e^-$-reduction step resulting in a monoanionic $[Fe^{I}Fe^{0}]^-$ state. This intermediate is sufficiently basic to be protonated by HOTs and enables the generation of a bridging hydride intermediate $(Fe^{I}-\mu H-Fe^{0})$ (Fig. 98). Subsequently, this bridging hydride species undergoes a second reduction at potentials milder than -1.59 V (-1.2 V *vs.* SCE) yielding $[Fe^{0}-\mu H-Fe^{0}]^-$. This double-reduced state can then undergo further protonation either at the metal centre resulting in breaking of the metal–metal bond and leads to formation of a dihydridic $Fe^{II}Fe^{II}$ state. Likewise, the formation of an intermediate possessing a bridging hydride as well as carbonyl with concomitant Fe–S bond cleavage and protonated sulphur was suggested.[380,498,499] This thiol carrying intermediate, on further reduction at $E = -1.84$ V (-1.45 V *vs.* SCE) generates an anionic species, which releases H_2 and transforms back to the singly reduced $[Fe^{I}Fe^{0}]^-$ state ($K = 1.7 \times 10^8$).

On the other hand, H_2 release from the dihydride intermediate of $Fe_2(pdt)(CO)_6$ is slow ($K = 10^4$ *vs.* 1.7×10^8).[380,498,499] Notably, when $Fe_2(pdt)(CO)_6$ was assessed in the presence of weaker acids such as AcOH, the catalysis progressed *via* a $Fe^{0}Fe^{0}$ state formed at more negative potentials -2.35 V.[466]

Contrary, as the azadithiolate models possesses a basic amine, the catalytic cycle can start with an initial protonation step of the bridgehead followed by a single-electron reduction.
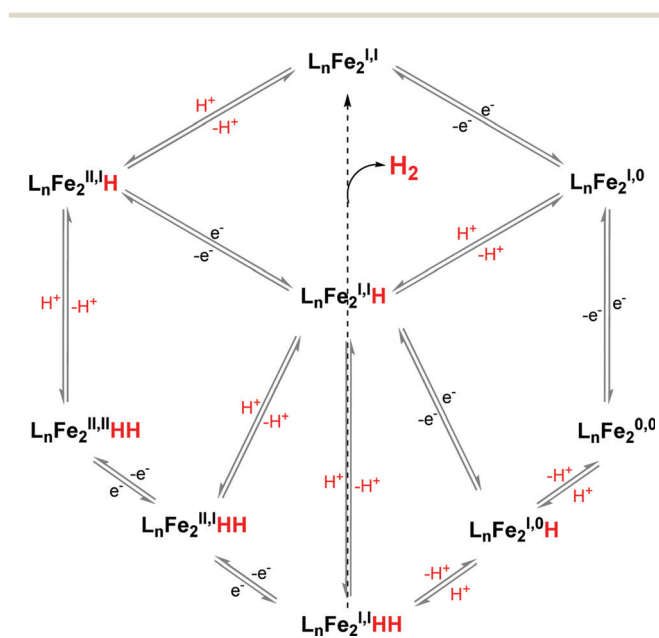

Fig. 97 Commonly observed electron and proton transfer pathways facilitated by subsite models.
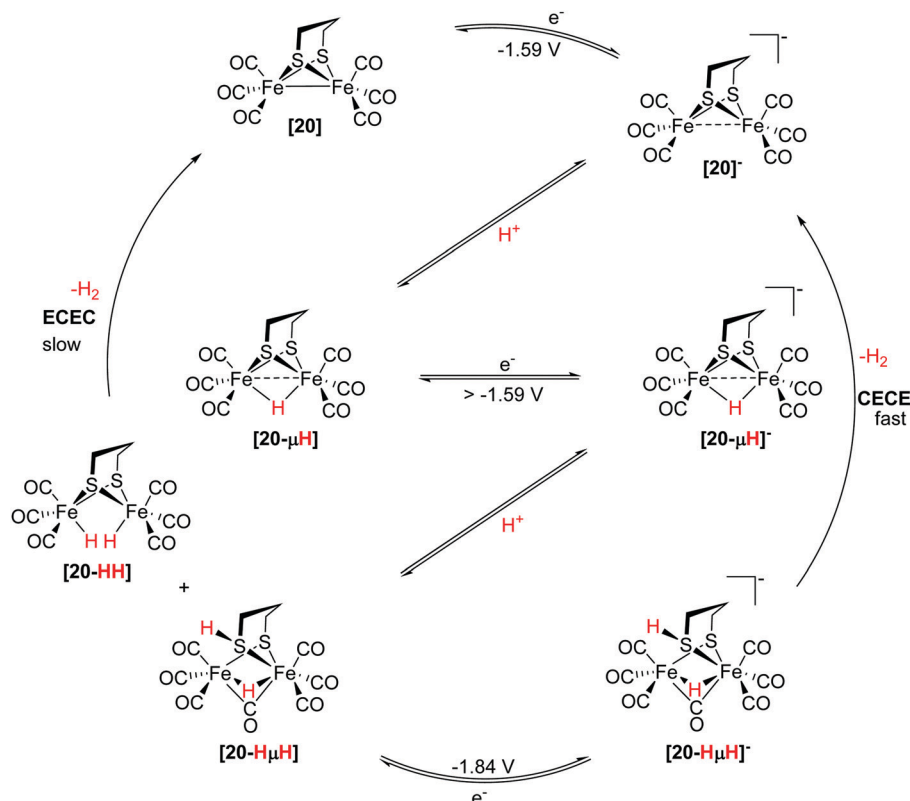
1756 | *Chem. Soc. Rev.*, 2021, **50**, 1668–1784

This journal is © The Royal Society of Chemistry 2021

Fig. 98 Catalytic pathway for proton reduction by $Fe_2(pdt)(CO)_6$.

However, the protonation behaviour of azadithiolate modified models strongly depends on the basicity of the bridgehead amine (and with it the substitution thereon) and strength of the employed acid. The interplay between these factors greatly affects the mechanism of the proton reduction. For instance, **2** is protonated with moderately strong acids such as HOTs (or Cl_3CCOOH) at the bridgehead nitrogen leading to inter-mediate $[2\text{-}NH]^+$ which undergoes reduction at -1.27 V. Hereafter, the Fe site is rendered more basic than the amine (ΔpK_a 3.3). Thus, internal H^+ transfer takes place leading to a metal protonated-terminal hydride state $[2\text{-}NtH]$ (Fig. 99 scheme A).[500] Contrastingly, for N-protonated intermediates of $Fe_2(adt^R)(CO)_6$ (R = iPr, $CH_2CH_2OCH_3$), no such tautomeri-sation is observed. The high electron density at the bridgehead nitrogen by the electron donating substituents was suggested to restrict the H^+ transfer. Furthermore, as depicted in Fig. 99 scheme B, the reduced $[2\text{-}N^RH]$ intermediate takes up a second proton and subsequently yields the bridging hydride state $[2\text{-}N^RH\mu H]^+$ which after additional $1e^-$ reduction regenerates the Fe^IFe^I state. Moreover, with stronger acids such as $HBF_4 \cdot OEt_2$ further protonation of the $[2\text{-}N^R(H)_2]$ gives an $[2\text{-}N^R(H)_3]^+$ state and regenerates the singly protonated reduced species $[2\text{-}N^RH]$ upon reductive H_2 elimination (Fig. 99 scheme B').[458,501,502] In the case of **2**, after the terminal hydride state is achieved, the catalytic cycle proceeds with a second protona-tion step resulting in double-protonated state $[2\text{-}NHtH]^+$. Further reduction of this species gives $[2\text{-}NHtH]$, which releases H_2 and achieves the Fe^IFe^I state (Fig. 99 scheme A).

Notably, when utilizing weaker acids (*e.g.* CH_3COOH), $Fe_2(adt^R)(CO)_6$ models adopt a pathway similar to the PDT derivatives (Fig. 99 scheme C). Here the model must take up electrons before being protonated and the adjacent amine is not involved in the overall hydrogen formation mechanism. *E.g.*, $Fe_2(adt)(CO)_6$ is protonated by $ClCH_2COOH$ ($pK_a = 15.3$) at the metal centre ($pK_a = 17.1$) only upon undergoing $1e^-$ reduction at -1.60 V. There is also a possibility to establish a concerted proton electron transfer pathway resulting in $[2\text{-}NHtH]$ from $[2\text{-}NtH]^+$ (Fig. 99 scheme C'). However, this pathway has not been explored in detail and thus will not be further discussed.[500]

Underlining the control of acidic strength on the catalytic pathway, $Fe_2(adt^R)(CO)_6$ (R = p-C_6H_4COOMe, **301**)[460] was shown to adopt two different pathways for the proton reduction depending on the strength of the utilized acid. In case of CF_3COOH, the complexes follow an ECCE mechanism as the reduced state can be protonated twice. Subsequent reduction generates H_2. Contrarily, with HOAc an EECC mechanism is observed. Herein, only the dianionic complex of the models is basic enough to be protonated by weak acids and conse-quently H_2 is only released at very negative potentials.[491] The catalytic efficiencies with CF_3COOH (TON = 10.6) were shown to be larger than with HOAc (TON = 4).[460] Similarly, in case of a missing suitable protonation site, it is justified that the double-reduced species is protonated generating H_2 *via* an EECC mechanism with weak acids. Hereby it can be ascer-tained that the weaker acid (HOAc) requires the Fe^0Fe^0 state
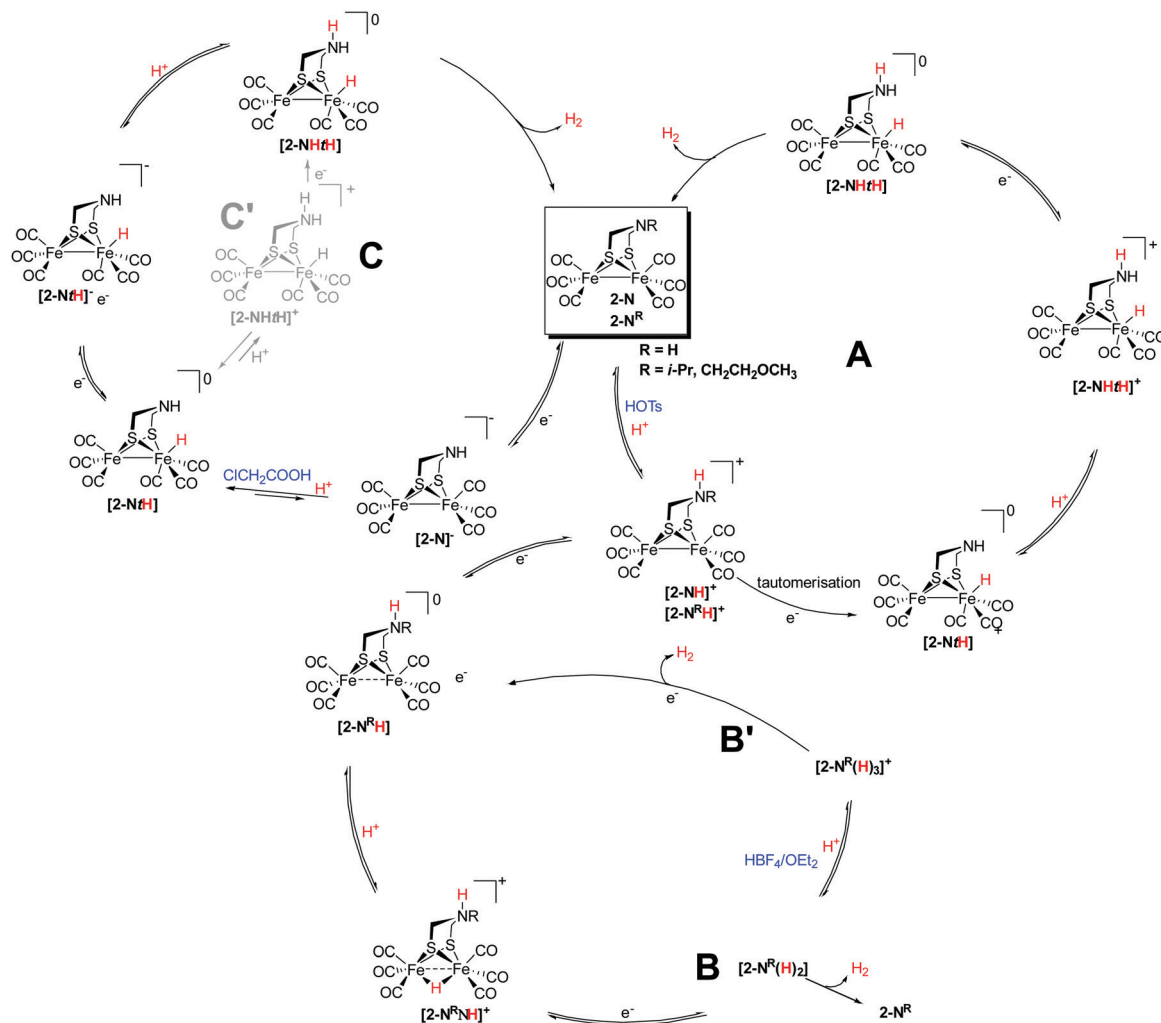
This journal is © The Royal Society of Chemistry 2021

Chem. Soc. Rev., 2021, **50**, 1668–1784 | **1757**

Fig. 99 Catalytic pathways for the proton reduction by $Fe_2(adt)(CO)_6$ and $Fe_2(adt^R)(CO)_6$ analogues with acids of varying strength.

for catalytic activity.[134,190,192,195,466,481] Contrastingly, the presence of a stronger acid such as HOTf, $HClO_4$ or $HBF_4\cdot OEt_2$ leads to a CEEC mechanism.[177,194,196,456,481]

As discussed in Section 4.3, BDT models possess a metal site that is sufficiently electron deficient and hence readily undergo a $2e^-$-reduction yielding the Fe^0Fe^0 state. This state participates in the catalytic cycle, generating H_2 from HOAc upon double-protonation following an EECC mechanism. However, with HOTs the monoanionic mono-protonated state formed undergoes another reduction resulting in dianionic state, which only then releases H_2 and reforms the Fe^IFe^0 state (Fig. 100).[467,468]

A similar observation was made for phosphorus-substituted model **64**. In the absence any of acid, model **64** is reduced *via* a concerted two-electron process. Contrary, when HOTs is added, the double-reduced state undergoes two successive protonation steps to yield a dihydride. Herein, each iron was suggested to bind a hydride affording [**64-2***t***H**]. Upon release of H_2, this state reverts back to Fe^IFe^I. Another plausible route involves a one-electron reduction of [**64-2***t***H**] resulting in the monoanionic state with concomitant H_2 evolution. The former pathway is
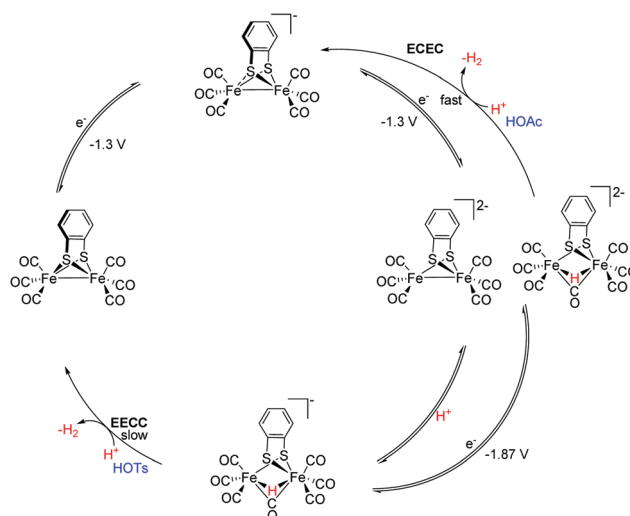

Fig. 100 Catalytic pathway for proton reduction by **149**.

considered to eliminate H_2 at slower rates due to the larger spatial separation of the two hydrides in [**64-2***t***H**].[503]

Along this line, **170** catalyses the proton reduction *via* two different pathways from HOTs.

(1) Protonation of the reduced state leads to [**170-H**]. This protonation is followed by another reduction and protonation and results in [**170-HH**]. The thus obtained intermediate can now either directly release H_2 by formation of **170** or undergo further reduction thereby releasing H_2 from [**170-HH**]$^-$ resulting in **170**$^-$.[239]

(2) The naphthalene substituted imine model **302** herein follow a CECE mechanism to reduce protons from HOTs.[251] The acid protonates the imino substituent, resulting in imine protonated state [**302–H**]$^+$, which is reduced at slightly positive potential than the parent model **302** resulting in [**302-NH**]$^+$. [**302-NH**]$^+$ undergoes a second protonation followed by reduction to give [**302-HNH**]$^+$ which releases H_2.[251] Notably, the pyrazine modified models **303**[229] reduce protons from HOAc wherein the aromatic ring nitrogen acts as internal site of protonation. The protonated state undergoes reduction followed by another protonation at the nitrogen. Reduction of the diprotonated state yields the Fe^0Fe^0 state, which evolves dihydrogen and closes the catalytic cycle.

Another example wherein the acid strength influences the proton reduction pathway is the tetranuclear model **164**. When strong acids such as CX_3COOH (X = Cl, F) were employed as the proton source, the dianionic state was rapidly protonated and releases H_2. Contrarily, in the presence of the weaker acid $CH_2ClCOOH$ the mono-protonated dianionic state either undergoes a further two-electron reduction resulting in the [**164**]$^{3-}$ state, which on further reaction with two protons releases H_2 from the [**164-HH**]$^{2-}$ (Fig. 101).[235]

The influence of the ring-substituents on different catalytic pathways for the proton reduction can be demonstrated by **163** and **162** in the presence of $HBF_4 \cdot OEt_2$. In case of **163**, a direct protonation of the model is not observed and was explained by the interaction of the nitrogen lone-pair with the ring sulphur π-electrons. Thus, an EC mechanism for the proton reduction was proposed based on electrochemical data. In contrast, **162** reveals a protonation at the ring nitrogen. This protonation is followed by two 1e$^-$-reduction steps leading to [Fe^0Fe^0N-NH]$^-$, which then reacts back to the parent model upon liberating H_2.[234]

6.6.2 Influence of ligand substitution on the mechanism

6.6.2.1 Models with innocent ligands. To obtain an enhanced basicity at the metal centre and to avoid ligand protonation related complications, numerous models with innocent phosphine and carbene ligands have been designed (Section 4.7). These substituted models have more negative reduction
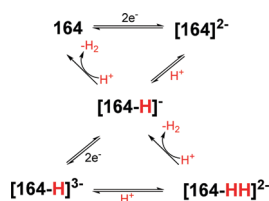

Fig. 101 Catalytic pathway displayed by tetrametallic complex **164**.

potentials (E_{pc}) than their corresponding hexacarbonyl complexes. Compensating this trend, their catalytic potentials (E_{cat}) are, however, often anodically shifted. Due to the increased basicity of the metal core, the models are readily protonated at the metal centre resulting in terminal hydrides or along the metal–metal bond yielding bridging hydrides.[445] These protonated intermediates undergo facile reduction. Notably, **219pdt** follows the CECE catalytic pathway involving the [**219pdt-µH**] state.[153] The $P(OMe)_3$ disubstituted complex and similar complexes follow a CE pathway for proton reduction.[482,485]

Notably, the bridgehead amine in $Fe_2(adt^R)(CO)_{6-n}(L)_n$ (R = Ph, C_3H_6COOH L = PMe_3) remains the favoured protonation site.[151,191,210,455] However, the electrochemical activity of the hexacarbonyl and phosphine disubstituted complexes differ significantly. In case of unsubstituted models, the protonation exclusively occurs at the bridgehead nitrogen, while in diphosphine substituted models the direct protonation at the Fe–Fe bond is possible as well resulting in potential catalysis CECE pathways. Interestingly, PMe_3 mono- and disubstituted analogues of **109** and **110**, with *n*- and isobutyric acid *N*-substitutions, were reported to even use water as proton source and revealed catalytic activity under neutral conditions at approx. -2 V (Fig. 106).[191]

In the proposed catalytic enzymatic pathways, the terminal hydride state is of key relevance for the hydrogen development (Fig. 19–21). Nevertheless, this state is rarely observed for hexacarbonyl complexes. However, unsymmetric substitution patterns at the diiron centre, with electron donating ligand were shown to assist in achieving such terminal hydride (see Section 5.3). Barton and Rauchfuss investigated model **233pdt** and found that addition of $HBF_4 \cdot OEt_2$ to a solution of **233pdt** in DCM at 0 °C resulted in a terminal hydride state. Notably, this complex catalyses proton reduction at -1.49 V compared to -1.78 V for the bridging isomer.[154] Furthermore, the catalytic cycle proceeds with a second protonation of the one-electron reduced terminal hydride species followed by the release of H_2. Subsequent reduction at less negative potentials regenerates **233pdt**. In contrast to the bridging hydride [**233pdt-µH**]$^+$, the model [**233pdt-*t*H**]$^+$ comprising a terminal hydride is capable of generating H_2 with a TOF of 5 s^{-1} with $HBF_4 \cdot OEt_2$.[154]

Likewise, the adt counterpart, (**233adt**), was investigated for its catalytic activity in DCM using acids of different strengths ($ClCH_2COOH$ (pK_a = 15.30), CF_3COOH (pK_a = 12.65) and $HBF_4 \cdot OEt_2$ (pK_a > 2)) at 0 °C (Fig. 102).[451] In all cases, the catalytic cycle begins with a protonation of the bridgehead amine, followed by an intramolecular proton transfer to the metal centre to afford [**233adt-*t*H**]$^{2+}$. With $ClCH_2COOH$, the cycle proceeds with the reduction of [**233adt-*t*H**]$^+$ to afford [**233pdt-*t*H**] which upon protonation and another reduction releases H_2.[451,504] With stronger acids (*e.g.* $HBF_4 \cdot OEt_2$ or CF_3COOH), the bridgehead amine of [**233adt-*t*H**]$^+$ is protonated further and the reduction of the double-protonated species gives a [**233adt-η^2-(H)$_2$**]$^+$ intermediate state. This state then returns to the Fe^IFe^I state upon reductive loss of H_2. Moreover, this study also highlights the catalytic importance of the terminal hydride states and shows that terminal-hydride species generate H_2 much faster (TON 5000 s^{-1} at -1.49 V)

This journal is © The Royal Society of Chemistry 2021

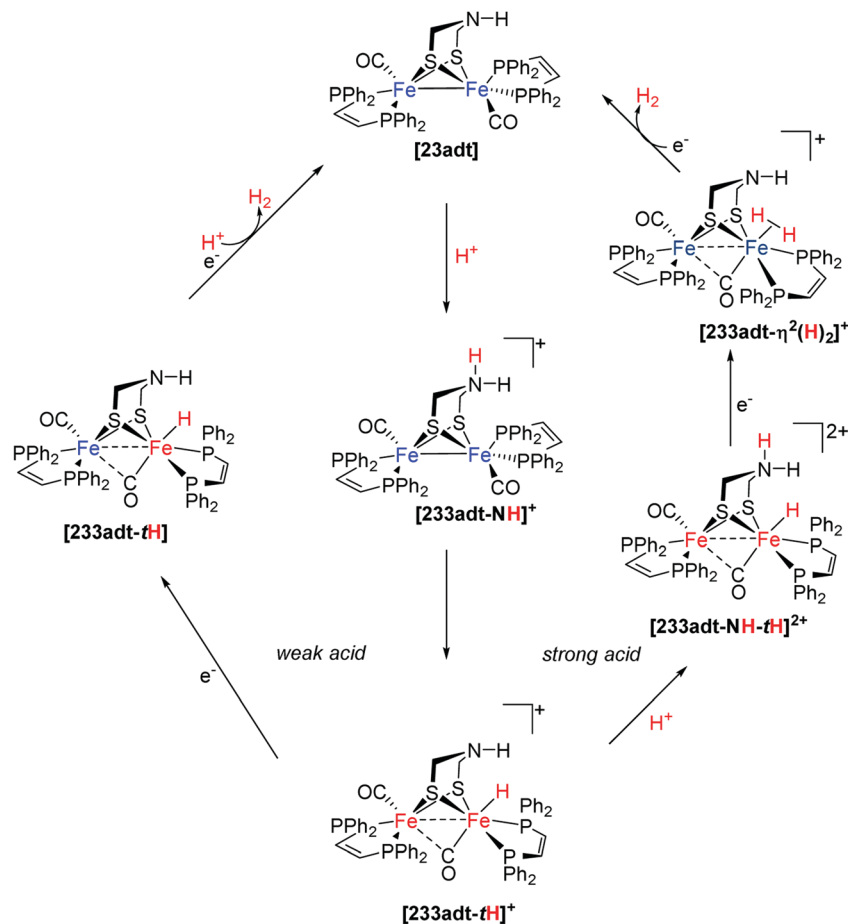*Chem. Soc. Rev.*, 2021, **50**, 1668–1784 | **1759**

Fig. 102 Catalytic pathways adopted by **233adt** in presence of acids of different strength.

as compared to the bridging congeners (TON = 20 at −1.72 V).[451,504]

Likewise, the phosphine and carbene substituted asymmetric model $Fe_2(pdt)(CO)_4(\kappa^2\text{-}I_{Me}(CH_2)_2PPh_2)$ (**304**) forms a terminal hydride at low temperature (−90 °C) with $HBF_4 \cdot OEt_2$. Notably, this terminal hydride is inaccessible at room temperature.[450] It was suggested that catalysis proceeds *via* the bridging hydride intermediate. Other carbene-substituted models, which have been studied for proton reduction, also proceed with a CE mechanism for H₂ formation, majorly proceeding *via* μ-H state with moderately strong acids (CF_3COOH)[197,363] as well with strong acids $(HBF_4 \cdot OEt_2)$.[291]

6.6.2.2 Models with protonable ligands. Besides the protonation of the bridgehead amine in adt-subsite models, a basic residue can be also present at the additional coordinating ligands.[152,505] Active site analogues having proton responsive ligands such as PNP, pyridine and bipyridine attracted interest and the pendant basic sites were anticipated to relay protons to the metal centre and aid the proton–hydride formation for efficient H₂ release (Fig. 103).

Herein, **294Me** undergoes N-ligand protonation upon protonation with $HBF_4 \cdot OEt_2$ in acetone. Remarkably, in DCM a tautomerism resulting in μ-H was observed.[152] A similar proton

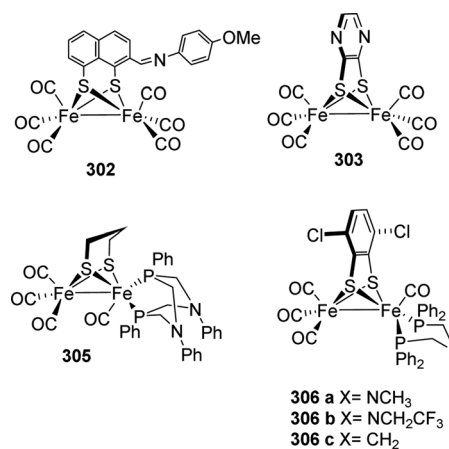**Fig. 103** Structure of selected models discussed in this section.

migration was observed for $Fe_2(pdt)(CO)_4(\kappa^2\text{-}L)$ (**305**, L = $(PhP(CH_2)_2NPh)_2)$ with CX_3SO_3H (X = F, H) resulting in the catalytically active μ-H state.[461] In **294R** (R = Ph, Me), the pendant basic site is rendered free to take up additional protons after transfer of proton to the metal centre. Although proton transfer reactions to the metal centres are observed and cause an anodic shift of the catalytic potential. Yet, the rate

1760 | *Chem. Soc. Rev.,* 2021, **50**, 1668–1784

This journal is © The Royal Society of Chemistry 2021

constants for HER are low due to sluggish proton transfer and H_2 release.[352]

Along this line, **306a–c** with similar diphosphine ligands $((Ph_2PCH_2)_2X$, X = NCH_3 (**a**), NCH_2CF_3 (**b**), CH_2 (**c**)) was examined. The study displays the proton directing influence of the chelating ligand. In case of **306a**, the amine was protonated with $HBF_4 \cdot OEt_2$, while in **306b** a hydride bridging the Fe centres was observed. In contrast, in case of **306c** which lacks an amine group, protonation at the bridging sulphur was detected.[225] Thus, it seems that pendant basic sites are not the first choice for protonation and the sequence of protonation depends on strength of acid and the corresponding basic site in the mimic. This preference was also illustrated by **307a,b** $(Fe_2(pdt)(CO)_5(PPh_2(CH_2)_nPy)$ ($n = 0$ (**a**), 1 (**b**)), wherein protonation with HOTf occurs primarily at the Fe–Fe bond and only thereafter at the N-pyridyl in the phosphine ligand.[505] Also, it is to be noted that a secondary sphere protonation might not always be fruitful, *e.g.* while the PTA ligand (1,3,5-triaza-7-phosphaadamantane) is protonated, this protonation is catalytically not very relevant.[302] Likewise, $[Fe_2(pdt)(CO)_5(CN)]^-$ (**215**) undergoes protonation with HOTs at the cyanide ligand but displayed no significant catalytic activity.[153] In contrast, $[Fe_2(adt)(CO)_5(CN)]^-$ (**308**) was found to be catalytically active with HOAc (as well with $Cl_2CHCOOH$). The detailed catalytic mechanism remains to be elucidated – however, the difference in catalytic activity of **215** and **308** could be reasoned by the involvement of bridgehead nitrogen.[478]

Notably, the unsymmetrical model $[Fe_2(pdt)(CO)_4(CN)(PMe_3)]^-$ (**214**) exhibits proton reduction activity in the presence of acids (HOTs, H_2SO_4) at -1.4 V (-1.0 V *vs.* NHE). IR and ^{1}H-NMR spectroscopic investigation revealed direct protonation of the Fe–Fe bond affording a bridging hydride. On further reaction with HOTs, protonation of the coordinated cyanide likewise occurs.[150] The double-protonated species undergoes reduction resulting in mixed-valent state which heterolytically releases H_2. Notably, no external protons were required to move the cycle forward from the $[HFe^{1.5}_2(pdt)(CO)_4(CNH)(PMe_3)]$ state. Thus, H_2 was released upon intramolecular hydride transfer. In contrast, the direct congener, $[\mathbf{219pdt}\text{-}\boldsymbol{\mu}\mathbf{H}]^+$ [423,424] requires additional protons to slowly form H_2. Moreover, $[Fe_2(pdt)(CO)_4(P(OMe)_3)(CN)]^-$ (**309**) is protonated solely at the cyanide ligand by HOTs, while $HBF_4 \cdot OEt_4$ protonates the complex at the metal centre as well as the ligand. Yet, the model displayed no catalytic activity.[153] These examples clearly demonstrate the control of reactivity *via* the ancillary ligand protonation and highlights that the catalytic activity is achieved through a crucial electronic balance around the metal centres and efficient proton relays from non-remote transferring basic sites.[150,153]

Evidently, for $Fe_2(bdt)(CO)_6$ the introduction of one or two pyridyl-appended phosphine ligands (PPy_3) proved to be extremely beneficial. Not only does the pyridyl site act as a potential site of protonation, but also solubilizes the complex in aqueous conditions. Having achieved a precise balance of the increased electron density at the Fe centre from phosphine ligands and a proximal protonation site, the mimic displays a $TOF = 1.8 \times 10^7$ s^{-1}

at -0.90 V *vs.* NHE for $Fe_2(bdt)(CO)_5(PPy_3)$ (**310**) and 2.7×10^8 s^{-1} at -0.97 V *vs.* NHE for $Fe_2(bdt)(CO)_4(PPy_3)_2$ (**311**) with dilute H_2SO_4.[506]

6.6.2.3 Models with redox-active ligands. The active machinery of the enzyme comprises a cubic [4Fe–4S]-cluster attached *via* cysteinyl ligand to the [2Fe–2S]-core. Subsequently, surrogates for the cubic cluster were investigated. With an exception of the appended [4Fe–4S]-cluster to a [2Fe–2S]-model reported by Pickett *et al.*,[416] no such elaborate artificial systems have been reported. Instead, mimics with smaller and less complicated redox active ligands such as bipyridyl,[371,507] phenanthroline[507] and phosphole[493] have been designed.

Also, in the IMes-substituted pdt complex **248** the presence of the NHC ligand alters the general pathway of the proton reduction. Due to involvement of the IMes ligand, **248** undergoes two successive reduction steps and the first reduction takes place at the metal centre, while the second occurs at the ligand. Hence, it was proposed that **248** follows an EECC mechanism and thus is able to generate H_2 from weak acids. Following this double-reduction, protonation at the Fe site forms [H–Fe^{II}Fe^I]. This state undergoes a second protonation along with concomitant internal electron transfer regenerating a Fe^{I}Fe^I state along with H_2 evolution.[362] A similar proton reduction mechanism was noted for in the presence of a bipyridyl ligand in complex **312**.[371] Herein, the generated dianion is protonated by AcOH. In contrast, in the presence of strong acids such as $HBF_4 \cdot Et_2O$ and HOTs, **312** displays different of proton reductions behaviour (Fig. 104). Due to the bipyridyl ligand, the electron density at the FeFe centre is significantly increased and the metal–metal bond is protonated by the stronger acids resulting in a bridging hydride state $[\mathbf{312}\text{-}\boldsymbol{\mu}\mathbf{H}]^+$. The reduced species $[\mathbf{312}\text{-}\boldsymbol{\mu}\mathbf{H}]$ is then protonated,
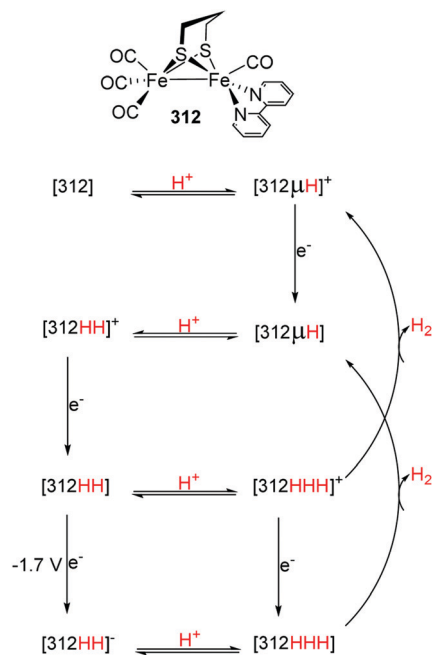
Fig. 104 Catalytic pathway for HER from $HBF_4 \cdot OEt_2$ by **312**.[371]

This journal is © The Royal Society of Chemistry 2021

Chem. Soc. Rev., 2021, **50**, 1668–1784 | **1761**

followed by another electron and proton uptake resulting in [**312-3H**]$^+$ which on reductive elimination gives H$_2$. However, this pathway did not account for the catalytic peak observed at -1.7 V. Therefore, it was proposed that [**312-HH**] undergoes a single-electron reduction at this potential to yield [**312-HH**]$^-$. This state is then converted to [**312-3H**] upon protonation which on releasing H$_2$ forms the [**312-μH**] state.[371] Hence, in the presence of strong acids either [**312-μH**]$^+$ is the proton reduction catalyst and operates *via* a ECEC or [**312-μH**] following a CECE mechanism.

Another example wherein the ligand actively participates in the catalytic pathway is **313** modified with a phosphole. The complex displays three cathodic peaks – the first corresponds to the reduction of the ligand.[493] The other two peaks are associated with two single-electron transfers to the diiron centre resulting into Fe^{0}Fe^0. According to spectroelectro-chemical and theoretical modelling data, the catalytic cycle is initiated by a proton-coupled electron transfer and proto-nation occurring at -1.44 V. Here, protonation occurs at the Fe centre, leading to a mixed valent bridging hydride state [Fe^{II}Fe^{I}μ-H] and another at the pyridine nitrogen of the ligand, which serves as the second protonation site. This double-protonated state undergoes a second two-electron reduction at -2.00 V accompanied by another ligand proto-nation (Fig. 105). This state was determined to be the resting state of the catalyst. The protonation and subsequent release of H$_2$ from this state is the rate-determining step of the reaction. Hence, in this cycle the ligand serves as an electron reservoir and is involved in electron transfer to the metal centre. Additionally, **313** also catalyses proton reduction from dilute H$_2$SO$_4$ with an overpotential of 0.66 V and TOF 7×10^4 s^{-1}.[493]

In addition to the aforementioned models, many other mimics with redox active ligands such (bma = 2,3-bis(diphenylphosphino)
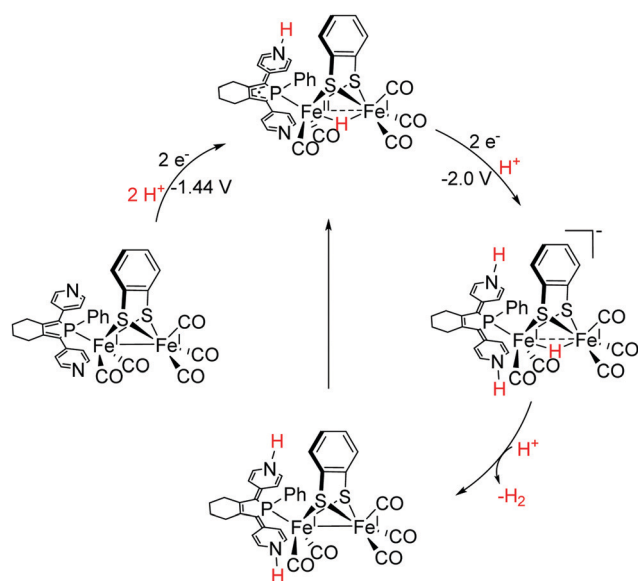
maleic anhydride (bma), bpcd (4,5-bis(diphenylphosphino)-4-cyclopenten-1,3-dione)),[311,313,314,508] fullerene,[509] ferrocene[312,349] and carborane bis-phosphine[510] have been reported. However, involvement of these redox active moieties in catalytic mechanisms is either questionable or remains to be investigated in detail.

Based upon numerous detailed investigations of hydrogen evolution activity by diverse Fe^{I}Fe^I subsite models, the observed trends and generic behaviour can be summarised as follows:

• To enable H$_2$ evolution from weak acids by hexacarbonyl models, these complexes are required to undergo reduction before being protonated.

• CO-substitution by stronger donating ligands such as phosphines or carbenes cause the diiron core to attain increased basicity. Thus, the catalytic cycle may begin *via* direct metal protonation.

• If there is an accessible basic site available in the model complex and an acid of suitable strength is employed, the catalytic cycle is facilitated by its protonation.

• Involvement of a redox active ligand can cause a double reduction to occur, *i.e.* one at the metal centre and another at the attached ligand before the model is protonated.

• In case of bidentate substitution at the Fe centre, the chelating isomer is reported to be more efficient for H$_2$ generation than the symmetrically substituted bridging counterpart.

• pK_a of acid used as the proton source determines the adopted catalytic pathway for H$_2$ evolution and has profound influence on the catalytic activity and over-potentials.

Conclusively, extensive electrochemical analysis revealed various mechanisms (EECC, ECEC, ECCE, CECE, CEEC) and shed light on the involved iron centres redox behaviour within the H$_2$ evolution activity in acidic media.

6.6.3 Influence of water as solvent on the mechanism. Numerous model complexes with modified secondary sphere have been designed to realise catalysis in aqueous electrolytes.[165,511–514] Many of these systems are also photocatalytically active and will be discussed in Section 7. Thus for the Fe^{I}Fe^I models to achieve electrocatalysis in presence of water, the bridgehead groups were modified (Section 4.1) or ligands assisting in solubility and stability were appended.[302,486] Herein, introduction of functiona-lized sugar on the diiron core hexacarbonyl, resulted in **33** & **34**. These models were soluble in H$_2$O : CH$_3$CN (5 : 1) and were found to be catalytically active in presence of acetic acid at potential of *ca.* -1.6 V for **38** and *ca.* -1.8 V for **39** (*vs.* Ag$^{+/0}$ 0.01 M AgNO$_3$).[133]

Attempts to achieve proton reduction catalysis in water are not limited to the modifications of the bridgehead substituents but have been extended to systems with modified ligands such as phosphines[129,130] and peptides.[306] Herein, tris(morpholino)-phosphine (TMP) mono and disubstituted pdt models were tested for their proton reduction capabilities in different water : acetonitrile mixtures in the presence of AcOH.[129] Both models proved to be electrocatalytically active operating *via* ECCE mechanism. Similar effects were reported for the introduction of a charged, quarternary ammonium-modified PNP ligand, enabling H$_2$ production from HOAc in MeCN following the same mechanism.[130] First, the reduced monoanion [Fe^{I}Fe^0]$^-$ is protonated resulting in [H-Fe^{II}Fe^I] which on further

Fig. 105 HER by **313** with an appended redox active ligand from Et$_3$NHBF$_4$ in DCM.

1762 | *Chem. Soc. Rev.*, 2021, **50**, 1668–1784

This journal is © The Royal Society of Chemistry 2021

Fig. 106 Proton reduction in H$_2$O by model **110PMe$_3$**.[191]

protonation produces [HH-Fe^{II}Fe^{I}]$^{+}$. This species generates H$_2$ upon reduction and the starting complex is regenerated. Notably, an increased catalytic activity (TON$_{bridging}$ = 14.4 in MeCN *vs.* 25.7 in MeCN:H$_2$O (3:2)) in mixed-solvent systems was reported for these complexes.[129,130] Likewise, electrochemical properties of peptide modified models were significantly affected by presence of water and showed an up to 0.1 V anodic shift in their reduction potentials along with increased catalytic currents.[306]

Furthermore, adt-models **109** to **111** with carboxylic acid functionalities were synthesised and studied for their redox activity to benefit from the hydrogen bonding properties of their carboxylic acid residues. Cathodic scans displayed reduction peaks (*ca.* −1.6 V) which shift about 400 mV towards less negative potentials upon addition of one or two equivalents of HOTf suggesting protonation of nitrogen of the adt-bridge. Notably, complex **109** displayed an additional reduction peak, which was attributed to the proton coupled one-electron reduction process assisted by the carboxylic acid group.[191]

Furthermore, improved, second generation mimics were achieved upon replacing two carbonyls with PMe$_3$ and were tested for their catalytic capabilities in water. Model **110PMe$_3$** showed exclusive enhancement in reductive peak upon addition of one equivalent of water. However, in case of model **109PMe$_3$** a small increasing peak at −1.7 V was observed, with subsequent addition of water which shifted to −1.5 V. Herein, the carboxylate group was involved in stabilising the protonated amine (Fig. 106) *via* hydrogen bonding. Distant orientation of carboxylate in **111PMe$_3$** might, however limit this stabilisation and hence no comparable catalysis for this model was recorded.[191]

6.7 Immobilisation of H-cluster models on electrodes

At the end of Section 4.2.3.1 we already mentioned that carboxylic acid functionalised [FeFe]-hydrogenase models are suitable for the attachment to surfaces. This is based on their reactivity towards amines that might be covalently bound to *e.g.* glassy carbon or fluorine doped tin oxide (FTO) electrodes, forming amides.[141] This general concept to attach a homogeneous catalyst to electrode surfaces to generate immobilised systems was utilised by several groups.[142,515,516] Interestingly the results are diverse. A gold or carbon immobilised pdt-model and a FTO immobilised bdt-model catalyse proton reduction from HBF$_4$·Et$_2$O acidic and chloroacetic acid acidic acetonitrile solutions, respectively but are rapidly inactivated by the loss of carbonyl ligands, catalyst leaching or hydrolysis under these conditions.[515,516] Conversely, no catalytic proton reduction was found for an *o*-xyldt-model that was immobilised *via* a carbon surface bound *p*-tolylformamide.[142] Other immobilisation techniques include formation of triazoles *via* Cu(I)-catalysed Huisgen addition or formation of an Au–S bond *via* thiols.[517–519] Latter includes a pdt-like model that comprises a −PH$_2$(CH$_2$)$_2$SH ligand for the attachment and is therefore the only surface attached model that is not bound *via* the bridging disulphide. Interestingly, thus study revealed that the parent compound **314** is inactive regarding proton reduction in solution, while its immobilised counterpart shows catalytic proton reduction upon addition of acetic acid. This phenomenon was explained by the inability of **314** to undergo a reduction process to a Fe^{0}Fe^I or Fe^{0}Fe^0 species, which was however shown to be at −1.87 V and −2.24 V *vs.* Fc$^{0/+}$, respectively by Liu *et al.* in 2009[215] and is also visible in the respective cyclic voltammograms in the works by Darensbourg and coworkers.[518,519] Four years later, Zaffaroni *et al.* described a 160 mV anodically shifted operational overpotential for the FTO immobilised bdt-model compared to its homogenous counterpart.[516] This kinetic effect due to the binding of an homogeneous catalyst to an electrode surface might have been the reason for the observation of Darensbourg and coworkers

Fig. 107 Schematic presentation of covalent attachment for the [FeFe]-hydrogenase model **314** on modified graphite surfaces. Reproduced from ref. 517 with permission from The Royal Society of Chemistry.

as well. In 2017, Dey and coworkers reported on the first adt-like model that was covalently linked to a graphite electrode surface *via* Huisgen addition (Fig. 107). In the opposite to the systems described above, this system is reported to be stable for several hours under turn-over conditions and shows a high faradaic yield of 90.7% for H_2 evolution after 1200 s.[517]

6.8 Perspective for the electrocatalytic proton reduction by H-cluster models

The electrochemical investigations coupled with theoretical calculations as well as spectroscopic investigations significantly contributed to describe different pathways for proton reduction by the [FeFe]-hydrogenase models. It has to be noted that the strength of the acid employed significantly affects the proton reduction pathways. The models possessing intrinsic bases, such as the bridgehead amine, conduct protonation at milder potentials in comparison to the models lacking such sites. Furthermore, the donating capabilities of the ligands also influences the attainable redox states in the proton reduction catalytic cycles. When the carbonyl ligands are substituted by donor ligands, the reduction potential of the models display cathodic shifts. Accompanying this cathodic shift, the protonation is facilitated due to increased electron density at the metallic centre. A few terminal hydride bearing species have been observed and it has been ascertained that the terminal hydride species are more efficient catalysts in comparison to the thermodynamically more stable bridging hydride state.

Even after the aforementioned advances, challenges to develop systems with matching efficiencies to the natural system exists. Unlike the enzyme, the majority of the models are catalytically active in organic solvents and utilize organic acids to generate H_2. They do not follow the bio-catalytic pathway. Nonetheless the electrochemical studies on the synthetic systems impressively uncovered the interplay between the basicity and reduction potentials of the models and shed light on the hydrogen generation mechanism.

VII Photocatalytic proton reduction by H-cluster models

The development of artificial systems that efficiently mimic the natural photosynthetic pathways and allow for a conversion of solar energy into storable and useable forms has gained major attention.[520–522] Due to their unprecedented H_2 generation capacity, [FeFe]-hydrogenases are considered a suitable choice for engineering sustainable photocatalytic machineries although these natural enzymes are not photocatalytically active by themselves. Nonetheless, the need to develop renewable alternatives for H_2 production, drives the hydrogenase community to take profound interest in designing such systems. Numerous models of the [FeFe]-hydrogenase have been previously described, which in conjunction with suitable light harvesting systems could form promising systems for light-to-fuel conversion technologies (Fig. 108).

Photocatalytic hydrogen producing assemblies are commonly comprised of a photosensitizer (PS) capable of harvesting light along with a proton reducing catalyst, a sacrificial electron donor, which is capable of restoring the actual redox state of the sensitizer, and a proton donor. For diiron-complexes in particular, a potential mechanism for the H_2 formation involves photon absorption by the sensitizer (organic moieties, semiconductors), followed by an electron transfer from the photoexcited sensitizer to the diiron catalytic centre.

1764 | *Chem. Soc. Rev.*, 2021, **50**, 1668–1784

This journal is © The Royal Society of Chemistry 2021

Fig. 108 Potential mechanism for the photosensitised hydrogen evolution. PS = photosensitizer, SED = sacrificial electron donor.

Subsequently, protonation of the reduced catalyst takes place. This process is followed by another electron transfer to the bimetallic catalytic centre resulting in H_2 formation, thereby closing the cycle.[521,523]

A variety of architectures with different photocatalytic abilities have been designed and will be discussed herein. These systems either vary in the choice of photosensitizer or the proton reduction centre. In general, two approaches were adopted to link photosensitizers to the active site models. In the first strategy, attachment of the chromophore to the bridgehead atom through chemical modifications was performed. Furthermore, the photosensitive moiety can be directly linked to the diiron site.

7.1 Covalent attachment of photosensitizers to H-cluster models

7.1.1 Attachment to the dithiolate bridge. Following the above-mentioned strategy, Ott and coworkers designed elaborate systems. The first example reported by the researches is comprised of an adt-model functionalised with a modified $[Ru(terpy)_2]^{2+}$ complex (terpy = 2,6-bis(2-pyridyl)pyridine) connected via an ethynyl linker (**315**, Fig. 109). The linker provides

separation of the photosensitizer and the catalytic centre along with enhancing the excited state lifetime of $[Ru(terpy)_2]^{2+}$. In comparison to the non-derivatised Ru sensitizer, this system displays a 30% quenching of the MLCT state. Nonetheless, electron transfer to the catalytic site was not observed and the amount of H_2 generated was low.[524] Additionally, a modified PDT model (Fig. 109) was linked to the $[Ru(bpy)_3]^{2+}$ sensitizer through an amide linkage to afford **316**. However, no electron relay between the photosensitizer and the diiron site was observed, which was explained by the high flexibility of the linker in homogenous solutions. The electron transfer from the excited photosensitizer to the diiron site thus becomes thermodynamically unfavourable.[525]

Following these reports, Song et al. incorporated a tetraphenylporphyrin group (TPP) on the bridgehead nitrogen of $Fe_2(adt^R)(CO)_6$ (R = p-C_6H_4CHO), via covalent bonding resulting in **317**.[526] With the improved light absorbance of TPP and the longer excited state lifetime, it was anticipated to be favourable for the electron transfer processes towards the diiron site. Indeed, the electron was shown to be readily transferred from the photoexcited sensitizer to the diiron center.[526]

Subsequently, a three-component system, **318** built from $Fe_2(adt^R)(CO)_6$, a Re-photosensitizer and ferrocene was established. Here, the catalytic site and the sensitizer were separated by an ethynyl linker that provided appropriate separation for fast electron transfer without electron recombination at the sensitizer. Utilizing ascorbic acid as proton source and as the sacrificial electron donor, the system displayed a TON of 0.35.[527]

Despite of their obvious potentials noble metal-based photosensitizers are not particularly desirable due to their expensive production and involvement in complex deteriorating
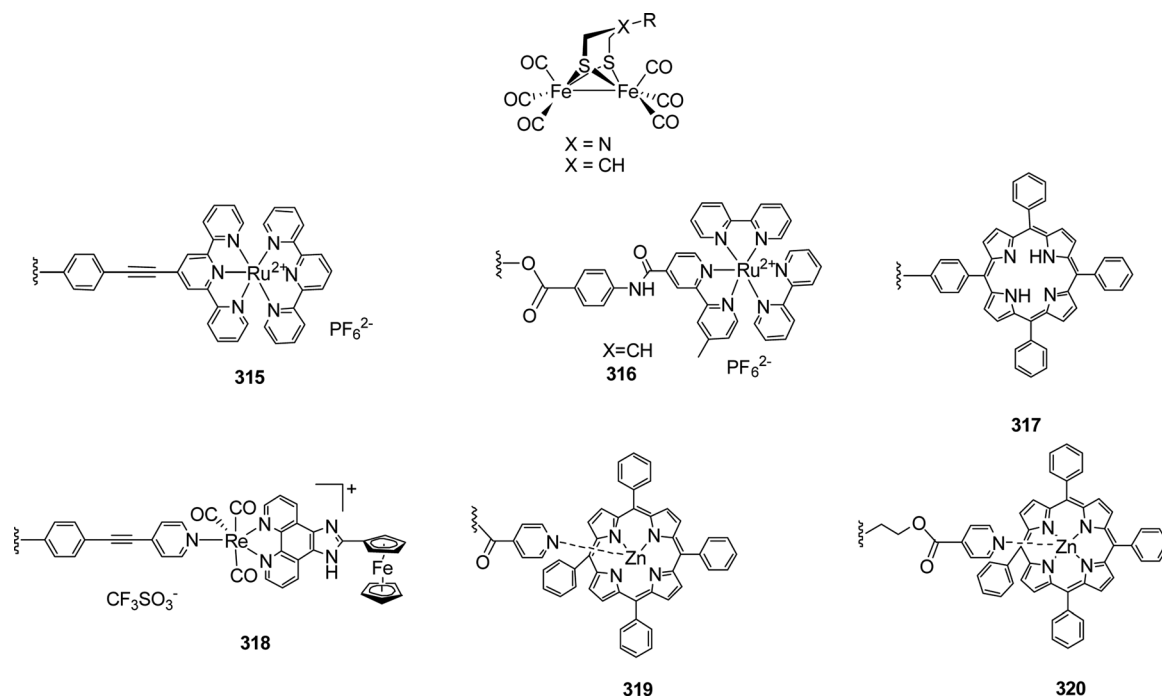

Fig. 109 Models **315** to **320**. Examples of $Fe_2(xdt^R)(CO)_6$ models modified for photocatalytic purposes.

This journal is © The Royal Society of Chemistry 2021

Chem. Soc. Rev., 2021, **50**, 1668–1784 | **1765**

pathways. As a noble metal free alternative, a zinc tetraphenyl-porphyrin (ZnTPP) unit linked to ADT *via* the amine bridge (**319**) to achieve considerable photochemical HER activity. As expected, significant fluorescence quenching was observed suggesting an intramolecular electron transfer from ZnTPP to the diiron centre. However, the exact electron transfer pathway for such systems remains elusive.[188] Along this line, complex **320** was established and investigated for its H_2 production capability. Interestingly, the complex **320** revealed a faster electron transfer from the TPP moiety to the diiron unit as compared with the covalently linked systems. The newly established complex also allowed to overcome charge recombination required for fast catalytic conversion processes but only showed low turnover numbers. This behaviour was ascribed to the photo instability of the catalyst.[528] Along this modification strategy, model **181** was reported comprising a covalently attached ZnTPP/naphthalene unit. A thermodynamically favourable electron transfer from the sensitizer to the catalytic site was suggested based on electrochemical investigations with the first reduction potential of the mimic being less negative than the oxidation potential of the photoexcited ZnTPP unit (-1.65 V *vs.* -1.74 V).[251] In addition, Wasielewski and coworkers investigated the reactivity of **321a–c**. It was observed that employing a second electron donor in these systems is beneficial, increasing the lifetime of the reduced diiron centre and facilitates the catalytic activity. Likewise, upon extending the linker length between the photosensitizer and the catalytic site, the electron transfer to the diiron centres is favoured and the electron recombination time period increases by a factor of 7.5. Hence, only **321c** displayed significant photocatalytic activity with the additional phenyl group disfavouring quenching due to efficient energy transfer to the ferrocene moiety. However, the observed photocatalytic activity is limited by degradation of the diiron centre upon irradiation (Fig. 110).[252]

7.1.2 Attachment by CO-ligand substitution. As the secondary amine of the adt-bridge was believed to play a crucial role in the proton reduction, modifying this position was
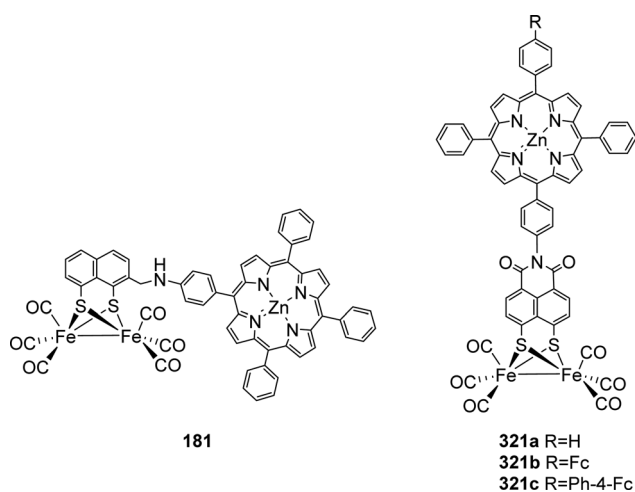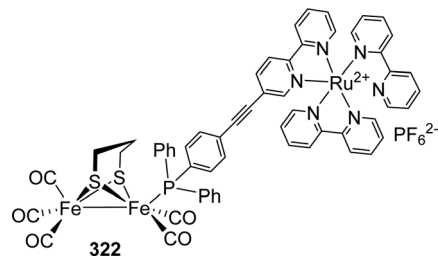

Fig. 111 Model **322** with direct attachment of the photosensitiser to metal centre.

anticipated to severely influence the hydrogen evolution. Likewise, the electron relay machinery is linked to the iron centre *via* a cysteinyl ligand in the natural system. Therefore, a direct linkage of the photoactive groups to the iron centre emerged as an attractive design strategy. A first approach to realize such a system was provided by the synthesis of **322**. Subsequently, electrochemical studies revealed that the bridging acetylenic ligand (Fig. 111) is the most easily reduced component. Furthermore, the generated oxidised diiron site is unstable, which accounts for the light sensitivity of the dyad and limits further photochemical investigations and catalytic applications.[529]

In a comparable approach, complex **323** was prepared. Herein, the platinum(II)-polypyridyl alkynyl sensitizer is attached *via* an isonitrile group to the $Fe_2(pdt)(CO)_5$ moiety.[530] The resulting system displayed long-lived MLCT states. However, the important reduction of the Fe^IFe^0 state is thermodynamically unfeasible and thus explains the overall low catalytic efficiency.[530] Furthermore, a series of cyanide ligand modified hydrogenase mimics was reported (**324a–c**, Fig. 112) using rhenium photosensitizers as prospective catalyst systems but revealed comparable problems.[531]

Kluwer and coworkers reported a macromolecular system carrying two photosensitizers covalently attached to the Fe centres *via* phosphine groups $[Fe_2(pdt)(CO)_4\{PPh_2(4-py)\}_2]$ and modified this complex with zinc(II)porphyrin chromophores **325** (Fig. 113). However, this design strategy proved to be unsatisfactory as only two turnovers per catalyst under optimized conditions were observed.[532] Rauchfuss and coworkers reported on the photocatalytic activity of [**219**pdt-μH]$^+$ and [**231**pdt-μH]$^+$ in the presence of ferrocene as recyclable electron donor. Strikingly, this system was shown to overcome the limitation of the otherwise required high reduction potentials for the hexacarbonyl systems (-1.33, -1.4 V *vs.* -1.66 V for **20**).[533]

7.2 Photocatalytic multi-component systems

Although a significant number of reports exists for photosensitizer-bound proton reduction sites, all systems display severe limitations and none of them allows for sufficient H_2 generation. An alternative strategy to build photocatalytic hydrogenase mimics is the use of multicomponent systems *i.e.* consisting of unlinked photosensitizers and H_2-formation sites. One of the early reports in this field describes the incorporation of quantum dots (QDs) as potential photosensitizers. Quantum dots possess superior visible light absorption
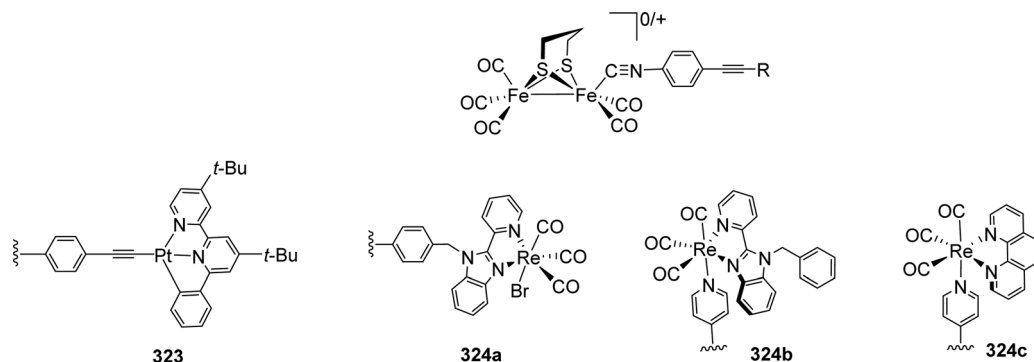

Fig. 110 Modified models of **170** for photocatalytic activity.

1766 | *Chem. Soc. Rev.*, 2021, **50**, 1668–1784

This journal is © The Royal Society of Chemistry 2021

Fig. 112 Cyanide modified photocatalytic systems with Pt- and Re-complexes.

375a R_1=Ph
375b R_1=(4-MeO)Ph

Fig. 113 Porphyrin modified supramolecular models relevant for photocatalysis.

abilities and importantly, are stable under aqueous conditions. Notably, 3-mercaptopropionic stabilised nanocrystal quantum dots in the presence of a [2Fe–2S]-cluster and ascorbic acid revealed promising turnover numbers and turnover frequencies of up to 505 and 50 h^{-1} within 10 h of illumination.[534]

Likewise, the utilization of Ru-based light harvesters was suggested as a potential replacement for the biologically relevant [4Fe–4S]-clusters in an artificial system. Due to its similar reduction potential compared to that of the diiron dithiolate hexacarbonyl complex, [Ru(bpy)$_3$]$^{2+}$ was proposed as an efficient photo sensitizer. Upon adopting the diethyldithiocarbamate anion (dtc$^-$) as an electron donor, the challenge of reverse electron transfer was surmounted, as the electron transfer generated thiyl radicals, from the dithiolate anions, which underwent quick dimerization and thus extend the excited state lifetime of [Ru(bpy)$_3$]$^+$. Still, this system suffered from photo-bleaching and protonation of the anionic quencher.[535] Multiple phosphine variants of pdt (**20**) and adt^{Bn} (**91**) models were subsequently investigated utilizing ascorbic acid and [Ru(bpy)$_3$]$^{2+}$ and achieved a maximal TON of 4.3 under optimum conditions.[536]

Especially the chlorine substituted bdt model **150** is a suitable candidate for studying the photochemical H$_2$ production due to its less negative reduction potential in combination with its high stability and capability to undergo reversible reductions. Along this line, a composite system consisting of this particular mimic, [Ru(bpy)$_3$]$^{2+}$ as photosensitizer and

ascorbic acid as proton and electron donor was subsequently investigated and revealed a TON of 200 along with a TOF of 2.7 min^{-1} in DMF/H$_2$O solutions at pH of 5.5.[537]

7.3 Confinement of the photocatalytic system

Although chemists have succeeded in designing active site analogues, in which the photosensitizer is attached to the catalytic site, yet such systems are far away from any application as these systems are limited in stability, solubility and H$_2$ generation. An alternative strategy to achieve an appreciable activity similar to that of the natural system, the skilful alteration of the secondary coordination sphere of the catalyst was anticipated to tune the solubility and stability.

Notably, the microenvironment influences the photocatalytic performance considerably – to this end, catalytic diiron models were either embedded in a polymeric scaffold or incorporated into nanomaterials, generating improved heterogeneous proton reduction assemblies that will be described in the following sections.[165,187,511,538–541]

7.3.1 Polymer support

7.3.1.1 Synthetic polymers. Polymers are one potential support to incorporate the catalytic centre and photosensitizer as they allow to shape the environment of the catalyst and allow for the encapsulation of additional substrates. For instance, the sulphonate modified adt-model Fe$_2$(adt^R)(CO)$_6$ (**326**, R = p-C$_6$H$_4$SO$_3$$^-Na^+$) along with Ru-polypyridine based photosensitizers were grafted onto a phospholipid membrane (DOPC 1,2-dioleoyl-*sn-glycero*-3-phosphocholine). This self-assembled system displayed a significantly increased photocatalytic activity under acidic conditions (pH 2.6) in comparison to the non-immobilised models. A reason for this performance enhancement was found in the close proximity of the relay groups involved in electron transfer processes. The highest photocatalytic activity was reported utilizing ascorbic acid with a TON of 57.

In addition, activity tests for catalysts embedded in lipids were conducted as well and an activity enhancement was observed with lipid layers with higher order such as DOPC and DMPC (1,2-dimyristoyl-*sn-glycero*-3-phosphocholine). However, the activity of these membrane assemblies is yet still limited by photosensitizer degradation.[542]

Furthermore, a series of macro models was established upon reacting Fe$_2$S$_2$(CO)$_6$ with a Fréchet-type dendron in

This journal is © The Royal Society of Chemistry 2021
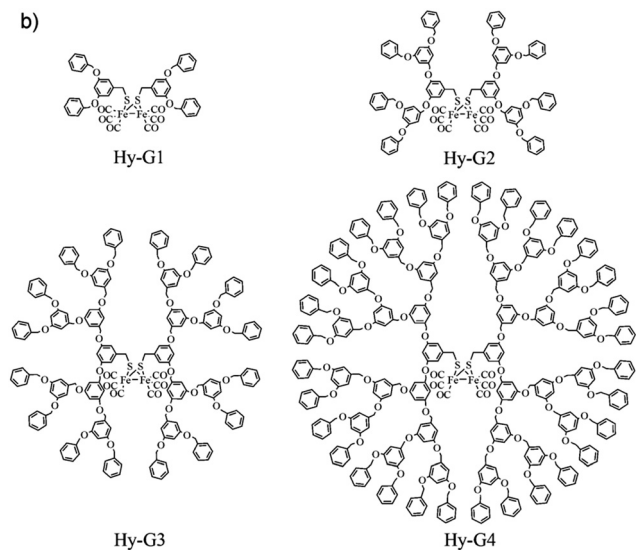
Chem. Soc. Rev., 2021, **50**, 1668–1784 | **1767**

Fig. 114 Structures of dendrimer based [2Fe]$_H$ mimics. Reprinted from ref. 511 with permission from John Wiley and Sons, Copyright 2013.

THF (Fig. 114). The resulting dendrites were likewise studied for their photocatalytic activity in the presence of [Ir(ppy)$_2$-(bpy)]PF$_6$ (ppy = 2-phenylpyridine, bpy = 2,2′-bipyridine) as the photosensitizer and triethylamine as the sacrificial electron donor in water/acetone (1 : 9) mixtures. Notably, the largest dendrimer (Fig. 114, Hy-G4) displayed a high TON of 22 200 with a TOF of 7240 h^{-1}. The hydrophobic environment created by the dendrite around the catalytic site was herein suggested to allow for a close interaction of the neutral sensitizer and the charged photosensitizer and reasoned to be origin of the high activity.[511]

Furthermore, a three-component assembly – branched poly-ethyleneimine functionalised with an isocyanide ligand modified pdt mimic (**327**), MPA–CdSe quantum dots and ascorbic acid – was shown to be photocatalytically active in water over a broad pH range and provided high TON values of up to 10 600 at neutral pH. Herein, incorporating MPA–CdSe QDs into the systems was found to be beneficial as these are easily dispersed in water and have intense photon absorbing properties. Likewise, the branched polymer has numerous amine groups, which are capable of binding to the specific mimic and potentially act as proton relays to the catalytic site. Most important, the polymer stabilizes the CdSe quantum dots against aggregation and thus contributes significantly to the high activity and stability.[538]

A breakthrough study for the photocatalytic H$_2$ production was reported on systems containing an isocyanide PDT model which was attached to polyacrylic acid (PAA) (Fig. 115).[165] Here, the hydrophilic PAA assists in the solubilisation of the otherwise insoluble catalyst system in water and TONs of up to 27 135 and TOF 3.6 s^{-1} were obtained at pH 4. Notably, due to the surrounding PAA, the 2-mercaptobenzoic acid (MAA) stabilized CdSe quantum dots (QDs) were protected from aggregation. Furthermore, the polymer brings the sensitizer and the catalytic site in close proximity to each other and thereby allows for an enhanced electron transfer.[165]
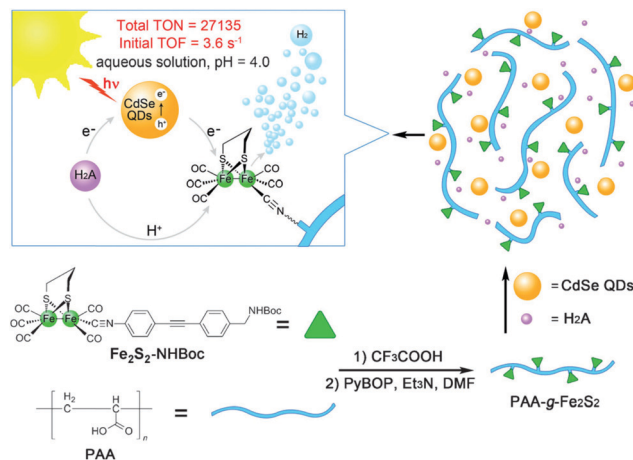

Fig. 115 Synthetic pathway towards modified pdt and representation of catalytic activity. Reprinted from ref. 165 with permission from John Wiley and Sons, Copyright 2013.

7.3.1.2 Peptides and proteins. As an alternative to synthetic polymers, a combination of active site models with biological scaffolds was used to tune the secondary coordination sphere and with it to optimize catalyst solubility and activity – for example, **219pdt** was encapsulated in a low molecular weight hydrogelator (Fmoc–Leu–Leu). This secondary sphere prevents the polymerization of **219pdt** and is hence positively affecting its stability (Fig. 116). Notably, a network of H-bonds was observed when the model is implemented within the gel confirming a significantly higher stability in aqueous media.[512]

In addition, the covalent attachment of modified Fe$_2$(pdt)(CO)$_6$ to the cavity of a β-barrel protein apo-nitrobindin (apo-NB) was reported. Model **328** bearing a maleimide group covalently binds to cysteine residue (Q96C mutant) within the protein and this assembly along with [Ru(bpy)$_3$]$^{2+}$ and ascorbate in 50 mM Tris/HCl at pH 4.0 and 25 °C allowed for the generation of hydrogen (TON up to 130 for 6 h).[543]

Furthermore, employing cytochrome *C* which functions as native electron relay in the natural system, an artificial metalloenzyme was constructed *via* attaching the [2Fe–2S]-site to the CXXC motif (Cys14, Cys17) of the apo-enzyme, giving a Fe$_2$(S-Cys)$_2$(CO)$_6$ unit. Subsequently, this synthetic machinery was studied for photocatalytic H$_2$ development using [Ru(bpy)$_3$]$^{2+}$ and ascorbic acid. The assembly in aqueous media generates H$_2$

Fig. 116 Model **328** for attachment to the β-barrel protein.

with a TON of 80 over 2 h at pH 4.7.[544] To further investigate the electron transfer process between the photosensitizer and the catalytic centre, a more elaborate system was designed, wherein the ruthenium sensitizer was coordinated to the adjacent histidine residue (CXXCH sequence) of cytochrome C_{556}. After 2 h of irradiation, catalytic activity for the photo-induced hydrogen development with a TON of 9 at pH 8.5 was observed.[545]

Although Ru-based photosensitisers and pdt-derived model **23** were non-covalently encapsulated in a hydrophobic (horse spleen) apo-ferritin cavity, this confinement enhances the solubility of the components along with providing a close proximity for an improved electron exchange. However, the highest recorded TON for such a system was 5 and the photosensitizer $[Ru(bpy)_2(dpqp)]^{2+}$ was found to limit the activity of the system.[546] In contrast, if the sensitizer $[Ru(bpy)_3]^{2+}$ was not incorporated in the ferritin pocket and rather homogenised in solution, a TON of 31 was reported.[547]

Recently, Li and coworkers reported self-assembled ovalbumin (OVA) nanogels which incorporate **20**. This incorporation improved the photocatalytic efficiency for H_2 evolution in acid aqueous solution by 15% under optimized conditions. It is important to mention that acid induced structural changes (unfolding of α-helix to β-sheets) within the nanogels contribute massively to the overall performance.[548] **20** was likewise linked to an artificial dithiol amino acid, which was in turn incorporated into an alpha helical peptide scaffold. This assembly, using $[Ru(bpy)_3]^{2+}$ and ascorbate generates H_2 with a TON of 84 in acidic aqueous solutions under light irradiation.[513]

7.3.1.3 Polysaccharides and oligosaccharides. To imitate the protein cavity of hydrogenases and to favour catalytically active intermediates Darensbourg and coworkers incorporated **326** into a β-dextrin. The anionic sulfonate group herein assists in the dissolution of the complex within dextrin. Notably, upon protonation with HOAc in water, the system displayed an electrocatalytic peak at −1.4 V *vs.* Ag/AgCl. However, ^{13}C-NMR studies revealed that the encapsulation of the model into dextrin is rather dynamic and not sufficient enough to artificially reproduce the natural protein environment.[131] Also, an improved version of this model with various phosphine ligands (PTA, PMe$_3$, P(OMe)$_3$, PPh$_3$) was reported, but these models display rather unsatisfactory reduction properties.[189] Following this research Sun *et al.* studied the photocatalysis of this encapsulated system using Rose Bengal as well as Eosin Y as sensitizers.[549] These organic sensitizers also participated in the host–guest interaction with β- and γ-dextrins and allowed for a faster electron transfer processes from the photosensitizer to the diiron centre. This improved electron transfer resulted in an enhanced quantum efficiency for the system.

In another attempt, chitosan – a naturally occurring polysaccharide – was used to greatly improve the solubility and photo dependent H_2 producing ability of **91** in the presence of CdTe quantum dots capped with 3-mercaptopropionic acid (MPA–CdTe QDs) and ascorbic acid. Along this line, chitosan can be converted into a multi cationic system when its surface amine and phenolic groups are exposed to acidic conditions.

These cationic species show great affinity for the negatively charged MPA–CdTe QDs and in return favour the electron transfer process to the imbedded catalyst. Here, the confined environment provided by chitosan allows for a close interaction of the catalyst, photosensitizer and the proton donor and results in an unprecedented TON of up to 52 800 and a TOF of 1.40 s^{-1} Seemingly, a modified environment to increase the stability of the catalyst and to overcome limitations of the non-modified systems is of utmost importance.[539]

7.3.2 Micelle systems. Molecules bearing amphiphilic groups undergo self-assembly to form water-soluble clusters. This assembly allows the application of hydrogenase mimics to conduct catalysis under aqueous conditions. To achieve photocatalysis in water, the adt^{Ph} and adt^{Bn} complexes **90** and **91** were both incorporated into sodium dodecyl sulphate (SDS) micelles along with Re^I(4,4′-dimethylbpy)(CO)$_3$Br or Re^I(1,10-phenanthroline)(CO)$_3$Br as photosensitizer. However, this attempt only afforded low amounts of H_2 (TON 0.13).[550] In a similar approach, **20** was embedded in a self-assembling system by using an amphiphilic P-NB polymer,[132,551] resulting in an active system in water and displaying a TON of 133 in the presence of $[Ru(bpy)_3]^{2+}$ and ascorbic acid. The close proximity of the electron donor and the catalytic site, established due to micellar incorporation, facilitates the electron transfer.[132]

Along this line of modification, **149** displayed reasonable catalytic activity (TON 117) in water under basic conditions (at pH 10.5) upon incorporation into sodium dodecyl sulphate (SDS) micelles. Eosin Y was herein utilized as a photosensitizer and triethyl amine as electron donor. In the absence of the SDS micelles, the catalytic activity of the complex is lowered to one fourth of the maximum activity.[514]

7.3.3 Metal–organic frameworks and molecular sieves. Another strategy to enhance the photoactive performance is to use metal–organic frameworks (MOFs). MOFs are 3D systems built from covalent linkage of metal ions and organic moieties. They are capable of loading the catalysts on top of their surfaces and also possess the advantages of easy product separation, reusability, and enhanced stability due to their heterogeneous nature. Moreover, they can provide structural support along with their organic groups imitating the second coordination spheres of natural systems. Following this strategy, a novel assembly was described with **329** attached to a robust zirconium-porphyrin based metal–organic framework (ZrPF). Along this line, the zinc-porphyrin [tetrakis(4-carboxy-phenyl porphyrin) zinc (ZnTCPP)] was linked to the Zr cations of the framework *via* carboxylic groups. Here, the ZnTCPP moiety acts as anchor for the diiron site within its cavity along with its function as photosensitizer. The zirconium-porphyrin MOF ZrPF is a chemically stable, rigid framework with a high surface area and enables light dependent H_2 activity. After irradiating (>420 nm) the catalytic system for 120 min in the presence of ascorbic acid in water at pH 5 about 3.5 μmol H_2 were detected.[552]

Utilizing the same conceptual approach, **330** loaded onto the zirconium terephthalic acid MOF UiO-66(Zr) revealed an improved photocatalytic activity in presence of ascorbic acid
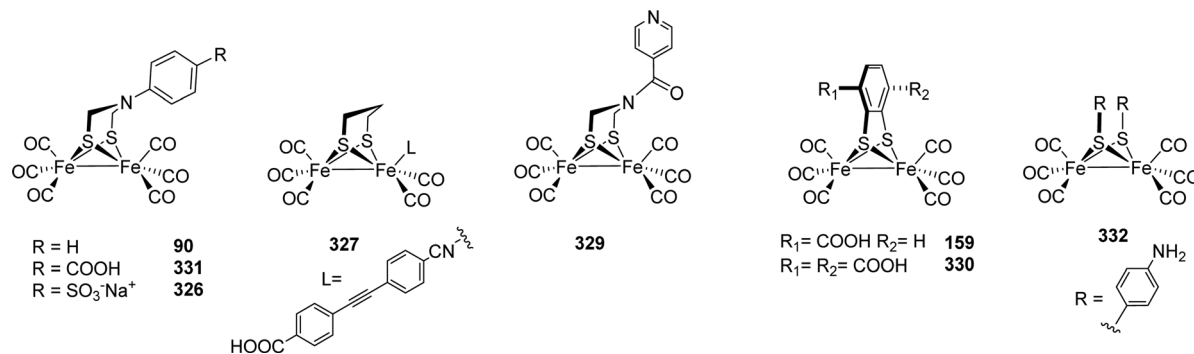
This journal is © The Royal Society of Chemistry 2021

Chem. Soc. Rev., 2021, **50**, 1668–1784 | **1769**

Fig. 117   Subsite models for photocatalytic HER systems.

and $[Ru(bpy)_3]^{2+}$ as compared to the individual components and likewise circumvents the undesired charge recombination.[553] As studies on this system revealed a potential clogging of channels by ion pairs generated by reduction of catalyst, **159** was loaded onto *e.g.* the chromium MOF MIL-101 which revealed enlarged pore sizes of 29–34 Å as compared to UiO-66(Zr) with 8–11 Å. Subsequent photochemical investigation with different catalyst to MOF ratios revealed that H$_2$ production is proportional to catalyst loading in the MOF thus following first order kinetics.[554]

In addition, bis(2-phenylpyridine)(2,2′-bipyridine)iridium(III) chromophores were introduced on a diiron hydrogenase mimic by click-chemistry. The modified chromophores were then incorporated into a K$^+$-exchanged molecular sieve, MCM-41. When examined for their photocatalytic activity in presence of triethylamine (TEA), CH$_3$CN and H$_2$O (9:1) at pH 10, the composite enabled the formation of 11.8 µL H$_2$ with 5.5 mg composite and a loading 19.1 µmol g^{-1}. The enhanced activity of the incorporated system was attributed to the complex stabilisation by the molecular sieve.[555]

7.4   Attachment of the photocatalytic system to nanoparticles

To overcome the limitations of high cost and insufficient stability associated with above mentioned complexes, semiconductors can likewise be employed as photosensitizers. Prerequisites of an ideal semiconductor are a large band gap possessing a conduction band with a redox potential capable of reducing protons as well as good water solubility. In that sense, two sub-site models, **90** and **331** were incorporated onto the surface of ZnS. ZnS is a noble metal-free and highly photoactive material. However, it suffers from a rapid recombination of the generated electron/holes pairs.[556,557] To this end, when the diiron subsite models are adsorbed on the ZnS surface and triethanolamine (TEOA) was used as the electron donor, photocatalytic experiments showed a TON of 3400 and 4950 for C1&ZnS and C2&ZnS in DMF:H$_2$O system (9:1).[187] Similarly, aniline functionalised **332** adsorbed on ZnS nanoparticles was stable for up to 38 h of irradiation and displayed a TON of 2607 and initial TOF of 100 h^{-1} in presence of ascorbic acid at pH 4.6.[540]

Furthermore, **159** was attached to the surface of an oligoethylene glycol shell modified ZnO along with the natural pigment betanin as the light harvester. The modified ZnO

nanocrystals revealed an extended excited electron lifetime in the conduction band and showed enhanced charge separation as well as accumulation of reactive electrons for the photocatalytic process. With trifluoroacetic the system displayed a TON of 11 and stability up to 6 h. Under otherwise unmodified catalyst conditions, solely a stability of up to 2 h was observed.[541] Furthermore, with modified nano cathodes *i.e.* cross-linked indium phosphide nanocrystal array grafted with Fe$_2$S$_2$(CO)$_6$ (**1**), a photoelectrochemical efficiency of more than 60% was witnessed at −0.9 V *vs.* SCE (Fig. 117).[558]

7.5   Tailoring the photocatalytic proton reduction by H-cluster models

These studies report significant developments in tailoring artificial scaffolds for the light-dependent hydrogen generation and support the crucial role of the microenvironment in tuning the properties of these systems. Also, remarkable progress was achieved in obtaining functional systems under aqueous conditions or systems which avoid the use of noble metals for hydrogen generation. Presently, investigations of mechanistic pathways are under progress to provide detailed explanation of the functioning of these systems. Nonetheless, to match the activities of the natural systems, further modulations are required to generate systems which are suitable for incorporation in technological devices.

VIII   Conclusion

In conclusion, we herein highlight the development in the [FeFe]-hydrogenase research over the last decades. While initially, structural alterations of mimics along with spectroscopic investigations were performed to understand the natural enzyme, pinpoint its various states and relate them to electronic and structural changes in the active centre, later investigations focused mainly on the electrochemical properties of such systems with the aim to find suitable proton reduction catalysts. Recently, the understanding of the enzymatic properties as well as direct alteration of the entire enzyme became the focus of many investigations due to the possibility to implement artificial synthetic mimics into the natural environment. However, concerning the enzyme and its functional mechanism, important questions remain to be answered. Up to date, no

conclusive evidence was presented allowing for the determination of an exact consecutive sequence of proton/electron transfer events in the catalytic cycle. Hence, several plausible catalytic cycles were presented, and future investigations will have to provide evidence in favour of one over the others. Furthermore, understanding of the functional role of the enzyme backbone surrounding the H-cluster is deficient, *e.g.* reflected in the potential role of a second substrate/proton channel in the native enzymes. Along this line, artificial surroundings of the H-cluster such as polymers are expected to be a growing field of interest. In general, however, we expect hydrogenase-research to become more applications oriented. For example, enzymes, entire cells or well-designed mimics may serve as efficient catalysts in energy storage applications such as fuel cells or electrolysers for water splitting. Furthermore, a functional coupling to sustainable energy supplies such as photovoltaics appears to be a promising approach. With these ideas in mind, we believe that hydrogenase research is and will be a vivid field of enzymatic research that is now on the verge of advancing to the exploration of potential technological applications. At the same time smart ideas are demanded to advance to the level of understanding further to a yet unprecedent detail. We hope that this review gives the interested reader an overview on this topic and allows him to find hitherto unresolved research questions to fuel this interesting research with novel ideas worth pursuing in the near future.

List of abbreviations

ap	Apical
ba	Basal
BSA	Bovine serum albumin
ENDOR	Electron nuclear double resonance
E_{pa}	Anodic peak potential
E_{pc}	Cathodic peak potential
EPR	Electron paramagnetic resonance
Fe_d	Distal (or rotated) iron atom in $[2Fe]_H$ referred to $[4Fe]_H$
Fe_p	Proximal (or unrotated) iron atom $[2Fe]_H$ referred to $[4Fe]_H$
FTO	Fluorine doped tin oxide
HER	Hydrogen evolution reaction
hfc	Hyperfine coupling
HYSCORE	Hyperfine sublevel correlation
IR	infrared
MLCT	Metal-to-ligand charge transfer
NRVS	Nuclear resonance vibrational spectroscopy
NHE	Normal hydrogen electrode
OCP	Open circuit potential
PCET	Proton-coupled electron transfer
PET	Photon-driven electron transfer
PS	Photosensitizer
PTP	Proton transfer pathway
QDs	Quantum dots
r.t.	Room temperature

SDM	Site directed mutagenesis
SHE	Standard hydrogen electrode
SEC	Spectroelectrochemistry
TOF	Turnover frequency
TON	Turnover number
WT	Wild type
XAE	X-ray absorption and emission
XRD	X-ray diffraction

Proteins

HydG	Maturase protein
HydE	Maturase protein
HydF	Maturase protein
apo-HydA	Hydrogenase lacking $[2Fe]_H$
HydA	Maturated hydrogenase
HydS	Sensory hydrogenase
*Cr*HydA1(XDT)	[FeFe]-hydrogenase from *C. reinhardtii* with an xdt bridged $[2Fe]_H$
*Cp*I	Hydrogenase I from *C. pasteurianum*
*Cp*II	Hydrogenase II from *C. pasteurianum*
*Dd*H	Hydrogenase from *D. desulfuricans*

Compounds and groups

bda	benzylideneacetone/(*E*)-4-phenylbut-3-en-2-one
BIAN-R	Bis(arylimino)acenaphthene
Bn	Benzyl
DCM	Dichloromethane
DDQ	2,3-Dichloro-5,6-dicyano-1,4-benzoquinone
DHG	Dehydroglycine
DMF	Dimethylformamide
DMPC	1,2-Dimyristoyl-*sn-glycero*-3-phosphatidylcholine
DOPC	1,2-Dioleoyl-*sn-glycero*-3-phosphatidylcholine
dtc$^-$	Diethyldithiocarbamate
Fc	Ferrocene
Fc*	Decamethylferrocene
Fmoc	Fluorenylmethoxycarbonyl protecting group
hmds	Hexamethyldisilazide
HOAc	Acetic acid
HOTf	Trifluoromethanesulfonic acid
HOTs	*p*-Toluenesulfonic acid
HOB	Hydroxybenzyl
H_4folate	Tetrahydrofolate
MAA	2-Mercaptobenzoic acid
MeCN	Acetonitrile
MOF	metal–organic framework
MPA	3-Mercaptopropionic acid
NaDT	Sodium dithionite
NB	Nitrobindin
NMI	Naphthalene monoimide
OVA	Ovalbumin
PAA	Polyacrylic acid
PLP	Pyridoxal phosphate

This journal is © The Royal Society of Chemistry 2021

Chem. Soc. Rev., 2021, **50**, 1668–1784 | 1771

POEGMA	Poly(oligo(ethyleneglycol)methyl ether methacrylate)
ppy	2-Phenylpyridine
py	Pyridyl
SAM	S-Adenosyl-L-methionine
SDS	Sodium dodecyl sulphate
TEA	Triethylamine
TEOA	Triethanolamine
TFA	Trifluoroacetic acid
THF	Tetrahydrofuran
TMP	Tris(morpholino)phosphine
tol	Methylphenyl
5′-DA•	5′-Deoxyadenosyl radical
5′-DAH	5′-Deoxyadenosine
[BAr^F]$^-$	tetrakis(3,5-bis(trifluoromethyl)phenyl)borane or tetra(pentafluorophenyl)borane

Dithiolates and derivatives

adSe	Bis(selenidomethyl)amine
adt	Bis(sulfidomethyl)amine
adt^{BH3}	Borane bis(sulfidomethyl)amine
adt^{Bn}	N-Benzylbis(sulfidomethyl)amine
adt^{Me}	N-Methylbis(sulfidomethyl)amine
adt^{MeBH3}	Borane N-methylbis(sulfidomethyl)amine
adt$^{n\text{-propyl}}$	N-Propylbis(sulfidomethyl)amine
adt^{SMe}	N-(Methylthio)ethylbis(sulfidomethyl)amine
bdt	1,2-Benzenedithiolate
bdt^{3Me}	3-Methyl-1,2-benzenedithiolate
bdt^{4Me}	4-Methyl-1,2-benzenedithiolate
Cl$_2$bdt	3,6-Dichloro-1,2-benzenedithiolate
cbdt	3-Carboxybenzene-1,2-dithiolate
dcbdt	1,4-Dicarboxybenzene-2,3-dithiolate
edt	1,2-Ethanedithiolate
pdt^{Et}	2,2-Diethyl-1,3-propanedithiolate
pdt^{Me}	2,2-Dimethyl-1,3-propanedithiolate
odt	Bis(sulfidomethyl)ether
o-xyldt	1,2-Bis(sulfidomethyl)benzene
pdSe	1,3-Propanediselenolate
pdt	1,3-Propanedithiolate
pdt^{MeSBn}	2-Methyl-2-((benzylthio)methyl)propane-1,3-dithiolate
pdt^{MeSMe}	2-Methyl-2-((methylthio)methyl)propane-1,3-dithiolate
sdt	Bis(sulfidomethyl)sulfide
xdt	Dithiolate ligand

Iron–sulfur clusters

ADSe	Fe$_2$((SeCH$_2$)$_2$NH)(CO)$_6$ or derivatives
ADT	Fe$_2$((SCH$_2$)$_2$NH)(CO)$_6$ or derivatives
BDT	Fe$_2$(S$_2$C$_6$H$_4$)(CO)$_6$ or derivatives
EDT	Fe$_2$((SCH$_2$)$_2$)(CO)$_6$ or derivatives
ODT	Fe$_2$((SCH$_2$)$_2$O)(CO)$_6$ or derivatives
PDT	Fe$_2$((SCH$_2$)$_2$CH$_2$)(CO)$_6$ or derivatives
SDT	Fe$_2$((SCH$_2$)$_2$S)(CO)$_6$ or derivatives

[2Fe]$_H$	[2Fe–2S]-cluster in the active site of [FeFe]-hydrogenases
[4Fe]$_H$	[4Fe–4S]-cluster in the active site of [FeFe]-hydrogenases
H-cluster	Active site of [FeFe]-hydrogenases

Ligands

bma	2,3-Bis(diphenylphosphino)maleic anhydride
bpcd	4,5-Bis(diphenylphosphino)-4-cyclopenten-1,3-dione
bpy	2,2′-Bipyridine
Cp	Cyclopentadienyl
dcpm	Bis(dicyclohexylphosphino)methane
dmpe	1,2-Bis(dimethylphosphino)ethane
dppb	1,4-Bis(diphenylphosphino)butane
dppe	1,2-Bis(diphenylphosphino)ethane
dppf	1,1′-Bis(diphenylphosphino)ferrocene
dppm	Bis(diphenylphosphino)methane
dppn	1,8-Bis(diphenylphosphino)naphthalene
dppp	1,3-Bis(diphenylphosphino)propane
dppv	(Z)-1,2-Bis(diphenylphosphino)ethene
IMe	1,3-Dimethylimidazol-2-ylidene
IMeMes	1-Mesityl-3-methylimidazol-2-ylidene
IMes	1,3-Dimesitylimidazol-2-ylidene
Me$_2$dppm	1,1-Bis(diphenylphosphino)-1-methylethane
NHC	N-heterocyclic carbene
NMI	Naphthalene monoimide
PNP	N,N-Phosphinoamine ligands
PTA	1,3,5-Triaza-7-phosphaadamantane
terpy	2,6-Bis(2-pyridyl)pyridine
TPP	Tetraphenylporphyrin
triphos	Phenyl bis(diphenylphosphinoethyl)phosphine

Amino acids

Ala (A)	Alanine
Arg (R)	Arginine
Asp (D)	Aspartic acid
Cys (C)	Cysteine
EPA	3-(Diethylphosphorothioyl)alanine
Gln (Q)	Glutamine
Glu (E)	Glutamic acid
Gly (G)	Glycine
His (H)	HistidineI
IPA	3-(Diisopropylphosphorothioyl)alanine
Leu (L)	Leucine
Met (M)	Methionine
PPA	3-(Diphenylphosphorothioyl)alanine
Ser (S)	Serine
Tyr (Y)	Tyrosine

Microorganisms

C. acetobutylicum	Clostridium acetobutylicum (Gram-positive)
C. pasteurianum	Clostridium pasteurianum (Gram-positive)
C. reinhardtii	Chlamydomonas reinhardtii

D. desulfuricans   *Desulfovibrio desulfuricans* (Gram-negative)
E. coli   *Escherichia coli* (Gram-negative)
T. maritima   *Thermotoga maritima* (Gram-negative)
S. obliquus   *Scenedesmus obliquus*

Conflicts of interest

There are no conflicts to declare.

Acknowledgements

References

1 W. Lubitz, H. Ogata, O. Rüdiger and E. Reijerse, *Chem. Rev.*, 2014, **114**, 4081–4148.

2 S. T. Stripp and T. Happe, *Dalton Trans.*, 2009, 9960–9969.

3 J. W. Peters, W. N. Lanzilotta, B. J. Lemon and L. C. Seefeldt, *Science*, 1998, **282**, 1853–1858.

4 D. W. Mulder, E. S. Boyd, R. Sarma, R. K. Lange, J. A. Endrizzi, J. B. Broderick and J. W. Peters, *Nature*, 2010, **465**, 248–251.

5 W. E. Broderick and J. B. Broderick, *JBIC, J. Biol. Inorg. Chem.*, 2019, **24**, 769–776.

6 D. L. M. Suess, J. M. Kuchenreuther, L. De La Paz, J. R. Swartz and R. D. Britt, *Inorg. Chem.*, 2016, **55**, 478–487.

7 P. Dinis, B. M. Wieckowski and P. L. Roach, *Curr. Opin. Struct. Biol.*, 2016, **41**, 90–97.

8 R. C. Driesener, M. R. Challand, S. E. McGlynn, E. M. Shepard, E. S. Boyd, J. B. Broderick, J. W. Peters and P. L. Roach, *Angew. Chem., Int. Ed.*, 2010, **49**, 1687–1690.

9 J. M. Kuchenreuther, S. J. George, C. S. Grady-Smith, S. P. Cramer and J. R. Swartz, *PLoS One*, 2011, **6**, e20346.

10 P. Dinis, D. L. M. Suess, S. J. Fox, J. E. Harmer, R. C. Driesener, L. De La Paz, J. R. Swartz, J. W. Essex, R. D. Britt and P. L. Roach, *Proc. Natl. Acad. Sci. U. S. A.*, 2015, **112**, 1362–1367.

11 D. L. M. Suess, I. Bürstel, L. De La Paz, J. M. Kuchenreuther, C. C. Pham, S. P. Cramer, J. R. Swartz and R. D. Britt, *Proc. Natl. Acad. Sci. U. S. A.*, 2015, **112**, 11455–11460.

12 G. Rao, S. A. Pattenaude, K. Alwan, N. J. Blackburn, R. D. Britt and T. B. Rauchfuss, *Proc. Natl. Acad. Sci. U. S. A.*, 2019, **116**, 20850–20855.

13 J. N. Betz, N. W. Boswell, C. J. Fugate, G. L. Holliday, E. Akiva, A. G. Scott, P. C. Babbitt, J. W. Peters, E. M. Shepard and J. B. Broderick, *Biochemistry*, 2015, **54**, 1807–1818.

14 Y. Nicolet, J. K. Rubach, M. C. Posewitz, P. Amara, C. Mathevon, M. Atta, M. Fontecave and J. C. Fontecilla-Camps, *J. Biol. Chem.*, 2008, **283**, 18861–18872.

15 R. Rohac, P. Amara, A. Benjdia, L. Martin, P. Ruffié, A. Favier, O. Berteau, J.-M. Mouesca, J. C. Fontecilla-Camps and Y. Nicolet, *Nat. Chem.*, 2016, **8**, 491–500.

16 G. Rao, L. Tao and R. David Britt, *Chem. Sci.*, 2020, **11**, 1241–1247.

17 H. Li and T. B. Rauchfuss, *J. Am. Chem. Soc.*, 2002, **124**, 726–727.

18 S. E. McGlynn, E. M. Shepard, M. A. Winslow, A. V. Naumov, K. S. Duschene, M. C. Posewitz, W. E. Broderick, J. B. Broderick and J. W. Peters, *FEBS Lett.*, 2008, **582**, 2183–2187.

19 S. E. McGlynn, S. S. Ruebush, A. Naumov, L. E. Nagy, A. Dubini, P. W. King, J. B. Broderick, M. C. Posewitz and J. W. Peters, *JBIC, J. Biol. Inorg. Chem.*, 2007, **12**, 443–447.

20 A. G. Scott, R. K. Szilagyi, D. W. Mulder, M. W. Ratzloff, A. S. Byer, P. W. King, W. E. Broderick, E. M. Shepard and J. B. Broderick, *Dalton Trans.*, 2018, **47**, 9521–9535.

21 M. Bortolus, P. Costantini, D. Doni and D. Carbonera, *Int. J. Mol. Sci.*, 2018, **19**, 3118.

22 I. Czech, A. Silakov, W. Lubitz and T. Happe, *FEBS Lett.*, 2010, **584**, 638–642.

23 I. Czech, S. Stripp, O. Sanganas, N. Leidel, T. Happe and M. Haumann, *FEBS Lett.*, 2011, **585**, 225–230.

24 E. M. Shepard, S. E. McGlynn, A. L. Bueling, C. S. Grady-Smith, S. J. George, M. A. Winslow, S. P. Cramer, J. W. Peters and J. B. Broderick, *Proc. Natl. Acad. Sci. U. S. A.*, 2010, **107**, 10448–10453.

25 F. Vallese, P. Berto, M. Ruzzene, L. Cendron, S. Sarno, E. De Rosa, G. M. Giacometti and P. Costantini, *J. Biol. Chem.*, 2012, **287**, 36544–36555.

26 J. Esselborn, C. Lambertz, A. Adamska-Venkatesh, T. Simmons, G. Berggren, J. Noth, J. Siebel, A. Hemschemeier, V. Artero, E. Reijerse, M. Fontecave, W. Lubitz and T. Happe, *Nat. Chem. Biol.*, 2013, **9**, 607–609.

27 G. Berggren, A. Adamska, C. Lambertz, T. R. Simmons, J. Esselborn, M. Atta, S. Gambarelli, J.-M. Mouesca, E. Reijerse, W. Lubitz, T. Happe, V. Artero and M. Fontecave, *Nature*, 2013, **499**, 66–69.

28 Y. Nicolet, C. Piras, P. Legrand, C. E. Hatchikian and J. C. Fontecilla-Camps, *Structure*, 1999, **7**, 13–23.

29 A. Silakov, B. Wenk, E. Reijerse and W. Lubitz, *Phys. Chem. Chem. Phys.*, 2009, **11**, 6592.

30 Y. Nicolet, A. L. de Lacey, X. Vernède, V. M. Fernandez, E. C. Hatchikian and J. C. Fontecilla-Camps, *J. Am. Chem. Soc.*, 2001, **123**, 1596–1601.

31 J. F. Siebel, A. Adamska-Venkatesh, K. Weber, S. Rumpel, E. Reijerse and W. Lubitz, *Biochemistry*, 2015, **54**, 1474–1483.

32 L. Kertess, F. Wittkamp, C. Sommer, J. Esselborn, O. Rüdiger, E. J. Reijerse, E. Hofmann, W. Lubitz, M. Winkler, T. Happe and U.-P. Apfel, *Dalton Trans.*, 2017, **46**, 16947–16958.

This journal is © The Royal Society of Chemistry 2021

Chem. Soc. Rev., 2021, **50**, 1668–1784 | **1773**

33 C. Sommer, C. P. Richers, W. Lubitz, T. B. Rauchfuss and E. J. Reijerse, *Angew. Chem., Int. Ed.*, 2018, **57**, 5429–5432.

34 N. Khanna, C. Esmieu, L. S. Meszaros, P. Lindblad and G. Berggren, *Energy Environ. Sci.*, 2017, **10**, 1563–1567.

35 L. S. Mészáros, P. Ceccaldi, M. Lorenzi, H. J. Redman, E. Pfitzner, J. Heberle, M. Senger, S. T. Stripp and G. Berggren, *Chem. Sci.*, 2020, **11**, 4608–4617.

36 L. S. Meszaros, B. Nemeth, C. Esmieu, P. Ceccaldi and G. Berggren, *Angew. Chem., Int. Ed.*, 2018, **57**, 2596–2599.

37 A. Wegelius, N. Khanna, C. Esmieu, G. D. Barone, F. Pinto, P. Tamagnini, G. Berggren and P. Lindblad, *Energy Environ. Sci.*, 2018, **11**, 3163–3167.

38 H. Gaffron, *Nature*, 1939, **143**, 204–205.

39 H. Gaffron, *Am. J. Bot.*, 1940, **27**, 273–283.

40 M. Winkler, *Int. J. Hydrogen Energy*, 2002, **27**, 1431–1439.

41 T. Happe and J. D. Naber, *Eur. J. Biochem.*, 1993, **214**, 475–481.

42 A. Hemschemeier, S. Fouchard, L. Cournac, G. Peltier and T. Happe, *Planta*, 2007, **227**, 397–407.

43 M. Winkler, B. Heil, B. Heil and T. Happe, *Biochim. Biophys. Acta, Gene Struct. Expression*, 2002, **1576**, 330–334.

44 T. Happe and A. Kaminski, *Eur. J. Biochem.*, 2002, **269**, 1022–1032.

45 L. Florin, A. Tsokoglou and T. Happe, *J. Biol. Chem.*, 2001, **276**, 6125–6132.

46 M. Forestier, P. King, L. Zhang, M. Posewitz, S. Schwarzer, T. Happe, M. L. Ghirardi and M. Seibert, *Eur. J. Biochem.*, 2003, **270**, 2750–2758.

47 M. Winkler, C. Maeurer, A. Hemschemeier and T. Happe, *Biohydrogen III*, Elsevier, 2004, pp. 103–115.

48 C. V. Popescu and E. Münck, *J. Am. Chem. Soc.*, 1999, **121**, 7877–7884.

49 A. Silakov, E. J. Reijerse, S. P. J. Albracht, E. C. Hatchikian and W. Lubitz, *J. Am. Chem. Soc.*, 2007, **129**, 11447–11458.

50 K. Laun, I. Baranova, J. Duan, F. Wittkamp, U.-P. Apfel, T. Happe, M. Senger and S. T. Stripp, *ChemRxiv*, 2019, 1–5.

51 M. Senger, S. Mebs, J. Duan, O. Shulenina, K. Laun, L. Kertess, F. Wittkamp, U.-P. Apfel, T. Happe, M. Winkler, M. Haumann and S. T. Stripp, *Phys. Chem. Chem. Phys.*, 2018, **2018**, 3128–3140.

52 M. Senger, K. Laun, F. Wittkamp, J. Duan, M. Haumann, T. Happe, M. Winkler, U.-P. Apfel and S. T. Stripp, *Angew. Chem., Int. Ed.*, 2017, **56**, 16503–16506.

53 A. K. Justice, G. Zampella, L. D. Gioia and T. B. Rauchfuss, *Chem. Commun.*, 2007, 2019–2021.

54 S. P. J. Albracht, W. Roseboom and E. C. Hatchikian, *JBIC, J. Biol. Inorg. Chem.*, 2006, **11**, 88–101.

55 D. W. Mulder, M. W. Ratzloff, E. M. Shepard, A. S. Byer, S. M. Noone, J. W. Peters, J. B. Broderick and P. W. King, *J. Am. Chem. Soc.*, 2013, **135**, 6921–6929.

56 W. Roseboom, A. L. De Lacey, V. M. Fernandez, E. C. Hatchikian and S. P. J. Albracht, *JBIC, J. Biol. Inorg. Chem.*, 2006, **11**, 102–118.

57 C. Kamp, A. Silakov, M. Winkler, E. J. Reijerse, W. Lubitz and T. Happe, *Biochim. Biophys. Acta, Bioenerg.*, 2008, **1777**, 410–416.

58 A. Silakov, C. Kamp, E. Reijerse, T. Happe and W. Lubitz, *Biochemistry*, 2009, **48**, 7780–7786.

59 M. Senger, S. Mebs, J. Duan, F. Wittkamp, U.-P. Apfel, J. Heberle, M. Haumann and S. T. Stripp, *Proc. Natl. Acad. Sci. U. S. A.*, 2016, 201606178.

60 A. Adamska, A. Silakov, C. Lambertz, O. Rüdiger, T. Happe, E. Reijerse and W. Lubitz, *Angew. Chem., Int. Ed.*, 2012, **51**, 11458–11462.

61 N. Chongdar, J. A. Birrell, K. Pawlak, C. Sommer, E. J. Reijerse, O. Rüdiger, W. Lubitz and H. Ogata, *J. Am. Chem. Soc.*, 2018, **140**, 1057–1068.

62 B. J. Lemon and J. W. Peters, *Biochemistry*, 1999, **38**, 12969–12973.

63 A. Silakov, B. Wenk, E. Reijerse, S. P. J. Albracht and W. Lubitz, *JBIC, J. Biol. Inorg. Chem.*, 2009, **14**, 301–313.

64 S. Mebs, R. Kositzki, J. Duan, L. Kertess, M. Senger, F. Wittkamp, U.-P. Apfel, T. Happe, S. T. Stripp, M. Winkler and M. Haumann, *Biochim. Biophys. Acta, Bioenerg.*, 2018, **1859**, 28–41.

65 D. Schilter and T. B. Rauchfuss, *Angew. Chem., Int. Ed.*, 2013, **52**, 13518–13520.

66 A. J. Pierik, M. Hulstein, W. R. Hagen and S. P. J. Albracht, *Eur. J. Biochem.*, 1998, **258**, 572–578.

67 J. Duan, S. Mebs, K. Laun, F. Wittkamp, J. Heberle, T. Happe, E. Hofmann, U.-P. Apfel, M. Winkler, M. Senger, M. Haumann and S. T. Stripp, *ACS Catal.*, 2019, **9**, 9140–9149.

68 V. Fourmond, C. Greco, K. Sybirna, C. Baffert, P.-H. Wang, P. Ezanno, M. Montefiori, M. Bruschi, I. Meynial-Salles, P. Soucaille, J. Blumberger, H. Bottin, L. De Gioia and C. Léger, *Nat. Chem.*, 2014, **6**, 336–342.

69 M. Mirmohades, A. Adamska-Venkatesh, C. Sommer, E. Reijerse, R. Lomoth, W. Lubitz and L. Hammarström, *J. Phys. Chem. Lett.*, 2016, **7**, 3290–3293.

70 K. Laun, S. Mebs, J. Duan, F. Wittkamp, U.-P. Apfel, T. Happe, M. Winkler, M. Haumann and S. Stripp, *Molecules*, 2018, **23**, 1669.

71 R. Gilbert-Wilson, J. F. Siebel, A. Adamska-Venkatesh, C. C. Pham, E. Reijerse, H. Wang, S. P. Cramer, W. Lubitz and T. B. Rauchfuss, *J. Am. Chem. Soc.*, 2015, **137**, 8998–9005.

72 S. Mebs, J. Duan, F. Wittkamp, S. T. Stripp, T. Happe, U.-P. Apfel, M. Winkler and M. Haumann, *Inorg. Chem.*, 2019, **58**, 4000–4013.

73 P. Chernev, C. Lambertz, A. Brünje, N. Leidel, K. G. V. Sigfridsson, R. Kositzki, C.-H. Hsieh, S. Yao, R. Schiwon, M. Driess, C. Limberg, T. Happe and M. Haumann, *Inorg. Chem.*, 2014, **53**, 12164–12177.

74 A. Adamska-Venkatesh, D. Krawietz, J. Siebel, K. Weber, T. Happe, E. Reijerse and W. Lubitz, *J. Am. Chem. Soc.*, 2014, **136**, 11339–11346.

75 M. Winkler, M. Senger, J. Duan, J. Esselborn, F. Wittkamp, E. Hofmann, U.-P. Apfel, S. T. Stripp and T. Happe, *Nat. Commun.*, 2017, **8**, 16115.

76 C. Sommer, A. Adamska-Venkatesh, K. Pawlak, J. A. Birrell, O. Rüdiger, E. J. Reijerse and W. Lubitz, *J. Am. Chem. Soc.*, 2017, **139**, 1440–1443.

77 J. A. Birrell, V. Pelmenschikov, N. Mishra, H. Wang, Y. Yoda, K. Tamasaku, T. B. Rauchfuss, S. P. Cramer, W. Lubitz and S. DeBeer, *J. Am. Chem. Soc.*, 2020, **142**, 222–232.

78 V. Pelmenschikov, J. A. Birrell, C. C. Pham, N. Mishra, H. Wang, C. Sommer, E. Reijerse, C. P. Richers, K. Tamasaku, Y. Yoda, T. B. Rauchfuss, W. Lubitz and S. P. Cramer, *J. Am. Chem. Soc.*, 2017, **139**, 16894–16902.

79 J. Duan, M. Senger, J. Esselborn, V. Engelbrecht, F. Wittkamp, U.-P. Apfel, E. Hofmann, S. T. Stripp, T. Happe and M. Winkler, *Nat. Commun.*, 2018, **9**, 4726.

80 S. Mebs, M. Senger, J. Duan, F. Wittkamp, U.-P. Apfel, T. Happe, M. Winkler, S. T. Stripp and M. Haumann, *J. Am. Chem. Soc.*, 2017, **139**, 12157–12160.

81 H. Ogata, T. Krämer, H. Wang, D. Schilter, V. Pelmenschikov, M. van Gastel, F. Neese, T. B. Rauchfuss, L. B. Gee, A. D. Scott, Y. Yoda, Y. Tanaka, W. Lubitz and S. P. Cramer, *Nat. Commun.*, 2015, **6**, 7890.

82 S. Katz, J. Noth, M. Horch, H. S. Shafaat, T. Happe, P. Hildebrandt and I. Zebger, *Chem. Sci.*, 2016, **7**, 6746–6752.

83 G. Filippi, F. Arrigoni, L. Bertini, L. De Gioia and G. Zampella, *Inorg. Chem.*, 2015, **54**, 9529–9542.

84 E. J. Reijerse, C. C. Pham, V. Pelmenschikov, R. Gilbert-Wilson, A. Adamska-Venkatesh, J. F. Siebel, L. B. Gee, Y. Yoda, K. Tamasaku, W. Lubitz, T. B. Rauchfuss and S. P. Cramer, *J. Am. Chem. Soc.*, 2017, **139**, 4306–4309.

85 S. Rumpel, C. Sommer, E. Reijerse, C. Farès and W. Lubitz, *J. Am. Chem. Soc.*, 2018, **140**, 3863–3866.

86 D. W. Mulder, Y. Guo, M. W. Ratzloff and P. W. King, *J. Am. Chem. Soc.*, 2017, **139**, 83–86.

87 F. Wittkamp, M. Senger, S. T. Stripp and U.-P. Apfel, *Chem. Commun.*, 2018, **54**, 5934–5942.

88 M. Haumann and S. T. Stripp, *Acc. Chem. Res.*, 2018, **51**, 1755–1763.

89 J. Esselborn, N. Muraki, K. Klein, V. Engelbrecht, N. Metzler-Nolte, U.-P. Apfel, E. Hofmann, G. Kurisu and T. Happe, *Chem. Sci.*, 2016, **7**, 959–968.

90 A. Adamska-Venkatesh, T. R. Simmons, J. F. Siebel, V. Artero, M. Fontecave, E. Reijerse and W. Lubitz, *Phys. Chem. Chem. Phys.*, 2015, **17**, 5421–5430.

91 P. Rodríguez-Maciá, K. Pawlak, O. Rüdiger, E. J. Reijerse, W. Lubitz and J. A. Birrell, *J. Am. Chem. Soc.*, 2017, **139**, 15122–15134.

92 C. C. Pham, D. W. Mulder, V. Pelmenschikov, P. W. King, M. W. Ratzloff, H. Wang, N. Mishra, E. E. Alp, J. Zhao, M. Y. Hu, K. Tamasaku, Y. Yoda and S. P. Cramer, *Angew. Chem., Int. Ed.*, 2018, **57**, 10605–10609.

93 A. J. Cornish, B. Ginovska, A. Thelen, J. C. S. da Silva, T. A. Soares, S. Raugei, M. Dupuis, W. J. Shaw and E. L. Hegg, *Biochemistry*, 2016, **55**, 3165–3173.

94 A. J. Cornish, K. Gartner, H. Yang, J. W. Peters and E. L. Hegg, *J. Biol. Chem.*, 2011, **286**, 38341–38347.

95 M. Senger, V. Eichmann, K. Laun, J. Duan, F. Wittkamp, G. Knoer, U.-P. Apfel, T. Happe, M. Winkler, J. Heberle and S. Timo Stripp, *J. Am. Chem. Soc.*, 2019, **141**, 17394–17403.

96 D. W. Mulder, M. W. Ratzloff, M. Bruschi, C. Greco, E. Koonce, J. W. Peters and P. W. King, *J. Am. Chem. Soc.*, 2014, **136**, 15394–15402.

97 D. Priem, T.-K. Ha and A. Bauder, *J. Chem. Phys.*, 2000, **113**, 169–175.

98 S. Aloisio, P. E. Hintze and V. Vaida, *J. Phys. Chem. A*, 2002, **106**, 363–370.

99 B. Ginovska-Pangovska, M.-H. Ho, J. C. Linehan, Y. Cheng, M. Dupuis, S. Raugei and W. J. Shaw, *Biochim. Biophys. Acta, Bioenerg.*, 2014, **1837**, 131–138.

100 M. W. Ratzloff, M. B. Wilker, D. W. Mulder, C. E. Lubner, H. Hamby, K. A. Brown, G. Dukovic and P. W. King, *J. Am. Chem. Soc.*, 2017, **139**, 12879–12882.

101 M. W. Ratzloff, J. H. Artz, D. W. Mulder, R. T. Collins, T. E. Furtak and P. W. King, *J. Am. Chem. Soc.*, 2018, **140**, 7623–7628.

102 C. Lorent, S. Katz, J. Duan, C. J. Kulka, G. Caserta, C. Teutloff, S. Yadav, U.-P. Apfel, M. Winkler, T. Happe, M. Horch and I. Zebger, *J. Am. Chem. Soc.*, 2020, **142**(12), 5493–5497.

103 C. Greening, A. Biswas, C. R. Carere, C. J. Jackson, M. C. Taylor, M. B. Stott, G. M. Cook and S. E. Morales, *ISME J.*, 2016, **10**, 761–777.

104 P. Knörzer, A. Silakov, C. E. Foster, F. A. Armstrong, W. Lubitz and T. Happe, *J. Biol. Chem.*, 2012, **287**, 1489–1499.

105 M. L. K. Sanchez, C. Sommer, E. Reijerse, J. A. Birrell, W. Lubitz and R. Brian Dyer, *J. Am. Chem. Soc.*, 2019, **141**, 16064–16070.

106 S. Y. Reece, J. M. Hodgkiss, J. Stubbe and D. G. Nocera, *Philos. Trans. R. Soc., B*, 2006, **361**, 1351–1364.

107 C. Costentin, M. Robert and J.-M. Savéant, *Acc. Chem. Res.*, 2010, **43**, 1019–1029.

108 J. W. Peters, *Science*, 1998, **282**, 1853–1858.

109 D. Seyferth and R. S. Henderson, *J. Organomet. Chem.*, 1981, **218**, C34–C36.

110 X. Wang, Z. Wei, X. Jiang, J. Zhao and X. Liu, *Inorg. Chim. Acta*, 2012, **392**, 112–117.

111 C. Alvarez-Toledano, E. Delgado, B. Donnadieu, E. Hernández, G. Martín and F. Zamora, *Inorg. Chim. Acta*, 2003, **351**, 119–122.

112 C. Alvarez-Toledano, J. Enríquez, R. A. Toscano, M. Martínez-García, E. Cortés-Cortés, Y. M. Osornio, O. García-Mellado and R. Gutiérrez-Pérez, *J. Organomet. Chem.*, 1999, **577**, 38–43.

113 R. B. King, *J. Am. Chem. Soc.*, 1963, **85**, 1584–1587.

114 A. Legadec, R. Dabard, B. Misterkiewicz, A. Le Rouzic and H. Patin, *J. Organomet. Chem.*, 1987, **326**, 381–387.

115 P. C. Ellgen and J. N. Gerlach, *Inorg. Chem.*, 1973, **12**, 2526–2532.

116 A. Winter, L. Zsolnai and G. Hüttner, *Z. Naturforsch., B: Anorg. Chem., Org. Chem.*, 1982, **37**, 1430–1436.

117 E. S. Donovan, G. S. Nichol and G. A. N. Felton, *J. Organomet. Chem.*, 2013, **726**, 9–13.

118 M. Razavet, A. L. Cloirec, S. C. Davies, D. L. Hughes and C. J. Pickett, *J. Chem. Soc., Dalton Trans.*, 2001, 3551–3552.

This journal is © The Royal Society of Chemistry 2021

Chem. Soc. Rev., 2021, **50**, 1668–1784 | 1775

119 W.-N. Cao, F. Wang, H.-Y. Wang, B. Chen, K. Feng, C.-H. Tung and L.-Z. Wu, *Chem. Commun.*, 2012, **48**, 8081.

120 J. L. Stanley, T. B. Rauchfuss and S. R. Wilson, *Organometallics*, 2007, **26**, 1907–1911.

121 N. Wen, F. Xu, Y. Feng and S. Du, *J. Inorg. Biochem.*, 2011, **105**, 1123–1130.

122 B. J. Petro, A. K. Vannucci, L. T. Lockett, C. Mebi, R. Kottani, N. E. Gruhn, G. S. Nichol, P. A. J. Goodyer, D. H. Evans, R. S. Glass and D. L. Lichtenberger, *J. Mol. Struct.*, 2008, **890**, 281–288.

123 A. R. Koray and M. L. Ziegler, *J. Organomet. Chem.*, 1979, **169**, C34–C36.

124 S. Lotz, P. H. Van Rooyen and M. M. Van Dyk, *Organometallics*, 1987, **6**, 499–505.

125 D. Seyferth and G. B. Womack, *J. Am. Chem. Soc.*, 1982, **104**, 6839–6841.

126 A. Shaver, O. Lopez and D. N. Harpp, *Inorg. Chim. Acta*, 1986, **119**(1), 13–18.

127 A. Shaver, P. J. Fitzpatrick, K. Steliou and I. S. Butler, *J. Organomet. Chem.*, 1979, **172**, C59–C62.

128 H. Abul-Futouh, L. R. Almazahreh, M. K. Harb, H. Görls, M. El-khateeb and W. Weigand, *Inorg. Chem.*, 2017, **56**, 10437–10451.

129 S. Gao, H. Guo, X. Peng, X. Zhao, Q. Duan, Q. Liang and D. Jiang, *New J. Chem.*, 2013, **37**, 1437–1444.

130 L.-C. Song, Y.-X. Wang, X.-K. Xing, S.-D. Ding, L.-D. Zhang, X.-Y. Wang and H.-T. Zhang, *Chem. – Eur. J.*, 2016, **22**, 16304–16314.

131 M. L. Singleton, J. H. Reibenspies and M. Y. Darensbourg, *J. Am. Chem. Soc.*, 2010, **132**, 8870–8871.

132 F. Wang, M. Wen, K. Feng, W.-J. Liang, X.-B. Li, B. Chen, C.-H. Tung and L.-Z. Wu, *Chem. Commun.*, 2016, **52**, 457–460.

133 U.-P. Apfel, Y. Halpin, M. Gottschaldt, H. Görls, J. G. Vos and W. Weigand, *Eur. J. Inorg. Chem.*, 2008, 5112–5118.

134 U.-P. Apfel, Y. Halpin, H. Görls, J. G. Vos, B. Schweizer, G. Linti and W. Weigand, *Chem. Biodiversity*, 2007, **4**, 2138–2148.

135 U.-P. Apfel, C. R. Kowol, F. Kloss, H. Görls, B. K. Keppler and W. Weigand, *J. Organomet. Chem.*, 2011, **696**, 1084–1088.

136 R. Trautwein, L. R. Almazahreh, H. Görls and W. Weigand, *Z. Anorg. Allg. Chem.*, 2013, **639**, 1512–1519.

137 L.-C. Song, C.-G. Li, J. Gao, B.-S. Yin, X. Luo, X.-G. Zhang, H.-L. Bao and Q.-M. Hu, *Inorg. Chem.*, 2008, **47**, 4545–4553.

138 M. Razavet, S. C. Davies, D. L. Hughes, J. E. Barclay, D. J. Evans, S. A. Fairhurst, X. Liu and C. J. Pickett, *Dalton Trans.*, 2003, 586–595.

139 M. Razavet, S. C. Davies, D. L. Hughes and C. J. Pickett, *Chem. Commun.*, 2001, 847–848.

140 F. Xu, C. Tard, X. Wang, S. K. Ibrahim, D. L. Hughes, W. Zhong, X. Zeng, Q. Luo, X. Liu and C. J. Pickett, *Chem. Commun.*, 2008, 606–608.

141 C. M. Thomas, O. Rüdiger, T. Liu, C. E. Carson, M. B. Hall and M. Y. Darensbourg, *Organometallics*, 2007, **26**, 3976–3984.

142 V. Vijaikanth, J.-F. Capon, F. Gloaguen, P. Schollhammer and J. Talarmin, *Electrochem. Commun.*, 2005, **7**, 427–430.

143 S. K. Ibrahim, X. Liu, C. Tard and C. J. Pickett, *Chem. Commun.*, 2007, 1535.

144 P. I. Volkers, T. B. Rauchfuss and S. R. Wilson, *Eur. J. Inorg. Chem.*, 2006, 4793–4799.

145 M. K. Harb, T. Niksch, J. Windhager, H. Görls, R. Holze, L. T. Lockett, N. Okumura, D. H. Evans, R. S. Glass, D. L. Lichtenberger, M. El-khateeb and W. Weigand, *Organometallics*, 2009, **28**, 1039–1048.

146 M. K. Harb, U.-P. Apfel, J. Kübel, H. Görls, G. A. N. Felton, T. Sakamoto, D. H. Evans, R. S. Glass, D. L. Lichtenberger, M. El-khateeb and W. Weigand, *Organometallics*, 2009, **28**, 6666–6675.

147 H. Abul-Futouh, M. El-khateeb, H. Görls and W. Weigand, *Heteroat. Chem.*, 2018, **29**, e21446.

148 R. Trautwein, L. R. Almazahreh, H. Görls and W. Weigand, *Dalton Trans.*, 2015, **44**, 18780–18794.

149 L.-C. Song, Q.-L. Li, Z.-H. Feng, X.-J. Sun, Z.-J. Xie and H.-B. Song, *Dalton Trans.*, 2013, **42**, 1612–1626.

150 F. Gloaguen, J. D. Lawrence and T. B. Rauchfuss, *J. Am. Chem. Soc.*, 2001, **123**, 9476–9477.

151 G. Eilers, L. Schwartz, M. Stein, G. Zampella, L. de Gioia, S. Ott and R. Lomoth, *Chem. – Eur. J.*, 2007, **13**, 7075–7084.

152 S. Ezzaher, J.-F. Capon, F. Gloaguen, F. Y. Pétillon, P. Schollhammer, J. Talarmin and N. Kervarec, *Inorg. Chem.*, 2009, **48**, 2–4.

153 F. Gloaguen, J. D. Lawrence, T. B. Rauchfuss, M. Bénard and M.-M. Rohmer, *Inorg. Chem.*, 2002, **41**, 6573–6582.

154 B. E. Barton and T. B. Rauchfuss, *Inorg. Chem.*, 2008, **47**, 2261–2263.

155 R. Zaffaroni, T. B. Rauchfuss, A. Fuller, L. De Gioia and G. Zampella, *Organometallics*, 2013, **32**, 232–238.

156 R. S. Glass, N. E. Gruhn, E. Lorance, M. S. Singh, N. Y. T. Stessman and U. I. Zakai, *Inorg. Chem.*, 2005, **44**, 5728–5737.

157 U.-P. Apfel, D. Troegel, Y. Halpin, S. Tschierlei, U. Uhlemann, H. Görls, M. Schmitt, J. Popp, P. Dunne, M. Venkatesan, M. Coey, M. Rudolph, J. G. Vos, R. Tacke and W. Weigand, *Inorg. Chem.*, 2010, **49**, 10117–10132.

158 R. Goy, L. Bertini, H. Görls, L. De Gioia, J. Talarmin, G. Zampella, P. Schollhammer and W. Weigand, *Chem. – Eur. J.*, 2015, **21**, 5061–5073.

159 R. Goy, L. Bertini, C. Elleouet, H. Görls, G. Zampella, J. Talarmin, L. De Gioia, P. Schollhammer, U.-P. Apfel and W. Weigand, *Dalton Trans.*, 2015, **44**, 1690–1699.

160 H. Abul-Futouh, L. R. Almazahreh, T. Sakamoto, N. Y. T. Stessman, D. L. Lichtenberger, R. S. Glass, H. Görls, M. El-Khateeb, P. Schollhammer, G. Mloston and W. Weigand, *Chem. – Eur. J.*, 2017, **23**, 346–359.

161 H. Abul-Futouh, M. El-khateeb, H. Görls, K. Jamil Asali and W. Weigand, *Dalton Trans.*, 2017, **46**, 2937–2947.

162 M. Hissler, P. W. Dyer and R. Réau, *Coord. Chem. Rev.*, 2003, **244**, 1–44.

163 B. Zhong Tang, X. Zhan, G. Yu, P. P. S. Lee, Y. Liu and D. Zhu, *J. Mater. Chem.*, 2001, **11**, 2974–2978.

1776 | *Chem. Soc. Rev.*, 2021, **50**, 1668–1784

This journal is © The Royal Society of Chemistry 2021

164 R. Goy, U.-P. Apfel, C. Elleouet, D. Escudero, M. Elstner, H. Görls, J. Talarmin, P. Schollhammer, L. González and W. Weigand, *Eur. J. Inorg. Chem.*, 2013, 4466–4472.

165 F. Wang, W.-J. Liang, J.-X. Jian, C.-B. Li, B. Chen, C.-H. Tung and L.-Z. Wu, *Angew. Chem., Int. Ed.*, 2013, 52, 8134–8138.

166 K. N. Green, J. L. Hess, C. M. Thomas and M. Y. Darensbourg, *Dalton Trans.*, 2009, 4344–4350.

167 H.-J. Fan and M. B. Hall, *J. Am. Chem. Soc.*, 2001, 123, 3828–3829.

168 J. D. Lawrence, H. Li, T. B. Rauchfuss and M.-M. Rohmer, *Angew. Chem., Int. Ed.*, 2001, 40, 1768–1772.

169 J. D. Lawrence, H. Li and T. B. Rauchfuss, *Chem. Commun.*, 2001, 1482–1483.

170 Z. Wang, J.-H. Liu, C.-J. He, S. Jiang, B. Åkermark and L.-C. Sun, *J. Organomet. Chem.*, 2007, 692, 5501–5507.

171 R. Angamuthu, M. E. Carroll, M. Ramesh and T. B. Rauchfuss, *Eur. J. Inorg. Chem.*, 2011, 1029–1032.

172 W. Hieber and J. Gruber, *Z. Anorg. Allg. Chem.*, 1958, 296, 91–103.

173 W. Gao, L.-C. Song, B.-S. Yin, H.-N. Zan, D.-F. Wang and H.-B. Song, *Organometallics*, 2011, 30, 4097–4107.

174 A. M. Lunsford, J. H. Blank, S. Moncho, S. C. Haas, S. Muhammad, E. N. Brothers, M. Y. Darensbourg and A. A. Bengali, *Inorg. Chem.*, 2016, 55, 964–973.

175 N. Lalaoui, T. Woods, T. B. Rauchfuss and G. Zampella, *Organometallics*, 2017, 36, 2054–2057.

176 A. Rana, P. Kumar Das, B. Mondal, S. Dey, D. Crouthers and A. Dey, *Eur. J. Inorg. Chem.*, 2018, 3633–3643.

177 W. Gao, J. Liu, C. Ma, L. Weng, K. Jin, C. Chen, B. Åkermark and L. Sun, *Inorg. Chim. Acta*, 2006, 359, 1071–1080.

178 L.-C. Song, J.-H. Ge, J. Yan, H.-T. Wang, X. Luo and Q.-M. Hu, *Eur. J. Inorg. Chem.*, 2008, 164–171.

179 Z. Wang, J. Liu, C. He, S. Jiang, B. Åkermark and L. Sun, *Inorg. Chim. Acta*, 2007, 360, 2411–2419.

180 W. Gao, J. Liu, B. Åkermark and L. Sun, *J. Organomet. Chem.*, 2007, 692, 1579–1583.

181 L.-C. Song, X. Luo, Y.-Z. Wang, B. Gai and Q.-M. Hu, *J. Organomet. Chem.*, 2009, 694, 103–112.

182 Y. Si, C. Ma, M. Hu, H. Chen, C. Chen and Q. Liu, *New J. Chem.*, 2007, 31, 1448.

183 W. Gao, J. Ekström, J. Liu, C. Chen, L. Eriksson, L. Weng, B. Åkermark and L. Sun, *Inorg. Chem.*, 2007, 46, 1981–1991.

184 Y.-L. Li, Y. Wu, J. Wei, J. Wei, B. Xie, L.-K. Zou, J. Cheng, Z. Wang, J. He, M.-L. Wu and P.-H. Zhao, *Polyhedron*, 2017, 135, 231–236.

185 J. He, C.-L. Deng, Y. Li, Y.-L. Li, Y. Wu, L.-K. Zou, C. Mu, Q. Luo, B. Xie, J. Wei, J.-W. Hu, P.-H. Zhao and W. Zheng, *Organometallics*, 2017, 36, 1322–1330.

186 H.-G. Cui, M. Wang, W.-B. Dong, L.-L. Duan, P. Li and L.-C. Sun, *Polyhedron*, 2007, 26, 904–910.

187 X.-W. Song, H.-M. Wen, C.-B. Ma, M.-Q. Hu, H. Chen, H.-H. Cui and C.-N. Chen, *Appl. Organomet. Chem.*, 2014, 28, 267–273.

188 L.-C. Song, M.-Y. Tang, S.-Z. Mei, J.-H. Huang and Q.-M. Hu, *Organometallics*, 2007, 26, 1575–1577.

189 M. L. Singleton, D. J. Crouthers, R. P. Duttweiler, J. H. Reibenspies and M. Y. Darensbourg, *Inorg. Chem.*, 2011, 50, 5015–5026.

190 L.-C. Song, B.-S. Yin, Y.-L. Li, L.-Q. Zhao, J.-H. Ge, Z.-Y. Yang and Q.-M. Hu, *Organometallics*, 2007, 26, 4921–4929.

191 W. Gao, J. Sun, T. Åkermark, M. Li, L. Eriksson, L. Sun and B. Åkermark, *Chem. – Eur. J.*, 2010, 16, 2537–2546.

192 L.-C. Song, L.-X. Wang, B.-S. Yin, Y.-L. Li, X.-G. Zhang, Y.-W. Zhang, X. Luo and Q.-M. Hu, *Eur. J. Inorg. Chem.*, 2008, 291–297.

193 M. E. Ahmed, S. Dey, M. Y. Darensbourg and A. Dey, *J. Am. Chem. Soc.*, 2018, 140, 12457–12468.

194 T. Liu, M. Wang, Z. Shi, H. Cui, W. Dong, J. Chen, B. Åkermark and L. Sun, *Chem. – Eur. J.*, 2004, 10, 4474–4479.

195 L.-C. Song, J.-H. Ge, X.-G. Zhang, Y. Liu and Q.-M. Hu, *Eur. J. Inorg. Chem.*, 2006, 3204–3210.

196 S. Jiang, J. Liu, Y. Shi, Z. Wang, B. Åkermark and L. Sun, *Dalton Trans.*, 2007, 896–902.

197 S. Jiang, J. Liu, Y. Shi, Z. Wang, B. Åkermark and L. Sun, *Polyhedron*, 2007, 26, 1499–1504.

198 S. Gao, J. Fan, S. Sun, X. Peng, X. Zhao and J. Hou, *Dalton Trans.*, 2008, 2128–2135.

199 A. D. Merinero, A. Collado, L. Casarrubios, M. Gómez-Gallego, C. Ramírez de Arellano, A. Caballero, F. Zapata and M. A. Sierra, *Inorg. Chem.*, 2019, 58(23), 16267–16278.

200 L.-C. Song, P.-H. Zhao, Z.-Q. Du, M.-Y. Tang and Q.-M. Hu, *Organometallics*, 2010, 29, 5751–5753.

201 L. R. Almazahreh, U.-P. Apfel, W. Imhof, M. Rudolph, H. Görls, J. Talarmin, P. Schollhammer, M. El-khateeb and W. Weigand, *Organometallics*, 2013, 32, 4523–4530.

202 F. Wittkamp, E. B. Boydas, M. Roemelt and U.-P. Apfel, *Catalysts*, 2020, 10, 522.

203 P. Das, J.-F. Capon, F. Gloaguen, F. Y. Pétillon, P. Schollhammer, J. Talarmin and K. W. Muir, *Inorg. Chem.*, 2004, 43, 8203–8205.

204 L.-C. Song, Z.-Y. Yang, H.-Z. Bian, Y. Liu, H.-T. Wang, X.-F. Liu and Q.-M. Hu, *Organometallics*, 2005, 24, 6126–6135.

205 L.-C. Song, B. Gai, Z.-H. Feng, Z.-Q. Du, Z.-J. Xie, X.-J. Sun and H.-B. Song, *Organometallics*, 2013, 32, 3673–3684.

206 L.-C. Song, J.-S. Chen, G.-J. Jia, Y.-Z. Wang, Z.-L. Tan and Y.-X. Wang, *Organometallics*, 2019, 38, 1567–1580.

207 L.-C. Song, M. Cao, Z.-Q. Du, Z.-H. Feng, Z. Ma and H.-B. Song, *Eur. J. Inorg. Chem.*, 2014, 1852.

208 M. Hu, L. Yan, J. Li, Y. Wang, P. Zhao and X. Liu, *Appl. Organomet. Chem.*, 2019, 33, e4949.

209 L.-C. Song, Z.-Y. Yang, H.-Z. Bian and Q.-M. Hu, *Organometallics*, 2004, 23, 3082–3084.

210 B. E. Barton, M. T. Olsen and T. B. Rauchfuss, *J. Am. Chem. Soc.*, 2008, 130, 16834–16835.

211 L.-C. Song, Z.-Y. Yang, Y.-J. Hua, H.-T. Wang, Y. Liu and Q.-M. Hu, *Organometallics*, 2007, 26, 2106–2110.

212 J. Windhager, M. Rudolph, S. Bräutigam, H. Görls and W. Weigand, *Eur. J. Inorg. Chem.*, 2007, 2748–2760.

213 L.-C. Song, Q.-S. Li, Z.-Y. Yang, Y.-J. Hua, H.-Z. Bian and Q.-M. Hu, *Eur. J. Inorg. Chem.*, 2010, 1119–1128.

This journal is © The Royal Society of Chemistry 2021

Chem. Soc. Rev., 2021, 50, 1668–1784 | 1777

214 J. Windhager, H. Görls, H. Petzold, G. Mloston, G. Linti and W. Weigand, *Eur. J. Inorg. Chem.*, 2007, 4462–4471.

215 T. Liu, B. Li, M. L. Singleton, M. B. Hall and M. Y. Darensbourg, *J. Am. Chem. Soc.*, 2009, **131**, 8296–8307.

216 J. Windhager, R. A. Seidel, U.-P. Apfel, H. Görls, G. Linti and W. Weigand, *Chem. Biodiversity*, 2008, **5**, 2023–2041.

217 J. Messelhäuser, K. U. Gutensohn, I.-P. Lorenz and W. Hiller, *J. Organomet. Chem.*, 1987, **321**, 377–388.

218 V. C.-C. Wang, C. Esmieu, H. J. Redman, G. Berggren and L. Hammarström, *Dalton Trans.*, 2020, **49**, 858–865.

219 J. S. McKennis and E. P. Kyba, *Organometallics*, 1983, **2**, 1249–1251.

220 J. A. Cabeza, M. A. Martínez-García, V. Riera, D. Ardura and S. García-Granda, *Organometallics*, 1998, **17**, 1471–1477.

221 J.-F. Capon, F. Gloaguen, P. Schollhammer and J. Talarmin, *J. Electroanal. Chem.*, 2004, **566**, 241–247.

222 L. Schwartz, P. S. Singh, L. Eriksson, R. Lomoth and S. Ott, *C. R. Chim.*, 2008, **11**, 875–889.

223 M. Cheng, Y. Yu, X. Zhou, Y. Luo and M. Wang, *ACS Catal.*, 2019, **9**, 768–774.

224 S. Gao, Y. Liu, Y. Shao, D. Jiang and Q. Duan, *Coord. Chem. Rev.*, 2020, **402**, 213081.

225 S. Ezzaher, A. Gogoll, C. Bruhn and S. Ott, *Chem. Commun.*, 2010, **46**, 5775.

226 E. S. Donovan, J. J. McCormick, G. S. Nichol and G. A. N. Felton, *Organometallics*, 2012, **31**, 8067–8070.

227 D. Streich, M. Karnahl, Y. Astuti, C. W. Cady, L. Hammarström, R. Lomoth and S. Ott, *Eur. J. Inorg. Chem.*, 2011, 1106–1111.

228 J. Chen, A. K. Vannucci, C. A. Mebi, N. Okumura, S. C. Borowski, M. Swenson, L. T. Lockett, D. H. Evans, R. S. Glass and D. L. Lichtenberger, *Organometallics*, 2010, **29**, 5330–5340.

229 G. Durgaprasad, R. Bolligarla and S. K. Das, *J. Organomet. Chem.*, 2011, **696**, 3097–3105.

230 G. B. Hall, J. Chen, C. A. Mebi, N. Okumura, M. T. Swenson, S. E. Ossowski, U. I. Zakai, G. S. Nichol, D. L. Lichtenberger, D. H. Evans and R. S. Glass, *Organometallics*, 2013, **32**, 6605–6612.

231 W. Zhong, L. Wu, W. Jiang, Y. Li, N. Mookan and X. Liu, *Dalton Trans.*, 2019, **48**, 13711–13718.

232 J. Zhao, Z. Wei, X. Zeng and X. Liu, *Dalton Trans.*, 2012, **41**, 11125.

233 S. Pullen, S. Maji, M. Stein and S. Ott, *Dalton Trans.*, 2019, **48**, 5933–5939.

234 G. Durgaprasad, R. Bolligarla and S. K. Das, *J. Organomet. Chem.*, 2012, **706–707**, 37–45.

235 L. Chen, M. Wang, F. Gloaguen, D. Zheng, P. Zhang and L. Sun, *Inorg. Chem.*, 2013, **52**, 1798–1806.

236 L. Chen, M. Wang, F. Gloaguen, D. Zheng, P. Zhang and L. Sun, *Chem. – Eur. J.*, 2012, **18**, 13968–13973.

237 W. P. Brezinski, M. Karayilan, K. E. Clary, N. G. Pavlopoulos, S. Li, L. Fu, K. Matyjaszewski, D. H. Evans, R. S. Glass, D. L. Lichtenberger and J. Pyun, *Angew. Chem., Int. Ed.*, 2018, **57**, 11898–11902.

238 X. Zhu, W. Zhong and X. Liu, *Int. J. Hydrogen Energy*, 2016, **41**, 14068–14078.

239 R. J. Wright, C. Lim and T. D. Tilley, *Chem. – Eur. J.*, 2009, **15**, 8518–8525.

240 C. Figliola, L. Male, P. N. Horton, M. B. Pitak, S. J. Coles, S. L. Horswell and R. S. Grainger, *Organometallics*, 2014, **33**, 4449–4460.

241 C. Topf, U. Monkowius and G. Knör, *Inorg. Chem. Commun.*, 2012, **21**, 147–150.

242 G. Qian, W. Zhong, Z. Wei, H. Wang, Z. Xiao, L. Long and X. Liu, *New J. Chem.*, 2015, **39**, 9752–9760.

243 G. Qian, H. Wang, W. Zhong and X. Liu, *Electrochim. Acta*, 2015, **163**, 190–195.

244 H. Abul-Futouh, Y. Zagranyarski, C. Müller, M. Schulz, S. Kupfer, H. Görls, M. El-khateeb, S. Gräfe, B. Dietzek, K. Peneva and W. Weigand, *Dalton Trans.*, 2017, **46**, 11180–11191.

245 C. Topf, M. Kaiser, U. Monkowius and G. Knoer, *Inorg. Chem. Commun.*, 2017, **77**, 47–50.

246 W. Zhong, Z. Xiao, G. Qian and X. Liu, *Electrochim. Acta*, 2017, **247**, 779–786.

247 H. Abul-Futouh, A. Skabeev, D. Botteri, Y. Zagranyarski, H. Görls, W. Weigand and K. Peneva, *Organometallics*, 2018, **37**, 3278–3285.

248 A. P. S. Samuel, D. T. Co, C. L. Stern and M. R. Wasielewski, *J. Am. Chem. Soc.*, 2010, **132**, 8813–8815.

249 P. Li, S. Amirjalayer, F. Hartl, M. Lutz, B. de Bruin, R. Becker, S. Woutersen and J. N. H. Reek, *Inorg. Chem.*, 2014, **53**, 5373–5383.

250 C. A. Mebi, B. C. Noll, R. Gao and D. Karr, *Z. Anorg. Allg. Chem.*, 2010, **636**, 2550–2554.

251 C. Figliola, L. Male, S. L. Horswell and R. S. Grainger, *Eur. J. Inorg. Chem.*, 2015, 3146–3156.

252 P. Poddutoori, D. T. Co, A. P. S. Samuel, C. Hoon Kim, M. T. Vagnini and M. R. Wasielewski, *Energy Environ. Sci.*, 2011, **4**, 2441–2450.

253 X.-W. Song, X.-J. Gao, H.-X. Liu, H. Chen and C.-N. Chen, *Inorg. Chem. Commun.*, 2016, **70**, 1–3.

254 H. Reihlen, A. V. Friedolsheim and W. Oswald, *Justus Liebigs Ann. Chem.*, 1928, **465**, 72–96.

255 L. F. Dahl and C.-H. Wei, *Inorg. Chem.*, 1963, **2**, 328–333.

256 W. Hieber and P. Spacu, *Z. Anorg. Allg. Chem.*, 1937, **233**, 353–364.

257 W. Hieber and C. Scharfenberg, *Berichte Dtsch. Chem. Ges. B Ser.*, 1940, **73**, 1012–1021.

258 Y. Li and T. B. Rauchfuss, *Chem. Rev.*, 2016, **116**, 7043–7077.

259 C. He, M. Wang, X. Zhang, Z. Wang, C. Chen, J. Liu, B. Åkermark and L. Sun, *Angew. Chem., Int. Ed.*, 2004, **43**, 3571–3574.

260 A. K. Jones, B. R. Lichtenstein, A. Dutta, G. Gordon and P. L. Dutton, *J. Am. Chem. Soc.*, 2007, **129**, 14844–14845.

261 X. de Hatten, E. Bothe, K. Merz, I. Huc and N. Metzler-Nolte, *Eur. J. Inorg. Chem.*, 2008, 4530–4537.

262 K. D. Watenpaugh, L. C. Sieker and L. H. Jensen, *J. Mol. Biol.*, 1979, **131**, 509–522.

263 T. Tsukihara, K. Fukuyama, M. Nakamura, Y. Katsube, N. Tanaka, M. Kakudo, K. Wada, T. Hase and H. Matsubara, *J. Biochem.*, 1981, **90**, 1763–1773.

1778 | *Chem. Soc. Rev.*, 2021, **50**, 1668–1784

This journal is © The Royal Society of Chemistry 2021

264 Z. Yu, M. Wang, P. Li, W. Dong, F. Wang and L. Sun, *Dalton Trans.*, 2008, 2400–2406.

265 Y. Si, M. Hu and C. Chen, *C. R. Chim.*, 2008, **11**, 932–937.

266 N. Wen, F.-F. Xu, R.-P. Chen and S.-W. Du, *J. Organomet. Chem.*, 2014, **756**, 61–67.

267 J. A. Cabeza, M. A. Martínez-García, V. Riera, D. Ardura, S. García-Granda and J. F. Van der Maelen, *Eur. J. Inorg. Chem.*, 1999, 1133–1139.

268 C.-H. Chang, M.-H. Chen, W.-S. Du, J. Gliniak, J.-H. Lin, H.-H. Wu, H.-F. Chan, J.-S. K. Yu and T.-K. Wu, *Chem. – Eur. J.*, 2015, **21**, 6617–6622.

269 A. K. Justice, R. C. Linck and T. B. Rauchfuss, *Inorg. Chem.*, 2006, **45**, 2406–2412.

270 A. K. Justice, R. C. Linck, T. B. Rauchfuss and S. R. Wilson, *J. Am. Chem. Soc.*, 2004, **126**, 13214–13215.

271 M. E. Carroll, J. Chen, D. E. Gray, J. C. Lansing, T. B. Rauchfuss, D. Schilter, P. I. Volkers and S. R. Wilson, *Organometallics*, 2014, **33**, 858–867.

272 S. Ding, P. Ghosh, A. M. Lunsford, N. Wang, N. Bhuvanesh, M. B. Hall and M. Y. Darensbourg, *J. Am. Chem. Soc.*, 2016, **138**, 12920–12927.

273 H. Gao, J. Huang, L. Chen, R. Liu and J. Chen, *RSC Adv.*, 2013, **3**, 3557–3565.

274 R. D. Adams, B. Captain, O.-S. Kwon and S. Miao, *Inorg. Chem.*, 2003, **42**, 3356–3365.

275 R. D. Adams and S. Miao, *Inorg. Chem.*, 2004, **43**, 8414–8426.

276 S. Tsukada, T. Abe, N. Abe, S. Nakashima, K. Yamamoto and T. Gunji, *Dalton Trans.*, 2020, **49**, 9048–9056.

277 X. Zhao, I. P. Georgakaki, M. L. Miller, J. C. Yarbrough and M. Y. Darensbourg, *J. Am. Chem. Soc.*, 2001, **123**, 9710–9711.

278 X. Zhao, I. P. Georgakaki, M. L. Miller, R. Mejia-Rodriguez, C.-Y. Chiang and M. Y. Darensbourg, *Inorg. Chem.*, 2002, **41**, 3917–3928.

279 M. Schmidt, S. M. Contakes and T. B. Rauchfuss, *J. Am. Chem. Soc.*, 1999, **121**, 9736–9737.

280 Ö. F. Erdem, M. Stein, S. Kaur-Ghumaan, E. J. Reijerse, S. Ott and W. Lubitz, *Chem. – Eur. J.*, 2013, **19**, 14566–14572.

281 I. Ugi, D. Marquarding, H. Klusacek, P. Gillespie and F. Ramirez, *Acc. Chem. Res.*, 1971, **4**, 288–296.

282 E. J. Lyon, I. P. Georgakaki, J. H. Reibenspies and M. Y. Darensbourg, *J. Am. Chem. Soc.*, 2001, **123**, 3268–3278.

283 F. Gloaguen, J. D. Lawrence, M. Schmidt, S. R. Wilson and T. B. Rauchfuss, *J. Am. Chem. Soc.*, 2001, **123**, 12518–12527.

284 P. Russegger and J. Brickmann, *Chem. Phys. Lett.*, 1975, **30**, 276–278.

285 J. A. Altmann, K. Yates and I. G. Csizmadia, *J. Am. Chem. Soc.*, 1976, **98**, 1450–1454.

286 E. P. A. Couzijn, J. C. Slootweg, A. W. Ehlers and K. Lammertsma, *J. Am. Chem. Soc.*, 2010, **132**, 18127–18140.

287 C. Moberg, *Angew. Chem., Int. Ed.*, 2011, **50**, 10290–10292.

288 E. J. Lyon, I. P. Georgakaki, J. H. Reibenspies and M. Y. Darensbourg, *Angew. Chem., Int. Ed.*, 1999, **38**, 3178–3180.

289 A. L. Cloirec, S. C. Davies, D. J. Evans, D. L. Hughes, C. J. Pickett, S. P. Best and S. Borg, *Chem. Commun.*, 1999, 2285–2286.

290 B. C. Manor, M. R. Ringenberg and T. B. Rauchfuss, *Inorg. Chem.*, 2014, **53**, 7241–7247.

291 J.-F. Capon, S. El Hassnaoui, F. Gloaguen, P. Schollhammer and J. Talarmin, *Organometallics*, 2005, **24**, 2020–2022.

292 I. P. Georgakaki, L. Thomson, E. J. Lyon, M. B. Hall and M. Y. Darensbourg, *Coord. Chem. Rev.*, 2003, **238–239**, 255–266.

293 J. Windhager, U.-P. Apfel, T. Yoshino, N. Nakata, H. Görls, M. Rudolph, A. Ishii and W. Weigand, *Chem. – Asian J.*, 2010, **5**, 1600–1610.

294 A. S. Pandey, T. V. Harris, L. J. Giles, J. W. Peters and R. K. Szilagyi, *J. Am. Chem. Soc.*, 2008, **130**, 4533–4540.

295 W. S. Knowles, *Angew. Chem., Int. Ed.*, 2002, **41**, 1998–2007.

296 R. Noyori, *Angew. Chem., Int. Ed.*, 2002, **41**, 2008–2022.

297 ed. *Metal-Catalyzed Cross-Coupling Reactions*, A. de Meijere and F. Diederich, Wiley, 1st edn, 2004.

298 W. Strohmeier and F.-J. Müller, *Chem. Ber.*, 1967, **100**, 2812–2821.

299 C. A. Tolman, *J. Am. Chem. Soc.*, 1970, **92**, 2953–2956.

300 C. A. Tolman, *J. Am. Chem. Soc.*, 1970, **92**, 2956–2965.

301 H. Clavier and S. P. Nolan, *Chem. Commun.*, 2010, **46**, 841.

302 R. Mejia-Rodriguez, D. Chong, J. H. Reibenspies, M. P. Soriaga and M. Y. Darensbourg, *J. Am. Chem. Soc.*, 2004, **126**, 12004–12014.

303 Z. Wang, W. Jiang, J. Liu, W. Jiang, Y. Wang, B. Åkermark and L. Sun, *J. Organomet. Chem.*, 2008, **693**, 2828–2834.

304 Z. Zhao, M. Wang, W. Dong, P. Li, Z. Yu and L. Sun, *J. Organomet. Chem.*, 2009, **694**, 2309–2314.

305 H.-H. Cui, N.-N. Wu, J.-Y. Wang, M.-Q. Hu, H.-M. Wen and C.-N. Chen, *J. Organomet. Chem.*, 2014, **767**, 46–53.

306 S. Roy, T.-A. D. Nguyen, L. Gan and A. K. Jones, *Dalton Trans.*, 2015, **44**, 14865–14876.

307 H. Cui, M. Hu, H. Wen, G. Chai, C. Ma, H. Chen and C. Chen, *Dalton Trans.*, 2012, **41**, 13899.

308 L.-C. Song, F.-X. Luo, B.-B. Liu, Z.-C. Gu and H. Tan, *Organometallics*, 2016, **35**, 1399–1408.

309 X.-F. Liu and B.-S. Yin, *J. Coord. Chem.*, 2010, **63**, 4061–4067.

310 Y.-C. Liu, C.-H. Lee, G.-H. Lee and M.-H. Chiang, *Eur. J. Inorg. Chem.*, 2011, 1155–1162.

311 S. Ghosh, G. Hogarth, N. Hollingsworth, K. B. Holt, S. E. Kabir and B. E. Sanchez, *Chem. Commun.*, 2014, **50**, 945–947.

312 S. Kaur-Ghumaan, A. Sreenithya and R. B. Sunoj, *J. Chem. Sci.*, 2015, **127**, 557–563.

313 Y. Si, K. Charreteur, J.-F. Capon, F. Gloaguen, F. Y. Pétillon, P. Schollhammer and J. Talarmin, *J. Inorg. Biochem.*, 2010, **104**, 1038–1042.

314 S. Ghosh, N. Hollingsworth, M. Warren, D. A. Hrovat, M. G. Richmond and G. Hogarth, *Dalton Trans.*, 2019, **48**, 6051–6060.

315 J. A. De Beer, R. J. Haines, R. Greatrex and N. N. Greenwood, *J. Organomet. Chem.*, 1971, **27**, C33–C35.

This journal is © The Royal Society of Chemistry 2021

Chem. Soc. Rev., 2021, **50**, 1668–1784 | **1779**

316 J. A. de Beer, R. J. Haines, R. Greatrex and N. N. Greenwood, *J. Chem. Soc. A*, 1971, 3271–3282.

317 P. Li, M. Wang, C. He, G. Li, X. Liu, C. Chen, B. Åkermark and L. Sun, *Eur. J. Inorg. Chem.*, 2005, 2506–2513.

318 D. Zheng, M. Wang, L. Chen, N. Wang and L. Sun, *Inorg. Chem.*, 2014, **53**, 1555–1561.

319 F. Huo, J. Hou, G. Chen, D. Guo and X. Peng, *Eur. J. Inorg. Chem.*, 2010, 3942–3951.

320 R. Zaffaroni, T. B. Rauchfuss, D. L. Gray, L. De Gioia and G. Zampella, *J. Am. Chem. Soc.*, 2012, **134**, 19260–19269.

321 Z. Wang, J. He, S. Lü, W. Jiang, Y. Wu, J. Jiang, Y. Xie, C. Mu, A. Li, Y. Li and Q. Li, *Appl. Organomet. Chem.*, 2019, **33**, e5184.

322 M. Johnson, J. Thuman, R. G. Letterman, C. J. Stromberg, C. E. Webster and E. J. Heilweil, *J. Phys. Chem. B*, 2013, **117**, 15792–15803.

323 R. Kania, P. W. J. M. Frederix, J. A. Wright, R. V. Ulijn, C. J. Pickett and N. T. Hunt, *J. Chem. Phys.*, 2012, **136**, 044521.

324 J. A. Wright and C. J. Pickett, *Chem. Commun.*, 2009, 5719.

325 A. Jablonskytė, J. A. Wright and C. J. Pickett, *Dalton Trans.*, 2010, **39**, 3026.

326 F. I. Adam, G. Hogarth and I. Richards, *J. Organomet. Chem.*, 2007, **692**, 3957–3968.

327 G. Hogarth, S. E. Kabir and I. Richards, *Organometallics*, 2010, **29**, 6559–6568.

328 S. Ghosh, B. E. Sanchez, I. Richards, M. N. Haque, K. B. Holt, M. G. Richmond and G. Hogarth, *J. Organomet. Chem.*, 2016, **812**, 247–258.

329 L.-C. Song, C.-G. Li, J.-H. Ge, Z.-Y. Yang, H.-T. Wang, J. Zhang and Q.-M. Hu, *J. Inorg. Biochem.*, 2008, **102**, 1973–1979.

330 S. Ghosh, G. Hogarth, N. Hollingsworth, K. B. Holt, I. Richards, M. G. Richmond, B. E. Sanchez and D. Unwin, *Dalton Trans.*, 2013, **42**, 6775.

331 N. Wang, M. Wang, T. Liu, P. Li, T. Zhang, M. Y. Darensbourg and L. Sun, *Inorg. Chem.*, 2008, **47**, 6948–6955.

332 G. Hogarth, M. O'Brien and D. A. Tocher, *J. Organomet. Chem.*, 2003, **672**, 29–33.

333 P.-H. Zhao, Z.-Y. Ma, M.-Y. Hu, J. He, Y.-Z. Wang, X.-B. Jing, H.-Y. Chen, Z. Wang and Y.-L. Li, *Organometallics*, 2018, **37**, 1280–1290.

334 Y.-L. Li, Z.-Y. Ma, J. He, M.-Y. Hu and P.-H. Zhao, *J. Organomet. Chem.*, 2017, **851**, 14–21.

335 F. I. Adam, G. Hogarth, I. Richards and B. E. Sanchez, *Dalton Trans.*, 2007, 2495–2498.

336 S. Ezzaher, J.-F. Capon, F. Gloaguen, F. Y. Pétillon, P. Schollhammer, J. Talarmin, R. Pichon and N. Kervarec, *Inorg. Chem.*, 2007, **46**, 3426–3428.

337 A. K. Justice, G. Zampella, L. De Gioia, T. B. Rauchfuss, J. I. van der Vlugt and S. R. Wilson, *Inorg. Chem.*, 2007, **46**, 1655–1664.

338 S. Ezzaher, J.-F. Capon, F. Gloaguen, F. Y. Pétillon, P. Schollhammer and J. Talarmin, *Inorg. Chem.*, 2007, **46**, 9863–9872.

339 L.-C. Song, W. Gao, X. Luo, Z.-X. Wang, X.-J. Sun and H.-B. Song, *Organometallics*, 2012, **31**, 3324–3332.

340 S. Ezzaher, J.-F. Capon, F. Gloaguen, N. Kervarec, F. Y. Pétillon, R. Pichon, P. Schollhammer and J. Talarmin, *C. R. Chim.*, 2008, **11**, 906–914.

341 S. Munery, J.-F. Capon, L. De Gioia, C. Elleouet, C. Greco, F. Y. Pétillon, P. Schollhammer, J. Talarmin and G. Zampella, *Chem. – Eur. J.*, 2013, **19**, 15458–15461.

342 F. I. Adam, G. Hogarth, S. E. Kabir and I. Richards, *C. R. Chim.*, 2008, **11**, 890–905.

343 L.-C. Song, H.-T. Wang, J.-H. Ge, S.-Z. Mei, J. Gao, L.-X. Wang, B. Gai, L.-Q. Zhao, J. Yan and Y.-Z. Wang, *Organometallics*, 2008, **27**, 1409–1416.

344 W. Wang, T. B. Rauchfuss, C. E. Moore, A. L. Rheingold, L. De Gioia and G. Zampella, *Chem. – Eur. J.*, 2013, **19**, 15476–15479.

345 A. K. Justice, L. De Gioia, M. J. Nilges, T. B. Rauchfuss, S. R. Wilson and G. Zampella, *Inorg. Chem.*, 2008, **47**, 7405–7414.

346 W. Gao, J. Liu, B. Åkermark and L. Sun, *Inorg. Chem.*, 2006, **45**, 9169–9171.

347 M. Beyler, S. Ezzaher, M. Karnahl, M.-P. Santoni, R. Lomoth and S. Ott, *Chem. Commun.*, 2011, **47**, 11662.

348 M. R. Carlson, D. L. Gray, C. P. Richers, W. Wang, P.-H. Zhao, T. B. Rauchfuss, V. Pelmenschikov, C. C. Pham, L. B. Gee, H. Wang and S. P. Cramer, *Inorg. Chem.*, 2018, **57**, 1988–2001.

349 J. M. Camara and T. B. Rauchfuss, *Nat. Chem.*, 2012, **4**, 26–30.

350 N. Wang, M. Wang, T. Zhang, P. Li, J. Liu and L. Sun, *Chem. Commun.*, 2008, 5800.

351 N. Wang, M. Wang, J. Liu, K. Jin, L. Chen and L. Sun, *Inorg. Chem.*, 2009, **48**, 11551–11558.

352 S. Lounissi, G. Zampella, J.-F. Capon, L. De Gioia, F. Matoussi, S. Mahfoudhi, F. Y. Pétillon, P. Schollhammer and J. Talarmin, *Chem. – Eur. J.*, 2012, **18**, 11123–11138.

353 G. Hogarth and I. Richards, *Inorg. Chem. Commun.*, 2007, **10**, 66–70.

354 D. G. Unwin, S. Ghosh, F. Ridley, M. G. Richmond, K. B. Holt and G. Hogarth, *Dalton Trans.*, 2019, **48**, 6174–6190.

355 J. L. Nehring and D. M. Heinekey, *Inorg. Chem.*, 2003, **42**, 4288–4292.

356 J. D. Lawrence, T. B. Rauchfuss and S. R. Wilson, *Inorg. Chem.*, 2002, **41**, 6193–6195.

357 C. A. Boyke, T. B. Rauchfuss, S. R. Wilson, M.-M. Rohmer and M. Bénard, *J. Am. Chem. Soc.*, 2004, **126**, 15151–15160.

358 J. Hou, X. Peng, J. Liu, Y. Gao, X. Zhao, S. Gao and K. Han, *Eur. J. Inorg. Chem.*, 2006, 4679–4686.

359 W. A. Herrmann, *Angew. Chem., Int. Ed.*, 2002, **41**, 1290–1309.

360 M. Scholl, T. M. Trnka, J. P. Morgan and R. H. Grubbs, *Tetrahedron Lett.*, 1999, **40**, 2247–2250.

361 C. M. Thomas, T. Liu, M. B. Hall and M. Y. Darensbourg, *Inorg. Chem.*, 2008, **47**, 7009–7024.

362 J. W. Tye, J. Lee, H.-W. Wang, R. Mejia-Rodriguez, J. H. Reibenspies, M. B. Hall and M. Y. Darensbourg, *Inorg. Chem.*, 2005, **44**, 5550–5552.

1780 | *Chem. Soc. Rev.*, 2021, **50**, 1668–1784

This journal is © The Royal Society of Chemistry 2021

363 D. Morvan, J.-F. Capon, F. Gloaguen, A. Le Goff, M. Marchivie, F. Michaud, P. Schollhammer, J. Talarmin, J.-J. Yaouanc, R. Pichon and N. Kervarec, *Organometallics*, 2007, **26**, 2042–2052.

364 L. Duan, M. Wang, P. Li, Y. Na, N. Wang and L. Sun, *Dalton Trans.*, 2007, 1277–1283.

365 T. Liu and M. Y. Darensbourg, *J. Am. Chem. Soc.*, 2007, **129**, 7008–7009.

366 M.-Q. Hu, C.-B. Ma, X.-F. Zhang, F. Chen, C.-N. Chen and Q.-T. Liu, *Chem. Lett.*, 2006, **35**, 840–841.

367 M.-Q. Hu, C.-B. Ma, Y.-T. Si, C.-N. Chen and Q.-T. Liu, *J. Inorg. Biochem.*, 2007, **101**, 1370–1375.

368 K. Charreteur, J.-F. Capon, F. Gloaguen, F. Y. Pétillon, P. Schollhammer and J. Talarmin, *Eur. J. Inorg. Chem.*, 2011, 1038–1042.

369 L. Schwartz, J. Ekström, R. Lomoth and S. Ott, *Chem. Commun.*, 2006, 4206–4208.

370 Y. Zhang, M.-Q. Hu, H.-M. Wen, Y.-T. Si, C.-B. Ma, C.-N. Chen and Q.-T. Liu, *J. Organomet. Chem.*, 2009, **694**, 2576–2580.

371 S. Roy, T. L. Groy and A. K. Jones, *Dalton Trans.*, 2013, **42**, 3843.

372 P.-Y. Orain, J.-F. Capon, N. Kervarec, F. Gloaguen, F. Pétillon, R. Pichon, P. Schollhammer and J. Talarmin, *Dalton Trans.*, 2007, 3754.

373 P.-Y. Orain, J.-F. Capon, F. Gloaguen, F. Y. Pétillon, P. Schollhammer, J. Talarmin, G. Zampella, L. De Gioia and T. Roisnel, *Inorg. Chem.*, 2010, **49**, 5003–5008.

374 L. Wang, M. Gennari, F. G. Cantú Reinhard, J. Gutiérrez, A. Morozan, C. Philouze, S. Demeshko, V. Artero, F. Meyer, S. P. de Visser and C. Duboc, *J. Am. Chem. Soc.*, 2019, **141**, 8244–8253.

375 D. Brazzolotto, L. Wang, H. Tang, M. Gennari, N. Queyriaux, C. Philouze, S. Demeshko, F. Meyer, M. Orio, V. Artero, M. B. Hall and C. Duboc, *ACS Catal.*, 2018, **8**, 10658–10667.

376 L. Wang, M. Gennari, A. Barrozo, J. Fize, C. Philouze, S. Demeshko, F. Meyer, M. Orio, V. Artero and C. Duboc, *ACS Catal.*, 2020, **10**, 177–186.

377 M. Bruschi, P. Fantucci and L. De Gioia, *Inorg. Chem.*, 2003, **42**, 4773–4781.

378 J. W. Tye, M. Y. Darensbourg and M. B. Hall, *Inorg. Chem.*, 2006, **45**, 1552–1559.

379 M. Razavet, S. J. Borg, S. J. George, S. P. Best, S. A. Fairhurst and C. J. Pickett, *Chem. Commun.*, 2002, 700–701.

380 S. J. Borg, T. Behrsing, S. P. Best, M. Razavet, X. Liu and C. J. Pickett, *J. Am. Chem. Soc.*, 2004, **126**, 16988–16999.

381 M. T. Olsen, M. Bruschi, L. De Gioia, T. B. Rauchfuss and S. R. Wilson, *J. Am. Chem. Soc.*, 2008, **130**, 12021–12030.

382 C.-H. Hsieh, Ö. F. Erdem, S. D. Harman, M. L. Singleton, E. Reijerse, W. Lubitz, C. V. Popescu, J. H. Reibenspies, S. M. Brothers, M. B. Hall and M. Y. Darensbourg, *J. Am. Chem. Soc.*, 2012, **134**, 13089–13102.

383 R. D. Bethel, D. J. Crouthers, C.-H. Hsieh, J. A. Denny, M. B. Hall and M. Y. Darensbourg, *Inorg. Chem.*, 2015, **54**, 3523–3535.

384 R. H. Crabtree and M. Lavin, *Inorg. Chem.*, 1986, **25**, 805–812.

385 S. J. George, Z. Cui, M. Razavet and C. J. Pickett, *Chem. – Eur. J.*, 2002, **8**, 4037–4046.

386 A. K. Justice, T. B. Rauchfuss and S. R. Wilson, *Angew. Chem., Int. Ed.*, 2007, **46**, 6152–6154.

387 M. L. Singleton, N. Bhuvanesh, J. H. Reibenspies and M. Y. Darensbourg, *Angew. Chem., Int. Ed.*, 2008, **47**, 9492–9495.

388 W. Wang, T. B. Rauchfuss, L. Zhu and G. Zampella, *J. Am. Chem. Soc.*, 2014, **136**, 5773–5782.

389 J. M. Camara and T. B. Rauchfuss, *J. Am. Chem. Soc.*, 2011, **133**, 8098–8101.

390 W. Ziegler, H. Umland and U. Behrens, *J. Organomet. Chem.*, 1988, **344**, 235–247.

391 M. T. Olsen, T. B. Rauchfuss and S. R. Wilson, *J. Am. Chem. Soc.*, 2010, **132**, 17733–17740.

392 A. K. Justice, M. J. Nilges, T. B. Rauchfuss, S. R. Wilson, L. De Gioia and G. Zampella, *J. Am. Chem. Soc.*, 2008, **130**, 5293–5301.

393 M. T. Olsen, B. E. Barton and T. B. Rauchfuss, *Inorg. Chem.*, 2009, **48**, 7507–7509.

394 S. E. Landau, R. H. Morris and A. J. Lough, *Inorg. Chem.*, 1999, **38**, 6060–6068.

395 C. M. Thomas, M. Y. Darensbourg and M. B. Hall, *J. Inorg. Biochem.*, 2007, **101**, 1752–1757.

396 N. Wang, M. Wang, Y. Wang, D. Zheng, H. Han, M. S. G. Ahlquist and L. Sun, *J. Am. Chem. Soc.*, 2013, **135**, 13688–13691.

397 M. Cheng, M. Wang, D. Zheng and L. Sun, *Dalton Trans.*, 2016, **45**, 17687–17696.

398 D. Chouffai, G. Zampella, J.-F. Capon, L. D. Gioia, A. L. Goff, F. Y. Pétillon, P. Schollhammer and J. Talarmin, *Organometallics*, 2012, **31**, 1082–1091.

399 C. A. Boyke, J. I. van der Vlugt, T. B. Rauchfuss, S. R. Wilson, G. Zampella and L. De Gioia, *J. Am. Chem. Soc.*, 2005, **127**, 11010–11018.

400 J. I. van der Vlugt, T. B. Rauchfuss and S. R. Wilson, *Chem. – Eur. J.*, 2006, **12**, 90–98.

401 F. Arrigoni, S. Mohamed Bouh, C. Elleouet, F. Y. Pétillon, P. Schollhammer, L. De Gioia and G. Zampella, *Chem. – Eur. J.*, 2018, **24**, 15036–15051.

402 M. W. W. Adams, *Biochim. Biophys. Acta, Bioenerg.*, 1990, **1020**, 115–145.

403 M. Frey, *ChemBioChem*, 2002, **3**, 153–160.

404 X. Zhao, C.-Y. Chiang, M. L. Miller, M. V. Rampersad and M. Y. Darensbourg, *J. Am. Chem. Soc.*, 2003, **125**, 518–524.

405 Z. M. Heiden, G. Zampella, L. De Gioia and T. B. Rauchfuss, *Angew. Chem., Int. Ed.*, 2008, **47**, 9756–9759.

406 F. Z. Roussin, *Ann. Chim. Phys.*, 1858, **3**, 285–303.

407 A. R. Butler and I. L. Megson, *Chem. Rev.*, 2002, **102**, 1155–1166.

408 M. T. Olsen, A. K. Justice, F. Gloaguen, T. B. Rauchfuss and S. R. Wilson, *Inorg. Chem.*, 2008, **47**, 11816–11824.

409 C. M. Thomas, T. Liu, M. B. Hall and M. Y. Darensbourg, *Chem. Commun.*, 2008, 1563.

410 A. Silakov, J. L. Shaw, E. J. Reijerse and W. Lubitz, *J. Am. Chem. Soc.*, 2010, **132**, 17578–17587.

This journal is © The Royal Society of Chemistry 2021

Chem. Soc. Rev., 2021, **50**, 1668–1784 | **1781**

411 A. Petuker, K. Merz, C. Merten and U.-P. Apfel, *Inorg. Chem.*, 2016, **55**, 1183–1191.

412 A. Q. Daraosheh, M. K. Harb, J. Windhager, H. Görls, M. El-khateeb and W. Weigand, *Organometallics*, 2009, **28**, 6275–6280.

413 G. Zampella, M. Bruschi, P. Fantucci, M. Razavet, C. J. Pickett and L. De Gioia, *Chem. – Eur. J.*, 2005, **11**, 509–533.

414 Ö. F. Erdem, L. Schwartz, M. Stein, A. Silakov, S. Kaur-Ghumaan, P. Huang, S. Ott, E. J. Reijerse and W. Lubitz, *Angew. Chem., Int. Ed.*, 2011, **50**, 1439–1443.

415 Ö. F. Erdem, L. Schwartz, M. Stein, A. Silakov, S. Kaur-Ghumaan, P. Huang, S. Ott, E. J. Reijerse and W. Lubitz, *Angew. Chem.*, 2011, **123**, 1475–1479.

416 C. Tard, X. Liu, S. K. Ibrahim, M. Bruschi, L. D. Gioia, S. C. Davies, X. Yang, L.-S. Wang, G. Sawers and C. J. Pickett, *Nature*, 2005, **433**, 610–613.

417 D. E. Schwab, C. Tard, E. Brecht, J. W. Peters, C. J. Pickett and R. K. Szilagyi, *Chem. Commun.*, 2006, 3696.

418 M. Bruschi, C. Greco, G. Zampella, U. Ryde, C. J. Pickett and L. De Gioia, *C. R. Chim.*, 2008, **11**, 834–841.

419 L.-C. Song, J. Yan, Y.-L. Li, D.-F. Wang and Q.-M. Hu, *Inorg. Chem.*, 2009, **48**, 11376–11381.

420 C. Tard, X. Liu, D. L. Hughes and C. J. Pickett, *Chem. Commun.*, 2005, 133–135.

421 M. H. Cheah, C. Tard, S. J. Borg, X. Liu, S. K. Ibrahim, C. J. Pickett and S. P. Best, *J. Am. Chem. Soc.*, 2007, **129**, 11085–11092.

422 P. Surawatanawong and M. B. Hall, *Inorg. Chem.*, 2010, **49**, 5737–5747.

423 K. Fauvel, R. Mathieu and R. Poilblanc, *Inorg. Chem.*, 1976, **15**, 976–978.

424 M. S. Arabi, R. Mathieu and R. Poilblanc, *J. Organomet. Chem.*, 1979, **177**, 199–209.

425 R. J. Haines, J. A. de Beer and R. Greatrex, *J. Chem. Soc., Dalton Trans.*, 1976, 1749–1757.

426 R. Mathieu and R. Poilblanc, *J. Organomet. Chem.*, 1977, **142**, 351–355.

427 M. S. Arabi, R. Mathieu and R. Poilblanc, *Inorg. Chim. Acta*, 1979, **34**, L207–L208.

428 J. J. Bonnet, R. Mathieu, R. Poilblanc and J. A. Ibers, *J. Am. Chem. Soc.*, 1979, **101**, 7487–7496.

429 R. Mathieu, R. Poilblanc, P. Lemoine and M. Gross, *J. Organomet. Chem.*, 1979, **165**, 243–252.

430 N. J. Taylor, M. S. Arabi and R. Mathieu, *Inorg. Chem.*, 1980, **19**, 1740–1742.

431 P. M. Treichel, R. A. Crane, R. Matthews, K. R. Bonnin and D. Powell, *J. Organomet. Chem.*, 1991, **402**, 233–248.

432 I. P. Georgakaki, M. L. Miller and M. Y. Darensbourg, *Inorg. Chem.*, 2003, **42**, 2489–2494.

433 M. T. Olsen, D. L. Gray, T. B. Rauchfuss, L. D. Gioia and G. Zampella, *Chem. Commun.*, 2011, **47**, 6554.

434 M. T. Olsen, T. B. Rauchfuss and R. Zaffaroni, *Organometallics*, 2012, **31**, 3447–3450.

435 L.-C. Song, D.-J. Hong, Y.-Q. Guo and X.-Y. Wang, *Organometallics*, 2018, **37**, 4744–4752.

436 J. W. Tye, M. Y. Darensbourg and M. B. Hall, *THEOCHEM*, 2006, **771**, 123–128.

437 B. E. Barton, G. Zampella, A. K. Justice, L. De Gioia, T. B. Rauchfuss and S. R. Wilson, *Dalton Trans.*, 2010, **39**, 3011–3019.

438 J. I. van der Vlugt, T. B. Rauchfuss, C. M. Whaley and S. R. Wilson, *J. Am. Chem. Soc.*, 2005, **127**, 16012–16013.

439 S. Tschierlei, S. Ott and R. Lomoth, *Energy Environ. Sci.*, 2011, **4**, 2340.

440 J. M. Savariault, J. J. Bonnet, R. Mathieu and J. Galy, *C. R. Seances Acad. Sci., Ser. C*, 1977, **284**, 663–665.

441 X. Zhao, Y.-M. Hsiao, C.-H. Lai, J. H. Reibenspies and M. Y. Darensbourg, *Inorg. Chem.*, 2002, **41**, 699–708.

442 S. L. Matthews and D. M. Heinekey, *Inorg. Chem.*, 2010, **49**, 9746–9748.

443 Y.-C. Liu, K.-T. Chu, Y.-L. Huang, C.-H. Hsu, G.-H. Lee, M.-C. Tseng and M.-H. Chiang, *ACS Catal.*, 2016, **6**, 2559–2576.

444 R. H. Morris, *Chem. Rev.*, 2016, **116**, 8588–8654.

445 P. I. Volkers and T. B. Rauchfuss, *J. Inorg. Biochem.*, 2007, **101**, 1748–1751.

446 D. Yang, Y. Li, B. Wang, X. Zhao, L. Su, S. Chen, P. Tong, Y. Luo and J. Qu, *Inorg. Chem.*, 2015, **54**, 10243–10249.

447 M.-H. Chiang, Y.-C. Liu, S.-T. Yang and G.-H. Lee, *Inorg. Chem.*, 2009, **48**, 7604–7612.

448 M. H. Cheah, S. J. Borg, M. I. Bondin and S. P. Best, *Inorg. Chem.*, 2004, **43**, 5635–5644.

449 M. G. I. Galinato, C. M. Whaley, D. Roberts, P. Wang and N. Lehnert, *Eur. J. Inorg. Chem.*, 2011, 1147–1154.

450 D. Morvan, J.-F. Capon, F. Gloaguen, F. Y. Pétillon, P. Schollhammer, J. Talarmin, J.-J. Yaouanc, F. Michaud and N. Kervarec, *J. Organomet. Chem.*, 2009, **694**, 2801–2807.

451 M. E. Carroll, B. E. Barton, T. B. Rauchfuss and P. J. Carroll, *J. Am. Chem. Soc.*, 2012, **134**, 18843–18852.

452 X. Yu, C.-H. Tung, W. Wang, M. T. Huynh, D. L. Gray, S. Hammes-Schiffer and T. B. Rauchfuss, *Organometallics*, 2017, **36**, 2245–2253.

453 F. Wang, M. Wang, X. Liu, K. Jin, W. Dong, G. Li, B. Åkermark and L. Sun, *Chem. Commun.*, 2005, 3221.

454 F. Wang, M. Wang, X. Liu, K. Jin, W. Dong and L. Sun, *Dalton Trans.*, 2007, 3812–3819.

455 L. Schwartz, G. Eilers, L. Eriksson, A. Gogoll, R. Lomoth and S. Ott, *Chem. Commun.*, 2006, 520–522.

456 S. Ott, M. Kritikos, B. Åkermark, L. Sun and R. Lomoth, *Angew. Chem., Int. Ed.*, 2004, **43**, 1006–1009.

457 S. Jiang, J. Liu and L. Sun, *Inorg. Chem. Commun.*, 2006, **9**, 290–292.

458 J.-F. Capon, S. Ezzaher, F. Gloaguen, F. Y. Pétillon, P. Schollhammer and J. Talarmin, *Chem. – Eur. J.*, 2008, **14**, 1954–1964.

459 J. L. Stanley, Z. M. Heiden, T. B. Rauchfuss, S. R. Wilson, L. De Gioia and G. Zampella, *Organometallics*, 2008, **27**, 119–125.

460 L.-C. Song, J.-H. Ge, X.-F. Liu, L.-Q. Zhao and Q.-M. Hu, *J. Organomet. Chem.*, 2006, **691**, 5701–5709.

461 S. Lounissi, J.-F. Capon, F. Gloaguen, F. Matoussi, F. Y. Pétillon, P. Schollhammer and J. Talarmin, *Chem. Commun.*, 2011, **47**, 878–880.

462 W. Dong, M. Wang, X. Liu, K. Jin, G. Li, F. Wang and L. Sun, *Chem. Commun.*, 2006, 305–307.

463 S. Ezzaher, P.-Y. Orain, J.-F. Capon, F. Gloaguen, F. Y. Pétillon, T. Roisnel, P. Schollhammer and J. Talarmin, *Chem. Commun.*, 2008, 2547.

464 Y. Wang, M. Wang, L. Sun and M. S. G. Ahlquist, *Chem. Commun.*, 2012, **48**, 4450.

465 Y. Wang and M. S. G. Ahlquist, *Dalton Trans.*, 2013, **42**, 7816.

466 D. Chong, I. P. Georgakaki, R. Mejia-Rodriguez, J. Sanabria-Chinchilla, M. P. Soriaga and M. Y. Darensbourg, *Dalton Trans.*, 2003, 4158–4163.

467 J.-F. Capon, F. Gloaguen, P. Schollhammer and J. Talarmin, *J. Electroanal. Chem.*, 2006, **595**, 47–52.

468 G. A. N. Felton, A. K. Vannucci, J. Chen, L. T. Lockett, N. Okumura, B. J. Petro, U. I. Zakai, D. H. Evans, R. S. Glass and D. L. Lichtenberger, *J. Am. Chem. Soc.*, 2007, **129**, 12521–12530.

469 R. J. Wright, W. Zhang, X. Yang, M. Fasulo and T. D. Tilley, *Dalton Trans.*, 2012, **41**, 73–82.

470 M. Mirmohades, S. Pullen, M. Stein, S. Maji, S. Ott, L. Hammarström and R. Lomoth, *J. Am. Chem. Soc.*, 2014, **136**, 17366–17369.

471 J. P. H. Oudsen, B. Venderbosch, D. J. Martin, T. J. Korstanje, J. N. H. Reek and M. Tromp, *Phys. Chem. Chem. Phys.*, 2019, **21**, 14638–14645.

472 R. J. Wright, W. Zhang, X. Yang, M. Fasulo and T. D. Tilley, *Dalton Trans.*, 2011, **41**, 73–82.

473 M. L. Singleton, R. M. Jenkins, C. L. Klemashevich and M. Y. Darensbourg, *C. R. Chim.*, 2008, **11**, 861–874.

474 D. Zheng, M. Wang, L. Chen, N. Wang, M. Cheng and L. Sun, *Chem. Commun.*, 2014, **50**, 9255–9258.

475 P. S. Singh, H. C. Rudbeck, P. Huang, S. Ezzaher, L. Eriksson, M. Stein, S. Ott and R. Lomoth, *Inorg. Chem.*, 2009, **48**, 10883–10885.

476 L. Schwartz, L. Eriksson, R. Lomoth, F. Teixidor, C. Viñas and S. Ott, *Dalton Trans.*, 2008, 2379.

477 L.-C. Song, B. Gai, H.-T. Wang and Q.-M. Hu, *J. Inorg. Biochem.*, 2009, **103**, 805–812.

478 C. Esmieu and G. Berggren, *Dalton Trans.*, 2016, **45**, 19242–19248.

479 C.-G. Li, Y. Zhu, X.-X. Jiao and X.-Q. Fu, *Polyhedron*, 2014, **67**, 416–421.

480 I. K. Pandey, S. M. Mobin, N. Deibel, B. Sarkar and S. Kaur-Ghumaan, *Eur. J. Inorg. Chem.*, 2015, 2875–2882.

481 W.-G. Wang, H.-Y. Wang, G. Si, C.-H. Tung and L.-Z. Wu, *Dalton Trans.*, 2009, 2712–2720.

482 F. Gloaguen, D. Morvan, J.-F. Capon, P. Schollhammer and J. Talarmin, *J. Electroanal. Chem.*, 2007, **603**, 15–20.

483 F. Arrigoni, S. Mohamed Bouh, L. De Gioia, C. Elleouet, F. Y. Pétillon, P. Schollhammer and G. Zampella, *Chem. – Eur. J.*, 2017, **23**, 4364–4372.

484 J. Hou, X. Peng, Z. Zhou, S. Sun, X. Zhao and S. Gao, *J. Organomet. Chem.*, 2006, **691**, 4633–4640.

485 D. Morvan, J.-F. Capon, F. Gloaguen, P. Schollhammer and J. Talarmin, *Eur. J. Inorg. Chem.*, 2007, 5062–5068.

486 Y. Na, M. Wang, K. Jin, R. Zhang and L. Sun, *J. Organomet. Chem.*, 2006, **691**, 5045–5051.

487 P. Li, M. Wang, C. He, X. Liu, K. Jin and L. Sun, *Eur. J. Inorg. Chem.*, 2007, 3718–3727.

488 Y. Wang, Z. Li, X. Zeng, X. Wang, C. Zhan, Y. Liu, X. Zeng, Q. Luo and X. Liu, *New J. Chem.*, 2009, **33**, 1780.

489 P. Li, M. Wang, J. Pan, L. Chen, N. Wang and L. Sun, *J. Inorg. Biochem.*, 2008, **102**, 952–959.

490 G. Si, W.-G. Wang, H.-Y. Wang, C.-H. Tung and L.-Z. Wu, *Inorg. Chem.*, 2008, **47**, 8101–8111.

491 P.-H. Zhao, M.-Y. Hu, J.-R. Li, Z.-Y. Ma, Y.-Z. Wang, J. He, Y.-L. Li and X.-F. Liu, *Organometallics*, 2019, **38**, 385–394.

492 K. Charreteur, M. Kdider, J.-F. Capon, F. Gloaguen, F. Y. Pétillon, P. Schollhammer and J. Talarmin, *Inorg. Chem.*, 2010, **49**, 2496–2501.

493 R. Becker, S. Amirjalayer, P. Li, S. Woutersen and J. N. H. Reek, *Sci. Adv.*, 2016, **2**, e1501014.

494 G. A. N. Felton, C. A. Mebi, B. J. Petro, A. K. Vannucci, D. H. Evans, R. S. Glass and D. L. Lichtenberger, *J. Organomet. Chem.*, 2009, **694**, 2681–2699.

495 C. A. Mebi, D. S. Karr and B. C. Noll, *Polyhedron*, 2013, **50**, 164–168.

496 I. Kumar Pandey, M. Natarajan, H. Faujdar, F. Hussain, M. Stein and S. Kaur-Ghumaan, *Dalton Trans.*, 2018, **47**, 4941–4949.

497 A. Darchen, H. Mousser and H. Patin, *J. Chem. Soc., Chem. Commun.*, 1988, (14), 968–970.

498 S. J. Borg, M. I. Bondin, S. P. Best, M. Razavet, X. Liu and C. J. Pickett, *Biochem. Soc. Trans.*, 2005, **33**, 3–6.

499 C. Greco, G. Zampella, L. Bertini, M. Bruschi, P. Fantucci and L. De Gioia, *Inorg. Chem.*, 2007, **46**, 108–116.

500 M. Bourrez, R. Steinmetz and F. Gloaguen, *Inorg. Chem.*, 2014, **53**, 10667–10673.

501 R. M. Bullock and M. L. Helm, *Acc. Chem. Res.*, 2015, **48**, 2017–2026.

502 J.-F. Capon, F. Gloaguen, F. Y. Pétillon, P. Schollhammer and J. Talarmin, *C. R. Chim.*, 2008, **11**, 842–851.

503 M. H. Cheah, S. J. Borg and S. P. Best, *Inorg. Chem.*, 2007, **46**, 1741–1750.

504 D. Schilter, J. M. Camara, M. T. Huynh, S. Hammes-Schiffer and T. B. Rauchfuss, *Chem. Rev.*, 2016, **116**, 8693–8749.

505 P. Li, M. Wang, L. Chen, J. Liu, Z. Zhao and L. Sun, *Dalton Trans.*, 2009, 1919.

506 R. Zaffaroni, W. I. Dzik, R. J. Detz, J. I. van der Vlugt and J. N. H. Reek, *Eur. J. Inorg. Chem.*, 2019, 2498–2509.

507 S. Ghosh, A. Rahaman, K. B. Holt, E. Nordlander, M. G. Richmond, S. E. Kabir and G. Hogarth, *Polyhedron*, 2016, **116**, 127–135.

508 C. Greco and L. De Gioia, *Inorg. Chem.*, 2011, **50**, 6987–6995.

509 Y.-C. Liu, T.-H. Yen, Y.-J. Tseng, C.-H. Hu, G.-H. Lee and M.-H. Chiang, *Inorg. Chem.*, 2012, **51**, 5997–5999.

510 M. Karnahl, S. Tschierlei, Ö. F. Erdem, S. Pullen, M.-P. Santoni, E. J. Reijerse, W. Lubitz and S. Ott, *Dalton Trans.*, 2012, **41**, 12468.

This journal is © The Royal Society of Chemistry 2021

Chem. Soc. Rev., 2021, **50**, 1668–1784 | **1783**

511 T. Yu, Y. Zeng, J. Chen, Y.-Y. Li, G. Yang and Y. Li, *Angew. Chem., Int. Ed.*, 2013, **52**, 5631–5635.

512 P. W. J. M. Frederix, R. Kania, J. A. Wright, D. A. Lamprou, R. V. Ulijn, C. J. Pickett and N. T. Hunt, *Dalton Trans.*, 2012, **41**, 13112–13119.

513 A. Roy, C. Madden and G. Ghirlanda, *Chem. Commun.*, 2012, **48**, 9816.

514 C. Orain, F. Quentel and F. Gloaguen, *ChemSusChem*, 2014, **7**, 638–643.

515 A. Le Goff, V. Artero, R. Metayé, F. Moggia, B. Jousselme, M. Razavet, P. D. Tran, S. Palacin and M. Fontecave, *Int. J. Hydrogen Energy*, 2010, **35**, 10790–10796.

516 R. Zaffaroni, R. J. Detz, J. I. van der Vlugt and J. N. H. Reek, *ChemSusChem*, 2018, **11**, 209–218.

517 M. E. Ahmed, S. Dey, B. Mondal and A. Dey, *Chem. Commun.*, 2017, **53**, 8188–8191.

518 J. Sanabria-Chinchilla, A. Javier, D. Crouthers, J. H. Baricuatro, M. Y. Darensbourg and M. P. Soriaga, *Electrocatalysis*, 2014, **5**, 5–7.

519 B. Chmielowiec, F. H. Saadi, J. H. Baricuatro, A. Javier, Y.-G. Kim, G. Sun, M. Y. Darensbourg and M. P. Soriaga, *J. Electroanal. Chem.*, 2014, **716**, 63–70.

520 M. Karayilan, W. P. Brezinski, K. E. Clary, D. L. Lichtenberger, R. S. Glass and J. Pyun, *Angew. Chem., Int. Ed.*, 2019, **58**, 7537–7550.

521 R. Lomoth and S. Ott, *Dalton Trans.*, 2009, 9952.

522 T. R. Simmons, G. Berggren, M. Bacchi, M. Fontecave and V. Artero, *Coord. Chem. Rev.*, 2014, **270–271**, 127–150.

523 L.-Z. Wu, B. Chen, Z.-J. Li and C.-H. Tung, *Acc. Chem. Res.*, 2014, **47**, 2177–2185.

524 S. Ott, M. Kritikos, B. Åkermark and L. Sun, *Angew. Chem., Int. Ed.*, 2003, **42**, 3285–3288.

525 H. Wolpher, M. Borgström, L. Hammarström, J. Bergquist, V. Sundström, S. Styring, L. Sun and B. Åkermark, *Inorg. Chem. Commun.*, 2003, **6**, 989–991.

526 L.-C. Song, M.-Y. Tang, F.-H. Su and Q.-M. Hu, *Angew. Chem., Int. Ed.*, 2006, **45**, 1130–1133.

527 H.-Y. Wang, G. Si, W.-N. Cao, W.-G. Wang, Z.-J. Li, F. Wang, C.-H. Tung and L.-Z. Wu, *Chem. Commun.*, 2011, **47**, 8406–8408.

528 X. Li, M. Wang, S. Zhang, J. Pan, Y. Na, J. Liu, B. Åkermark and L. Sun, *J. Phys. Chem. B*, 2008, **112**, 8198–8202.

529 J. Ekström, M. Abrahamsson, C. Olson, J. Bergquist, F. B. Kaynak, L. Eriksson, L. Sun, H.-C. Becker, B. Åkermark, L. Hammarström and S. Ott, *Dalton Trans.*, 2006, 4599–4606.

530 W.-G. Wang, F. Wang, H.-Y. Wang, C.-H. Tung and L.-Z. Wu, *Dalton Trans.*, 2012, **41**, 2420.

531 W.-G. Wang, F. Wang, H.-Y. Wang, G. Si, C.-H. Tung and L.-Z. Wu, *Chem. – Asian J.*, 2010, **5**, 1796–1803.

532 A. M. Kluwer, R. Kapre, F. Hartl, M. Lutz, A. L. Spek, A. M. Brouwer, P. W. N. M. van Leeuwen and J. N. H. Reek, *Proc. Natl. Acad. Sci. U. S. A.*, 2009, **106**, 10460–10465.

533 W. Wang, T. B. Rauchfuss, L. Bertini and G. Zampella, *J. Am. Chem. Soc.*, 2012, **134**, 4525–4528.

534 F. Wang, W.-G. Wang, X.-J. Wang, H.-Y. Wang, C.-H. Tung and L.-Z. Wu, *Angew. Chem., Int. Ed.*, 2011, **50**, 3193–3197.

535 Y. Na, J. Pan, M. Wang and L. Sun, *Inorg. Chem.*, 2007, **46**, 3813–3815.

536 Y. Na, M. Wang, J. Pan, P. Zhang, B. Åkermark and L. Sun, *Inorg. Chem.*, 2008, **47**, 2805–2810.

537 D. Streich, Y. Astuti, M. Orlandi, L. Schwartz, R. Lomoth, L. Hammarström and S. Ott, *Chem. – Eur. J.*, 2010, **16**, 60–63.

538 W.-J. Liang, F. Wang, M. Wen, J.-X. Jian, X.-Z. Wang, B. Chen, C.-H. Tung and L.-Z. Wu, *Chem. – Eur. J.*, 2015, **21**, 3187–3192.

539 J.-X. Jian, Q. Liu, Z.-J. Li, F. Wang, X.-B. Li, C.-B. Li, B. Liu, Q.-Y. Meng, B. Chen, K. Feng, C.-H. Tung and L.-Z. Wu, *Nat. Commun.*, 2013, **4**, 2695.

540 F. Wen, X. Wang, L. Huang, G. Ma, J. Yang and C. Li, *ChemSusChem*, 2012, **5**, 849–853.

541 M. V. Pavliuk, A. M. Cieślak, M. Abdellah, A. Budinská, S. Pullen, K. Sokołowski, D. L. A. Fernandes, J. Szlachetko, E. L. Bastos, S. Ott, L. Hammarström, T. Edvinsson, J. Lewiński and J. Sá, *Sustainable Energy Fuels*, 2017, **1**, 69–73.

542 S. Troppmann, E. Brandes, H. Motschmann, F. Li, M. Wang, L. Sun and B. König, *Eur. J. Inorg. Chem.*, 2016, 554–560.

543 A. Onoda, Y. Kihara, K. Fukumoto, Y. Sano and T. Hayashi, *ACS Catal.*, 2014, **4**, 2645–2648.

544 Y. Sano, A. Onoda and T. Hayashi, *Chem. Commun.*, 2011, **47**, 8229–8231.

545 Y. Sano, A. Onoda and T. Hayashi, *J. Inorg. Biochem.*, 2012, **108**, 159–162.

546 W. Chen, X. Cai, L. Ji, X. Li, X. Wang, X. Zhang, Y. Gao and F. Feng, *Photosynth. Res.*, 2019, **142**, 169–180.

547 W. Chen, S. Li, X. Li, C. Zhang, X. Hu, F. Zhu, G. Shen and F. Feng, *Chem. Sci.*, 2019, **10**, 2179–2185.

548 S. Li, W. Chen, X. Hu and F. Feng, *ACS Appl. Bio Mater.*, 2020, **3**, 2482–2488.

549 X. Li, M. Wang, D. Zheng, K. Han, J. Dong and L. Sun, *Energy Environ. Sci.*, 2012, **5**, 8220.

550 H.-Y. Wang, W.-G. Wang, G. Si, F. Wang, C.-H. Tung and L.-Z. Wu, *Langmuir*, 2010, **26**, 9766–9771.

551 K. Feng, N. Xie, B. Chen, L.-P. Zhang, C.-H. Tung and L.-Z. Wu, *Macromolecules*, 2012, **45**, 5596–5603.

552 K. Sasan, Q. Lin, C. Mao and P. Feng, *Chem. Commun.*, 2014, **50**, 10390–10393.

553 S. Pullen, H. Fei, A. Orthaber, S. M. Cohen and S. Ott, *J. Am. Chem. Soc.*, 2013, **135**, 16997–17003.

554 S. Roy, V. Pascanu, S. Pullen, G. G. Miera, B. Martín-Matute and S. Ott, *Chem. Commun.*, 2017, **53**, 3257–3260.

555 W. Wang, T. Yu, Y. Zeng, J. Chen, G. Yang and Y. Li, *Photochem. Photobiol. Sci.*, 2014, **13**, 1590–1597.

556 M. Riazian and M. Yousefpoor, *Int. J. Smart Nano Mater.*, 2020, **11**, 47–64.

557 G.-J. Lee and J. J. Wu, *Powder Technol.*, 2017, **318**, 8–22.

558 T. Nann, S. K. Ibrahim, P.-M. Woi, S. Xu, J. Ziegler and C. J. Pickett, *Angew. Chem., Int. Ed.*, 2010, **49**, 1574–1577.

1784 | *Chem. Soc. Rev.*, 2021, **50**, 1668–1784

This journal is © The Royal Society of Chemistry 2021